Geochronology and fluid evolution of the Qulong porphyry system: Implications for porphyry deposit formation

YANG LI

Geochronology and fluid evolution of the Qulong porphyry system: Implications for porphyry deposit formation

Yang Li

University College

A thesis submitted in partial fulfilment of the requirements

for the degree of Doctor of Philosophy at Durham University

Department of Earth Sciences, Durham University

October, 2016

Although none of this had even a hope of any practical application in my life, much of what I stumbled into by following my curiosity and intuition turned out to be priceless later on.

—— Steve Jobs

Abstract

Understanding the metal enrichment process and rate in porphyry Cu systems (PCS) is critical to underpin the genetic model of PCS and refine the template for exploration, of which robust temporal constrain is the key. In addition, fluid evolution paths constrained by bulk analysis potentially suffer problems of contamination. Based on detailed field geology and petrographic study, this PhD thesis addresses the timescales and fluid evolution process of the world class Qulong porphyry Cu-Mo deposit, Tibet, China, by applying high precision geochronology and high spatial resolution isotope analysis.

A fluid inclusion study indicates that the bulk mineralization at Qulong was deposited between 425 and 280 ^{o}C under hydrostatic pressure conditions. The depth of formation of the Qulong porphyry Cu-Mo system is estimated at ~2.7 km, which implies ~2.3 km of erosion has occurred since its formation. Zircon CA-ID-TIMS U-Pb geochronology constrains the emplacement ages of the Rongmucuola pluton, the P porphyry and quartz aplite to 17.142 ± 0.014/0.014/0.023 (analytical/plus tracer/plus decay constant uncertainty), 16.009 ± 0.016/0.017/0.024 and 15.166 ± 0.010/0.011/0.020 Ma, respectively. Molybdenite ID-NTIMS Re-Os geochronology suggests that the bulk mineralization at Qulong was deposited through multiple shorted lived pulses (~ tens of kyrs) between 16.126 ± 0.008/0.060/0.077 and 15.860 ± 0.010/0.058/0.075 Ma, with a duration of 266 ± 13 kyrs. Quartz SIMS oxygen isotope analysis indicates a periodic interplay between meteoric and magmatic fluids and continuing increase of meteoric water from ~10 to ~25 % volume percent during the ore-forming process. As a result meteoric water is invoked as the main trigger for metal deposition at Qulong.

The major conclusions of this study from Qulong are supported by numerical modelling, titanium diffusion and high precision studies, and have implications for understanding porphyry systems worldwide, for example, multiple and cyclic magmatic-hydrothermal fluid pulses cooled by meteoric water are fundamental for ore formation.

Declaration

I declare that this thesis, which I submit for the degree of Doctor of Philosophy at Durham University, is my own work and not substantially the same as any which has previously been submitted at this or any other university.

Yang Li

University College, Durham University

October 2016

Acknowledgements

Now it comes to the end of my PhD journey, though only marks the start of my research adventure. Before I thank the individuals who made this journey lovely, I would like to thank all the funding agencies that have made this research possible. Durham University and China Scholarship Council generously funded my entire PhD study, with contribution from a NERC-NIGL facility grant. In addition, I received several research grants that have allowed me to travel to Tibet for fieldtrips, conduct analytical work in several labs across the oceans and attend national and international conferences. Namely, these funding agencies are the Society of Economic Geologists, the Geological Society of London, International Association of GeoChemistry, Universities' China Committee in London, Mineralogical Society and University College of Durham University.

As my primary supervisor, Prof. David Selby designed this project with me and brought me to Durham. He is a fantastic supervisor who respects my interests and keeps me on track. As the first source of advice, he is particularly efficient in sending feedback and always has the door (both physical and spiritual) open for discussions. He has really made this ponding journey enjoyable without loading pressure on me. He is not niggardly of praise, even when every time the returned manuscript is full of comments and corrections. Prof. Colin Macpherson, who is my second supervisor at Durham, gave me enormous help in the past three years. Although he is busy in most times as head of department, but always be able to arrange time to discuss my research, solve my puzzle, lead me back on track and give me encouragements. Dave introduced me to Dr. Daniel Condon, and they together opened the chamber of high precision geochronology to me. Dan is a great supervisor, in addition to train me under microscope and in the clean lab, he also inspired me to think and explore the world beyond economic geology. Dr. Xian-Hua Li was exceptionally supportive during my study, I got full support from him both in the SIMS lab and in supervision. Whenever I need help, from scientific questions to career choices, he is always there to read my emails or answer my phone calls. My special thanks goes to Prof. Jian-Wei Li, who offered enormous help during this journey, he is the one who took me to the academia world, and supported me in every aspect over the past years. I benefited hugely from Prof. You-Ye Zheng. He

lighted up my curiosity in chronological problems of mineral deposits when I was an undergraduate student, and then paved the way for my research in Tibet and beyond.

During this PhD, I was lucky to work with many people and study in different labs. It was great fun and very beneficial to work and have discussions with Jia Chang and Rui Wang. The SIMS lab in IGG-CAS supported my analysis there, with help from the staffs and students. Especially Hong-Xia Ma, Jiao Li, Xiao-Yan Jiang, Guo-Qiang Tang, Yu Liu who were very helpful during my visits. Simon Tapster from NIGL-BGS needs to be mentioned for his assistance and patience in the lab and his constructive comments and suggestions on my research. Prof. Martin Feely and Dr. Alessandra Costanzo are acknowledged for letting me conducting fluid inclusion research in NUIG.

I need to mention Miss Kate Horan, Prof. Jeremy Richards, Dr. Richard Sillitoe, Prof. Bruce Yardley, Prof. Mark Allen, Dr. Richard Brown, Prof. Massimo Chiaradia for sharing their expertise and helping me in different aspects. I must thank all my friends in Durham, although the list is too long to name. The cooking talents of all Chinese students/visitors in Earth Sciences are unforgivable. The parties, jokes and beers are amazing, with credit going to my great mates in the department. For people across the oceans, it is great to know you are always there. Of course, I need to thank the great staff both in the department and college, who helped me out over the past years. Also someone who needs to be mentioned is Jun-Wei Guo, as a friend accompanying me through thick and thin over the past tens of years, there is a fantastic world waiting for us to explore together. I want to thank Xiao-Yan Zhang for the accompaniment and encouragements; you are always my unfailing source of motivation.

Most importantly, I must thank my family, especially my mom, and my aunt (who passed away during my PhD). Without your endless understanding and love I could not go this far.

YANG LI, October-2016

Contents

Chapter 4 SIMS quartz oxygen isotopic composition of the Qulong porphyry Cu-Mo deposit, Tibet, China: Implications for metal deposition triggered by fluid mixing· 147

4.1 Introduction· ·148

4.2 Geological framework of Qulong· 151

4.3 Samples and analytical methods· 152

4.3.1 Samples· ·152

4.3.2 SIMS quartz oxygen isotope analytical method· · · · · · · · · · · · · ·153

4.3.3 Fluid oxygen isotopic composition and source constrains · · · · · ·155

4.4 Results· ·155

4.4.1 Oxygen isotope of quartz and zircon from Rongmucuola pluton·155

4.4.2 Quartz of the sinusoidal vein· 155

4.4.3 Textures and oxygen isotope of quartz grains associated with mineralization· 156

4.5 Discussion· 157

4.5.1 Primary oxygen isotope signature of vein quartz· · · · · · · · · · · · · 157

4.5.2 Equilibrium oxygen fractionation between quartz and water· · · ·159

4.5.3 Oxygen isotope of ore-forming fluid and meteoric water contribution· 161

4.6 Fluid mixing induced cooling as a trigger for ore formation· · · · · · · · · · 164

4.6.1 Significance of decompression, boiling, magnetite crystallization and water-rock interaction· 164

4.6.2 Metals deposition triggered by fluid mixing· · · · · · · · · · · · · · · · ·166

4.7 Conclusion· ·167

4.8 References· ·169

4.9 List of figures · 174

4.10 List of tables · 176

Chapter 5 Conclusions and outlook · 195

5.1 Nature of ore-forming fluid of the Qulong Cu-Mo deposit · · · · · · · · · · · 196

5.2 Timescale and cooling history of Qulong porphyry system · · · · · · · · · · · 197

5.3 Meteoric water involvement triggered metal deposition at Qulong · · · · · 198

5.4 Outlook · 199

5.5 References · 202

Chapter 1

Introduction

1.1 Porphyry copper deposits

Porphyry Cu systems are magmatic-hydrothermal deposits in which sulfide minerals precipitate from magmatic aqueous solutions at elevated temperatures (typically 300-450 ^{o}C), and are characterized by large tonnages and relatively low ore grades (Robb, 2009; Richards, 2011; Cooke et al., 2014). The deposit name is draw from the porphyritic texture of dike- and plug-like intrusions commonly associated spatially and genetically with mineralization (Seedorff et al., 2005). As the world's primary source of copper, molybdenum, rhenium with additional significant contribution of gold (Sillitoe, 2010), they have fascinated economic geologists and excited miners for over a century, but with deposits exposed at the surface having been mostly discovered, it is now increasingly challenging to find new discoveries (Richards, 2013; Wilkinson, 2013; Richards, 2016).

Globally, the majority of known porphyry copper deposits are genetically related to intermediate to felsic calcalkaline magmas in volcano-plutonic arcs above subduction zones, e.g., the Andes. However, recently, a considerable amount of porphyry copper deposits are been described that formed in a post subduction or collisional tectonic setting, e.g., the Gangdese porphyry copper belt (Seedorff et al., 2005; Hou et al., 2009; Richards, 2009, 2013; Chiaradia et al., 2014; Richards, 2015).

Porphyry copper deposits are arguably the most studied deposit type, but debate continues regarding the ore-forming process (Kouzmanov and Pokrovski, 2012; Chiaradia et al., 2014; Cooke et al., 2014), e.g., lifespan of mineralization, prolonged mineralization duration or multiple short-lived cycles, fluid evolution process and triggers for sulfide precipitation. These are the topics that this PhD will explore.

1.2 Gangdese porphyry copper belt and Qulong porphyry Cu-Mo deposit

In comparison to porphyry deposits hosted in subduction settings, considerably fewer porphyry deposits are documented in collisional and post subduction settings. The Gangdese porphyry copper belt is a newly discovered metallogenic belt in a post subduction setting (Hou et al., 2009). The Gangdese magmatic belt records prolonged magmatic events that are associated with the Neo-Tethyan ocean northward subduction, initial India-Asia collision, Indian slab breakoff and intracontinental convergence (Wang et al., 2015; Zhu et al., 2015). The Oligo-Miocene intermediate-felsic igneous rocks in the Gangdese magmatic belt show a sharp longitudinal distinction in the distribution of porphyry-type mineralization with a boundary at ~89^{o} E, with most discovered deposits being associated with Miocene granitoid plutons in the east, while plutons in the western part are mostly barren (Wang et al., 2015). The eastern part of the Gangdese magmatic belt is termed as Gangdese porphyry copper belt (GPCB), which contains >20 porphyry copper systems formed in a post-collisional (India-Asian) setting, as represented by Qulong, Jiama, Lakang'e, Dabu, Tinggong, Zhunuo, Chuibaizi, Bangpu, Nuri, Zhibula (Hou et al., 2009; Zheng et al., 2015). The Qulong porphyry Cu-Mo deposit is the largest both in the belt and in China (Zheng et al., 2004; Yang et al., 2009), and hosts 2200 million tonnes of ore comprising 0.5 % Cu and 0.03 % Mo (Li et al., 2016). As a representative deposit in GPCB, and an example in post-collisional setting, Qulong is selected to conduct this research.

1.3 Principles of high precision geochronology

High precision geochronology is integral to testing hypotheses regarding the correlation, cause, and rates of events (Schmitz and Kuiper, 2013), and has been used

in this study to investigate the metal enrichment process in PCS. As the foundation of this study is built on high precision geochronology, the first principle of high precision geochronology is illustrated by molybdenite Re-Os geochronology. For isotope dilution based zircon U-Pb geochronology, the principles are the same as molybdenite Re-Os geochronology, despite its unique dual decay system (Schoene, 2014).

1.3.1 Decay equation and model age

All radiometric dating methods rely on the decay of a parent isotope to a daughter isotope with a fixed half-life (Schoene, 2014; Stein, 2014). This basic principle is illustrated here for Re-Os isotopic system as it is the only geochronometer that can directly date the ore minerals (sulfides, e.g., molybdenite) that this study focuses on:

$$^{187}Os_{present} = {}^{187}Os_{initial} + {}^{187}Re_{present}(e^{\lambda t} - 1) \quad [1]$$

where $^{187}Os_{present}$ and $^{187}Re_{present}$ represent the present mole concentration (moles) or number of atoms of ^{187}Os and ^{187}Re in a given sample (e.g., molybdenite), respectively. The initial ^{187}Os ($^{187}Os_{initial}$) stands for the mole concentration (moles) or number of ^{187}Os atoms when isotopic system of the sample becomes closed. Lambda (λ) is the decay constant of ^{187}Re (Smoliar et al., 1996; Selby et al., 2007) and t is the time in years since the isotopic system became closed until AD1950 (so-called present). Obviously equation [1] is only valid when no disturbance of the isotopic system occurred post-closure of the isotopic systematics.

In some mineral systems, as is commonly the case for molybdenite (Selby and Creaser, 2001; Stein et al., 2001; Markey et al., 2003; Stein, 2014), the

contribution of initial osmium for age calculation is negligible ($^{187}Os_{initial} \approx 0$). In this case, the equation [1] is simplified to:

$$^{187}Os_{present} = {}^{187}Re_{present} (e^{\lambda t} - 1) \qquad [2]$$

The "age" can be solved by measuring the current moles of ^{187}Os and ^{187}Re in a single sample. For equation [1], when the $^{187}Os_{initial}$ is not negligible, the moles of $^{187}Os_{initial}$ need to be determined by measuring initial Os concentration with assumed initial osmium isotopic composition (Markey et al., 2003; Stein, 2014; Zimmerman et al., 2014). Alternatively, the age can be solved through regression of a suite of co-genetic samples, which is the so-called isochron method (Faure, 1977) and not discussed here.

1.3.2 Isotope dilution

Isotope dilution is the most precise and accurate method for element concentration measurement and is the ideal choice for high precision geochronology (Vogl, 2013; Schoene, 2014; Stracke et al., 2014; Condon et al., 2015; McLean et al., 2015). For isotope dilution analysis, initially a known quantity of an element having one enriched isotope - the spike or tracer - is added to a known quantity of sample. The concentration of the target element or isotope is determined by measuring the isotopic composition of the mixture. Modern isotope dilution now typically uses a spike with two enriched isotopes, the so-called double spike technique (Rudge et al., 2009; Stracke et al., 2014). Isotope dilution can be applied to any element with two or more isotopes (Stracke et al., 2014). Equation [4] and [5] illustrate the principle of isotope dilution for Os isotopes determination.

$$R = \frac{W_{sample} * {}^{187}Os^{mole}_{sample} + W_{spike} * {}^{187}Os^{mole}_{spike}}{W_{sample} * {}^{188}Os^{mole}_{sample} + W_{spike} * {}^{188}Os^{mole}_{spike}} \qquad [4]$$

$$Q = \frac{W_{sample} * {}^{190}Os^{mole}_{sample} + W_{spike} * {}^{190}Os^{mole}_{spike}}{W_{sample} * {}^{188}Os^{mole}_{sample} + W_{spike} * {}^{188}Os^{mole}_{spike}} \quad [5]$$

Where R and Q are the measured $^{187}Os/^{188}Os$ and $^{190}Os/^{188}Os$ ratio of the mixture by mass spectrometry, respectively. W_{sample} and W_{spike} refer to the weight of sample and spike, respectively. ${}^{1xx}Os^{mole}_{sample/spike}$ is the mole concentration of ^{1xx}Os in the sample or spike. For the spike, these concentrations and isotopic compositions are known through calibration. Solving the three unknowns from equation [4] and [5] is possible as the $^{190}Os/^{188}Os$ value of the sample is known. A special case for this approach is molybdenite, which contains negligible common Os, and only radiogenic ^{187}Os. In this case, a solution bearing natural Os isotopic composition can be used as spike, and equation [4] can be simplified and solved directly. As the spike is calibrated against gravimetric reference solutions prepared by accurate weighting, isotope dilution is a primary analytical method which has the potential to directly trace back to SI units through accurate weighting (Markey et al., 2003; Condon et al., 2015; McLean et al., 2015). The target isotope's concentration is determined from the spike, thus its precision will never be better than that of the spike, which makes spike calibration the most critical step for high precision measurements (Markey et al., 2003; Schoene, 2014; Stein, 2014; Stracke et al., 2014; Condon et al., 2015). A further benefit for isotopic dilution is when the sample and spike have achieved complete isotopic composition homogenization, there is no requirement for 100 % element recovery, this makes isotope dilution ideal for analysis which need element separation and purification prior to analysis (Stracke et al., 2014; Condon et al., 2015).

As well as the spike calibration, mass dependent fractionation during mass spectrometry analysis also influences the data quality (Doucelance and Manhes, 2001;

Markey et al., 2003). For elements which have more than 2 isotopes, mass dependent fractionation can be best monitored by double spike technique or by using natural occurring isotopes (Stracke et al., 2014). For samples which have only two isotopes, depending on the analytical methods used, the fractionation can be corrected by total evaporation, sample-standard bracketing or adding other isotopic composition known elements (e.g. Ir and W for Re) (Suzuki et al., 2004; Vogl, 2013; Stein and Hannah, 2014). For high precision geochronology, thermal ionization mass spectrometry (TIMS) remains the best choice for its ability to maintain ion beam stability for hours of analysis as well as high ion transportation efficiency (Creaser et al., 1991; Vogl, 2013; Schoene, 2014).

1.3.3 Data quality evaluation

Data quality generally is evaluated by accuracy and precision. Precision is a measurement of the reproducibility of analysis while accuracy is the closeness of agreement between a measured value and the true value (Schoene et al., 2013; Schoene, 2014). Accuracy and precision are independent of each other. It is ideal to have data with both high precision and high accuracy, but this is difficult for natural samples due to the complexity in geological history, as well as analytical challenges (Schoene et al., 2013; Schoene, 2014).

Here we use uncertainties to characterise the dispersion of the quantity value being attributed to the subject of a measurement that includes components arising from both random and systematic measurement uncertainties. Random uncertainties refer to those varying in an unpredictable manner in replicate measurement (e.g., sample weight, isotope ratio measured by mass spectrometry). Systematic uncertainties are those remain constant or vary in predictable ways across replicate

measurements (e.g., age uncertainty arising from decay constant uncertainty or spike calibration) (Condon et al., 2015; McLean et al., 2015). As stated by Ludwig (2003a), the uncertainty of measurements is as important as the data itself. Modern geochronology reveals that no sample or mineral is identical homogenous (Bowring, 2006; Schoene et al., 2013), and the uncertainty will increasingly be dominated by geological scatter with an increase in analytical precision.

As represented in U-Pb studies, rather than using a single analysis, many analyses have been pooled together by applying statistical models. Weighted mean is a widely used statistical model, which can significantly reduce the final uncertainty through accounting for scatter caused by random analytical uncertainty. By weighting each analysis according to the inverse square of its errors, a data set with high sample numbers (n) will yield better precision. But this should be used with great caution, as this approach is based on the assumptions that the data set represents repeat measurements of the true value, which can not be tested in most cases unless all the uncertainties are estimated correctly (Bowring, 2006; Schmitz and Kuiper, 2013; Horstwood et al., 2016). Consequently reducing the uncertainty from high n and low precision datasets takes the risk of having statistical robust, but incorrect data (Schoene, 2014). Fortunately, the goodness of fit of the data set to the statistical model can be evaluated by mean square of weighted deviates (MSWD) of the weighted mean (Wendt and Carl, 1991). A MSWD>>1 suggests it is difficult to fit the data to the statistical model, and this offset either arises from geological scatter or underestimation of analytical uncertainties (Ludwig, 2003b). A MSWD<<1 indicates the data is easily fitted to the statistical model, this generally due to overestimation of analytical uncertainties (Wendt and Carl, 1991; Kalsbeek, 1992; Ludwig, 2003b; York et al., 2004; Schoene, 2014). The MSWD value should be

close to unity when the geological scatter and analytical uncertainties are well balanced, e.g., the measured parameters can be regarded as true values with current analytical precision (Ludwig, 2003b; Horstwood et al., 2016). An argument describing the acceptable distribution of MSWD values for a given number of a dataset is given by Wendt and Carl (1991) and can be represented by the following equation (Schoene, 2014):

$$\sigma_{MSWD} = (2/(N - 2))^{0.5} \quad [5]$$

As discussed by Wendt and Carl (1991), the acceptable MSWD value is a function of n, and MSWD equal to 1 is not always the critical point for evaluating the quality of small data set. In addition, MSWD values can not be used to assess accuracy of the dataset or open system behaviour, especially for data sets with small number or poor analysis (Kalsbeek, 1992; Wendt, 1992; Horstwood et al., 2016).

When data are compared, the uncertainties should be accounted for first. For data using the same method in the same laboratory, under same conditions, the tracer calibration and decay constant uncertainties can be ignored, as they are systematic uncertainties. The same is true for standard reproducibility uncertainties (Chiaradia et al., 2013; Schoene et al., 2013). In contrast, when data are collected from different laboratories, using the same method, the tracer calibration uncertainty becomes random uncertainty and needs to be evaluated. As long as the same radiometric system is used, the decay constant uncertainty can be ignored, but needs to be accounted for when comparing data across multiple radiometric systems (Kuiper et al., 2008). The latter uncertainty currently controls the resolution when comparing data between different radiometric geochronometers.

It is recommended all data and plots should always be presented with 2 sigma (2σ) uncertainty to maximize the possibility that the true data point lies within the

quoted uncertainties interval (Horstwood et al., 2016). In general, 2 sigma uncertainty indicates that ~95.45 % of the data fall within this interval during replicated measurements. This needs to be distinguished between the 95 % conf. error reported by Isoplot (Ludwig, 2003b). In the default setting of *Isoplot*, when the data fits the statistic model, as evaluated by the probability of fit, the 95 % conf. error is calculated by multiplying the 1 sigma error by 2. However, when the dataset fails to fit the statistic model, the 95 % conf. error in *Isoplot* is calculated by multiplying the 1 sigma error with the square root of the MSWD value and the student's-t value for n-1 degree of freedom (Brooks et al., 1972).

1.4 Current understanding of porphyry ore-forming process and aims of this study

1.4.1 Temporal constrains of mineralization process

The duration of porphyry Cu deposit formation is controversial, with studies suggesting over a million years, with others arguing for much shorter timescales (tens of thousands of years) (Chiaradia et al., 2014). For deposits with prolonged duration of formation, multiple magmatic-mineralization pulses are essential as demonstrated both by field observation (Sillitoe, 2010) and analytical approaches (Stein, 2014; Zimmerman et al., 2014; Spencer et al., 2015). However, for deposits with shorter lifetime, it is not clear yet whether they form throughout the lifetime or during multiple intermittent pluses. Also questionable is the timescale of each mineralization pulse, if multiple mineralization pulses are present. Additionally, the dynamic magmatic-hydrothermal process may reset chronometers with low closure temperatures and add uncertainties to thermochronology studies. The answers for these questions will shape our understandings for metals enrichment processes, e.g.,

are multiple mineralization pulses necessary to form giant deposits, or is a prolonged mineralization duration essential for economic deposits? Based on veinlet classification and fluid inclusion study of Chapter 2, these questions are explored in Chapter 3, in which high precision Re-Os and U-Pb geochronology are used to refine the timeframe of the world class Qulong porphyry Cu-Mo deposit. Chapter 4 further investigates the fluid evolution under an absolute timeframe.

Chapter 2 constrains the fluid P-T-X conditions during ore formation at Qulong. In order to assess fluid evolution paths, a detailed description of the geology, alteration and mineralization at Qulong is presented. All the field investigations and drill cores samples collection were conducted by the author, with help from Dr Rui Wang from CSIRO, Australia, and Mr. Jia Chang from CUG, China. All sample preparations were completed by the author. Laboratory work and data evaluation of the fluid inclusion study were conducted by the author at the National University of Ireland, Galway (NUIG). Zircon SIMS oxygen isotope and U-Pb analysis were carried out by the author in Institute of Geology and Geophysics, Chinese Academy of Sciences, Beijing (IGGCAS). The chapter was written by the author with Prof. David Selby (supervisor at Durham), Prof. Martin Feely (supervisor at NUIG), Dr Alex Costanzo (collaborator at NUIG), and Prof. Xian-Hua Li (supervisor at IGGCAS) providing editorial comments and suggestions. A version of this chapter has been published in Mineralium Deposita, co-authored by David Selby, Martin Feely, Alext Costanzo and Xian-Hua Li.

Chapter 3 provides detailed high precision zircon U-Pb and molybdenite Re-Os dates to constrain the timescales of Qulong porphyry system, which has been further used to understand the ore-forming process and thermal history of Qulong. The sample set used in this chapter is the same as that used in chapter 2. Sample

preparation was conducted by the author. Zircon grains separation and CA-ID-TIMS U-Pb geochronology was conducted by the author in NERC Isotope Geosciences Laboratory (NIGL), British Geological Survey, UK, with help from Dr Daniel Condon and Simon Tapster. Molybdenite separations and Re-Os geochronology was undertaken by the author in Durham University under the supervision of Prof. David Selby. The chapter is written by the author with editorial comments and suggestions from Prof. David Selby (supervisor at Durham), Dr Daniel Condon (supervisor at NIGL) and Dr Simon Tapster (collaborator at NIGL). A version of this chapter will be submitted to Earth and Planetary Science Letters, with David Selby, Simon Tapster and Daniel Condon as co-authors.

1.4.2 Sulfide precipitation mechanism

Formation of economic valuable porphyry deposits requires efficient concentration of Cu-Mo-Au from metalliferous fluid in restricted space. Depressurization, fluid mixing and unmixing, cooling and water-rock interaction have been proposed as triggers for metal deposition, but the relative importance of these different processes in generating economic ore bodies has been the subject of much debate. The role of meteoric water is particularly controversial (Kouzmanov and Pokrovski, 2012; Cooke et al., 2014).

Stable isotope ratio and fluid inclusions combined with numerical simulation have been used to suggest progressive involvement of meteoric water during ore-forming process, but such an external component is considered negligible in the early stages of mineralization and has limited contribution to ore-formation (Stein and Hannah, 1985; Cooke and McPhail, 2001; Watanabe and Hedenquist, 2001; Ulrich et al., 2002; Rusk et al., 2008). Other studies, however, argue that meteoric water is an

essential component during the entire ore-forming process (Friedman et al., 1974; Sun and Eadington, 1987; Hedenquist and Aoki, 1991; Sheets et al., 1996; Selby et al., 2001; Weis et al., 2012).

Understanding the physical and chemical conditions of mineralization process in porphyry deposits relies largely on H-O isotope and fluid inclusion data of gangue minerals, commonly quartz (Cooke et al., 2014). A temporal relationship between ore sulfides and gangue minerals used to measure fluid inclusion and isotope geochemistry must be established unequivocally to provide a tight constraint on the evolution of ore fluids (Harris and Golding, 2002; Redmond et al., 2004). However, the complicated textures of silicate minerals clearly indicate multiple generations of fluid evolution and add uncertainties to the information inferred from bulk analysis (Allan and Yardley, 2007; Tanner et al., 2013; Vasyukova et al., 2013; Fekete et al., 2016). Further, there is growing evidence suggesting that porphyry ore formation is multi-pulsed, and results in overlapping or repetitions of veinlets as demonstrated both by field investigations and analytical approaches (Sillitoe, 2010; Stein, 2014). In this case, due to a lack of deposit-wide crosscutting relationship, traditional alteration and veinlet chronology can not be correlated at the deposit-scale with confidence. These uncertainties require the need to test fluid evolution through *in-situ* analysis with absolute chronology.

Chapter 4 presents quartz SIMS oxygen isotope data, with formation temperature and ages constrained by fluid inclusion and geochronology studies in Chapter 2 and Chapter 3, respectively. The original approach used here permits tracing the fluid evolution path under an absolute timeframe and evaluates the triggers of sulfide precipitation. The samples used in this chapter are the same sample set used in Chapter 2 and Chapter 3, with additional samples collected by the

author. The sample preparation, SIMS quartz oxygen isotope analysis and data evaluation was conducted by the author in IGGCAS. The chapter was written by the author with editorial comments and suggestions from Prof. David Selby (supervisor at Durham) and Prof. Xian-Hua Li (supervisor at IGGCAS). A version of this chapter will be submitted to Geochimica et Cosmochimica Acta, co-authored by Xian-Hua Li and David Selby.

Chapter 5 summarizes the research of this thesis and discusses potential outlook for future studies to establish the temporal evolution of porphyry Cu systems using high precision geochronology.

1.5 References

Allan, M.M., Yardley, B.W.D., 2007. Tracking meteoric infiltration into a magmatic-hydrothermal system: A cathodoluminescence, oxygen isotope and trace element study of quartz from Mt. Leyshon, Australia. Chemical Geology 240, 343-360.

Bowring, S.A.S., B. ; Crowley, J. L. ; Ramezani, J. ; Condon, D. J. , 2006. High-Precision U-Pb Zircon Geochronology and the Stratigraphic Record: Progress and Promise, in: Olszewski, T. (Ed.), Geochronology: emerging opportunities Paleontological Society Short Couse, New Haven, CT, pp. 25-46.

Brooks, C., Hart, S., Wendt, I., 1972. Realistic use of two - error regression treatments as applied to rubidium - strontium data. Reviews of Geophysics 10, 551-577.

Chiaradia, M., Schaltegger, U., Spikings, R., 2014. Time Scales of Mineral Systems-Advances in Understanding Over the Past Decade. Soc Econ Geol Spec P, 37-58.

Chiaradia, M., Schaltegger, U., Spikings, R., Wotzlaw, J.-F., Ovtcharova, M., 2013. How Accurately Can We Date the Duration of Magmatic-Hydrothermal Events in Porphyry Systems?—An Invited Paper. Economic Geology 108, 565-584.

Condon, D.J., Schoene, B., McLean, N.M., Bowring, S.A., Parrish, R.R., 2015. Metrology and traceability of U-Pb isotope dilution geochronology (EARTHTIME Tracer Calibration Part I). Geochimica Et Cosmochimica Acta 164, 464-480.

Cooke, D.R., Hollings, P., Wilkinson, J.J., Tosdal, R.M., 2014. 13.14 - Geochemistry of Porphyry Deposits, in: Turekian, H.D.H.K. (Ed.), Treatise on Geochemistry (Second Edition). Elsevier, Oxford, pp. 357-381.

Cooke, D.R., McPhail, D.C., 2001. Epithermal Au-Ag-Te mineralization, Acupan, Baguio district, Philippines: Numerical simulations of mineral deposition. Economic Geology and the Bulletin of the Society of Economic Geologists 96, 109-131.

Creaser, R.A., Papanastassiou, D.A., Wasserburg, G.J., 1991. Negative Thermal Ion Mass-Spectrometry of Osmium, Rhenium, and Iridium. Geochimica Et Cosmochimica Acta 55, 397-401.

Doucelance, R., Manhes, G., 2001. Reevaluation of precise lead isotope measurements by thermal ionization mass spectrometry: comparison with determinations by plasma source mass spectrometry. Chemical Geology 176, 361-377.

Faure, G., 1977. Principles of isotope geology.

Fekete, S., Weis, P., Driesner, T., Heinrich, C.A., Baumgartner, L., Bouvier, A.-S., 2016. The physical hydrology of magmatic-hydrothermal systems: High-resolution ^{18}O records of magmatic-meteoric water interaction from the Yankee Lode tin deposit (Mole Granite, Australia), EGU General Assembly 2016, pp. EGU2016-14338.

Friedman, I., Lipman, P.W., Obradovich, J.D., Gleason, J.D., Christiansen, R.L., 1974. Meteoric water in magmas. Science 184, 1069-1072.

Harris, A.C., Golding, S.D., 2002. New evidence of magmatic-fluid-related phyllic alteration: Implications for the genesis of porphyry Cu deposits. Geology 30, 335-338.

Hedenquist, J.W., Aoki, M., 1991. Meteoric Interaction with Magmatic Discharges in Japan and the Significance for Mineralization. Geology 19, 1041-1044.

Horstwood, M.S.A., Košler, J., Gehrels, G., Jackson, S.E., McLean, N.M., Paton, C., Pearson, N.J., Sircombe, K., Sylvester, P., Vermeesch, P., Bowring, J.F., Condon, D.J., Schoene, B., 2016. Community-Derived Standards for LA-ICP-MS U-(Th-)Pb Geochronology – Uncertainty Propagation, Age Interpretation and Data Reporting. Geostandards and Geoanalytical Research, n/a-n/a.

Hou, Z.Q., Yang, Z.M., Qu, X.M., Meng, X.J., Li, Z.Q., Beaudoin, G., Rui, Z.Y., Gao, Y.F., Zaw, K., 2009. The Miocene Gangdese porphyry copper belt generated during post-collisional extension in the Tibetan Orogen. Ore Geology Reviews 36, 25-51.

Kalsbeek, F., 1992. The Statistical Distribution of the Mean Squared Weighted Deviation - Comment - Isochrons, Errorchrons, and the Use of Mswd-Values - Discussion. Chemical Geology 94, 241-242.

Kouzmanov, K., Pokrovski, G.S., 2012. Hydrothermal controls on metal distribution in porphyry Cu (-Mo-Au) systems. Special Publication of the Society of Economic Geologists 16, 573–618.

Kuiper, K.F., Deino, A., Hilgen, F.J., Krijgsman, W., Renne, P.R., Wijbrans, J.R., 2008. Synchronizing rock clocks of Earth history. Science 320, 500-504.

Li, Y., Selby, D., Feely, M., Costanzo, A., Li, X.-H., 2016. Fluid inclusion characteristics and molybdenite Re-Os geochronology of the Qulong porphyry copper-molybdenum deposit, Tibet. Mineralium Deposita.

Ludwig, K., 2003a. Mathematical–statistical treatment of data and errors for 230Th/U geochronology. Reviews in Mineralogy and Geochemistry 52, 631-656.

Ludwig, K.R., 2003b. User's manual for Isoplot 3.00: a geochronological toolkit for Microsoft Excel. Kenneth R. Ludwig.

Markey, R., Hannah, J.L., Morgan, J.W., Stein, H.J., 2003. A double spike for osmium analysis of highly radiogenic samples. Chemical Geology 200, 395-406.

McLean, N.M., Condon, D.J., Schoene, B., Bowring, S.A., 2015. Evaluating uncertainties in the calibration of isotopic reference materials and multi-element isotopic tracers (EARTHTIME Tracer Calibration Part II). Geochimica Et Cosmochimica Acta 164, 481-501.

Redmond, P.B., Einaudi, M.T., Inan, E.E., Landtwing, M.R., Heinrich, C.A., 2004. Copper deposition by fluid cooling in intrusion-centered systems: New insights from the Bingham porphyry ore deposit, Utah. Geology 32, 217-220.

Richards, J., 2016. Clues to hidden copper deposits. Nature Geoscience 9, 195-196.

Richards, J.P., 2009. Postsubduction porphyry Cu-Au and epithermal Au deposits: Products of remelting of subduction-modified lithosphere. Geology 37, 247-250.

Richards, J.P., 2011. Magmatic to hydrothermal metal fluxes in convergent and collided margins. Ore Geology Reviews 40, 1-26.

Richards, J.P., 2013. Giant ore deposits formed by optimal alignments and combinations of geological processes. Nature Geoscience 6, 911-916.

Richards, J.P., 2015. Tectonic, magmatic, and metallogenic evolution of the Tethyan orogen: From subduction to collision. Ore Geology Reviews 70, 323-345.

Robb, L., 2009. Introduction to ore-forming processes. Wiley-Blackwell, Hoboken, New Jersey.

Rudge, J.F., Reynolds, B.C., Bourdon, B., 2009. The double spike toolbox. Chemical Geology 265, 420-431.

Rusk, B.G., Lowers, H.A., Reed, M.H., 2008. Trace elements in hydrothermal quartz: Relationships to cathodoluminescent textures and insights into vein formation. Geology 36, 547-550.

Schmitz, M.D., Kuiper, K.F., 2013. High-Precision Geochronology. Elements 9, 25-30.

Schoene, B., 2014. 4.10 - U–Th–Pb Geochronology, in: Turekian, H.D.H.K. (Ed.), Treatise on Geochemistry (Second Edition). Elsevier, Oxford, pp. 341-378.

Schoene, B., Condon, D.J., Morgan, L., McLean, N., 2013. Precision and Accuracy in Geochronology. Elements 9, 19-24.

Seedorff, E., Dilles, J., Proffett, J., Einaudi, M., Zurcher, L., Stavast, W., Johnson, D., Barton, M., 2005. Porphyry deposits: characteristics and origin of hypogene features. Economic Geology 100th Anniversary Volume 29, 251-298.

Selby, D., Creaser, R.A., 2001. Re-Os geochronology and systematics in molybdenite from the Endako porphyry molybdenum deposit, British Columbia, Canada. Economic Geology and the Bulletin of the Society of Economic Geologists 96, 197-204.

Selby, D., Creaser, R.A., Stein, H.J., Markey, R.J., Hannah, J.L., 2007. Assessment of the Re-187 decay constant by cross calibration of Re-Os molybdenite and U-Pb zircon chronometers in magmatic ore systems. Geochimica Et Cosmochimica Acta 71, 1999-2013.

Selby, D., Nesbitt, B.E., Creaser, R.A., Reynolds, P.H., Muehlenbachs, K., 2001. Evidence for a nonmagmatic component in potassic hydrothermal fluids of porphyry Cu-Au-Mo systems, Yukon, Canada. Geochimica Et Cosmochimica Acta 65, 571-587.

Sheets, R.W., Nesbitt, B.E., Muehlenbachs, K., 1996. Meteoric water component in magmatic fluids from porphyry copper mineralization, Babine Lake area, British Columbia. Geology 24, 1091-1094.

Sillitoe, R.H., 2010. Porphyry Copper Systems. Economic Geology 105, 3-41.

Smoliar, M.I., Walker, R.J., Morgan, J.W., 1996. Re-Os ages of group IIA, IIIA, IVA, and IVB iron meteorites. Science 271, 1099-1102.

Spencer, E.T., Wilkinson, J.J., Creaser, R.A., Seguel, J., 2015. The Distribution and Timing of Molybdenite Mineralization at the El Teniente Cu-Mo Porphyry Deposit, Chile. Economic Geology 110, 387-421.

Stein, H., Hannah, J., 2014. Rhenium–Osmium Geochronology: Sulfides, Shales, Oils, and Mantle, in: Rink, W.J., Thompson, J. (Eds.), Encyclopedia of Scientific Dating Methods. Springer Netherlands, pp. 1-25.

Stein, H.J., 2014. 13.4 - Dating and Tracing the History of Ore Formation, in: Turekian, H.D.H.K. (Ed.), Treatise on Geochemistry (Second Edition). Elsevier, Oxford, pp. 87-118.

Stein, H.J., Hannah, J.L., 1985. Movement and Origin of Ore Fluids in Climax-Type Systems. Geology 13, 469-474.

Stein, H.J., Markey, R.J., Morgan, J.W., Hannah, J.L., Schersten, A., 2001. The remarkable Re-Os chronometer in molybdenite: how and why it works. Terra Nova 13, 479-486.

Stracke, A., Scherer, E.E., Reynolds, B.C., 2014. 15.4 - Application of Isotope Dilution in Geochemistry, in: Turekian, H.D.H.K. (Ed.), Treatise on Geochemistry (Second Edition). Elsevier, Oxford, pp. 71-86.

Sun, S.S., Eadington, P.J., 1987. Oxygen Isotope Evidence for the Mixing of Magmatic and Meteoric Waters during Tin Mineralization in the Mole Granite, New-South-Wales, Australia. Economic Geology 82, 43-52.

Suzuki, K., Miyata, Y., Kanazawa, N., 2004. Precise Re isotope ratio measurements by negative thermal ionization mass spectrometry (NTI-MS) using total evaporation technique. International Journal of Mass Spectrometry 235, 97-101.

Tanner, D., Henley, R.W., Mavrogenes, J.A., Holden, P., 2013. Combining in situ isotopic, trace element and textural analyses of quartz from four magmatic-hydrothermal ore deposits. Contributions to Mineralogy and Petrology 166, 1119-1142.

Ulrich, T., Günther, D., Heinrich, C.A., 2002. The Evolution of a Porphyry Cu-Au Deposit, Based on LA-ICP-MS Analysis of Fluid Inclusions: Bajo de la Alumbrera, Argentina. Economic Geology 97, 1889-1920.

Vasyukova, O.V., Kamenetsky, V.S., Goemann, K., Davidson, P., 2013. Diversity of primary CL textures in quartz from porphyry environments: implication for origin of quartz eyes. Contributions to Mineralogy and Petrology 166, 1253-1268.

Vogl, J., 2013. Advances in isotope ratio mass spectrometry and required isotope reference materials. Mass Spectrom (Tokyo) 2, S0020.

Wang, R., Richards, J.P., Zhou, L.M., Hou, Z.Q., Stern, R.A., Creaser, R.A., Zhu, J.J., 2015. The role of Indian and Tibetan lithosphere in spatial distribution of Cenozoic magmatism and porphyry Cu-Mo deposits in the Gangdese belt, southern Tibet. Earth-Science Reviews 150, 68-94.

Watanabe, Y., Hedenquist, J., 2001. Mineralogic and stable isotope zonation at the surface over the El Salvador porphyry copper deposit, Chile. Economic Geology and the Bulletin of the Society of Economic Geologists 96, 1775-1797.

Weis, P., Driesner, T., Heinrich, C.A., 2012. Porphyry-copper ore shells form at stable pressure-temperature fronts within dynamic fluid plumes. Science 338, 1613-1616.

Wendt, I., 1992. The Statistical Distribution of the Mean Squared Weighted Deviation - Reply. Chemical Geology 94, 242-243.

Wendt, I., Carl, C., 1991. The Statistical Distribution of the Mean Squared Weighted Deviation. Chemical Geology 86, 275-285.

Wilkinson, J.J., 2013. Triggers for the formation of porphyry ore deposits in magmatic arcs. Nature Geoscience 6, 917-925.

Yang, Z.M., Hou, Z.Q., White, N.C., Chang, Z.S., Li, Z.Q., Song, Y.C., 2009. Geology of the post-collisional porphyry copper-molybdenum deposit at Qulong, Tibet. Ore Geology Reviews 36, 133-159.

York, D., Evensen, N.M., Martinez, M.L., Delgado, J.D., 2004. Unified equations for the slope, intercept, and standard errors of the best straight line. American Journal of Physics 72, 367-375.

Zheng, Y.-Y., Xue, Y.-X., Cheng, L.-J., Fan, Z.-H., Gao, S.-B., 2004. Finding,Characteristics and Significances of Qulong Superlarge Porphyry Copper (Molybdenum) Deposit, Tibet. Earth Sciences 29, 103-108.

Zheng, Y.Y., Sun, X., Gao, S.B., Wu, S., Xu, J., Jiang, J.S., Chen, X., Zhao, Z.Y., Liu, Y., 2015. Metallogenesis and the minerogenetic series in the Gangdese polymetallic copper belt. Journal of Asian Earth Sciences 103, 23-39.

Zhu, D.C., Wang, Q., Zhao, Z.D., Chung, S.L., Cawood, P.A., Niu, Y., Liu, S.A., Wu, F.Y., Mo, X.X., 2015. Magmatic record of India-Asia collision. Sci Rep 5, 14289.

Zimmerman, A., Stein, H.J., Morgan, J.W., Markey, R.J., Watanabe, Y., 2014. Re–Os geochronology of the El Salvador porphyry Cu–Mo deposit, Chile: Tracking analytical improvements in accuracy and precision over the past decade. Geochimica et Cosmochimica Acta 131, 13-32.

Chapter 2

Fluid inclusion characteristics and molybdenite Re-Os geochronology of the Qulong porphyry copper-molybdenum deposit, Tibet *

*A version of this chapter has been published in Mineralium Deposita (doi: 10.1007/s00126-016-0654-z), and co-authored with David Selby of Durham University, Martin Feely and Alessandra Costanzo of National University of Ireland, Galway and Xian-Hua Li of Institute of Geology and Geophysics, Chinese Academy of Sciences.

2.1 Introduction

The majority of porphyry copper deposits are situated within magmatic arcs and are genetically related to subduction processes, e.g., Central Chile (Cooke et al. (2005), but porphyry copper deposits are also associated with post-collisonal tectonic settings, e.g., the Gangdese Porphyry Copper Belt (GPCB), China (Yang et al., 2009; Hou et al., 2015) and Papua New Guinea-Irian Jaya (Cooke et al., 2005; Richards, 2013). In both subduction-related and post-collisional tectonic settings, porphyry copper deposits share a genetic association with magmatism and possess similar mineralization styles and alteration types (Richards, 2009; Hou et al., 2015).

Metals in porphyry copper deposits are considered to be deposited through the dynamic evolution of a magmatic-hydrothermal fluid that undergoes depressurization, cooling, chemical reactions with wall rocks (mainly the ore-hosting granite), and mixing with non-magmatic fluids (Seedorff et al., 2005; Richards, 2011; Cooke et al., 2014). As a result, porphyry systems are characterized by extensive vein formation associated with mineralization and alteration. Generally, hydrothermal alteration results in potassic, propylitic, sericitic (phyllic) and argillic assemblages, which are documented to occur as concentric alteration halos around the ore progenitor intrusions (Seedorff et al., 2005; Sillitoe, 2010). Fluid trapped by quartz and other host minerals during alteration and mineralization processes has a wide range of compositions, and is the only record of the ore-forming fluid (Bodnar et al., 2014). As such, fluid inclusions provide fundamental information on the physical and chemical nature of ore-forming fluids. This is critical for understanding the nature and

transportation-deposition mechanisms of ore-forming fluids in porphyry copper deposits (Wilkinson, 2001; Bodnar et al., 2014).

Additional fundamental questions regarding porphyry deposits include the time required to form these giant deposits and whether the metals accumulate in a single pulse or over several pulses (Chiaradia et al., 2014). The current methods used to constrain time-scales of porphyry systems include: 1) Ti in quartz diffusion and thermal numerical modelling (Cathles et al., 1997; Weis et al., 2012; Mercer et al., 2015); 2) calculation from metal concentration and fluid flow in active hydrothermal systems (Simmons and Brown, 2006, 2007); and 3) direct radiogenic dating (Sillitoe and Mortensen, 2010; Von Quadt et al., 2011; Zimmerman et al., 2014; Spencer et al., 2015). The reported time-scales of fossil porphyry deposits range from <0.1 to >4 m.y. The longer durations may reflect multiple magmatic-hydrothermal pulses or inaccurate dating approaches (e.g. lower precision dating). The development of high-precision geochronology, especially molybdenite Re-Os in recent years has permitted direct dating of the ore forming events associated with porphyry copper systems with precision better than tens of thousands years (Zimmerman et al., 2014; Spencer et al., 2015). As molybdenite is widely distributed in porphyry Cu deposits, Re-Os molybdenite dating is currently the best technique to constrain the ore formation duration of porphyry copper deposits.

Although extensive fluid inclusion research has been conducted to understand ore forming processes for subduction related porphyry deposits (Bodnar et al., 2014)and references therein), much less attention has been paid to post-collisional porphyry deposits (Hou et al., 2009). The world-class Qulong porphyry deposit, Tibet, is an excellent example of a porphyry system formed in a

post-collisional tectonic setting (Hou et al., 2015). Qulong was discovered in 1994 with significant exploration success commenced from 2002 (Zheng et al., 2004). This period of exploration uncovered a deposit with ≥2200 million tonnes ore. The average metal grade at Qulong deposit is 0.5 percent for Cu and 0.03 percent for Mo, making it the largest copper bearing porphyry system in China, and among the world's largest (top 25) porphyry copper deposits (Cooke et al., 2005; Yang et al., 2009; Qin et al., 2014). Therefore, to understand both the P-T-V-X conditions of Qulong, and the porphyry systems associated with post-collisional tectonic settings, we present fluid inclusion petrography data coupled with microthermometry and Laser Raman microspectroscopy data. We also present molybdenite Re-Os geochronology to constrain the timescale of the mineralization event. In addition, zircon U-Pb geochronology and oxygen isotope data allow us to constrain the origin of the syn-ore aplite and the nature of the ore-forming fluids.

2.2 Geological setting

2.2.1 Regional geology

The Gangdese porphyry copper belt is 50 km wide and ~400 km long, and is situated at the southwest margin of the Lhasa Terrane, southern Tibet (Fig. 2.1) (Zhang et al., 2014). The Lhasa Terrane records a protracted geologic history with a Precambrian crystalline basement underlying Paleozoic to Mesozoic marine strata and arc type volcanic rocks, together with Mesozoic and Cenozoic intrusions (Zhang et al., 2014). The Lhasa Terrane rifted from Gondwana during the Triassic or Middle-Late Jurassic and moved northward across the Neo-Tethyan Ocean before collision with Eurasia along the Bangonghu-Nujiang suture

during the Cretaceous (Zhu et al., 2011a; Zhu et al., 2011b; Zhang et al., 2014). The continental collision of India and Asia along the Indus-Yarlung Zangbo suture started at ~55 Ma (Rowley, 1996), with underthrusting of the Indian plate beginning at ~35 Ma (Ali and Aitchison, 2008; Wang et al., 2014a). Continued collision of the Indian and Asian plates resulted in the breakoff of the denser Indian plate beneath the Asian plate from west to east of Tibet at ~25 and ~15 Ma, respectively (Aitchison et al., 2007; Van Hinsbergen et al., 2012). Directly related to slab breakoff was magma generation which resulted in Oligo-Miocene magmatic rocks focused along the Gangdese belt (Hou et al., 2009; Van Hinsbergen et al., 2012; Wang et al., 2014a). The Oligo-Miocene magmatism is consistent spatially linked with N-S trending normal faults (Hou et al., 2009; Wang et al., 2014a; Wang et al., 2014b). Porphyry copper mineralization is commonly strictly associated with the Oligo-Miocene intrusions in the east segment of the Gangdese porphyry copper belt (Wang et al., 2015), of which the Qulong deposit is not only largest in this belt, but also in China (Zheng et al., 2004; Qin et al., 2014).

2.2.2 Magmatic rocks

The main igneous units present at Qulong include Jurassic volcanic and dacite-rhyolite intrusions, a pre-ore Miocene granite pluton, ore-related Miocene porphyries and aplite intrusions, and a post-ore quartz diorite. Features of these units are summarized in Table 2.1 and presented below.

Jurassic Yeba Formation and dacite-rhyolite porphyry

The Jurassic Yeba Formation is the most extensive unit in the Qulong district (Fig. 2.2A) and is comprised of basaltic and felsic lavas. The age of the formation

is constrained by a zircon LA-ICP-MS age of 166.0 ± 1.8 Ma in the felsic volcanoclastic rocks (Zhao et al., 2016). The Yeba Formation sequence is intruded by dacite-rhyolite and rhyolite porphyry stocks. These porphyry stocks are composed of quartz (20-25 vol%) and feldspar (8-10 vol%) as phenocrysts, with a quartz, K-feldspar and biotite as groundmass. Zircon grains from the rhyolite porphyry yielded a LA-ICP-MS U-Pb age of 160.7 ± 2.0 Ma (Zhao et al., 2016). Volcanic rocks from the Yeba Formation and the porphyry stocks show geochemical characteristics indicative of an arc-affinity, suggesting an origin related to Mesozoic Neo-Tethyan Ocean subduction (Yang et al., 2008b).

Rongmucuola pluton

The Jurassic Yeba Formation and dacite-rhyolite porphyry units are intruded by the ~8 km^2 Rongmucuola pluton (Fig. 2.2A and B). At its contact with the Rongmucuola pluton, the Yeba Formation exhibits intensive metamorphism as represented by pervasive hornfels (Yang et al., 2009). From east to west, the composition of the Rongmucuola pluton ranges from granodiorite to monzogranite (Fig. 2.3A), and has a variable grain size (medium to coarse), and ranges from being hypidiomorphic-granular to weakly porphyritic (Yang et al., 2009; Zhao et al., 2016). Mafic enclaves are quite common in the eastern portion of the pluton, but are rare in the west (Zhao et al., 2016). Despite the small compositional and textural variations, the entire pluton possesses a similar mineralogy and crystallization age (17.6 ± 0.3 Ma and 17.4 ± 0.4 Ma; zircon LA-ICP-MS U-Pb) (Zhao et al., 2016). The bulk of the Cu-Mo mineralization is hosted in the western part of the pluton that comprises coarse grained (5-10 mm) plagioclase (30-40 vol%), K-feldspar (20-30 vol%), and medium grained (2-5 mm)

quartz (15-20 vol%) and biotite (10-15 vol%), and accessory minerals such as apatite, magnetite, zircon, rutile; no titanite has been documented. The pluton is characterized by a porphyritic texture throughout, a progressive increase in alteration intensity from the surface to ~2000 m depth (predominantly silicification and potassic alteration), and exhibits a colour change from dark grey to grey.

P porphyry (monzogranite)

The western part of the Rongmucuola pluton is intruded by the P porphyry (Fig. 2.2A and B), which is considered to be the ore-forming porphyry (Yang et al., 2009; Hu et al., 2015; Zhao et al., 2016). The P porphyry has an exposure surface of 0.5 km^2, and an unknown vertical extent. The P porphyry comprises coarse grained (3-8 mm) plagioclase (10-20 vol%), quartz (5-15 vol%) and K-feldspar (~5 vol%) as phenocrysts, with a groundmass dominated by quartz and feldspar (Fig. 2.3B). The porphyry shows extensive alteration and mineralization. The feldspar phenocrysts possess distinctive embayed shapes, with the groundmass displaying different degrees of hypogene argillization as a result of either the complete or partial destruction of feldspar. Characteristic to the P porphyry is its quartz phenocrysts which occur as clusters of two or three and forms amalgamated "phenocrysts" (Fig. 2.3B). These quartz phenocrysts often show resorbed crystal margins and embayment textures (Fig. 2.3B) which indicate intense silicification (Chang and Meinert, 2004; Yang et al., 2009; Qin et al., 2014). Zircon LA-ICPMS U-Pb analysis yielded a 16.2 ± 0.3 Ma emplacement age for the P porphyry (Zhao et al., 2016).

X porphyry (monzogranite)

In the western portion of the Rongmucuola pluton, the X porphyry occurs with a surface outcrop of ~0.04 km^2; it is also present as irregular dikes in drill cores. The thickness of X porphyry dikes in drill cores varies from several to tens of centimeters (Zhao et al., 2016) (Fig. 2.2B). The X porphyry has similar composition to the P porphyry except for a greater abundance of biotite phenocrysts. The X porphyry possesses unidirectional solidification textures (UST), intensive potassic alteration and weak propylitic alteration, but in general it is poorly mineralized (Yang et al., 2009). No direct cross-cutting relationships between the P and X porphyry has been documented previously, or observed in this study. However, previous studies assume it post-dates the P porphyry because it cuts barren potassic stage quartz veins in the Rongmucuola pluton (Yang et al., 2009; Zhao et al., 2016). The reported zircon LA-ICP-MS U-Pb age is identical, within uncertainty, to that of the P porphyry (15.9 ± 0.3 Ma) (Zhao et al., 2016).

Aplite

In addition to the P and X porphyry units, fracture controlled, thin (several to tens of cm wide) aplite dykes (Fig. 3C&E) cross-cut the Rongmucuola pluton (Yang et al., 2009; Zhao et al., 2016). The aplite is widely distributed in drill cores but no cross-cutting relationship has been documented between the aplite and P or X porphyry. The aplite units are characterised by intergrowths of fine-grained (~1 mm) anhedral alkali feldspar and quartz (Yang et al., 2009; Zhao et al., 2016) with disseminated magnetite and pyrite throughout. The fine grained texture suggests that this aplite experienced rapid cooling and crystallized immediately after emplacement (Webber et al., 1999). It has been assumed that the aplite is coeval

or slightly older than the X porphyry as potassic stage irregular-planar quartz-K-feldspar veins truncate the aplite units (Yang et al., 2009). Further, this study has observed barren sinusoidal quartz veins within the mineralized aplite (documented below; Fig. 2.4A), which we interpret to have formed during the transition between the magmatic and hydrothermal stage. To date, no radiometric date has been reported for the aplite units.

Post-ore quartz diorite

Mineralization was cross cut by a quartz-diorite dyke. The dyke is tens of cm wide and 2-6 m in length. It hosts phenocrysts of ~0.5-1 cm diameter including plagioclase (~5 %), quartz (5 %) and hornlende (3 %) set within a matrix of plagioclase, hornblende, quartz and biotite (Fig. 2.3D). The quartz-diorite is typically fresh with only plagioclase phenocrysts exhibiting minor alteration to a low-temperature assemblage of calcite-chlorite-sericite (Fig. 2.3D) (Yang et al., 2009; Yang et al., 2015). This unit is the youngest intrusion recognized at Qulong and has a zircon SIMS U-Pb age of 15.3 ± 0.2 Ma (Zhao et al., 2016).

2.2.3 Hydrothermal breccia

In addition to the magmatic units mentioned above, a hydrothermal breccia associated with the formation of the porphyry mineralization is also documented at Qulong. The breccia exists as a pipe (~100 m in diameter) and cross cuts the Rongmucuola pluton. The breccia is predominantly composed of clasts (<10 cm) from the Rongmucuola granodiorite pluton and P porphyry, which are cemented by aplite. These clasts are intensively altered and mineralized (Yang et al., 2009; Zhao et al., 2016). In certain cases, the breccia possesses intense silicification with

hematite alteration, cemented by a clay mineral-dominated matrix (e.g. kaolinite, illite).

2.3 Hydrothermal alteration phases

Akin to porphyry copper deposits worldwide, Qulong has a clearly zoned mineralization and alteration pattern. The relative chronology of the alteration assemblage at Qulong is; a) veinlets associated with the magmatic-hydrothermal transition stage; b) potassic (K-feldspar, biotite) alteration stage; c) propylitic alteration (chloritization) assemblages, and d) phyllic alteration (sericite) phases. The alteration and mineralization phases at Qulong have been described by Yang et al. (2009) and Qin et al. (2014). Here we summarize these findings together with the observations of this study.

2.3.1 Magmatic-hydrothermal transition stage quartz veins

This study reports the first record of ~0.5 cm wide sinusoidal quartz veins at Qulong hosted within the aplite dyke (Fig. 2.4A). The veins bear K-feldspar rims (~1 mm wide) at both sides and have localised clusters of fine-grained (<0.3 mm) pyrite grains. These barren veins represent silica-saturated melts/fluid formed at the magmatic-hydrothermal transition stage before potassic alteration. This process is also represented by Unidirectional Solidification Textures (UST) hosted by the X porphyry (Yang et al., 2008a). The sinusoidal quartz veins and UST are taken to represent the magmatic-hydrothermal transition stage at Qulong.

2.3.2 Potassic alteration

Potassic stage alteration assemblages at Qulong include the barren biotite and quartz veins (generally 2 mm wide, Fig. 2.4B), chalcopyrite and molybdenite bearing quartz veins with K-feldspar halos, and chalcopyrite-molybdenite bearing quartz veins with biotite-feldspar-quartz assemblages (Fig. 2.4C-F). Potassic alteration phases are concentrated around the P porphyry and predominantly hosted by the Rongmucuola pluton and P porphyry, but also occur in the Yeba Formation and X porphyry. Cu-Mo bearing veins with K-feldspar halos are the main ore-bearing potassic alteration assemblages at Qulong. These veins generally have a width of 0.5-3 cm (Fig. 2.4D and E). The nature of potassic alteration is characterized by selective replacement of plagioclase to K-feldspar, and tends to be more extensive near the P porphyry where almost all plagioclase grains were replaced by sericite, kaolinite and illite. Veinlets containing biotite have been divided into three types: 1) vein fillings comprising coarse-grained biotite grains (0.1-0.4 mm); 2) yellow-brown coloured biotite alteration halos (generally < 0.1 mm in width) along irregular quartz or quartz-anhydrite veins; and 3) primary biotite grains replaced by secondary biotite in the Rongmucuola pluton (Yang et al., 2009). Potassic alteration is the main mineralization stage at Qulong and directly controls bulk Cu-Mo mineralization. A progressive increase in intensity of potassic alteration was documented in the Rongmucuola pluton from shallow to depth.

2.3.3 Propylitic alteration

Propylitic alteration is extensively developed at Qulong in both the Rongmucuola pluton and the Yeba Formation. The propylitic alteration is

characterized by pervasive weak chloritization of the primary biotite and intensive replacement of plagioclase by epidote in the Rongmucuola pluton (Fig. 2.4G-I) and Yeba Formation, respectively. Propylitic alteration in the X porphyry is relatively weak. In the Rongmucuola pluton, biotite, hornblende and plagioclase have experienced different degrees of replacement by chlorite-dominated assemblages. In the Yeba Formation, epidote dominated (>60 vol%) alteration assemblages, with quartz, chlorite and K-feldspar, are found as irregular to planar veins (1-2 mm wide). Generally, sulfides (e.g. pyrite, chalcopyrite) associated with propylitic alteration are less abundant than in the potassic alteration stage (Yang et al., 2009). Anhydrite veins (pink, 1-3 mm in grain size and ~0.5-2 cm wide) along with molybdenite mineralization (with minor chalcopyrite) fill in reopened potassic stage K-feldspar veins (Fig. 2.4J). It is thought that these sulfides (molybdenite + chalcopyrite) belong to the propylitic alteration stage given that the K-feldspar assemblages in these veins are partially replaced by late stage molybdenite and chlorite.

2.3.4 Phyllic and hypogene argillic alteration

Phyllic and hypogene argillic alteration phases are widely distributed and overprint early stage alteration assemblages at Qulong. Phyllic and argillic alteration phases are more intense in the P porphyry than that in the Rongmucuola pluton and the X porphyry. In most cases, the intensive phyllic and argillic alteration have overprinted all igneous textures in the P porphyry. Similar to the potassic alteration, a progressive enhancement of phyllic and argillic alterations has been documented from shallow to depth in the Rongmucuola pluton. The main mineral phases of the phyllic and argillic alteration assemblages are sericite,

pyrite, anhydrite and clay minerals, and these are spatially associated with minor chalcopyrite and molybdenite. These phases are generally fine-grained (0.5-3 mm) and difficult to recognize in hand specimen, but occasionally include coarse-grained (0.5-1 cm) pyrite and anhydrite crystals (Fig. 2.4 K and L).

2.4 Samples and methods

2.4.1 Samples

Representative quartz veins from the magmatic-hydrothermal transition stage, potassic alteration, propylitic and phyllic alteration stages were selected to study fluid inclusions, which allow us to constrain the nature and evolution of the ore-forming fluid. All the samples were collected from drill cores at 10 to ~600 meters.

All the magmatic units at Qulong have been dated by previous studies, except the ore-bearing aplite. One ore-bearing aplite sample (Fig. 2.3C) was selected to conduct secondary ion mass spectrometry (SIMS) zircon U-Pb geochronology. SIMS was also utilized to determine the oxygen isotope composition of the zircons in order to aid the understanding of the U-Pb data, as well as the nature of ore-forming fluids.

Six molybdenite bearing quartz veins utilized for fluid inclusion analysis were also targeted for Re-Os dating to further constrain the timing of sulfide mineralization. Samples were selected from the aplite with a weak potassic alteration of K-feldspar (313-145; Fig. 2.4C), the potassic alteration stage (313-460, 001-640; Fig. 2.4D and E), the potassic-propylitic transition (1605-334, Fig. 2.4J) and the phyllic stage (1605-155; 1605-33, Fig. 2.4K).

2.4.2 Microthermometry and laser Raman spectroscopy

Microthermometric analysis of vein quartz hosted fluid inclusions in doubly polished wafers was carried out at the Geofluids Research Laboratory, National University of Ireland, Galway, using a Linkam THMSG600 heating and freezing stage mounted on a Olympus transmitted light microscope. Synthetic fluid inclusion standards (pure CO_2 and pure water) were used (Baumgartner et al., 2014) at -56.6, 0, 10.2, and 374 °C to correct the accuracy of the stage. Measurements below 31.1 ^oC, the critical point of CO_2, are accurate to ±0.2 ^oC, and measurements above this temperature are accurate to ±1 ^oC. The volumetric fraction of phases in fluid inclusions was estimated at room temperature by reference to the volumetric chart of Roedder (1984). Bulk salinity was calculated from the final ice melting temperature, or halite dissolution temperature (Bodnar and Vityk, 1994) for hypersaline fluid inclusions. Homogenization conditions and isochores of individual fluid inclusion assemblages (FIAs) have been calculated with HokieFlincs_H_2O-NaCl program based on fluid inclusion volumetric data (P-V-T-X) (Steele-MacInnis et al., 2012).

Solid and gas phases from selected fluid inclusions were identified using laser Raman spectroscopy (LRS) at the Geofluids Research Laboratory, National University of Ireland Galway. The LRS analysis was conducted on a Horiba Lab Ram II spectrometer equipped with a 600 groove$\cdot mm^{-1}$ diffraction grating, confocal optics, a Peltier-cooled CCD detector (255 by 1024 pixel array at -67 °C) and an Olympus BX41 microscope arranged in 180° backscatter geometry. Sample excitation was achieved using a Ventus diode-pumped, continuous wavelength, 532 nm laser with a maximum power output of 50 mW. Raman analysis was carried out using a 100x objective lens resulting in a laser spot size

of ~2 μm. Excitation power at the sample typically ranged between 10 and 20 mW.

2.4.3 CL imaging and EDS mineral identification methods

CL imaging and mineral inclusion identification were conducted with a Hitachi SU-70 FEG SEM at the G., J., Russell electron microscopy facility at Durham University. Cathodoluminescence (CL) imaging was carried out at a 10 kV accelerating voltage with a beam current of 1.63 nA at 16.8 mm working distance. Secondary electron images were taken under the same accelerating voltage and working distance but at a lower beam current (0.6 nA). Mineral inclusions were identified by EDS with 15 kV accelerating voltage and 0.93 nA beam current at 15 mm working distance.

2.4.4 SIMS zircon oxygen isotope and U-Pb dating analytical method

Guided by CL images, zircon oxygen isotope analysis and U-Pb dating were carried out at the Institute of Geology and Geophysics, Chinese Academy of Sciences with CAMECA IMS-1280 SIMS and CAMECA IMS-1280HR SIMS, respectively. Sample preparation and instrument operation conditions are the same as in Li et al. (2009, 2010a,b) and are briefly summarized here. Zircon grains were mounted with zircon oxygen isotope standards (Penglai zircon and Qinghu zircon) (Li et al., 2010; Li et al., 2013) and zircon geochronology standards (Plešovice and Qinghu zircon) (Sláma et al., 2008; Li et al., 2013) and then polished and coated with gold.

For O analysis, the Cs^+ primary ion beam was accelerated at 10 kV, with an intensity of ca. 2 nA and rastered over a 10 μm area. The spot size (ellipse) was

about 10 × 20 μm in diameter. The normal incidence electron flood gun was used to compensate for sample charging during analysis with homogeneous electron density over a 100 μm oval area. A 60 eV energy window was used together with a mass resolution of ca. 2500. Oxygen isotopes were measured using multi-collection mode on two off-axis Faraday cups. The intensity of ^{16}O was typically 10^9 cps. The NMR (Nuclear Magnetic Resonance) probe was used for magnetic field control with stability better than 3 ppm over 16 h on mass ^{17}O. One analysis took ca. 5 min consisting of pre-sputtering (~120 s), automatic beam centering (~60 s) and integration of oxygen isotopes (20 cycles × 4 s, total 80 s). Uncertainties on individual analyses were usually better than 0.3-0.4 ‰ (2 SE). The instrumental mass fractionation factor (IMF) was corrected using Penglai zircon with a $\delta^{18}O$ value of 5.3 ‰ (Li et al., 2010). Measured $^{18}O/^{16}O$ ratios were normalized by using V-SMOW compositions ($^{18}O/^{16}O$ = 0.0020052), and then corrected for the IMF. An in-house zircon standard (Qinghu) was used to ascertain the veracity of the IMF and 15 measurements of Qinghu zircon in this research yielded a weighted mean of 5.49 ± 0.37 ‰ (2 SD), which is consistent with the recommended value of 5.4 ± 0.2 ‰ (Li et al., 2013).

During U-Pb analysis, zircon grains were sputtered by an O_2^- primary ion beam with an intensity of ca. 8 nA and a diameter of 20 μm. An ellipsoidal spot approximately 20 × 30 μm in size was created at the sample surface as the ion beam was at an angle with the sample surface. U-Pb concentration and isotopic compositions were calibrated against the Plešovice zircon standard. Common Pb was corrected using measured non-radiogenic ^{204}Pb and an average present day crustal Pb compositions (Stacey and Kramers, 1975). Concordia plot and ages are calculated by Isoplot 3.0 (Ludwig, 2003). The quality of the data was assessed by

analyzing the Qinghu zircon standard between samples. Five analyses of the Qinghu zircon standard during this study yielded a weighted average $^{206}Pb/^{238}U$ age of 160.1 ± 4.6 Ma (95 % conf.), which is in good agreement with the reported reference value of 159.5 ± 0.2 Ma (Li et al., 2013).

2.4.5 Molybdenite Re-Os dating method

Molybdenite (0.3-2 mm) bearing quartz veins were crushed in an agate pestle to 5 mesh and then hand-picked under a microscope to remove non-molybdenite bearing phases. A known amount of material was placed into a Savillex Teflon digestion vessel with 8 ml of 32N HF (ROMIL Ltd. UpA high-purity HF) and left at room temperature for 24 hours (Lawley and Selby, 2012). This digestion process was repeated until most of the quartz had been liberated. After this, the HF was removed by rinsing the material three times with MQ, followed by ethanol rinsing. The samples were then dried at 30 ^{o}C. The material was further purified by traditional heavy liquid floating technology, and the estimated purity was better than 95 %.

The Re-Os analytical protocol follows that documented by Selby and Creaser (2001). In brief, a known amount molybdenite aliquant and spike solution (^{185}Re plus isotopically normal Os) was loaded into a Carius tube with 15.5 N HCl (3 ml) and 16 N HNO_3 (6 ml), sealed, and digested at 220 ^{o}C for ~24 hours. Osmium was isolated from the acid medium using solvent extraction ($CHCl_3$) at room temperature and further purified by micro-distillation method. The rhenium fraction was separated by NaOH-acetone solvent extraction and standard anion column chromatography. Rhenium and osmium were loaded on to Ni and Pt filaments, respectively. The isotopic compositions were measured by negative

thermal ionization mass spectrometry (N-TIMS) (Creaser et al., 1991). Analyses were conducted on a Thermo Scientific TRITON mass spectrometer, with Re and Os isotopic compositions measured using static Faraday collection mode. The Re and Os isotopic composition analytical uncertainties are propagated with spike calibrations, sample and spike weighting uncertainty, reproducibility of Re and Os isotope standard values, as well as blank abundances and isotopic compositions. During the study, Re and Os blanks were 4 pg and 1 pg, respectively, with the $^{187}Os/^{188}Os$ of the blank being 0.25 ± 0.02. The molybenite Re-Os model age is calculated using the equation $t = \ln (^{187}Os/^{187}Re + 1)/\lambda$. All analytical uncertainties were propagated with, and without, the ^{187}Re decay constant uncertainty (Smoliar et al., 1996; Selby et al., 2007).

2.5 Fluid inclusion data

2.5.1 Classification strategy

The superimposition of multiple hydrothermal fluid pulses is a common phenomenon in hydrothermal ore deposits, and is particularly common in porphyry copper systems (Seedorff et al., 2005; Rusk et al., 2008; Richards, 2011). As a result of the superimposition of hydrothermal events it is common to find in one crystal fluid inclusions that were trapped during different stages of mineralization and record very different physical and chemical compositions (Audetat et al., 1998). As such, to avoid ambiguous results and to investigate the primary ore-forming fluids nature, only primary and pseudosecondary fluid inclusions were analyzed.

Fluid inclusions and fluid inclusion assemblages (FIAs) (Goldstein and Reynolds, 1994) are abundant in quartz veins from all alteration stages at Qulong

and range in size from 1 to 30 μm in diameter (Fig. 2.5). The majority of fluid inclusions examined in this study have a diameter between 6 and 15 μm. Primary fluid inclusions are defined when they are confined to a single growth zone (Fig. 2.5A).

However, given the fact that most of the quartz grains are anhedral and lack clear growth zonation under transmitted light microscope, like many porphyry copper deposits (Rusk et al., 2008), most fluid inclusions studied here are linearly distributed pseudosecondary fluid inclusions trapped during the healing of micron-sized intra-grain fractures/cracks (Fig. 2.5A-C). Secondary fluid inclusions (Fig. 2.5B), generally distributed along late stage fractures, have an unknown origin in relation to the mineralization (Fig. 2.5A) and were avoided during this study.

Based on phases observed at room temperature, five types of fluid inclusion assemblages have been defined. They are classified as: $LV_{0\text{-}25}$ (liquid-rich two-phase FIAs, Fig. 2.5F), $LV_{25\text{-}60}$ (liquid-vapor two-phase FIAs, Fig. 2.5E), $LV_{60\text{-}100}$ (vapor-rich two-phase FIAs, Fig. 2.5D and I), $LV_{H\pm OP}$ (halite bearing FIAs with or without opaque minerals, Fig. 2.5G and H) and LV_{OP} (opaque minerals bearing FIAs without halite presence, Fig. 2.5J and M) (L=liquid, V=vapor, subscript number = volume percentage of vapor in fluid inclusions, H ± OP = presence of halite and/or opaque minerals. e.g. $LV_{0\text{-}25}$ refers to two-phase fluid inclusions contain 0-25 vol% of vapor; LV_{OP} refers to fluid inclusions that contain opaque minerals without observed halite crystals). Halite in $LV_{H\pm OP}$ fluid inclusions was identified by its cubic shape and optical isotropy (Fig. 2.5G-J and L), with sylvite distinguished from halite by its sub-cubic form and lower relief. Halite is the dominant salt crystal. Anhydrite is also present in $LV_{H\pm OP}$ and LV_{OP} fluid

inclusions, and is identified by its transparent anisotropic prisms (Fig. 2.5K and L) with a diagnostic Raman signal (Burke, 2001). Hematite in $LV_{H\pm OP}$ and LV_{OP} fluid inclusions was easily recognized from its red colour, hexagonal shape and high reflection index (Fig. 2.5M). However, most of the opaque minerals in $LV_{H\pm OP}$ and LV_{OP} fluid inclusions were not identified due to their small size (<1 μm). In many cases a FIA comprises more than one type of fluid inclusions. In such cases the classification is defined by the main type of fluid inclusion in that FIA (Goldstein and Reynolds, 1994).

$LV_{0\text{-}25}$ type fluid inclusions commonly display negative crystal shapes (Fig. 2.5F), but also exhibit rounded to irregular shapes. These inclusions occur in trails, as scattered groups and isolated individuals.

$LV_{25\text{-}60}$ type fluid inclusions are dominated by negative crystal shapes and also exhibit rounded shapes (Fig. 2.5E), they occur in trails, as randomly distributed clusters and as isolated individuals, which are similar to the $LV_{0\text{-}25}$ type fluid inclusions.

$LV_{60\text{-}100}$ type fluid inclusions share similar distribution patterns as the $LV_{0\text{-}25}$ and $LV_{25\text{-}60}$ type fluid inclusions (Fig. 2.5 D and I). However, the difference between this type and $LV_{0\text{-}25}$ and $LV_{25\text{-}60}$ inclusions is that $LV_{60\text{-}100}$ homogenize to both the vapor (~30 % of them) and liquid (~70 % of them) phase.

$LV_{H\pm OP}$ type fluid inclusions host one or more halite daughter minerals ± opaque minerals (Fig. 2.5G, H and L), with variable volume percentages of vapor. Halite is the most common daughter minerals, but sylvite and anhydrite (Fig. 2.5K, L) are also observed. This type of fluid inclusion is either isolated or occurs as randomly distributed clusters and often contains small (~1 μm) unidentified opaque daughter minerals (Fig. 2.5G, H, J, L).

LV_{OP} type fluid inclusions host opaque minerals and anhydrite, but no other identifiable daughter phases at room temperature (Fig. 2.5J and M). They contain 5-60 vol% vapor phases, with the majority containing 10-20 vol% vapor. These inclusions are generally distributed as random clusters or as isolated individuals, but also spatially associated with halite-bearing fluid inclusions (Fig. 2.5J). These fluid inclusions are generally secondary or of an unknown origin, and are not further discussed. The distribution of the FIAs in the vein assemblages at Qulong are given in Table 4.

2.5.2 Microthermometry

The majority of fluid inclusions homogenize to liquid with subsequent dissolution of halite when present, except for LV_{60-100} type fluid inclusions, which 30 % of them homogenize to the vapor phase. A few halite bearing fluid inclusions also homogenize by halite dissolution. In most cases, the opaque minerals do not dissolve despite heating to 450-500 ^{o}C for 2-3 hours.

For the FIA bearing both LV_{25-60} and LV_{60-100} inclusions from a quartz vein representing the magmatic-hydrothermal transition stage (No.1 in Fig. 2.4A), the inclusions homogenize to liquid with Th of 340-360 ^{o}C and yield salinities of 2-6 wt. % NaCl equiv. (n = 18; Fig.6A).

All Th and salinity inclusion data for quartz bearing potassic alteration selvages are shown in Fig. 2.6B. One primary halite-bearing FIA ($LV_{H\pm OP}$, No. 2 in Fig. 2.6B) yield Th of 419-436 ^{o}C and salinities of 50-52 wt. % NaCl equiv. (n = 11). A pseudosecondary halite-bearing FIA ($LV_{H\pm OP}$, No.3) spatially associated with vapor-rich two-phase fluid inclusions (LV_{60-100}) yield identical Th (388-405 ^{o}C). The halite bearing fluid inclusions have salinities of 41-45 wt% NaCl equiv

(n = 8), with the vapor-rich two-phase fluid inclusions homogenizing to vapor possessing lower salinities (4-7 wt% NaCl equiv., n=6). Two pseudosecondary vapor-rich two-phase FIAs (No. 4 and 5) yield similar salinities (1-6 wt% NaCl equiv), but have different Th (385-400 and 360-370 ºC; n = 12 and 13, respectively). Two liquid-vapor two-phase (LV_{60-100}) pseudosecondary FIAs (No. 6) yield similar Th (335-355 ºC) and salinity (2-7 wt% NaCl equiv; n = 18).

All Th and salinity data for quartz veins bearing a propylitic alteration selvage are shown in Fig. 2.6C. Three pseudosecondary liquid-vapor two-phase (LV_{25-60}) FIAs (also include vapor-rich two-phase fluid inclusions, No. 7) yield identical Th (all homogenize to liquid) of 335-360 ºC and salinities of 1-7 wt% NaCl equiv (n = 31). One pseudosecondary liquid-vapor two-phase FIA (No. 8) give similar salinity values (2-7 wt% NaCl equiv), but slightly lower Th (318-332 ºC, n = 9). A further FIA (No. 9) comprising pseudosecondary liquid-rich two-phase fluid inclusions yield similar Th of 270-290 ºC and show broadly similar salinities of 2-11 wt% NaCl equiv (n = 14).

The Th and salinity inclusion data for a quartz bearing phyllic alteration selvage are shown in Fig. 2.6D. In general, salinities are similar between FIAs (No. 10-12), and range between 1 and 9 wt% NaCl equiv. In contrast, Th values vary within the FIAs from 265 to 340 ˚C. One pseudosecondary liquid-rich two-phase FIA (No. 12) yielded Th of 265-290 ºC and salinities of 1-8 wt% NaCl equiv (n = 13). Another pseudosecondary FIA (No. 11) yielded slightly higher Th (295-310 ºC) and possesses similar salinities (3-9 wt% NaCl equiv. n = 12). A slightly higher Th (325-340 ºC) is recorded by another pseudosecondary liquid-vapor two-phase FIA (No. 10), with salinities of 2-8 wt% NaCl equiv (n = 13).

2.6 Zircon U-Pb, O isotopes and mineral inclusions

2.6.1 SIMS zircon U-Pb and oxygen isotope data of the aplite

The zircon U-Pb and oxygen isotope data of the aplite are summarized in Table 2.2 and illustrated in Fig. 2.8 and 9, respectively. All analytical spots were located on areas with clear CL zonation, while sieve textured grains and mineral inclusions rich zones were avoided for potential Pb loss (Fig. 2.7). The U-Pb analysis was conducted at the same position after oxygen isotope analysis. The 37 U-Pb analyses plot on or near the Wetherill concordia curve between 140 and 185 Ma (Fig. 2.8A). These data are divided into two groups based on their $^{206}Pb/^{238}U$ age distribution (Fig. 2.8B). The first group consists of $^{206}Pb/^{238}U$ age values that vary from 140.7 to 156.3 Ma (n = 4). The $^{206}Pb/^{238}U$ age values from the second group (n = 33) range from 165.2 to 184.7 Ma and show a bimodal distribution (Fig. 2.8C). No systematic age variations were observed between the core and rim.

The zircon $\delta^{18}O$ values range from 4.2 to 5.5 ‰, and show a positive skewed asymmetric distribution (Fig. 2.9). Notably, 18 analyses yield an average of 4.85 ± 0.23 ‰ (1 SD) which is lower than the recommended mantle value (5.3 ± 0.3 ‰) (Valley et al., 2005), with the remaining 12 analyses within the mantle value (average = 5.31 ± 0.12 ‰, 1 SD). There is no trend in the $\delta^{18}O$ values between the zircon core and rim. Further, there is also no correlation between the $^{206}Pb/^{238}U$ age data and the $\delta^{18}O$ values.

2.6.2 Zircon hosted mineral inclusions

The zircon grains from the aplite are characterized by sieve textures and host abundant mineral inclusions that are predominantly in the core of the grains (Fig. 2.10). In addition to rutile and xenotime, feldspar, quartz and fluorapatite are also

frequently observed. Feldspar and quartz (15-40 mm) generally coexist and cross cut the zircon grains.

2.7 Molybdenite Re-Os data

Re-Os data are reported at 2 sigma level uncertainty in Table 2.3 and are graphically presented in Fig. 2.11. The Re-Os data uncertainties are presented with full propagation of the analytical uncertainties without/with the ^{187}Re decay constant uncertainty. Rhenium concentrations of the molybdenite samples vary from 64 to 324 ppm. As the purity of molybdenite samples studied here is better than 95 %, the recorded rhenium concentration variations relate directly to the abundance in the analyzed molybdenite sample. No relationship between rhenium concentration and age is observed. The Re-Os dates are in agreement with the relative chronology of the Qulong porphyry system; a) magmatic-hydrothermal transition, b) potassic alteration, c) propylitic alteration, and d) phyllic alteration (Fig. 2.11). Sample 313-145 from the aplite which hosts the sinusoidal quartz veins has a Re-Os model age of 16.10 ± 0.07 [0.08] Ma. Samples 313-460 and 001-640 with potassic selvages yield identical Re-Os dates of 16.11 ± 0.06 [0.08] Ma and 16.10 ± 0.07 [0.09] Ma, respectively. Sample 1605-334 with a propylitic selvage has a slightly younger date of 16.01 ± 0.06 [0.08] Ma. Two samples (1605-155 and 1605-33) with phyllic selvages yield further younger dates of 15.93 ± 0.06 [0.08] Ma and 15.88 ± 0.06 [0.08] Ma, respectively. As these samples are not cogenetic and indicate a resolvable timespan, no isochron or weighted average is presented.

2.8 Discussion

2.8.1 Geochronology of Qulong

A significant amount of geochronology data (U-Pb, Re-Os, Fig. 2.12) has been published in an attempt to constrain the timeframe of the magmatism and mineralization at Qulong. Published $^{206}Pb/^{238}U$ age data yield a weighted mean of 17.2 ± 0.9 Ma (LA-ICP-MS, N = 243, 1 SD) (Hu et al., 2015; Zhao et al., 2016) and 16.5 ± 1.1 Ma (SHRIMP, n = 38, 1 SD) (Li and Rui, 2004; Wang et al., 2006) for the Rongmucuola pluton (Fig. 2.12). For the syn-ore P porphyry $^{206}Pb/^{238}U$ age data yield a weighted mean of 16.3 ± 0.5 Ma (LA-ICP-MS, n = 15, 1 SD) (Zhao et al., 2016) and 17.1 ± 1.0 Ma (SHRIMP, n = 13, 1 SD) (Hou et al., 2004). The zircon grains from the X porphyry have $^{206}Pb/^{238}U$ age data that yield a weighted average of 15.9 ± 0.5 Ma (LA-ICP-MS, n = 18, 1 SD) (Zhao et al., 2016). The post-ore diorite has zircon $^{206}Pb/^{238}U$ age data that yield a weighted mean of 15.7 ± 0.4 Ma (LA-ICP-MS; n = 21, 1 SD) (Yang et al., 2015) and 15.3 ± 0.3 Ma (SIMS; n = 17, 1 SD) (Zhao et al., 2016). Published Re-Os molybdenite model ages via ICP-MS analysis constrain mineralization from 16.85 to 15.36 Ma, and have large uncertainties (0.19-1.94 Ma) (Meng et al., 2003; Zheng et al., 2004; Li et al., 2005; Wang et al., 2006). The current U-Pb and Re-Os data set is suggestive of a prolonged magmatic-hydrothermal evolution history at Qulong (>3 m.y, Fig. 12). However, the significance of these dates, in terms of magmatic-hydrothermal onset and demise, cannot be truly given before the systematic difference between the methods (SHRIMP, LA-ICP-MS, ICP-MS) and laboratories has been assessed (Von Quadt et al., 2011; Li et al., 2015; Schaltegger et al., 2015). In this case, the weighted mean of the $^{206}Pb/^{238}U$ age for all the zircon grains is certainly not a good estimation for the age of porphyry

emplacement (Schoene, 2014). Further, the standard deviations associated with the analysis also cannot be used to assess the magma evolution as there is no assessment for the variation which either reflects geological processes or analytical uncertainties. As such estimating the timescale of magmatism and mineralization at Qulong based on these data is impossible and further high-precision geochronology study is needed (e.g., CA-ID-TIMS; (Chiaradia et al., 2013; Schoene, 2014; Schaltegger et al., 2015)).

Given the observation that the aplite units intrude the Miocene Rongmucuola pluton (Fig. 2.3E) (Yang et al., 2009; Qin et al., 2014), and are truncated by quartz veins with potassic selvages (Yang et al., 2009), there should be no doubt that it is coeval or slightly older than the syn-ore P porphyry. However, zircon SIMS $^{206}Pb/^{238}U$ age data from the aplite yield concordant Jurassic ages (Fig. 2.8, 172-182 Ma). These zircon grains show clear zonation in CL images (Fig. 2.7) without evidence of contamination from inherent cores, and no systematic age variations between the core and the rim of the zircon grains. In addition, the concordia data sets argue against Pb loss, thus we conclude that the Jurassic dates are not an analytical manifestation or related to the disturbance of the U-Pb system, but in fact indicate there was no zircon growth during the crystallization of the aplite (Bea et al., 2007).

The aplite has been previously suggested to be a quench product of the magma that also produced the P porphyry (Yang et al., 2009). If this is the case, zircons with Jurassic cores should also be observed in the P porphyry unless all the old, inherited grains have been resorbed. As zircon is well known for its resistance in most geological conditions, plus the lack of Jurassic cores documented in zircon grains from the P porphyry (Hou et al., 2015), the aplite likely did not originate

from the same magma as the P porphyry. A possible scenario is the aplite represents rapid crystallization of a magma derived principally from melting of materials sharing similar geochemical signature as the Jurassic igneous units (e.g., the Yeba Formation) during the emplacement of the Miocene intrusions, e.g. during the emplacement of the P porphyry, and no Miocene zircon growth during its crystallization (Bea et al., 2007). The reason for no Miocene zircon growth is unclear, but potentially due to its rapid crystallization process, rather than a lack of Zr as otherwise these inherited zircons will be absent.

Although there is no direct constraint for the emplacement age of the aplite, its minimum crystallization age can be bracketed by a Re-Os age from molybdenite from the aplite unit (16.11 ± 0.06 [0.08] Ma; sample 313-145; this study). Thus the aplite was formed before the main potassic alteration-mineralization stage, and likely contemporaneous with the final crystallization of the P porphyry, with the fluids of the sinusoidal quartz vein hosted by the aplite recording the magmatic-hydrothermal transition (Lindsay et al., 1995).

The sieve textures and quartz-feldspar inclusions (Fig. 2.10) in the zircon grains of the aplite suggest the aplite experienced extensive interaction with hydrothermal fluids, e.g., the fluid associated with the sinusoidal quartz vein. The low $\delta^{18}O$ values (4.2-5.0 ‰, Table 2.2 and Fig. 2.9) from the aplite hosted zircon grains suggest these zircon are either crystallized from low $\delta^{18}O$ magma (Wang et al., 2011), or experienced alteration by low $\delta^{18}O$ fluid (Valley, 2003). However, subduction related Jurassic magmatic rocks in the Gangdese porphyry copper belt have $\delta^{18}O$ values of 5.5-7 ‰, so the low zircon $\delta^{18}O$ values may be best explained by low $\delta^{18}O$ fluid alteration (Taylor 1968).

The Re-Os dates for molybdenite from quartz veins bearing potassic, propylitic and phyllic selvages support the relative chronology of the hydrothermal evolution at Qulong (Fig. 2.11). Molybdenite in veins with potassic selvages yields identical Re-Os dates of 16.11 ± 0.06 [0.08] Ma and 16.10 ± 0.07 [0.09] Ma, with a slightly younger date (although overlapping within uncertainty) for the propylitic stage (16.01 ± 0.06 [0.08] Ma), and further younger ages for the phyllic stage (15.93 ± 0.06 [0.08] Ma and 15.88 ± 0.06 [0.08] Ma). To date, the Re-Os dates of this study provide the most robust timing constraints for the hydrothermal evolution at Qulong, suggesting a maximum duration of 350 kyr, which is much less than the uncertainties of the U-Pb (SHRIMP/LA-ICP-MS) dates for the P and X porphyry units, and the post-ore diorite.

A potential concern for an underestimation of the mineralization lifespan is that molybdenite may have formed entirely during the potassic phase, with some veins being overprinted by propylitic and phyllic alteration. However, no evidence of overprint/replacement of the molybdenite bearing veins was observed in this study. Furthermore, the argeement of the relative chronology shown by the alteration phases and the Re-Os molybdenite dates coupled with cessation of mineralization/hydrothermal activity represented by the 15.88 Ma phyllic assemblages in this study, and a 15.7 ± 0.2 Ma hydrothermal biotite Ar-Ar age (Zhao et al., 2016) agrue against a greater duration for hydrothermal activity.

2.8.2 Fluid compositions

The first ice-melting temperature for the majority of the two-phase aqueous fluid inclusions is < -23 ^{o}C, which indicates the presence of other chemical species besides NaCl and KCl (e.g. Ca, Fe and Mg) (Sterner and Bodnar, 1984;

Rusk et al., 2008). As anhydrite has been recognized throughout most of the alteration and mineralization assemblages (Zheng et al., 2004; Yang et al., 2009), and is present as daughter minerals in fluid inclusions (Fig. 2.5K and L), the fluid should be Ca-rich and oxidized (Wendt, 1992). Hematite is also a common opaque trapped mineral in the fluid inclusions (Fig. 2.5M). Therefore, it is reasonable to assume that the fluid contains Na, K, Ca, Fe, Cu and Mo, with the anions Cl and S. As all of the fluid inclusions have first ice-melting temperatures > -60 ºC, Br and Li are considered as insignificant in regards to the bulk composition of the hydrothermal fluids (Davis et al., 1990). CO_2 in $LV_{25\text{-}60}$ fluid inclusions is identified by Laser Raman, but only as a minor component (≤3.5 mol%) (Azbej et al., 2007). Furthermore, liquid CO_2 was not observed at room temperature, nor clathrate formation was recorded in this study.

The early K-feldspar halos show dissolution textures (e.g., sieve textures, Fig. 2.4D), with quartz phenocrysts in the P porphyry exhibiting diagnostic resorbed shapes with embayments (Fig. 2.3B) (Yang et al., 2009; Qin et al., 2014). This suggests that the hydrothermal fluid potentially contains corrosive acid, e.g. hydrofluoric acid (McPhie et al., 2011). Zircon grains from the aplite host abundant fluorapatite inclusions, together with the sieve textures related to hydrothermal alteration as demonstrated by low $\delta^{18}O$ values, are highly suggestive of the hypothesis that the hydrothermal fluid was fluorine rich. Similar quartz resorption textures have been recognized in Cu–Zn skarn at the Empire Mine, Idaho, and are attributed to high fluorine activities during the alteration and mineralization processes (Chang and Meinert, 2004). In addition, fluorine-rich fluids have also been proposed to explain the formation of amoeboid clasts in the Olympic Dam IOCG deposit (McPhie et al., 2011). However, no fluorite has been

recognized at Qulong (Zheng et al., 2004), this may indeed reflect that the fluorite minerals were dissolved by later stage hydrothermal fluids.

2.8.3 Trapping conditions constraints and depth estimation

Determining the formation depth of a porphyry copper ore deposit is challenging, as such the depth of porphyry ore formation for many deposits is not precisely constrained (Seedorff et al., 2005; Rusk et al., 2008). Fluid inclusion studies, however, are widely used to help model ore-fluid trapping pressures and to estimate the formation depths.

Without independent pressure and temperature estimates, the halite-bearing FIA from the potassic alteration stage that are spatially associated with vapor-rich two-phase fluid inclusions (Fig. 2.5I, No. 3 in Fig. 2.6B) provides the best estimation for the conditions of ore formation at Qulong. This association suggests fluid boiling. Therefore, the homogenization temperatures (388-405 ^{o}C with an average of 398 ^{o}C) and homogenization pressure (250-290 bar, average of 270 bar) (Steele-MacInnis et al., 2012) of this specific FIA equals the trapping temperature and pressure, respectively. This trapping pressure suggests a formation depth of 1 km at lithostatic pressure or 2.7 km at hydrostatic pressure, given this sample has a current depth of 0.4 km, either 0.6 or 2.3 km erosion occurred following ore formation.

For the sinusoidal quartz vein that represents the magmatic-hydrothermal transition stage, the liquid-vapor two-phase FIA (No. 1) yields Th of 350 ^{o}C. Typical ductile-brittle transition in high level systems (e.g. porphyry copper deposits), which represents mechanical failure of a magma chamber and release of hydrothermal fluids occurs at temperatures < 425 ^{o}C (Landtwing et al., 2005;

Richards, 2011). If we consider 425 ˚C as the uppermost trapping temperature for the FIA in the sinusoidal quartz vein, a ~0.7 kbar trapping pressure is determined (Fig. 2.13A). This pressure equals to ~2.7 km depth under lithostatic pressure and ~7 km under hydrostatic pressure. The lithostatic pressure inferred depth is consistent with the temporally later potassic alteration stage exhibiting boiling under hydrostatic pressure (No. 3, Fig. 2.13), this indicates that the sinusoidal vein was formed under lithostatic pressure.

Assuming trapping at hydrostatic conditions of 2.3-2.7 km depth for the rest of the FIAs, we present the best estimates for the trapping temperatures of fluids associated with potassic, propylitic and phyllic stages (Table 4). For potassic stage samples the pseudosecondary halite-bearing FIA yields average trapping temperature of 425 ^{o}C (No. 2, Fig. 2.13B). Two pseudosecondary vapor-rich two-phase FIAs yield average trapping temperature of 390 and 380 ^{o}C (No. 4 and 5, Fig. 2.13A). Two liquid-vapor two-phase pseudosecondary FIAs yield average trapping temperature of 360 ^{o}C (No. 6, Fig. 2.13A).

Three pseudosecondary liquid-vapor two-phase FIAs from the propylitic alteration stage yield trapping temperatures of 365 ^{o}C (No. 7, Fig. 2.13A), the pseudosecondary liquid-vapor two-phase FIA gives trapping temperature of 340 ^{o}C (No. 8, Fig. 2.13A), two pseudosecondary liquid-rich two-phase FIAs yield a trapping temperature of 290 ^{o}C (No. 9, Fig. 2.13A). For FIAs from the phyllic alteration stage, the pseudosecondary liquid-vapor two-phase fluid inclusions yield a trapping temperature of 345 ^{o}C (No. 10, Fig. 2.13A), while the pseudosecondary liquid-rich two-phase ones yield a trapping temperature of 310 and 285 ^{o}C (No. 11 and 12, Fig. 2.13A).

The fluid inclusion data presented here suggests the transition between lithostatic and hydrostatic pressure occurred at the initial stages of ore formation. The temperature at the magmatic-hydrothermal transition stage (450 ^{o}C) is significantly lower than that (573 ^{o}C) predicted by Yang et al. (2009). This may suggest meteoric water involvement during the crystallization of the aplite, as indicated by the low $\delta^{18}O$ values recorded in zircons within the aplite. During the mineralization process, the fluid pressure remained broadly similar, with temperatures decreasing from potassic to phyllic stages. The very steady fluid pressure at hydrostatic conditions during the mineralization process indicates that the Qulong system experienced mechanical failure of the magma chamber before the mineralization processes, e.g. explosive pressure release marked by the breccia pipes (Fig. 2.2).

In addition, our data suggests a minimum ~2.3 km of erosion since the formation of Qulong. This amount of erosion is, however in contrast with current estimates that state there has been no significant regional uplift or erosion in central Tibet since the Miocene (Rowley and Currie, 2006). Nevertheless, our fluid inclusion data, coupled with the absence of Miocene volcanism at Qulong, which is commonly observed in porphyry systems formed in extensional environments (Sillitoe, 2010), is indicative of appreciable erosion in the Qulong area. Further, the exposure of several other Miocene porphyry systems near Qulong without Miocene volcanic units (e.g., Jiama and Lakang'e; Fig. 2.1) may indicate that ~2 km of erosion is more widespread than previously considered.

2.9 Conclusion

Molybdenite Re-Os dating confirms that the bulk Cu and Mo mineralization at Qulong occurred between 16.10 ± 0.06 [0.08] Ma and 15.88 ± 0.06 [0.08] Ma

(bracketed value is with ^{187}Re decay constant uncertainty). This timeframe is much less than the uncertainties of published U-Pb and Re-Os data. Though the published geochronology data seems to suggest a long-lived intrusive episode of the Miocene granodioritic to monzonitic rocks at Qulong, it is impossible to use the weighted mean and uncertainty to address the emplacement age and duration of magmatism until high-precision data is available (e.g. zircon CA-ID-TIMS).

The purely Jurassic aged zircons in the syn-ore aplite possessing a low oxygen isotope composition (4.85 ± 0.23 ‰), and sieve textures and mineral inclusions (quartz, feldspar and fluorapatite) indicate that the aplite is a remelt of Jurassic rock with involvement of meteoric fluid.

The ore-forming fluid contains Na, K, Ca, Fe, Cu and Mo, along with Cl and S. Fluorine is also an essential component as demonstrated by the presence of fluorapatite in zircon grains, as well as the dissolution textures of K-feldspar from the potassic stage and quartz phenocrysts in the P porphyry. Fluid inclusion study confirms the magmatic-hydrothermal transition occurred at ~425 ^{o}C under lithostatic pressure, while potassic, propylitic and phyllic alteration occurred at hydrostatic pressure with temperature progressively decreasing from 425 to 280 ^{o}C. The fluid inclusion data presented here suggest the Qulong porphyry system was formed at a paleo depth of ~2.7 km. This implies that ~2.3 km of erosion has occurred at Qulong after its formation, which may be related with regional uplift in the Lhasa terrane.

2.10 References

Aitchison, J.C., Ali, J.R., Davis, A.M., 2007. When and where did India and Asia collide? Journal of Geophysical Research 112, n/a-n/a.

Ali, J.R., Aitchison, J.C., 2008. Gondwana to Asia: Plate tectonics, paleogeography and the biological connectivity of the Indian sub-continent from

the Middle Jurassic through latest Eocene (166-35 Ma). Earth-Science Reviews 88, 145-166.

Audetat, A., Gunther, D., Heinrich, C.A., 1998. Formation of a magmatic-hydrothermal ore deposit: insights with LA-ICP-MS analysis of fluid inclusions. Science 279, 2091-2094.

Azbej, T., Severs, M.J., Rusk, B.G., Bodnar, R.J., 2007. In situ quantitative analysis of individual H2O-CO2 fluid inclusions by laser Raman spectroscopy. Chemical Geology 237, 255-263.

Baumgartner, M., Bakker, R.J., Doppler, G., 2014. Re-equilibration of natural H2O-CO2-salt-rich fluid inclusions in quartz-Part 1: experiments in pure water at constant pressures and differential pressures at 600 degrees C. Contributions to Mineralogy and Petrology 168, 1-14.

Bea, F., Montero, P., Gonzalez-Lodeiro, F., Talavera, C., 2007. Zircon inheritance reveals exceptionally fast crustal magma generation processes in central iberia during the cambro-ordovician. Journal of Petrology 48, 2327-2339.

Bodnar, R.J., Lecumberri-Sanchez, P., Moncada, D., Steele-MacInnis, M., 2014. 13.5 - Fluid Inclusions in Hydrothermal Ore Deposits, in: Turekian, H.D.H.K. (Ed.), Treatise on Geochemistry (Second Edition). Elsevier, Oxford, pp. 119-142.

Bodnar, R.J., Vityk, M.O., 1994. Interpretation of microthermometric data for H2O-NaCl fluid inclusions, in: Prezzotti, B.D.V.a.M.L. (Ed.), Fluid inclusions in minerals: Methods and applications. Virginia Tech, pp. 117-130.

Burke, E.A.J., 2001. Raman microspectrometry of fluid inclusions. Lithos 55, 139-158.

Cathles, L.M., Erendi, A.H.J., Barrie, T., 1997. How long can a hydrothermal system be sustained by a single intrusive event? Economic Geology 92, 766-771.

Chang, Z.S., Meinert, L.D., 2004. The magmatic-hydrothermal transition - evidence from quartz phenocryst textures and endoskarn abundance in Cu-Zn skarns at the Empire Mine, Idaho, USA. Chemical Geology 210, 149-171.

Chiaradia, M., Schaltegger, U., Spikings, R., 2014. Time Scales of Mineral Systems-Advances in Understanding Over the Past Decade. Soc Econ Geol Spec P, 37-58.

Chiaradia, M., Schaltegger, U., Spikings, R., Wotzlaw, J.-F., Ovtcharova, M., 2013. How Accurately Can We Date the Duration of Magmatic-Hydrothermal Events in Porphyry Systems?—An Invited Paper. Economic Geology 108, 565-584.

Cooke, D.R., Hollings, P., Walsh, J.L., 2005. Giant porphyry deposits: Characteristics, distribution, and tectonic controls. Economic Geology 100, 801-818.

Cooke, D.R., Hollings, P., Wilkinson, J.J., Tosdal, R.M., 2014. 13.14 - Geochemistry of Porphyry Deposits, in: Turekian, H.D.H.K. (Ed.), Treatise on Geochemistry (Second Edition). Elsevier, Oxford, pp. 357-381.

Creaser, R.A., Papanastassiou, D.A., Wasserburg, G.J., 1991. Negative Thermal Ion Mass-Spectrometry of Osmium, Rhenium, and Iridium. Geochimica Et Cosmochimica Acta 55, 397-401.

Davis, D.W., Lowenstein, T.K., Spencer, R.J., 1990. Melting Behavior of Fluid Inclusions in Laboratory-Grown Halite Crystals in the Systems Nacl-H2o, Nacl-Kcl-H2o, Nacl-Mgcl2-H2o, and Nacl-Cacl2-H2o. Geochimica Et Cosmochimica Acta 54, 591-601.

Goldstein, R.H., Reynolds, T.J., 1994. Systematics of fluid inclusions in diagenetic minerals: SEPM Short Course 31. Society for Sedimentary Geology, 199.

Hou, Z.Q., Gao, Y.F., Qu, X.M., Rui, Z.Y., Mo, X.X., 2004. Origin of adakitic intrusives generated during mid-Miocene east-west extension in southern Tibet. Earth and Planetary Science Letters 220, 139-155.

Hou, Z.Q., Yang, Z.M., Lu, Y.J., Kemp, A., Zheng, Y.C., Li, Q.Y., Tang, J.X., Yang, Z.S., Duan, L.F., 2015. A genetic linkage between subduction- and collision-related porphyry Cu deposits in continental collision zones. Geology 43, 247-250.

Hou, Z.Q., Yang, Z.M., Qu, X.M., Meng, X.J., Li, Z.Q., Beaudoin, G., Rui, Z.Y., Gao, Y.F., Zaw, K., 2009. The Miocene Gangdese porphyry copper belt generated during post-collisional extension in the Tibetan Orogen. Ore Geology Reviews 36, 25-51.

Hu, Y.B., Liu, J.Q., Ling, M.X., Ding, W., Liu, Y., Zartman, R.E., Ma, X.F., Liu, D.Y., Zhang, C.C., Sun, S.J., Zhang, L.P., Wu, K., Sun, W.D., 2015. The formation of Qulong adakites and their relationship with porphyry copper deposit: Geochemical constraints. Lithos 220, 60-80.

Landtwing, M.R., Pettke, T., Halter, W.E., Heinrich, C.A., Redmond, P.B., Einaudi, M.T., Kunze, K., 2005. Copper deposition during quartz dissolution by cooling magmatic-hydrothermal fluids: The Bingham porphyry. Earth and Planetary Science Letters 235, 229-243.

Lawley, C.J.M., Selby, D., 2012. Re-Os GEOCHRONOLOGY OF QUARTZ-ENCLOSED ULTRAFINE MOLYBDENITE: IMPLICATIONS FOR ORE GEOCHRONOLOGY. Economic Geology 107, 1499-1505.

Li, G.-M., Liu, B., Qu, W.-J., Lin, F.-C., Yu, H.-Q., Feng, C.-Y., 2005. The porphyry- skarn ore- forming system in Gangdese Metallogenic Belt, southern Xizang: Evidence from molybdenite Re-Os age of porphyry- type copper deposits and skarn- type copper polymetallic deposits. Geotectonica et Metallogenia 29, 482-490.

Li, G.-M., Rui, Z.-Y., 2004. Diagenetic and Mineralization ages for the porphyry copper deposits in the Gangdise Metallogenic Belt, Southern Xizang. Geotectonica et Metallogenia 28, 165-170.

Li, X.H., Liu, X.M., Liu, Y.S., Su, L., Sun, W.D., Huang, H.Q., Yi, K., 2015. Accuracy of LA-ICPMS zircon U-Pb age determination: An inter-laboratory comparison. Sci China Earth Sci 58, 1722-1730.

Li, X.H., Long, W.G., Li, Q.L., Liu, Y., Zheng, Y.F., Yang, Y.H., Chamberlain, K.R., Wan, D.F., Guo, C.H., Wang, X.C., Tao, H., 2010. Penglai Zircon Megacrysts: A Potential New Working Reference Material for Microbeam Determination of Hf-O Isotopes and U-Pb Age. Geostandards and Geoanalytical Research 34, 117-134.

Li, X.H., Tang, G.Q., Gong, B., Yang, Y.H., Hou, K.J., Hu, Z.C., Li, Q.L., Liu, Y., Li, W.X., 2013. Qinghu zircon: A working reference for microbeam analysis of U-Pb age and Hf and O isotopes. Chinese Science Bulletin 58, 4647-4654.

Lindsay, D.D., Zentilli, M., Rivera, J.R.D.L., 1995. Evolution of an Active Ductile to Brittle Shear System Controlling Mineralization at the Chuquicamata Porphyry Copper Deposit, Northern Chile. International Geology Review 37, 945-958.

Ludwig, K.R., 2003. User's manual for Isoplot 3.00: a geochronological toolkit for Microsoft Excel. Kenneth R. Ludwig.

McPhie, J., Kamenetsky, V., Allen, S., Ehrig, K., Agangi, A., Bath, A., 2011. The fluorine link between a supergiant ore deposit and a silicic large igneous province. Geology 39, 1003-1006.

Meng, X.-J., Hou, Z.-Q., Gao, Y.-F., Huang, W., Qu, X.-M., Qu, W.-J., 2003. Re-Os dating for molybdenite from Qulong porphyry copper deposit in Gangdese metallogenic Belt, Xizangand its metallogenic significance. Geological Review 49, 660-666.

Mercer, C.N., Reed, M.H., Mercer, C.M., 2015. Time Scales of Porphyry Cu Deposit Formation: Insights from Titanium Diffusion in Quartz. Economic Geology 110, 587-602.

Qin, K.-Z., Xia, D.-X., Li, G.-M., Xiao, B., Duo, J., Jiang, G.-W., Zhao, J.-X., 2014. Qulong Porphyry-Skarn Cu-Mo Deposit, Tibet. Science Press, Beijing.

Richards, J.P., 2009. Postsubduction porphyry Cu-Au and epithermal Au deposits: Products of remelting of subduction-modified lithosphere. Geology 37, 247-250.

Richards, J.P., 2011. Magmatic to hydrothermal metal fluxes in convergent and collided margins. Ore Geology Reviews 40, 1-26.

Richards, J.P., 2013. Giant ore deposits formed by optimal alignments and combinations of geological processes. Nature Geoscience 6, 911-916.

Roedder, E., 1984. Fluid Inclusions. Mineralogical Society of America.

Rowley, D.B., 1996. Age of initiation of collision between India and Asia: A review of stratigraphic data. Earth and Planetary Science Letters 145, 1-13.

Rowley, D.B., Currie, B.S., 2006. Palaeo-altimetry of the late Eocene to Miocene Lunpola basin, central Tibet. Nature 439, 677-681.

Rusk, B.G., Reed, M.H., Dilles, J.H., 2008. Fluid inclusion evidence for magmatic-hydrothermal fluid evolution in the porphyry copper-molybdenum deposit at Butte, Montana. Economic Geology 103, 307-334.

Samson, I., Anderson, A., Marshall, D.D., 2003. Fluid inclusions: analysis and interpretation. Mineralogical Association of Canada.

Schaltegger, U., Schmitt, A.K., Horstwood, M.S.A., 2015. U-Th-Pb zircon geochronology by ID-TIMS, SIMS, and laser ablation ICP-MS: Recipes, interpretations, and opportunities. Chemical Geology 402, 89-110.

Schoene, B., 2014. 4.10 - U–Th–Pb Geochronology, in: Turekian, H.D.H.K. (Ed.), Treatise on Geochemistry (Second Edition). Elsevier, Oxford, pp. 341-378.

Seedorff, E., Dilles, J., Proffett, J., Einaudi, M., Zurcher, L., Stavast, W., Johnson, D., Barton, M., 2005. Porphyry deposits: characteristics and origin of hypogene features. Economic Geology 100th Anniversary Volume 29, 251-298.

Selby, D., Creaser, R.A., 2001. Re-Os geochronology and systematics in molybdenite from the Endako porphyry molybdenum deposit, British Columbia, Canada. Economic Geology and the Bulletin of the Society of Economic Geologists 96, 197-204.

Selby, D., Creaser, R.A., Stein, H.J., Markey, R.J., Hannah, J.L., 2007. Assessment of the Re-187 decay constant by cross calibration of Re-Os molybdenite and U-Pb zircon chronometers in magmatic ore systems. Geochimica Et Cosmochimica Acta 71, 1999-2013.

Sillitoe, R.H., 2010. Porphyry Copper Systems. Economic Geology 105, 3-41.

Sillitoe, R.H., Mortensen, J.K., 2010. Longevity of Porphyry Copper Formation at Quellaveco, Peru. Economic Geology 105, 1157-1162.

Simmons, S.F., Brown, K.L., 2006. Gold in magmatic hydrothermal solutions and the rapid formation of a giant ore deposit. Science 314, 288-291.

Simmons, S.F., Brown, K.L., 2007. The flux of gold and related metals through a volcanic arc, Taupo Volcanic Zone, New Zealand. Geology 35, 1099-1102.

Sláma, J., Košler, J., Condon, D.J., Crowley, J.L., Gerdes, A., Hanchar, J.M., Horstwood, M.S., Morris, G.A., Nasdala, L., Norberg, N., 2008. Plešovice zircon—a new natural reference material for U–Pb and Hf isotopic microanalysis. Chemical Geology 249, 1-35.

Smoliar, M.I., Walker, R.J., Morgan, J.W., 1996. Re-Os ages of group IIA, IIIA, IVA, and IVB iron meteorites. Science 271, 1099-1102.

Spencer, E.T., Wilkinson, J.J., Creaser, R.A., Seguel, J., 2015. The Distribution and Timing of Molybdenite Mineralization at the El Teniente Cu-Mo Porphyry Deposit, Chile. Economic Geology 110, 387-421.

Stacey, J.t., Kramers, J., 1975. Approximation of terrestrial lead isotope evolution by a two-stage model. Earth and Planetary Science Letters 26, 207-221.

Steele-MacInnis, M., Lecumberri-Sanchez, P., Bodnar, R.J., 2012. HOKIEFLINCS_H2O-NACL: A Microsoft Excel spreadsheet for interpreting microthermometric data from fluid inclusions based on the PVTX properties of H2O-NaCl. Computers & Geosciences 49, 334-337.

Sterner, S.M., Bodnar, R.J., 1984. Synthetic fluid inclusions in natural quartz I. Compositional types synthesized and applications to experimental geochemistry. Geochimica et Cosmochimica Acta 48, 2659-2668.

Valley, J.W., 2003. Oxygen isotopes in zircon. Zircon 53, 343-385.

Valley, J.W., Lackey, J.S., Cavosie, A.J., Clechenko, C.C., Spicuzza, M.J., Basei, M.A.S., Bindeman, I.N., Ferreira, V.P., Sial, A.N., King, E.M., Peck, W.H., Sinha, A.K., Wei, C.S., 2005. 4.4 billion years of crustal maturation: oxygen isotope ratios of magmatic zircon. Contributions to Mineralogy and Petrology 150, 561-580.

Van Hinsbergen, D.J., Lippert, P.C., Dupont-Nivet, G., McQuarrie, N., Doubrovine, P.V., Spakman, W., Torsvik, T.H., 2012. Greater India Basin hypothesis and a two-stage Cenozoic collision between India and Asia. Proceedings of the National Academy of Sciences 109, 7659-7664.

Von Quadt, A., Erni, M., Martinek, K., Moll, M., Peytcheva, I., Heinrich, C.A., 2011. Zircon crystallization and the lifetimes of ore-forming magmatic-hydrothermal systems. Geology 39, 731-734.

Wang, L.-L., Mo, X.-X., B, L., G-C, D., Zhao, Z.-D., 2006. Geochronology and geochemistry of the ore-bearing porphyry in Qulong Cu (Mo) deposit, Tibet. Acta Petrologica Sinica 22, 1001-1008.

Wang, R., Richards, J.P., Hou, Z.Q., Yang, Z.M., 2014a. Extent of underthrusting of the Indian plate beneath Tibet controlled the distribution of Miocene porphyry Cu-Mo +/- Au deposits. Mineralium Deposita 49, 165-173.

Wang, R., Richards, J.P., Hou, Z.Q., Yang, Z.M., Gu, Z.B., DuFrane, S.A., 2014b. Increasing Magmatic Oxidation State from Paleocene to Miocene in the Eastern Gangdese Belt, Tibet: Implication for Collision-Related Porphyry Cu-Mo +/- Au Mineralization. Economic Geology 109, 1943-1965.

Wang, R., Richards, J.P., Zhou, L.M., Hou, Z.Q., Stern, R.A., Creaser, R.A., Zhu, J.J., 2015. The role of Indian and Tibetan lithosphere in spatial distribution of Cenozoic magmatism and porphyry Cu-Mo deposits in the Gangdese belt, southern Tibet. Earth-Science Reviews 150, 68-94.

Wang, X.-C., Li, Z.-X., Li, X.-H., Li, Q.-L., Tang, G.-Q., Zhang, Q.-R., Liu, Y., 2011. Nonglacial origin for low-δ18O Neoproterozoic magmas in the South China Block: Evidence from new in-situ oxygen isotope analyses using SIMS. Geology 39, 735-738.

Webber, K.L., Simmons, W.B., Falster, A.U., Foord, E.E., 1999. Cooling rates and crystallization dynamics of shallow level pegmatite-aplite dikes, San Diego County, California. American Mineralogist 84, 708-717.

Weis, P., Driesner, T., Heinrich, C.A., 2012. Porphyry-copper ore shells form at stable pressure-temperature fronts within dynamic fluid plumes. Science 338, 1613-1616.

Wendt, I., 1992. The Statistical Distribution of the Mean Squared Weighted Deviation - Reply. Chemical Geology 94, 242-243.

Wilkinson, J.J., 2001. Fluid inclusions in hydrothermal ore deposits. Lithos 55, 229-272.

Yang, Z.-M., Hou, Z.-Q., Li, Z.-Q., Song, Y.-C., Xie, Y.-L., 2008a. Direct record of primary fluid exsolved from magma: Evidence from unidirectional solidification texture (UST) in quartz found in Qulong porphyry copper deposit, Tibet. Mineral Deposits 27, 188-199.

Yang, Z.-M., Hou, Z.-Q., Xia, D.-X., Song, Y.-C., Li, Z., 2008b. Relationship between Western Porphyry and mineralization in Qulong copper deposit of Tibet and its enlightenment to further exploration. Mineral Deposits 27, 28-36.

Yang, Z.M., Hou, Z.Q., White, N.C., Chang, Z.S., Li, Z.Q., Song, Y.C., 2009. Geology of the post-collisional porphyry copper-molybdenum deposit at Qulong, Tibet. Ore Geology Reviews 36, 133-159.

Yang, Z.M., Lu, Y.J., Hou, Z.Q., Chang, Z.S., 2015. High-Mg Diorite from Qulong in Southern Tibet: Implications for the Genesis of Adakite-like Intrusions and Associated Porphyry Cu Deposits in Collisional Orogens. Journal of Petrology 56, 227-253.

Zhang, Z.M., Dong, X., Santosh, M., Zhao, G.C., 2014. Metamorphism and tectonic evolution of the Lhasa terrane, Central Tibet. Gondwana Research 25, 170-189.

Zhao, J., Qin, K., Xiao, B., McInnes, B., Li, G., Evans, N., Cao, M., Li, J., 2016. Thermal history of the giant Qulong Cu–Mo deposit, Gangdese metallogenic belt, Tibet: Constraints on magmatic–hydrothermal evolution and exhumation. Gondwana Research 36, 390-409.

Zheng, Y.-Y., Xue, Y.-X., Cheng, L.-J., Fan, Z.-H., Gao, S.-B., 2004. Finding,Characteristics and Significances of Qulong Superlarge Porphyry Copper (Molybdenum) Deposit, Tibet. Earth Sciences 29, 103-108.

Zhu, D.C., Zhao, Z.D., Niu, Y.L., Dilek, Y., Mo, X.X., 2011a. Lhasa terrane in southern Tibet came from Australia. Geology 39, 727-730.

Zhu, D.C., Zhao, Z.D., Niu, Y.L., Mo, X.X., Chung, S.L., Hou, Z.Q., Wang, L.Q., Wu, F.Y., 2011b. The Lhasa Terrane: Record of a microcontinent and its histories of drift and growth. Earth and Planetary Science Letters 301, 241-255.

Zimmerman, A., Stein, H.J., Morgan, J.W., Markey, R.J., Watanabe, Y., 2014. Re–Os geochronology of the El Salvador porphyry Cu–Mo deposit, Chile: Tracking analytical improvements in accuracy and precision over the past decade. Geochimica et Cosmochimica Acta 131, 13-32.

2.11 List of figures

rich two-phase FIA; (E) Liquid-vapor two-phase FIA; (F) Liquid-rich two-phase FIA; (G) Halite bearing FIA with/without opaque; (H) Halite-bearing FIA with/without opaque; (I) Vapor rich two-phase FIA; (J) Two-phase FIA spatially associated with halite-bearing fluid inclusions; (K) Anhydrite bearing fluid inclusion; (L) Halite bearing fluid inclusion with anhydrite and opaque minerals; (M) Opaque mineral and hematite bearing fluid inclusions without halite.

Fig. 2.6 Th-salinity plots of fluid inclusions from the magmatic-hydrothermal transition stage (A), potassic stage (B), propylitic stage (C) and phyllic stage (D). The ages quoted in the figures are from quartz-enclosed molybdenite Re-Os dates obtained in this study (Table 2.3). Numbers in blue indicate the FIA number discussed in the text.

Fig. 2.7 CL images of zircon grains from aplite sample, with SIMS locations, and U-Pb and O isotope data. Blue numbers indicate the zircon grain number noted in the first column of Table 2.2.

Fig. 2.8 (A) Concordia plot of the aplite zircon SIMS U-Pb data, (B) weighted average $^{206}Pb/^{238}U$ age plot, and (C) histogram showing a bimodal distribution of the $^{206}Pb/^{238}U$ ages. Note the calculated weighted average data in Fig. 2.8C does not represent geological meaningful ages, but indicates the source of the magma. See text for discussion.

Fig. 2.9 Histogram of aplite zircon SIMS oxygen isotope data, with mantle zircon values from Valley et al. (2005). See text for discussion.

Fig. 2.10 Secondary electron image showing the type and distribution of mineral inclusions in zircon grains from the aplite sample.

Fig. 2.11 Molybdenite Re-Os dates obtained for quartz veins bearing potassic, propylitic and phyllic selvages.

Fig. 2.12 A compilation of all published zircon U-Pb (LA-ICP-MS, SHRIMP, SIMS) and molybdenite Re-Os (ICP-MS) data of the Miocene units and mineralization at Qulong. Also shown are the Re-Os dates obtained in this study. Our SIMS U-Pb zircons dates for the aplite are not shown as they are all Jurassic. See text for data sources and discussion.

Fig. 2.13 Trapping pressure and temperature of hydrothermal fluids at Qulong associated with the magmatic-hydrothermal transition, potassic, propylitic and phyllic alteration and mineralization; (A) Isochores for a 5 wt% NaCl equiv, and (B) 40 wt% NaCl equiv NaCl-H_2O system (Samson et al., 2003). Hydrostatic and lithostatic pressures are calculated based on a density of 1 and 2.6 g/cm^3, respectively. Numbers at coloured star symbol indicate the FIA number discussed in the text. (C) Fluid pressure-temperature evolution of Qulong.

2.12 List of tables

Figure 2.1

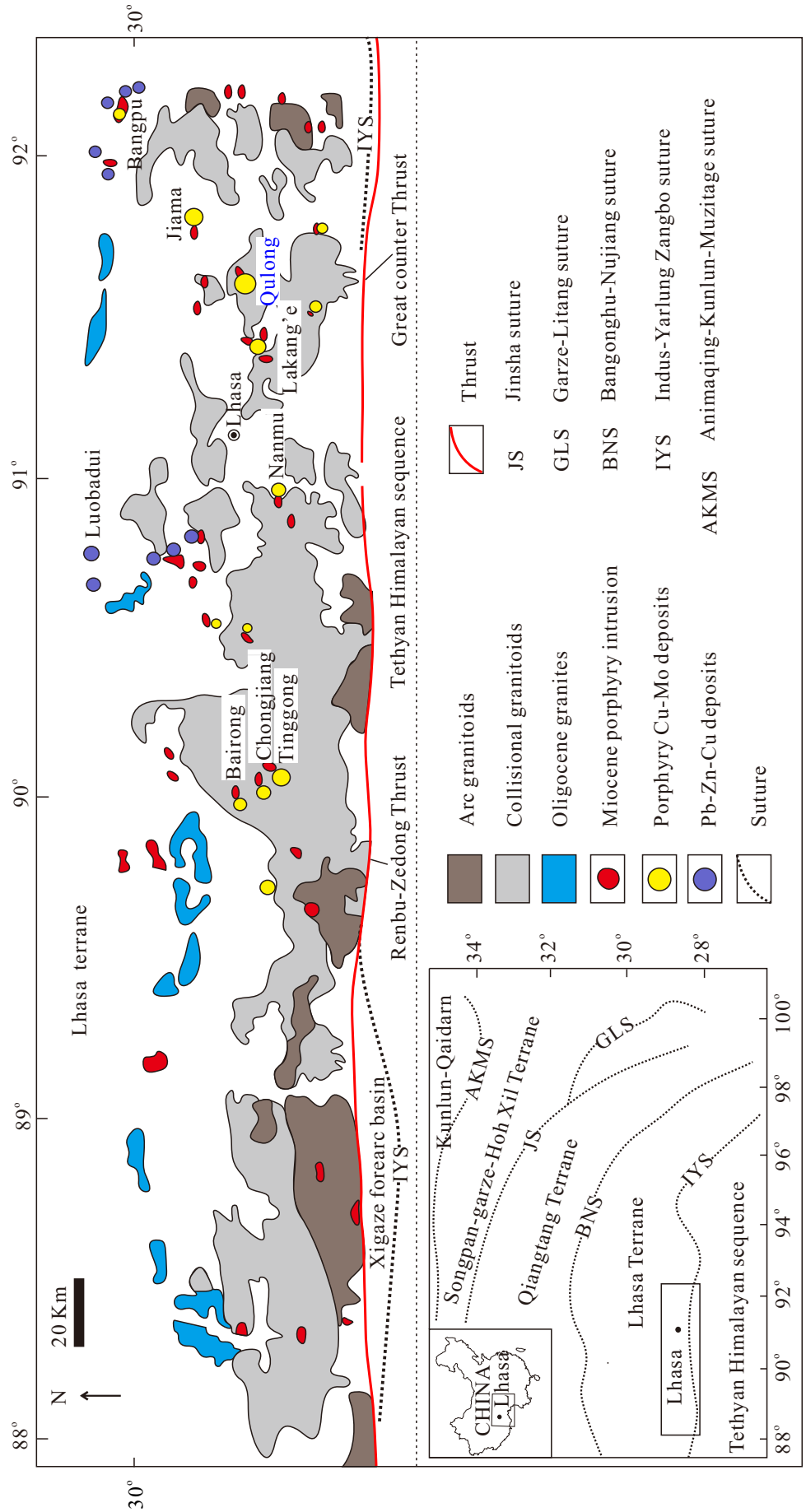
Bangpu
Jiama
Qulong
Lhasa
Lakang'e
Nanmu
Luobadui
Bairong
Chongjiang
Tinggong
Lhasa terrane
Xigaze forearc basin
IYS
Renbu-Zedong Thrust
Tethyan Himalayan sequence
Great counter Thrust
IYS
N
20 Km
88°
89°
90°
91°
92°
30°
Arc granitoids
Collisional granitoids
Oligocene granites
Miocene porphyry intrusion
Porphyry Cu-Mo deposits
Pb-Zn-Cu deposits
Suture
Thrust
JS Jinsha suture
GLS Garze-Litang suture
BNS Bangonghu-Nujiang suture
IYS Indus-Yarlung Zangbo suture
AKMS Animaqing-Kunlun-Muzitage suture
CHINA
Lhasa
Kunlun-Qaidarn
AKMS
Songpan-garze-Hoh Xil Terrane
JS
Qiangtang Terrane
GLS
BNS
Lhasa Terrane
IYS
Lhasa
Tethyan Himalayan sequence
34°
32°
30°
28°
88°
90°
92°
94°
96°
98°
100°

Figure 2.2

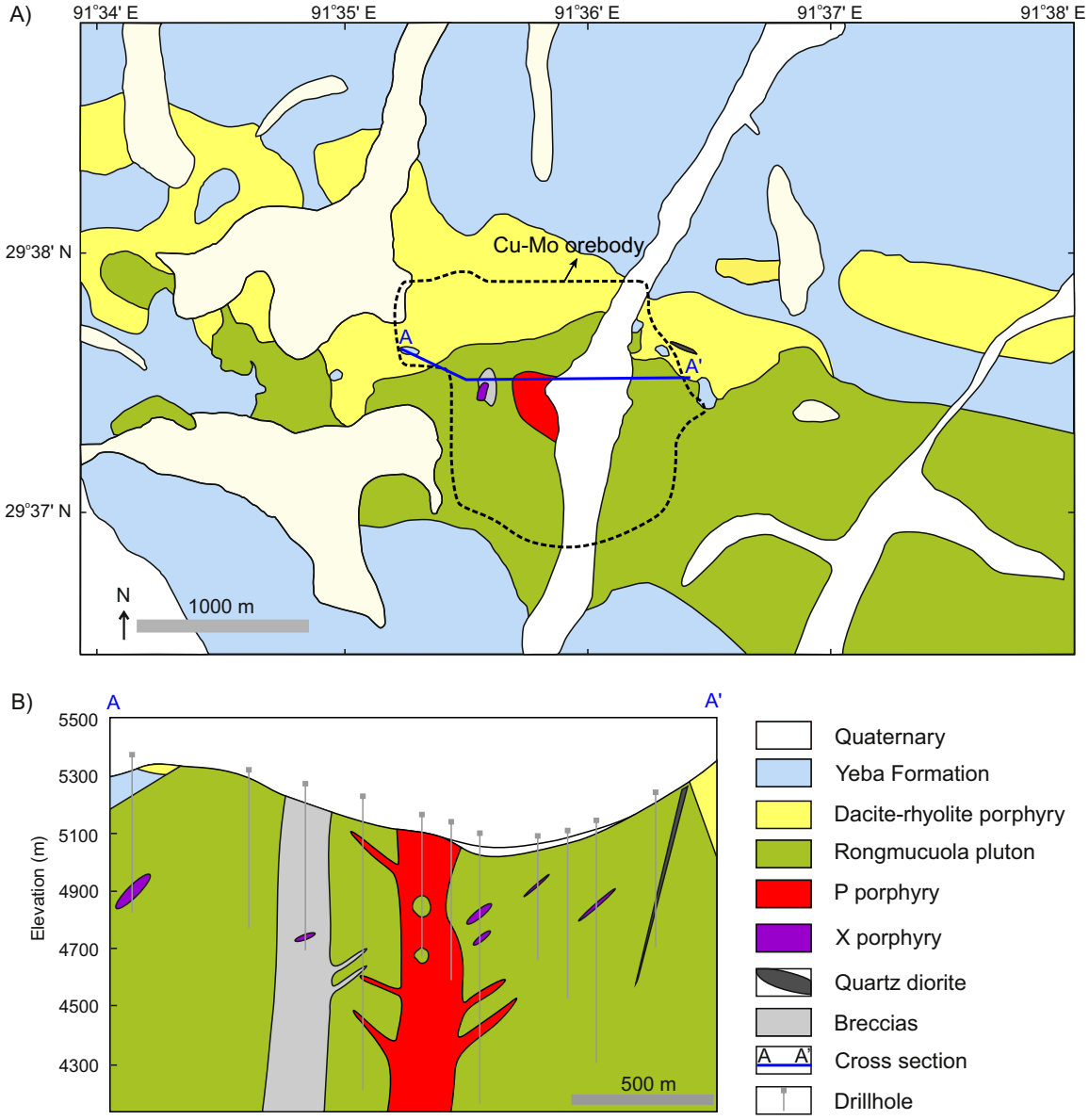
A)
91°34' E
91°35' E
91°36' E
91°37' E
91°38' E
29°38' N
29°37' N
Cu-Mo orebody
A
A'
N
1000 m
B)
A
A'
5500
5300
5100
4900
4700
4500
4300
Elevation (m)
500 m
Quaternary
Yeba Formation
Dacite-rhyolite porphyry
Rongmucuola pluton
P porphyry
X porphyry
Quartz diorite
Breccias
A A'
Cross section
Drillhole

Figure 2.3

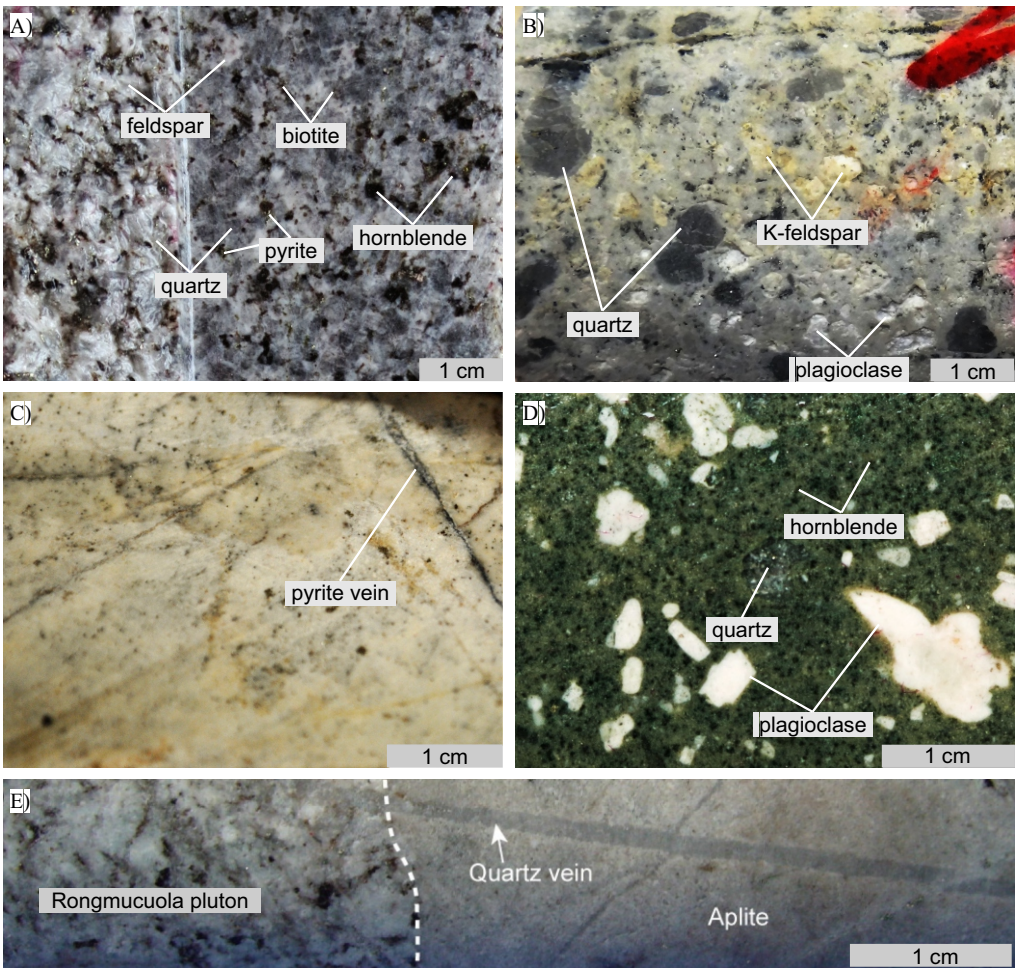
A)
feldspar
biotite
hornblende
pyrite
quartz
1 cm
B)
K-feldspar
quartz
plagioclase
1 cm
C)
pyrite vein
1 cm
D)
hornblende
quartz
plagioclase
1 cm
E)
Rongmucuola pluton
Quartz vein
Aplite
1 cm

Figure 2.4

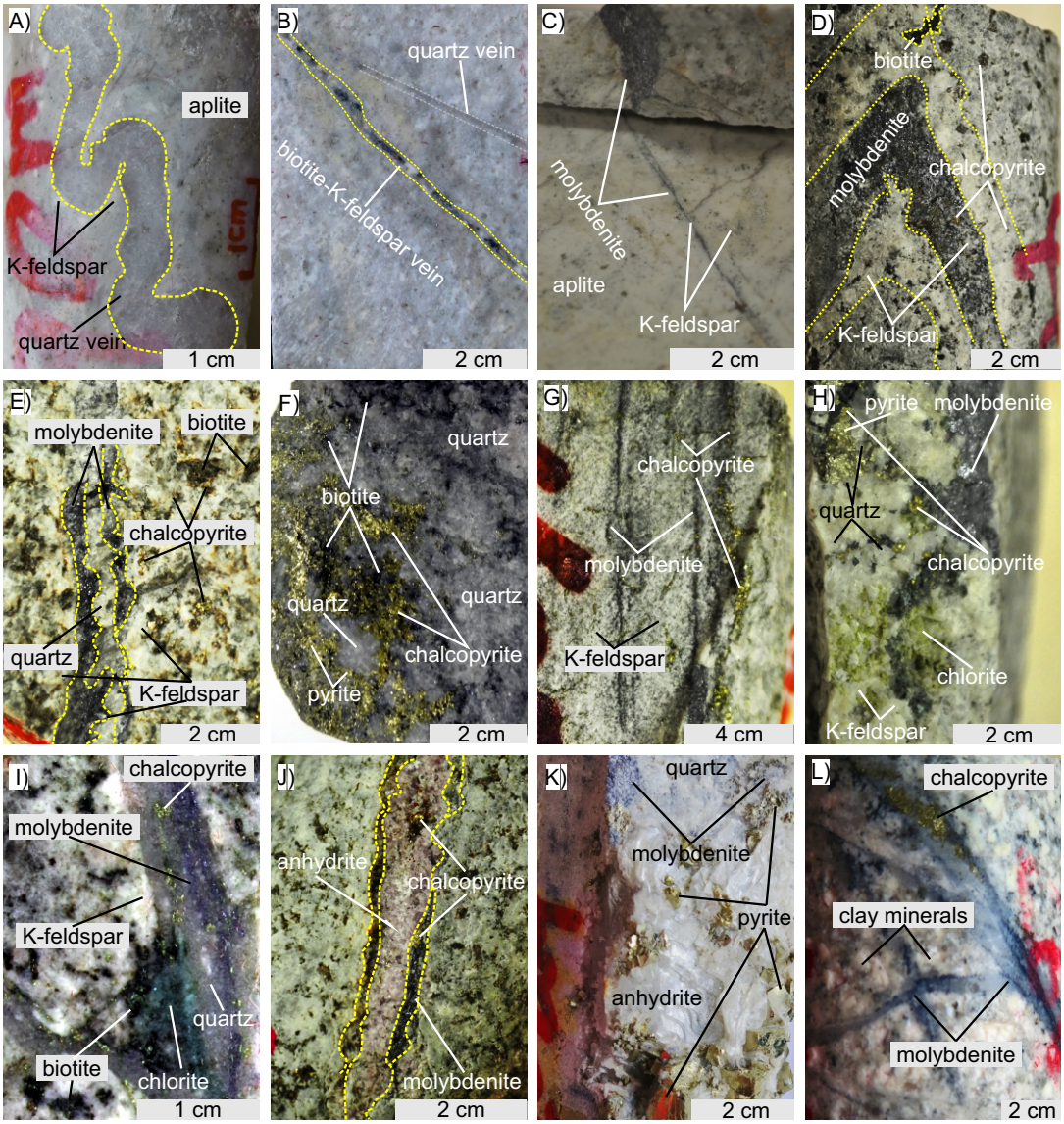
A)
aplite
K-feldspar
quartz vein
1 cm
B)
quartz vein
biotite-K-feldspar vein
2 cm
C)
molybdenite
aplite
K-feldspar
2 cm
D)
biotite
molybdenite
chalcopyrite
K-feldspar
2 cm
E)
molybdenite
biotite
chalcopyrite
quartz
K-feldspar
2 cm
F)
quartz
biotite
quartz
quartz
chalcopyrite
pyrite
2 cm
G)
chalcopyrite
molybdenite
K-feldspar
4 cm
H)
pyrite
molybdenite
quartz
chalcopyrite
chlorite
K-feldspar
2 cm
I)
chalcopyrite
molybdenite
K-feldspar
quartz
biotite
chlorite
1 cm
J)
anhydrite
chalcopyrite
molybdenite
2 cm
K)
quartz
molybdenite
pyrite
anhydrite
2 cm
L)
chalcopyrite
clay minerals
molybdenite
2 cm

Figure 2.5

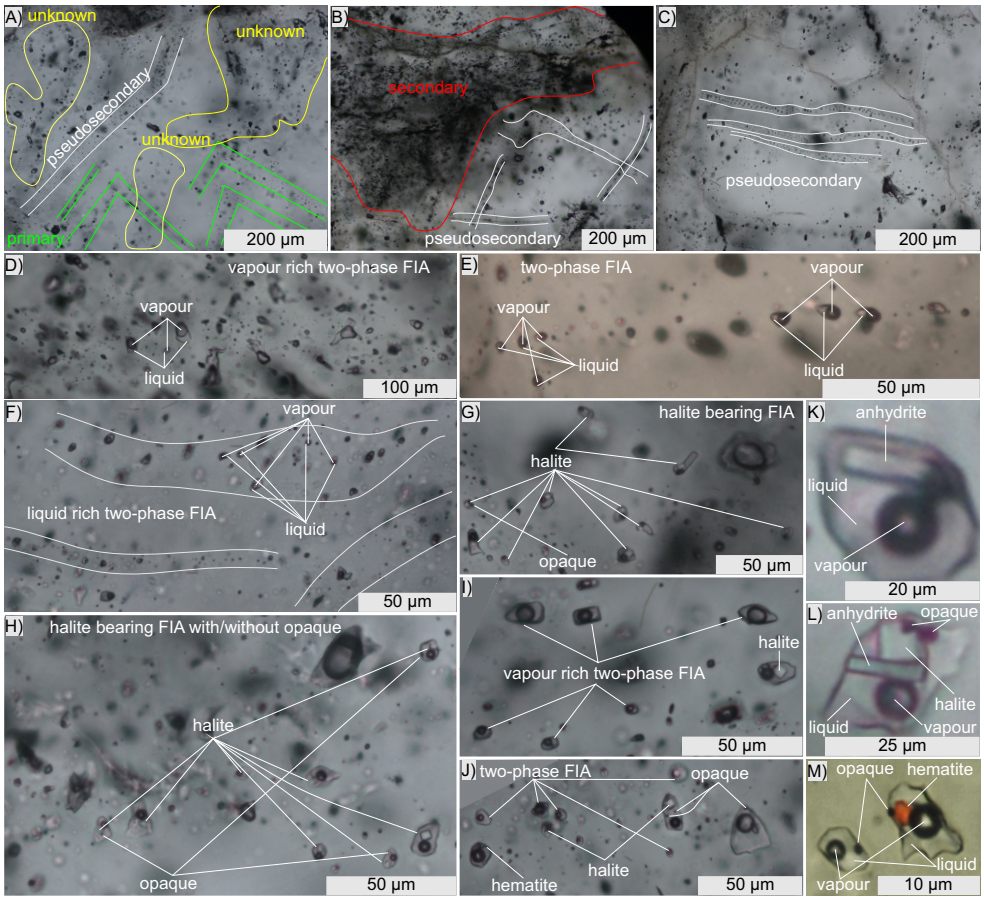
A) unknown
unknown
pseudosecondary
unknown
primary
200 μm
B)
secondary
pseudosecondary
200 μm
C)
pseudosecondary
200 μm
D)
vapour rich two-phase FIA
vapour
liquid
100 μm
E)
two-phase FIA
vapour
vapour
liquid
liquid
50 μm
F)
vapour
liquid rich two-phase FIA
liquid
50 μm
G)
halite bearing FIA
halite
opaque
50 μm
K)
anhydrite
liquid
vapour
20 μm
I)
halite
vapour rich two-phase FIA
50 μm
L)
anhydrite
opaque
halite
liquid
vapour
25 μm
H)
halite bearing FIA with/without opaque
halite
opaque
50 μm
J)
two-phase FIA
opaque
halite
hematite
50 μm
M)
opaque
hematite
liquid
vapour
10 μm

Figure 2.6

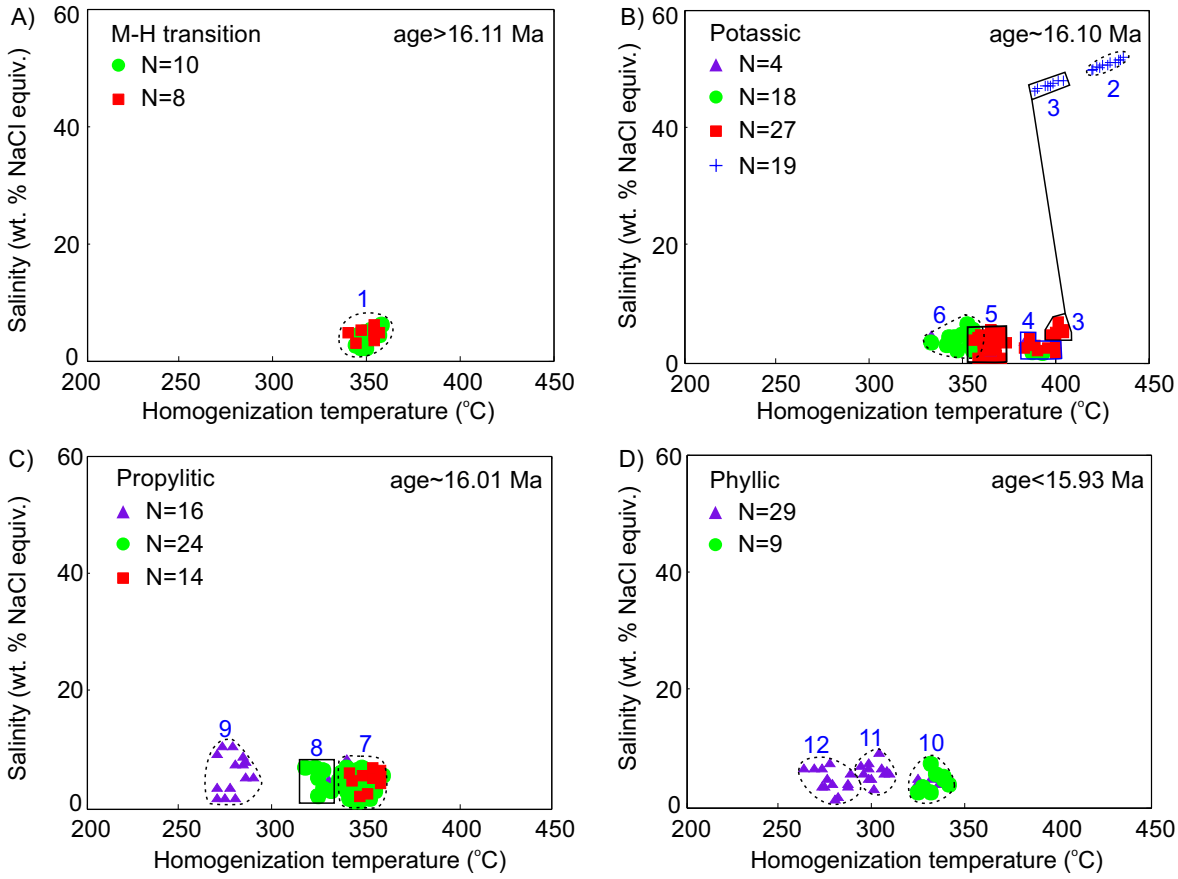
A)
M-H transition
age>16.11 Ma
N=10
N=8
1
B)
Potassic
age~16.10 Ma
N=4
N=18
N=27
N=19
1
2
3
4
5
6
C)
Propylitic
age~16.01 Ma
N=16
N=24
N=14
7
8
9
D)
Phyllic
age<15.93 Ma
N=29
N=9
10
11
12
Salinity (wt. % NaCl equiv.)
Homogenization temperature (°C)
0
20
40
60
200
250
300
350
400
450

Figure 2.7

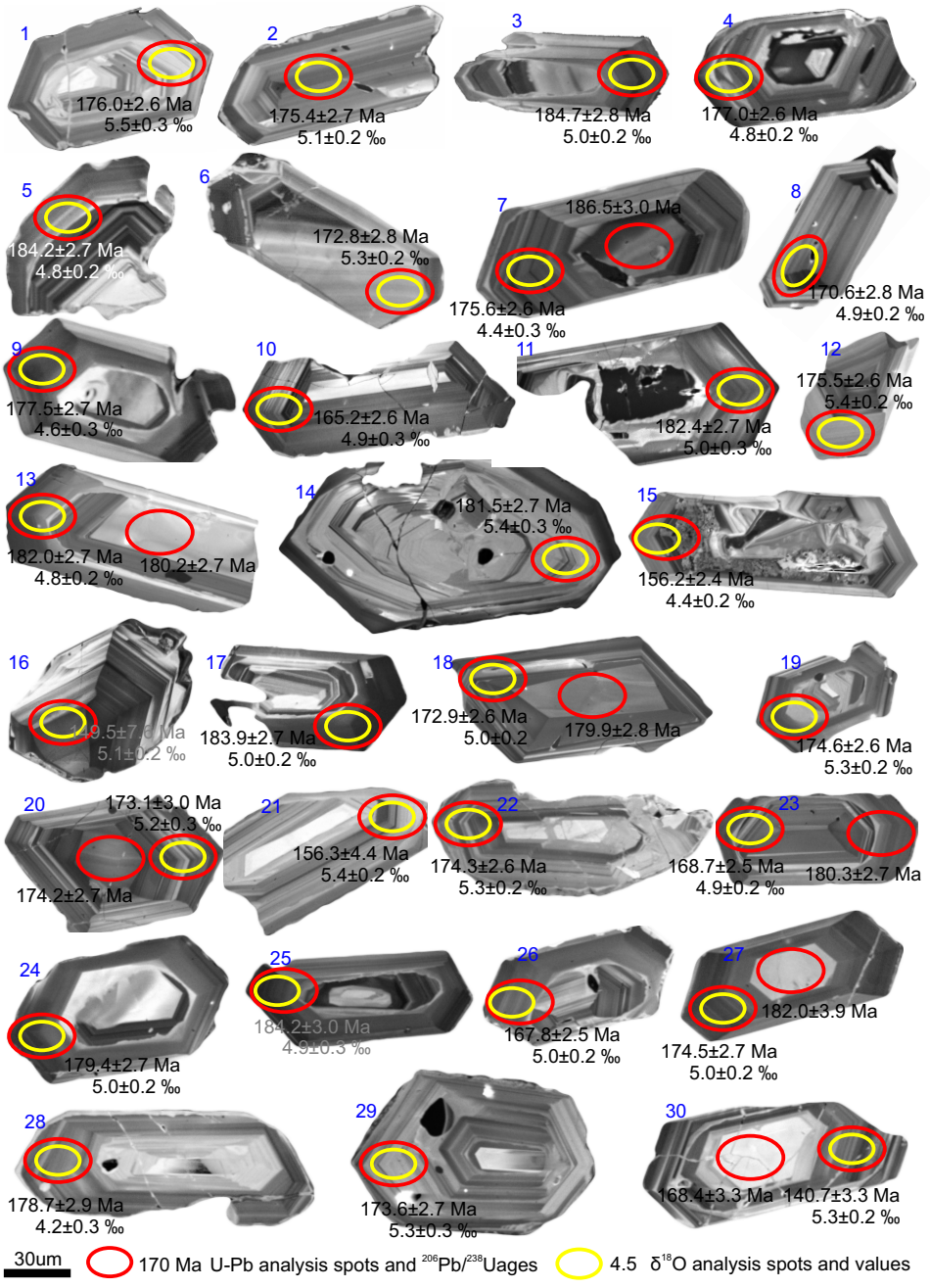
1
176.0±2.6 Ma
5.5±0.3 ‰
2
175.4±2.7 Ma
5.1±0.2 ‰
3
184.7±2.8 Ma
5.0±0.2 ‰
4
177.0±2.6 Ma
4.8±0.2 ‰
5
184.2±2.7 Ma
4.8±0.2 ‰
6
172.8±2.8 Ma
5.3±0.2 ‰
7
186.5±3.0 Ma
175.6±2.6 Ma
4.4±0.3 ‰
8
170.6±2.8 Ma
4.9±0.2 ‰
9
177.5±2.7 Ma
4.6±0.3 ‰
10
165.2±2.6 Ma
4.9±0.3 ‰
11
182.4±2.7 Ma
5.0±0.3 ‰
12
175.5±2.6 Ma
5.4±0.2 ‰
13
182.0±2.7 Ma
4.8±0.2 ‰
180.2±2.7 Ma
14
181.5±2.7 Ma
5.4±0.3 ‰
15
156.2±2.4 Ma
4.4±0.2 ‰
16
17
183.9±2.7 Ma
5.0±0.2 ‰
18
172.9±2.6 Ma
5.0±0.2
179.9±2.8 Ma
19
174.6±2.6 Ma
5.3±0.2 ‰
20
173.1±3.0 Ma
5.2±0.3 ‰
174.2±2.7 Ma
21
156.3±4.4 Ma
5.4±0.2 ‰
22
174.3±2.6 Ma
5.3±0.2 ‰
23
168.7±2.5 Ma
4.9±0.2 ‰
180.3±2.7 Ma
24
179.4±2.7 Ma
5.0±0.2 ‰
25
26
167.8±2.5 Ma
5.0±0.2 ‰
27
182.0±3.9 Ma
174.5±2.7 Ma
5.0±0.2 ‰
28
178.7±2.9 Ma
4.2±0.3 ‰
29
173.6±2.7 Ma
5.3±0.3 ‰
30
168.4±3.3 Ma
140.7±3.3 Ma
5.3±0.2 ‰
30um
170 Ma U-Pb analysis spots and 206Pb/238Uages
4.5 δ18O analysis spots and values

Figure 2.8

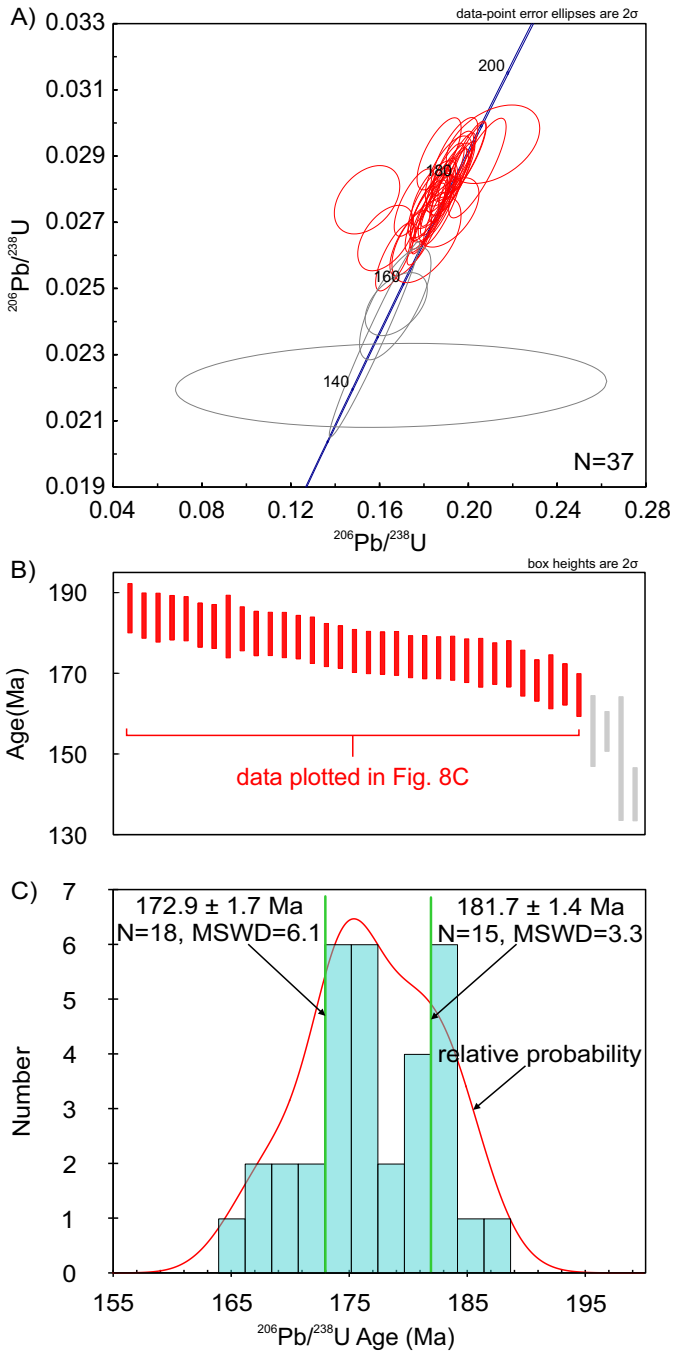
A)
data-point error ellipses are 2σ
200
180
160
140
N=37
$^{206}Pb/^{238}U$
B)
box heights are 2σ
Age(Ma)
data plotted in Fig. 8C
C)
172.9 ± 1.7 Ma
N=18, MSWD=6.1
181.7 ± 1.4 Ma
N=15, MSWD=3.3
relative probability
Number
$^{206}Pb/^{238}U$ Age (Ma)

Figure 2.9

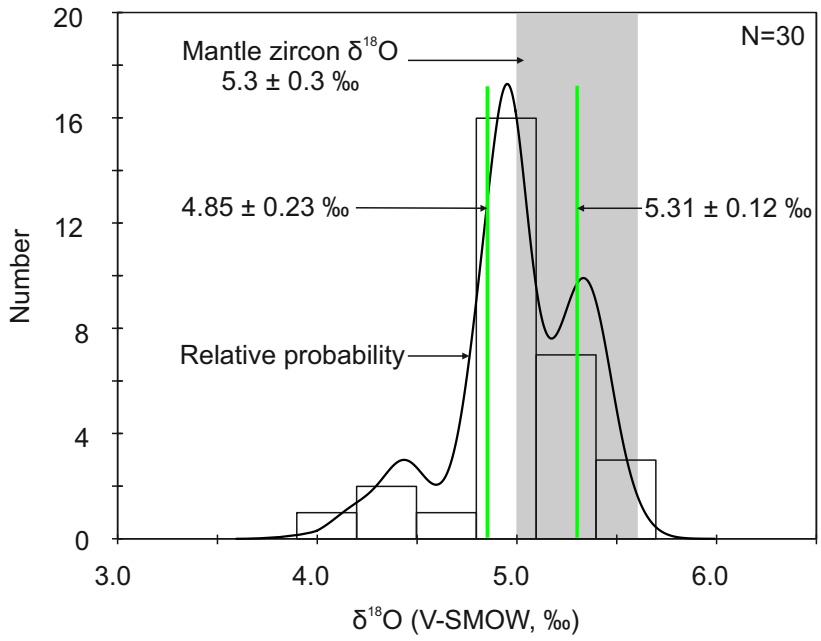
20
16
12
8
4
0
Number
N=30
Mantle zircon δ18O
5.3 ± 0.3 ‰
4.85 ± 0.23 ‰
5.31 ± 0.12 ‰
Relative probability
3.0
4.0
5.0
6.0
δ18O (V-SMOW, ‰)

Figure 2.10

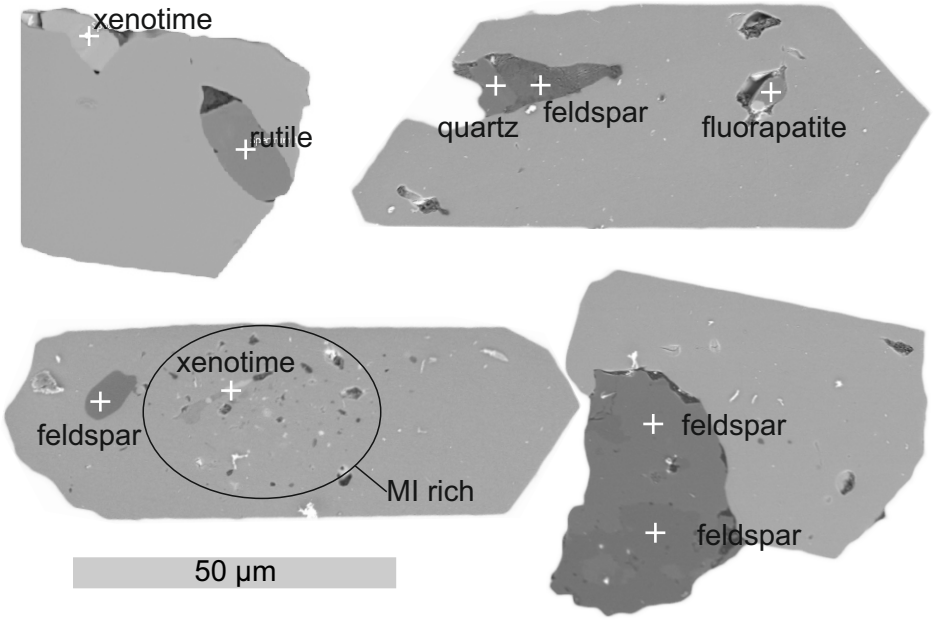
xenotime
rutile
quartz
feldspar
fluorapatite
xenotime
feldspar
MI rich
feldspar
feldspar
50 μm

Figure 2.11

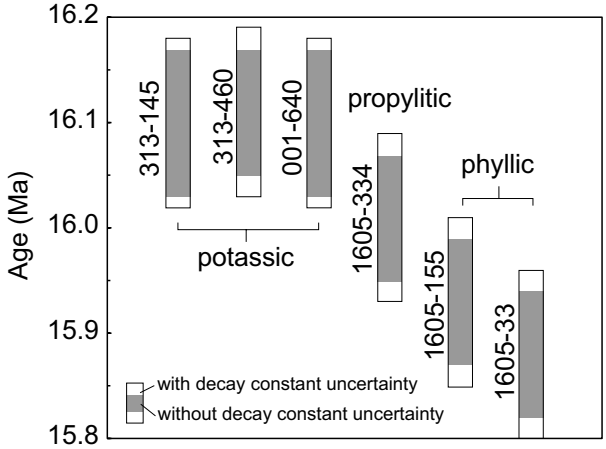
16.2
16.1
16.0
15.9
15.8
Age (Ma)
313-145
313-460
001-640
potassic
propylitic
1605-334
phyllic
1605-155
1605-33
with decay constant uncertainty
without decay constant uncertainty

Figure 2.12

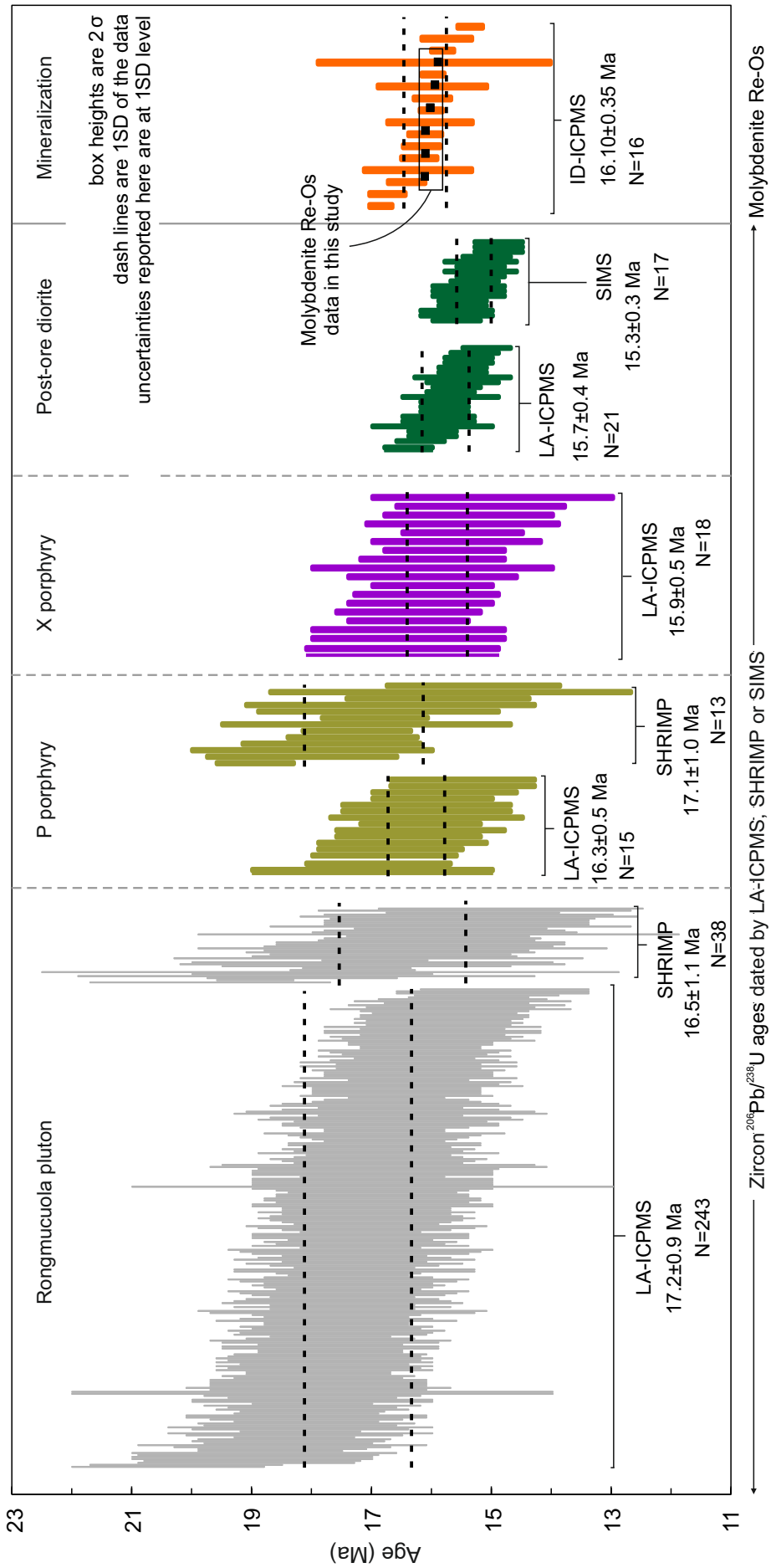
Mineralization
Post-ore diorite
X porphyry
P porphyry
Rongmucuola pluton
box heights are 2 σ
dash lines are 1SD of the data
uncertainties reported here are at 1SD level
Molybdenite Re-Os
data in this study
ID-ICPMS
16.10±0.35 Ma
N=16
SIMS
15.3±0.3 Ma
N=17
LA-ICPMS
15.7±0.4 Ma
N=21
LA-ICPMS
15.9±0.5 Ma
N=18
SHRIMP
17.1±1.0 Ma
N=13
LA-ICPMS
16.3±0.5 Ma
N=15
SHRIMP
16.5±1.1 Ma
N=38
LA-ICPMS
17.2±0.9 Ma
N=243
Age (Ma)
23
21
19
17
15
13
11
Zircon $^{206}Pb/^{238}U$ ages dated by LA-ICPMS, SHRIMP or SIMS
Molybdenite Re-Os

Figure 2.13

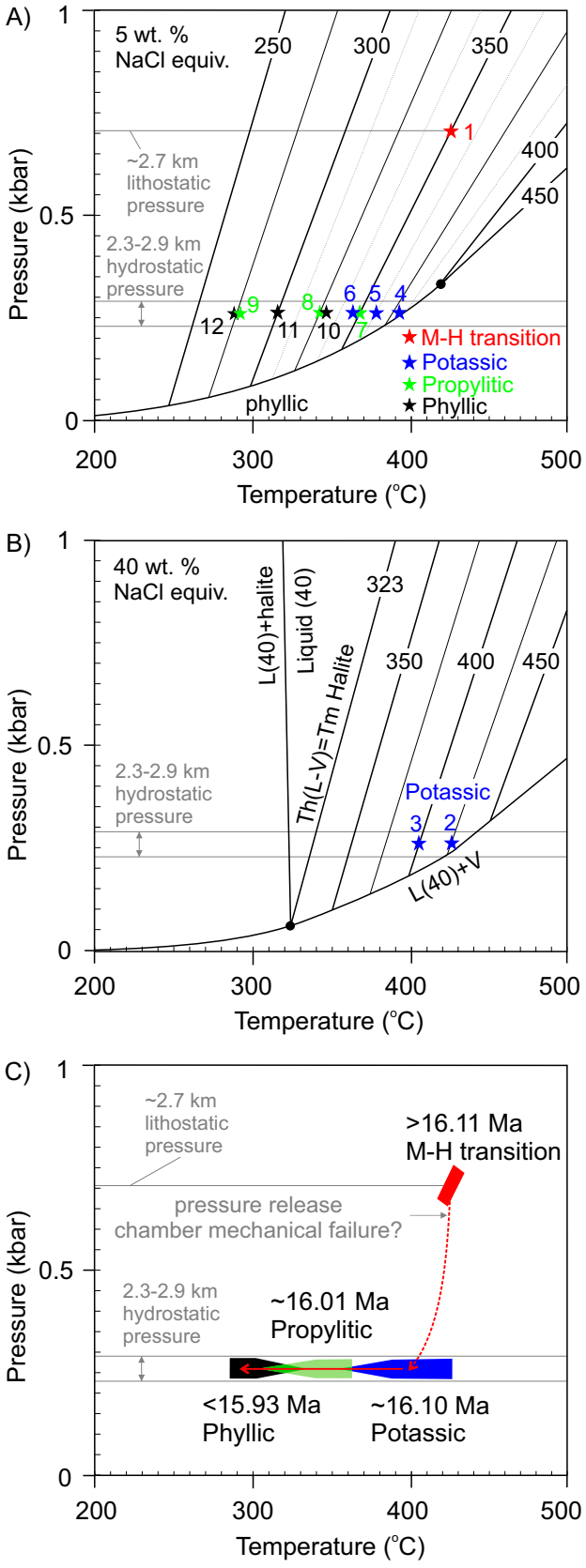
A)
5 wt. %
NaCl equiv.
250
300
350
400
450
~2.7 km
lithostatic
pressure
2.3-2.9 km
hydrostatic
pressure
1
2
3
4
5
6
7
8
9
10
11
12
M-H transition
Potassic
Propylitic
Phyllic
phyllic
Pressure (kbar)
Temperature (°C)
B)
40 wt. %
NaCl equiv.
L(40)+halite
Liquid (40)
Th(L-V)=Tm Halite
323
350
400
450
2.3-2.9 km
hydrostatic
pressure
Potassic
L(40)+V
C)
~2.7 km
lithostatic
pressure
>16.11 Ma
M-H transition
pressure release
chamber mechanical failure?
2.3-2.9 km
hydrostatic
pressure
~16.01 Ma
Propylitic
<15.93 Ma
Phyllic
~16.10 Ma
Potassic

Table 2.1. Geological summary for all magmatic units in the Qulong deposit including published ages.

Units	Distribution	Composition	Alteration and mineralization	Age (Mineral, method and data)
Yeba Formation	E-W direction in South Gangdese belt.	Andesitic crystal tuff, ignimbrite, and dacite; laminated slate, with interbedded sandstone and limestone; andesitic lava and volcanoclastic rocks.	Weak propylitic alteration, no mineralization except pyrite veins.	Zircon, LA-ICPMS U-Pb, 166.0 ± 1.8 Ma (Zhao et al. 2015).
Jurassic intrusions	Mid-western of Qulong	Dacite-rhyolite and rhyolite porphyry. quartz (20-25 vol%) and feldspar (8-10 vol%) as phenocrysts, with quartz and K-feldspar and biotite as groundmass.	Propylitic and phyllic alterations with abundant fracture controlled pyrite veins.	Zircon, SHRIMP U-Pb, 182.3 ± 1.5 Ma (Yang et al. 2009); Zircon, LA-ICPMS U-Pb, 160.7 ± 2.0 Ma (Zhao et al. 2015).
Rongmucuola pluton	East part of Qulong	Medium-coarse, hypidiomorphic-granular granodiorite. Coarse-grained (5-10 mm) plagioclase (30-40 vol%), K-feldspar (20-30 vol%), and medium grained (2-5 mm) quartz (15-20 vol%) and biotite (10-15 vol%), accessory minerals include apatite, magnetite, zircon, rutile.	Weak propylitic alteration, generally barren.	Zircon, LA-ICPMS U-Pb, 17.6 ± 0.3 Ma (Zhao et al. 2015).
	Central Qulong	Weakly porphyritic monzogranite. Coarse-grained (5-10 mm) plagioclase (30-40 vol%), K-feldspar (20-30 vol%), and medium grained (2-5 mm) quartz (15-20 vol%) and biotite (10-15 vol%), accessory minerals include apatite, magnetite, zircon, rutile.	Intensive potassic, propylitic and phyllic alteration and hosts the majority of the Cu-Mo in Qulong.	Zircon, LA-ICPMS U-Pb, 17.4 ± 0.4 Ma (Zhao et al. 2015).
P porphyry	Central Qulong	Coarse-grained monzogranite. Coarse-grained (3-8 mm) plagioclase (10-20 vol%), quartz (5-1-vol%) and K-feldspar (~5 vol%) as phenocrysts, the groundmass is dominated by quartz and feldspar.	Intensive potassic, propylitic and phyllic alteration and has been presumed as the ore-genitor porphyry.	Zircon, LA-ICPMS U-Pb, 16.2 ± 0.3 Ma (Zhao et al. 2015).
X porphyry	Central Qulong and drill cores	Coarse-grained biotite monzogranite. Mineralogy similar as P porphyry but contains more quartz.	Intensive potassic, weak propylitic and phyllic alteration, weak mineralized.	Zircon, LA-ICPMS U-Pb, 15.9 ± 0.3 Ma (Zhao et al. 2015).
Aplite	Central Qulong and drill cores	fine grained aplite Intergrowths of fine-grained (~1 mm) anhedral alkali feldspar and quartz.	Intensive potassic, weak propylitic and phyllic alteration, generally not mineralized.	No data reported
Quartz diorite dike	Mainly in drill cores	Quartz diorite dike Coarse phenocrysts (~0.5-1cm) of plagioclase (~5%), quartz (5%) and hornblende (3%) with a matrix comprise plagioclase and hornblende as well as quartz and biotite.	Weak phyllic alteration, post-mineralization thus barren.	Zircon, LA-ICPMS U-Pb, 15.3 ± 0.3 Ma (Zhao et al. 2015).

Table 2.2. Zircon SIMS U-Pb and oxygen isotope data for the aplite sample.

No	U ppm	Th ppm	Th/U	f_{206} %	$^{207}Pb/^{206}Pb$	±1σ %	$^{207}Pb/^{235}U$	±1σ %	$^{206}Pb/^{238}U$	±1σ %	rho	$t_{207/235}$ Ma	±1σ abs	$t_{206/238}$ Ma	±1σ abs	$\delta^{18}O$	±2σ abs
1	641	489	0.76	1.2	0.04044	3.59	0.15434	3.90	0.02768	1.52	0.39	145.7	5.3	176.0	2.6	5.5	0.25
2	972	1146	1.18	0.3	0.04799	1.48	0.18251	2.15	0.02758	1.56	0.72	170.2	3.4	175.4	2.7	5.1	0.21
3	3092	5055	1.63	0.5	0.04661	1.54	0.18681	2.17	0.02907	1.53	0.70	173.9	3.5	184.7	2.8	5.0	0.17
4	864	539	0.62	0.4	0.04813	1.75	0.18471	2.30	0.02783	1.50	0.65	172.1	3.7	177.0	2.6	4.8	0.22
5	1993	1466	0.74	0.0	0.04991	0.92	0.19948	1.76	0.02899	1.50	0.85	184.7	3.0	184.2	2.7	4.8	0.20
6	1738	1147	0.66	0.4	0.04831	1.36	0.18103	2.15	0.02718	1.66	0.77	168.9	3.3	172.8	2.8	5.3	0.18
7	2286	2007	0.88	0.2	0.04893	0.87	0.18634	1.74	0.02762	1.50	0.86	173.5	2.8	175.6	2.6	4.4	0.26
7	2011	1714	0.85	4.8	0.05215	3.73	0.21109	4.07	0.02936	1.65	0.40	194.5	7.2	186.5	3.0		
8	1734	2581	1.49	0.1	0.04892	0.93	0.18085	1.92	0.02681	1.68	0.88	168.8	3.0	170.6	2.8	4.9	0.20
9	1669	2079	1.25	0.1	0.04841	0.87	0.18631	1.75	0.02791	1.52	0.87	173.5	2.8	177.5	2.7	4.6	0.34
10	1824	1686	0.92	0.4	0.04666	1.41	0.16695	2.14	0.02595	1.61	0.75	156.8	3.1	165.2	2.6	4.9	0.25
11	807	575	0.71	0.1	0.04879	1.27	0.19305	1.97	0.02869	1.51	0.76	179.2	3.2	182.4	2.7	5.0	0.25
12	1747	2539	1.45	0.6	0.04616	1.47	0.17562	2.10	0.02759	1.51	0.72	164.3	3.2	175.5	2.6	5.4	0.16
13	3508	5644	1.61	0.2	0.04930	0.94	0.19470	1.78	0.02864	1.51	0.85	180.6	2.9	182.0	2.7	4.8	0.18
13	1816	11432	6.30	0.3	0.04850	1.06	0.18958	1.84	0.02835	1.50	0.82	176.3	3.0	180.2	2.7		
14	316	268	0.85	0.2	0.04854	1.66	0.19106	2.24	0.02855	1.51	0.67	177.5	3.7	181.5	2.7	5.4	0.29
15	3303	6149	1.86	1.5	0.04953	3.02	0.16749	3.41	0.02453	1.59	0.46	157.2	5.0	156.2	2.4	4.4	0.20
16	2283	2911	1.28	0.2	0.04873	1.12	0.15766	5.27	0.02346	5.15	0.98	148.7	7.3	149.5	7.6	5.1	0.24
17	2294	2295	1.00	0.0	0.05001	0.78	0.19960	1.69	0.02895	1.50	0.89	184.8	2.9	183.9	2.7	5.0	0.14
18	1501	3228	2.15	0.2	0.04848	1.02	0.18169	1.81	0.02718	1.50	0.83	169.5	2.8	172.9	2.6	5.0	0.20
18	877	1016	1.16	0.2	0.04922	1.26	0.19208	2.02	0.02831	1.57	0.78	178.4	3.3	179.9	2.8		
19	1485	3276	2.21	0.2	0.04812	1.14	0.18217	1.89	0.02746	1.50	0.80	169.9	3.0	174.6	2.6	5.3	0.21
20	1525	2750	1.80	0.1	0.04879	0.78	0.18309	1.92	0.02722	1.76	0.92	170.7	3.0	173.1	3.0	5.2	0.27
20	3278	6720	2.05	0.1	0.04981	0.87	0.18815	1.80	0.02739	1.58	0.88	175.1	2.9	174.2	2.7		
21	690	687	1.00	0.3	0.04937	2.74	0.16706	3.93	0.02454	2.82	0.72	156.9	5.7	156.3	4.4	5.4	0.21
22	617	437	0.71	0.1	0.04896	1.31	0.18504	1.99	0.02741	1.50	0.75	172.4	3.2	174.3	2.6	5.3	0.21
23	1186	1213	1.02	1.0	0.04449	2.76	0.16270	3.15	0.02652	1.52	0.48	153.1	4.5	168.7	2.5	4.9	0.19
23	1467	1589	1.08	0.0	0.04977	0.81	0.19465	1.74	0.02837	1.53	0.88	180.6	2.9	180.3	2.7		
24	1460	1373	0.94	0.1	0.04916	0.79	0.19130	1.70	0.02822	1.51	0.89	177.7	2.8	179.4	2.7	5.0	0.19
25	2846	2448	0.86	0.2	0.04846	1.49	0.19369	2.23	0.02899	1.66	0.74	179.8	3.7	184.2	3.0	4.9	0.25
26	1290	1724	1.34	0.5	0.04786	1.58	0.17403	2.20	0.02637	1.53	0.69	162.9	3.3	167.8	2.5	5.0	0.16
27	1593	1241	0.78	0.1	0.04852	1.50	0.18355	2.15	0.02744	1.54	0.72	171.1	3.4	174.5	2.7	5.0	0.20
27	2117	1235	0.58	0.0	0.05168	1.45	0.20405	2.59	0.02864	2.15	0.83	188.5	4.5	182.0	3.9		
28	891	650	0.73	0.1	0.04939	0.95	0.19137	1.88	0.02810	1.62	0.86	177.8	3.1	178.7	2.9	4.2	0.25
29	334	245	0.73	0.4	0.05077	2.47	0.19109	2.93	0.02730	1.57	0.54	177.6	4.8	173.6	2.7	5.3	0.27
30	577	392	0.68	5.5	0.05429	23.90	0.16522	24.02	0.02207	2.35	0.10	155.3	35.2	140.7	3.3	5.3	0.21
30	599	433	0.72	0.4	0.04963	2.89	0.18113	3.51	0.02647	2.00	0.57	169.0	5.5	168.4	3.3		

Table 2.3. Molybdenite Re-Os data

Sample #	Wt (g)	Re (ppm)	±	^{187}Re (ppm)	±	^{187}Os (ppb)	±	Age	±*
313-460	0.014	143.32	1.08	90.08	0.39	24.17	0.09	16.11	0.06[0.08]
313-145	0.021	64.44	1.94	40.50	0.15	10.86	0.03	16.10	0.07[0.09]
001-640	0.010	104.16	1.32	65.47	0.33	17.56	0.08	16.10	0.07[0.09]
1605-334	0.039	224.51	1.55	141.11	0.47	37.64	0.10	16.01	0.06[0.08]
1605-155	0.018	221.57	1.18	139.26	0.54	36.97	0.12	15.93	0.06[0.08]
1605-33	0.012	323.60	2.27	203.39	0.92	53.82	0.22	15.88	0.06[0.08]

*Data are presented with (bracketed value) and without ^{187}Re decay constant uncertainty (Smoliar et al. (1996); Selby et al. (2007).

Table 2.4. Fluid inclusion assemblages (FIAs) and their respective microthermometric data temperatures

FIA No.	Characteristics	Homogenized to	$T_{homogenization}$ °C	Salinity wt% NaCl equiv	$T_{trapping}$ ˚C
Magmatic-hydrothermal transition					
1	liquid-vapor two-phase and vapor-rich two-phase fluid inclusions	liquid	340-360 °C	2-6 wt%	425
Potassic alteration stage					
2	halite-bearing fluid inclusions	liquid	419-436	50-52 wt%	425
3	halite-bearing fluid inclusions and vapor-rich two-phase fluid inclusions	halite dissolution vapor	388-405	41-45 wt% 4-7 wt%	398
4	vapor-rich two-phase fluid inclusions	liquid	385-400	1-6 wt%	390
5	vapor-rich two-phase fluid inclusions	liquid	360-370	1-6 wt%	380
6	liquid-vapor two-phase fluid inclusions,	liquid	335-355	2-7 wt%	360
Propylitic alteration stage					
7	liquid-vapor two-phase fluid inclusions	liquid	335-360	1-7 wt%	365
8	liquid-vapor two-phase fluid inclusions	liquid	318-332	2-7 wt%	340
9	liquid-rich two-phase fluid inclusions	liquid	270-290	2-11 wt%	290
Phyllic alteration stage					
10	liquid-vapor two-phase fluid inclusions	liquid	325-340	2-8 wt%	345
11	liquid-rich two-phase fluid inclusions	liquid	295-310	3-9 wt%	310
12	liquid-rich two-phase fluid inclusions	liquid	265-290	1-8 wt%	285

Chapter 3

High precision U-Pb zircon and Re-Os molybdenite geochronology: Implications for the magmatic-hydrothermal evolution of the world class Qulong porphyry Cu-Mo system and global porphyry systems *

* A version of this chapter will be submitted to Earth and Planetary Science Letters, co-authored with David Selby, Simon Tapster and Daniel Condon.

3.1 Introduction

Metals forming porphyry copper deposits are derived from magma chamber at the depth, and then are transported by magmatic fluids through porphyry stocks to the shallow level (Sillitoe, 2010; Cooke et al., 2014). Although this model is widely accepted, the timescale of this process is poorly constrained, with studies suggesting tens of thousands years to several millions of years (Chiaradia et al., 2014).

The wide distribution of igneous rocks in porphyry Cu systems permit bracketing the timescale of ore formation via dating pre-ore and post-ore intrusions. Traditionally, in-situ zircon U-Pb dates are used to establish the timeframe of porphyry Cu systems and constrain the duration of ore formation (Sillitoe and Mortensen, 2010; Deckart et al., 2012). However, limited by the precision of microbeam analysis, the conclusions of these studies are controversial (Von Quadt et al., 2011; Chiaradia et al., 2013; Chiaradia et al., 2014; Schaltegger et al., 2015).

The development of high precision dating in recent years, e.g., CA-ID-TIMS zircon U-Pb and ID-N-TIMS molybdenite Re-Os, makes it possible to refine the timeframe and timescales of porphyry Cu systems (Chiaradia et al., 2013; Chiaradia et al., 2014). High precision zircon U-Pb geochronology argue that the lifetime of porphyry Cu deposits is at the tens to hundreds of kyr level with evidence supporting multiple magmatic-hydrothermal episodes (Von Quadt et al., 2011; Buret et al., 2016; Tapster et al., 2016b). These high precision dating studies are supported by numerical simulation and quartz titanium diffusion modelling, which suggest the duration of ore-formation is at several tens of kyrs (Weis et al., 2012; Mercer et al., 2015).

The most direct constrains for the duration of ore-formation come from dating the ore minerals. Applying high precision molybdenite Re-Os dating derived a mineralization duration for the El Salvador porphyry Cu-Mo deposit of 0.6 myr (Zimmerman et al., 2014), with the El Teniente porphyry Cu-Mo deposit shown to record multiple short-lived (<100,000 years) mineralization pulses over 1.7 myrs (Spencer et al., 2015). At Los Pelambres Cu–(Mo) deposit, the molybdenite Re-Os ages of the B veins are ~1 myrs younger than the ages of D veins and are interpreted to record multiple-pulsed mineralization (Stein, 2014).

Multiple magmatic-mineralization pulses is evident for deposits with prolonged duration of formation as demonstrated both by field observation (Sillitoe, 2010) and analytical approaches (Stein, 2014; Spencer et al., 2015). However, for deposits with a shorter formation duration, it is not clear yet whether they are formed consistently during the lifetime of the porphyry system or through multiple intermittent pulses. Also questionable is the timescale of a single mineralization episode, if multiple mineralization pulses are present. The answers for these questions will aid our understanding of metal enrichment, e.g., are multiple mineralization pulses necessary to form giant deposits, or is a prolonged mineralization duration essential for economic deposits? Moreover, if multiple magmatic-mineralization events are common in porphyry deposits, then it predicts thermal resetting for chronometers with low closure temperatures for thermochronology studies and leaves their interpretations problematic.

In this chapter, we test the spatial and temporal fluid evolution of the well-studied Qulong porphyry system by employing zircon chemical abrasion isotope dilution thermal ionization mass spectrometry (CA-ID-TIMS) U–Pb geochronology and molybdenite isotope dilution negative thermal ionization mass

spectrometry (ID-N-TIMS) Re-Os geochronology with precisions of ~0.1 %. Qulong only has one mineralization centre, which makes the deposit a relatively simple and ideal candidate for the research proposed above. The data is used to examine the spatial-temporal relationship between magmatism and mineralization. In addition to addressing the timescale and thermal history of this system, we further highlights the current understanding and future directions of high precision chronology studies in porphyry copper.

3.2 Geological background

The Qulong porphyry Cu-Mo deposit is located in the Gangdese magmatic belt (Fig. 3.1). This magmatic belt extends along the southern margin of the Lhasa terrane and has long been recognized as a significant porphyry metallogenic province (Zheng et al., 2004; Hou et al., 2009; Zheng et al., 2015). The belt records a prolonged tectono-magmatic history that directly relates to the Neo-Tethyan ocean northward subduction, the initial India-Asia collision, the Indian slab breakoff, and intracontinental convergence (Wang et al., 2015; Zhu et al., 2015). The Gangdese magmatic belt hosts a large number of small-volume granites and lava flows, which intruded or erupted between ~30 and 9 Ma (Fig. 3.1). Despite the good preservation and exposure of these Oligo-Miocene shallow crustal volcanic sequences and subvolcanic plutons, the central and western parts of the Gangdese magmatic belt are almost bereft of mineralization, and the majority of the known Cu-Mo-Au porphyry deposits are located within the eastern part of the belt (Fig. 3.1) (Hou et al., 2009; Richards, 2015; Wang et al., 2015).

The eastern part of the Gangdese magmatic belt is termed the Gangdese Porphyry Copper Belt which contains >20 porphyry copper systems that formed in

a post-collisional (India-Asian) tectonic setting (Hou et al., 2009; Richards, 2015; Zheng et al., 2015). Of these porphyry copper systems, 8 of them have Cu metals excess of 0.5 Mt, with Qulong being the largest no only in this belt, but also in China and hosts ~11 Mt Cu and >0.5 Mt Mo (Hou et al., 2009; Yang et al., 2009; Zheng et al., 2015; Li et al., 2016). The porphyry Cu systems of the Gangdese magmatic belt are predominately temporal and spatial associated with mid-Miocene (11.2 - 19.7 Ma) monzogranitic and quartz monzonitic plutons and stocks, which possess an adakitic geochemical affinity (Hou et al., 2009; Wang et al., 2015; Zheng et al., 2015). The origin of the associated magmas is attributed to partial melting of a thickened basaltic lower-crust (Hou et al., 2004; Hou et al., 2009; Wang et al., 2014; Richards, 2015). Throughout the belt the porphyry Cu systems predominantly show a strong spatial association with North-South striking normal fault systems (Wang et al., 2014; Wang et al., 2015).

3.2.1 Miocene intrusive units at Qulong

The Qulong porphyry Cu-Mo deposit is spatially associated with the Rongmucuola pluton, and aplite, P porphyry, X porphyry, two stages of breccia, and quartz diorite units (Fig. 3.1) (Zheng et al., 2004; Yang et al., 2009; Hu et al., 2015; Yang et al., 2015; Li et al., 2016; Zhao et al., 2016). The geology of the Qulong system is been described in detail by previous studies, which we discuss below. The predominate host to the mineralization at Qulong is the Rongmucuola pluton. This pluton intruded into the Jurassic volcanic and intrusive rocks. It has a surface exposure of ~8 km^2 and via drill core evidence is known to exist to a depth of >2 km (Fig. 3.1A). The Rongmucuola pluton is zoned, with composition varying from granodiorite to biotite monzogranite from east to west (Fig. 3.1) (Yang et al.,

2009; Li et al., 2016; Zhao et al., 2016). Despite this compositional variation, the entire pluton possesses a similar mineralogy (plagioclase, K-feldspar, quartz and biotite), however mineralization is only present in the western Rongmucuola pluton (Fig. 3.1A).

The western Rongmucuola pluton is cut by small aplite dikes, the P porphyry, the X porphyry and the breccia pipe. The relative chronology of these units defined by crosscutting relationships is presented in Figure 3.2A (Yang et al., 2009; Hu et al., 2015; Yang et al., 2015; Li et al., 2016; Zhao et al., 2016). The aplite has limited distribution in the drill cores and occurs as discontinuous (several to tens of centimetres wide) fracture controlled dikes which is only observed to have intruded into the Rongmucuola pluton. The aplite dykes are characterized by intergrowths of fine-grained (~1 mm) anhedral alkali feldspar and quartz with disseminated magnetite and pyrite (Yang et al., 2009; Li et al., 2016).

The P porphyry was emplaced into the centre of the western Rongmucuola pluton (Fig. 3.1A). No crosscutting relationship has been observed between the P porphyry and aplite units (this study; (Yang et al., 2009; Li et al., 2016; Zhao et al., 2016). The P porphyry has an exposure area of ~0.5 km^2 and extends to a depth of >1.8 km. The P porphyry is monzogranite in composition (plagioclase, quartz, K-feldspar), and occurs in the centre of the Qulong porphyry system (Fig. 3.1B) (Yang et al., 2009; Hu et al., 2015; Li et al., 2016; Zhao et al., 2016).

The X porphyry cross cuts both the western Rongmucuola pluton and the P porphyry (Fig. 3.1B, Zhao et al., 2016), and has only a limited distribution only being presence at shallow levels (value) as discontinuous irregular dikes with variable thickness from a few centimetres to 0.5 m (Yang et al., 2009). The X porphyry possesses a similar composition with that of the P porphyry, with the

exception to its biotite content (3-5 % in the X porphyry vs <3 % in the P porphyry) (Yang et al., 2009).

A hydrothermal breccia pipe (~100 m in diameter) is observed to only cross cut the Rongmucuola pluton (Fig. 3.1B). The breccia pipe contains two stages of breccia formation. The first stage breccia comprises clasts (<2 cm) of the mineralized and hydrothermally altered Rongmucuola pluton and the X porphyry (Yang et al., 2009). The second stage breccia cross cuts the first stage breccia and is characterized by fragments (1 – 10 cm) of mineralized and hydrothermally altered Rongmucuola pluton. A cement of a monzogranite composition is characteristic to both breccias (Yang et al., 2009).

The cessation of magmatism at Qulong is marked by a quartz diorite (plagioclase, quartz and hornblende), which intrudes the Rongmucuola pluton (Fig. 3.1B) as discontinues dikes with a thickness of 2 - 6 m. The quartz diorite has only been documented in drill cores in the centre of the deposit. This intrusion exhibits no to only limited alteration, which is typically shown by plagioclase phenocrysts, which in some cases show alteration of the crystal rims to calcite-chlorite-sericite and clay minerals (Yang et al., 2015).

3.2.2 Alteration and mineralization at Qulong

Mineralization is predominately (>80 %) hosted by the western Rongmucuola pluton. Drill core logging indicates that the bulk of the metals are directly associated with potassic stage alteration assemblages, though propylitic and phyllic alteration assemblages also contain Cu-Mo mineralization (Yang et al., 2009; Li et al., 2016). The most intensive potassic stage alteration exists in the central part of the deposit and is spatially associated with the P porphyry and the N-

S trending fault system. The less intensive potassic alteration assemblages extend from the centre of the deposit and is widely distributed in the western Rongmucuola pluton. Propylitic alteration assemblages predominately occur in the distal part of western Rongmucuola pluton, and overprint the potassic alteration assemblages. Phyllic alteration assemblages also widely distribute in the deposit, and almost overprint all earlier stage (potassic, propylitic) alteration assemblages (Yang et al., 2009; Li et al., 2016; Zhao et al., 2016). The Cu-Mo metals grades of the orebody exhibit concentrically zoned patterns around the P porphyry (Yang et al., 2009) and the N-S trending fault. Currently, with the small size and limited distribution of the aplite and the X porphyry, the P porphyry has been suggest as the main magmatic-hydrothermal fluid conduit at Qulong (Yang et al., 2009; Hu et al., 2015; Li et al., 2016; Zhao et al., 2016).

The ore minerals at Qulong are chalcopyrite and molybdenite, which are hosted by quartz vein assemblages in the western Rongmucuola pluton (Yang et al., 2009; Li et al., 2016). With the exception of barren quartz-biotite and biotite veins (generally 2 mm wide), mineralized quartz veins (0.5 - 3 cm wide) bearing potassic alteration selvages (K-feldspar, biotite-feldspar-quartz) are characterized by chalcopyrite and molybdenite (Li et al., 2016). Quartz veins (0.7 - 5 cm wide) bearing propylitic alteration assemblages (chlorite-dominated and in some cases contain pink anhydrite) comprise variable proportions of pyrite, chalcopyrite and molybdenite (Yang et al., 2009; Li et al., 2016). The mineralization possessing propylitic assemblages are apparently less abundance than that of the potassic alteration stage (Yang et al., 2009; Li et al., 2016). Phyllic alteration assemblages are poor mineralized, and are characterized by veinlets comprising pyrite, sericite, anhydrite that are spatially associated with minor chalcopyrite and molybdenite (Li

et al., 2016). Alteration and sulphide minerals of the phyllic alteration stage are generally fine-grained (0.5 - 3 mm), but occasionally include coarse-grained (0.5 - 1 cm) euhedral pyrite and anhydrite crystals (Li et al., 2016). The mineralization characteristics are discussed in further detail in relation to the sample set utilised for Re-Os molybdenite geochronology in section 3.1.

3.2.3 Previous Geochronology

The Qulong porphyry Cu deposit has been studied extensively with the aim to establish the timing of magmatism, mineralization and thermal history (Hou et al., 2004; Wang et al., 2006; Yang et al., 2009; Hu et al., 2015; Yang et al., 2015; Li et al., 2016; Zhao et al., 2016 and references therein). These studies established the timeframe of Qulong (Fig. 3.2A) via LA-ICPMS/SHRIMP/SIMS (U-Pb zircon) and ID-ICPMS (Re-Os molybdenite). These dates are presented in Figure 3.2B and Table 3.1 - 3.2.

The U-Pb zircon systematics from the Rongmucuola pluton yield dates from 19.5 ± 0.4 Ma (Yang et al., 2009) to 16.4 ± 0.4 Ma (Wang et al., 2006), with a weighted mean $^{206}Pb/^{238}U$ age of 17.2 ± 1.8 Ma (2 SD, n = 243, LA-ICP-MS), and 16.5 ± 2.2 Ma (2 SD, n = 38, SHRIMP). No age difference is observed between the eastern and western Rongmucuola pluton based on the zircon LA-ICPMS data (Zhao et al., 2016).

Zircon LA-ICP-MS and SHRIMP $^{206}Pb/^{238}U$ ages of 16.2 ± 0.4 (Zhao et al., 2016) and 17.58 ± 0.7 Ma (Hou et al., 2004), respectively are reported for the P porphyry. Zircon grains from the X porphyry yield a weighted mean LA-ICPMS $^{206}Pb/^{238}U$ age of 15.9 ± 0.4 Ma (Zhao et al., 2016). The emplacement/crystallization age of the aplite has not been constrained. This is

because the U-Pb systematics exhibit only inheritance from Jurassic zircons (Li et al., 2016). However, the minimum emplacement age of the aplite has been estimated as 16.11 ± 0.08 Ma via Re-Os dating of molybdenite within a cross cutting A-type quartz vein with discontinue K-feldspar selvage (Li et al., 2016). The U-Pb systematics of zircons from the post-ore quartz diorite yield LA-ICPMS and SIMS $^{206}Pb/^{238}U$ age of 15.7 ± 0.2 Ma (Yang et al., 2015) and 15.3 ± 0.3 Ma (Zhao et al., 2016), respectively.

Published molybdenite Re-Os dates are presented by 4 studies, which have focused on molybdenite from the Rongmucuola pluton (Meng et al., 2003; Zheng et al., 2004; Li et al., 2005; Wang et al., 2006). The Re-Os molybdenite dates range from 16.85 ± 0.20 Ma to 15.36 ± 0.22 Ma (age uncertainties include 0.35 % uncertainty in the decay constant of Smoliar et al. (1996). The previous Re-Os molybdenite dates suggest a mineralization duration of 1.49 ± 0.29 myrs. In addition, the timing of mineralization at Qulong has also been constrained from Ar-Ar dating of hydrothermal biotite from a potassic alteration selvage and sericite from a phyllic alteration selvage. Both biotite and sericite yield identical Ar-Ar plateau ages of 15.7 ± 0.2 Ma (Zhao et al., 2016).

As illustrated in Figure 3.2B, the emplacement ages of the intrusions constrained by *in-situ* U-Pb zircon dating have uncertainties of 0.6-2.2 Ma, and the mineralization ages constrained by ID-ICPMS molybdenite Re-Os dating have uncertainties of 0.20-1.94 Ma, which equates to uncertainties of 3.8-13.8 % and 1.3-12.1 %, respectively for the Qulong porphyry system. Although the previous studies provide a basic framework for the formation time of Qulong, the age data and their subsequent utility to precisely define the magmatic and mineralization event(s) and duration are hampered by the poor precision of the data.

3.3 Samples and Methods

To provide robust and precise time constraints for the Qulong porphyry Cu-Mo system, high precision CA-ID-TIMS zircon U-Pb geochronology (Condon et al., 2015; McLean et al., 2015) and ID-NTIMS molybdenite Re-Os dating (Markey et al., 2007; Zimmerman et al., 2014; Chelle-Michou et al., 2015; Spencer et al., 2015) are employed.

3.3.1 Samples

Representative samples of the western Rongmucuola pluton, P porphyry, and the quartz diorite were collected from drill core to conduct CA-ID-TIMS zircon U-Pb geochronology. The Rongmucuola pluton sample (1605-296) exhibits only minor hydrothermal alteration and mineralization, e.g., rims of the biotite and plagioclase are altered to sericite, and the groundmass possesses minor disseminated pyrite. The P porphyry is extensively hydrothermally altered and overprinted by multiple alteration assemblages. Sample (001-550) of the P porphyry possesses K-feldspar phenocrysts that exhibit an embayed morphology, with the groundmass displaying different degrees of hypogene alteration as a result of either complete or partial destruction of plagioclase feldspar to sericite/clay, and biotite to chlorite. The quartz diorite sample (1605-81) only exhibits minor alteration of rims of the plagioclase phenocrysts, which has been altered to calcite-chlorite-sericite and clay minerals. A previous study showed that the aplite contains only inherited Jurassic zircons, and therefore was not selected for further study (Li et al., 2016). The X porphyry has only been observed in drill core. The drill core has been completely exhausted of all the X porphyry by previous studies. As a result,

no material of the X porphyry is available for U-Pb zircon CA-ID-TIMS geochronology.

Thirteen molybdenite-bearing quartz veins are selected to conduct high precision ID-NTIMS Re-Os geochronology. The quartz veins of these samples are identical to those used to constrain P-T-X conditions of the fluids associated with the vein formation via a fluid inclusion study (Li et al., 2016). Of the 13 quartz veins, twelve veins are hosted by the western Rongmucuola pluton, with one vein being hosted by an aplite dyke. No quartz veins bearing molybdenite were observed in the P porphyry of this study nor have been documented (Yang et al., 2009).

The sampled quartz veins are classified as A, B and D veins based on previous studies (Yang et al., 2009; Li et al., 2016) and by following the vein terminology/classification of Gustafson and Hunt (1975) and (Sillitoe, 2010) (Fig. 3.3C). Three veins are classified as A veins, 7 veins are classified as B veins and the remaining 3 veins are D veins. Representative A, B and D veins are illustrated in Figure 3.3. The molybdenite in these veins is fine grained (<3 mm, and typically <1 mm) and are closely associated with the vein quartz (Li et al., 2016).

A veins are characterized by a 0.3 - 0.8 cm wide discontinuous granular quartz veinlets with narrow (< 3 mm) K-feldspar selvages. These veins host disseminated chalcopyrite and molybdenite (Fig. 3.3A). B veins are represented by veinlets (0.4 - 2 cm wide) comprising crystalline quartz with suture in the centre, and possess irregularly distributed K-feldspar selvage. The sulphide mineralization (molybdenite + chalcopyrite) is predominantly presence along the margin of the quartz vein (Fig. 3.3B). D quartz veins (0.5 - 6 cm) host euhedral pyrite, with sericite and anhydrite (0.1 and 1.5 cm) selvages (Fig. 3.3D). Minor chalcopyrite and molybdenite are disseminated within these veins.

3.3.2 CA-ID-TIMS zircon U-Pb analytical protocols

The methods for U-Pb geochronology are the same as previously documented by Tapster et al. (2016a). Mineral separation was carried out at the NERC Isotope Geosciences laboratory (NIGL), British Geological Survey (BGS), Nottingham, UK. Zircons were isolated from a ~1.5 kg drill core sample. After washing, samples were jaw crushed, disc milled and sieved (<355 µm mesh). Heavy minerals were concentrated using a Rogers table, Frantz electromagnetic separator and heavy liquids (diiodomethane). Zircon grains were then handpicked under a binocular microscope and mounted in epoxy, and then polished with a 0.25 µm diamond paste and finished at near-equatorial sections.

The mounts were coated with carbon for CL imaging, which was conducted with a Hitachi SU-70 FEG SEM at Durham University. Examination was carried out at 10-15 kv accelerating voltage with a beam current of 1.63 nA at 16.8 mm working distance under a high vacuum mode. Secondary electron images were taken using the same accelerating voltage and working distance, but at a lower beam current (0.6 nA).

Zircon grains without inclusions are no indication of inheritance (Fig. 3.8) are removed from the mounts and then individually thermally annealed in quartz crucibles at 900 ^{o}C for ~60 hours as part of the chemical abrasion process (Mattinson, 2005). The zircons were then individually ultrasonically cleaned in warm 4N HNO_3, and further rinsed with 4N HNO_3 and ultrapure acetone. The chemical abrasion is continued by loading the zircons individually into 300 µl FEP Teflon microcapsules with 29 N HF with trace 4N HNO_3. The microcapsules were placed in a self-sealing Parr^{TM} vessel at ~180 ^{o}C for 12 hours (Mattinson, 2005).

The leachate was removed, with the zircon fractions rinsed in 4N HNO_3, fluxed in 6N HCl at ~80 ^oC for several hours or overnight, and further rinsed in 4N HNO_3. The leached zircons were spiked with the mixed ^{202}Pb-^{205}Pb-^{233}U-^{235}U EARTHTIME tracer solutions (ET2535, Condon et al., 2015; McLean et al., 2015) before dissolution with ~120 µl of 29N HF and trace HNO_3 in parr^{TM} vessels at ~220 ^oC for 60 hours. Solutions of the equilibrated spike and dissolved zircon were evaporated and re-dissolved in Parr^{TM} vessels overnight in 3N HCl at 180 ^oC. Uranium and Pb were separated by standard HCl-based anion-exchange chemistry (Krogh, 1973) and evaporated to dryness with 2 µl of 0.05N H_3PO_4.

Uranium and Pb were loaded together on a single zone refined Re filament in a silica gel-phosphoric acid matrix (Gerstenberger and Haase, 1997). Isotope ratios were measured using a Thermo-Electron Triton Thermal Ionization Mass-Spectrometer. Lead isotopic compositions was measured by peak-hopping on a secondary electron multiplier detector (SEM). Uranium isotopic compositions were made in static Faraday mode on Faraday detectors equipped with 10^{12} Ω resistors for intensities greater than 4 mV or SEM peak hopping mode for low-U samples. Linearity characterization and dead time corrections (Pb = 24.5 ns; U = 22 ns) for SEM measurements were made from long-term monitoring of the NBS 982, NBS 981 and U 500 standards.

Isotope measurements were processed using the TRIPOLI software package (Bowring et al., 2011). Data reduction, error propagation, data calculation and presentation were conducted using ET_Redux and related algorithms (McLean et al., 2011). Mass bias for Pb was corrected with real-time $^{202}Pb/^{205}Pb$ ratios (Condon et al., 2015; McLean et al., 2015). Uranium was run as an oxide (UO_2), and corrected for isobaric interferences using a $^{18}O/^{16}O$ value of 0.00205. U mass

fractionation was calculated in real-time based on the isotopic composition of the tracer solutions. Decay constants are from Cheng et al. (2000) for ^{230}Th, Jaffey et al. (1971) for ^{238}U and ^{235}U, and the ^{238}U/^{235}U of Hiess et al. (2012).

All common Pb (Pbc) was attributed to an isotopic composition of the NIGL laboratory blank of ^{206}Pb/^{204}Pb = 18.099 ± 3.02 %, ^{207}Pb/^{204}Pb = 15.545 ± 1.758 % and ^{208}Pb/^{204}Pb = 37.824 ± 2.814 % (2σ uncertainties) for the analytical period. The high radiogenic Pb compared with common Pb in these zircon grains gives confidence that dates are robust (Table 3.4). The U blanks were assigned a value of 0.1 ± 0.02 pg (2σ) based upon total procedural blanks.

The preferential inclusion of ^{238}U and exclusion of ^{230}Th during zircon crystallization (Schärer, 1984), and thus eventual deficit in ^{206}Pb (younger apparent dates), was accounted for based upon the Th/U of the melt at the time of zircon crystallization (Schärer, 1984) as represented by the Th/U of the bulk samples (Yang et al., 2009), and the Th/U of individual zircon fractions analysed by ID-TIMS that derived initial Th from the ^{208}Pb measurement and date.

The Th/U values of the Rongmucuola pluton, the P porphyry and the quartz diorite are 4.0, 3.6 and 5.0, respectively (Yang et al., 2009). These values are used with an uncertainty of ± 2 (2 σ) to correct the ^{230}Th disequilibrium and yield the best age estimate of the zircons. The Th/U values of individual zircons may vary due to fractional crystallization, partition coefficients, temperature and oxidation state (Rubatto and Hermann, 2007; Luo and Ayers, 2009; Burnham and Berry, 2012). To account for all these complexities, we further investigate the sensitivity of the Th/U correction by varying the Th/U values within geologically feasible values (1 – 7, Table 3.3). As demonstrated by using the youngest group of 3 zircon dates from the P porphyry (Fig. 3.4), over a range of Th/U = 2-7, the inferred

emplacement age varies by less than 40 kyrs, with statistically acceptable MSWD values (e.g., <1.5, Fig. 3.5) maintained throughout. With Th/U of 2 - 7, the corrected ages only shift within ca. 20 kyr from the best age estimate and overlap within uncertainty (Fig. 3.4). Only at magmatic Th/U values approaching unity is a significantly younger date determined that appreciably differs from our preferred value. However, given that the Th/U values of the Rongmucuola pluton, the P porphyry and the quartz diorite are 4.0, 3.6 and 5.0, respectively (Yang et al., 2009), correcting for initial ^{230}Th disequilibrium using a Th/U ≤1 is a geologically unreasonable assumption.

3.3.3 ID-NTIMS molybdenite Re-Os

The molybdenite separation and Re-Os dating methods are adopted from previous studies (Selby and Creaser, 2001; Lawley and Selby, 2012). Molybdenite (0.3 - 3 mm grain size) bearing quartz veins were selected based on previous petrography and fluid inclusion study (Li et al., 2016), and then cut into several parts depending on molybdenite concentrations (Fig. 3.6). The vein fractionations were then individually crushed by an agate pestle to 5 mesh and then handpicked under a binocular microscope to remove non-molybdenite bearing phases and to examine the genetic association between quartz and molybdenite. The pre-purified materials were loaded into Teflon beakers with 10 ml 32 N HF to dissolve quartz at room temperature overnight (Lawley and Selby, 2012). This step was repeated until all the molybdenite are liberated. The molybdenite were rinsed with MQ three times and further rinsed with ethanol, and then dried at ~35 ^{o}C. The concentrated molybdenite aliquots were further purified (removal of any pyrite / chalcopyrite)

by hand under a binocular microscope. The purity of the mineral separate was better than 95 %.

For molybdenite digestion, a known amount of molybdenite (>20 mg) and spike solution (^{185}Re plus isotopically normal Os) was loaded into a Carius tube with 3 ml 15.5 N HCl and 6 ml 16 N HNO_3, sealed and digested at 220 ^{o}C for ~24 hours. Osmium was isolated from the acid medium using solvent extraction ($CHCl_3$) at room temperature and further purified by micro-distillation. The rhenium fraction was separated by NaOH-acetone solvent extraction and standard anion column chromatography. Rhenium and Os were loaded on to Ni and Pt filaments, respectively. The isotopic compositions were measured by negative thermal ionization mass spectrometry (N-TIMS) (Creaser et al., 1991). The mass spectrometer analysis were conducted on a Thermo Scientific TRITON mass spectrometer at Durham University, with Re and Os isotope compositions measured using static Faraday collection mode. The Re and Os isotope composition analytical uncertainties were propagated with spike calibrations, sample and spike weighting uncertainty, reproducibility of Re and Os isotope standard values, as well as blank abundances and isotope compositions. During this study, Re and Os blanks were 4 pg and <1 pg, respectively, with a ^{187}Os/^{188}Os of 0.24 ± 0.01 (n = 6). The high rhenium and osmium abundance (see results) in these samples results in negligible blanks correction (<0.035 %). The molybdenite Re-Os model age was calculated using the equation $t = \ln(^{187}Os/^{187}Re + 1)/\lambda$, in which λ is the decay constant (Smoliar et al., 1996). The variations of the model ages between the ^{187}Re decay constants of (Smoliar et al., 1996) and (Selby et al., 2007) is ~0.008 Ma, which is at the similar level with the analytical uncertainty.

To evaluate the accuracy and reproducibility of the analytical approach, the Henderson molybdenite reference material (RM8599) were run during the course of this study. Nine analyses of RM8599 during this study yield a weighted mean of 27.695 ± 0.038 (2σ, n = 9, Table 3.4, Fig. 3.7), which is in good agreement with the recommended value 27.656 ± 0.022 Ma (Markey et al., 2007; Zimmerman et al., 2014), and previous analysis at Durham (Lawley and Selby, 2012).

A further consideration, although negligible (Selby and Creaser, 2001; Stein et al., 2001; Stein, 2014), is the presence of common ^{187}Os in the molybdenite, which is not accounted for by the analytical method using a tracer solution with a normal Os isotope composition (Selby and Creaser, 2001; Markey et al., 2007). However, a body of evidence shows that the levels of common ^{187}Os in molybdenite are <~23 ppt, and typically < 6 ppt (Stein et al., 2001; Stein, 2014; Zimmerman et al., 2014; Spencer et al., 2015). These levels of common ^{187}Os will only alter the model ages of this study by 1-10 kyrs (with 33 of the 42 dates <3 kyrs). Further, our approach of obtaining multiple ages for several individual molybdenite separates from single vein, which yield reproducible ages, support the negligible presence of common ^{187}Os in molybdenite of the Qulong porphyry system (Table 3.6) (Stein, 2014).

3.4 Results

The U-Pb zircon and Re-Os molybdenite data are presented in Tables 3.5 and 3.6, and Figures 3.9 and 3.10. The uncertainties of U-Pb and Re-Os dates are presented as age ± x/y/z (internal/+tracer calibration/+decay constant uncertainties). The weighed mean date is determined from the youngest populations from each

sample (zircon and molybdenite), with the cause of any scatter evaluated by mean square weighted deviates (MSWD) value (Wendt and Carl, 1991).

3.4.1 Zircon U-Pb geochronology

The 8 zircons from the Rongmucuola pluton yield $^{206}Pb/^{238}U$ dates of ca. 17.975 - 17.057 Ma. The youngest date obtained from a single analysis is 17.057 ± 0.053/0.053/0.056 Ma, yet this date lacks the robustness of reproducibility. As such the preferred interpretation for the emplacement age is taken from the weighted mean date of 17.142 ± 0.014/0.014/0.023 Ma, calculated from the youngest cluster of dates that form a statistically acceptable population (MSWD = 1.12; n = 3). The older dates are interpreted as protracted zircon crystallisation in a large upper crustal magma chamber (Buret et al., 2016) and/or incorporation of inheritance.

Seven analyses from the P porphyry yield $^{206}Pb/^{238}U$ dates between 16.115 and 16.009 Ma. The analyses display two age groups that provide statistically distinguishable weighted mean dates of 16.065 ± 0.016/0.016/0.024 (n = 4; MSWD = 1.5) and 16.009 ± 0.016/0.017/0.024 (MSWD = 0.90; n = 3). The younger zircon group includes two fragments of a single elongate prismatic zircon grain (z4A and z4B, Fig. 3.8) which yield almost identical ages. This indicates within sample consistency of the U-Pb systematics. We consider the age of the older group of zircons to record the onset of crystallization for the P porphyry, with the age of the younger group being the best estimate for the emplacement age of the P porphyry. If this is correct, the U-Pb dates suggest that the duration of the crystallization of the P porphyry is 55 ± 23 kyrs.

Seven zircons from the post-ore quartz diorite yield $^{206}Pb/^{238}U$ dates of 15.189 - 15.116 Ma (Fig. 3.9). Six of the analyses yield a weighted mean date of

15.166 ± 0.010/0.011/0.020 (MSWD = 1.67) and is taken as the best estimate of the emplacement age. The oldest analyse likely reflects incorporation of xenocrystic and/or antecrystic zircon growth.

3.4.2 Molybdenite Re-Os geochronology

In total 13 veins were utilised for Re-Os molybdenite geochronology. For 10 veins, between 2-7 individual molybdenite separates were obtained for each vein. Overall, the Re abundances of the molybdenite samples range from 60 to 504 ppm, with the majority (>80%) possessing between 210 and 504 ppm (Table 3.6). The ^{187}Os contents range from 10 to 85 ppb.

For the 10 veins with multiple molybdenite separates (Table 3.6), 8 veins possess relatively similar Re abundances along the vein, with the remaining 2 veins exhibiting considerable variations, e.g., 274 - 454 ppm, 137 - 232 ppm (Veins; Table 3.6). Given that the molybdenite samples used in this study are pure separates (>95 %), it is unlikely that the variations observed in Re abundance are caused by variable digestions of none-molybdenite phases, e.g., quartz, chalcopyrite and pyrite. The exact reason for the variations in Re abundance is unknown. The samples in question are fine grained (<3 mm). Regardless of variations in Re concentration in the molybdenite along the vein, model ages of multiple analyses of that vein overlap within uncertainty. As such, a weighted average is calculated for these veins to provide the best estimate of the age of the vein. This approach is analogous to zircon U-Pb methodology. This approach demonstrates the consistency of the Re-Os systematics along a single vein, and suggests that the molybdenite vein is a single mineralization event within analytical uncertainty.

The weighted average Re-Os model dates range from 16.126 to 15.877 Ma and possess MSWD values between 0.43 and 5.0 (Fig. 3.10). With the exception of sample 1605-33 vein, all veins yield acceptable MSWD values for the number of analyses and suggest the main control of the uncertainties is analytical (Wendt and Carl, 1991; Ludwig, 2003). As such we interpret the weighted means as veins formation ages, with the exception of sample 1605-33 (Fig. 3.10) which we consider the dataset to represent multiple generations of molybdenite that are not recognized petrographically. For samples 1605-33, the youngest two analyses yield a weighted mean of 15.860 Ma with an MSWD value of 0.021. We interpret this age as the minimum formation age of the vein. For 3 veins with one analyse, given the confidence of data reproducibility from multiple analyses of the single vein, the data are interpreted as vein formation ages.

The vein formation ages span from 16.126 ± 0.008/0.060/0.077 (n = 3, MSWD = 1.9) to 15.860 ± 0.010/0.058/0.075 Ma (n = 2, MSWD = 0.021) and do not form one population (Fig. 3.10). Ages of A, B and D veins vary from 16.126 ± 0.008/0.060/0.077 (n = 3, MSWD = 1.9) to 16.040 ± 0.007/0.058/0.075 Ma (n = 4, MSWD = 0.69), from 16.107 ± 0.015/0.065/0.082 (n = 1) to 15.939 ± 0.006/0.058/0.075 Ma (n = 4, MSWD = 1.6), and from 16.088 ± 0.007/0.059/0.076 (n = 3, MSWD = 1.6) to 15.860 ± 0.010/0.058/0.075 Ma (n = 2, MSWD = 0.021), respectively. No relationship is observed between age and vein type, although the A veins as a whole are older than B and D veins (Fig. 3.11).

3.5 **Discussion**

3.5.1 A refined chronology of the Qulong porphyry system

The CA-ID-TIMS zircon U-Pb geochronology of this study provides significant improvements on the accuracy and precision of the dated intrusions at Qulong. Our U-Pb data constrain the emplacement age of the Rongmucuola pluton, P porphyry and quartz diorite to 17.142 ± 0.014/0.014/0.023, 16.009 ± 0.016/0.017/0.024, 15.166 ± 0.010/0.011/0.020 Ma, respectively. Our new dates support the relative chronology based on field observations (Fig. 3.2A) and also the data determined via in-situ U-Pb zircon techniques (Fig. 3.2B), but with a much higher precision/temporal resolution of ~0.1 %. We suggest that the uncertainties for the *in-situ* zircon dates come from analytical issues, e.g., U and Pb fractionation, matrix effects, common lead, standard heterogeneity, data reduction and sample problems, e.g., lead loss, inheritance. As a result this study supports the issues of over interpreting low precision data as previous discussed (Von Quadt et al. (2011); Schaltegger et al. (2015), and we reiterate that CA-ID-TIMS is necessary for resolving the magmatic timescale of young porphyry deposits, such as Qulong.

Field relationships show that the Rongmucuola pluton is pre-ore and is the oldest Miocene intrusion at Qulong. Additionally, the quartz diorite clearly post-dates mineralization, and no further evidence of magmatism is documented or observed (Yang et al., 2009; Hu et al., 2015; Yang et al., 2015; Li et al., 2016). In this regard, the new U-Pb dates of the Rongmucuola pluton and the quartz diorite constrain the duration of magmatism to 1.976 ± 0.017 myr.

Between the emplacement of the P porphyry and the quartz diorite (0.843 ± 0.019 myr), field relationships show that the X porphyry, followed by two stages of breccia, were emplaced (Fig. 3.2A). The aplite is only observed in the Rongmucuola pluton, and previous U-Pb zircon geochronology only showed

evidence of inheritance. However, based on a Re-Os molybdenite date from an A-type quartz vein cutting the aplite, the minimum emplacement age of the aplite is 16.126 ± 0.077 Ma (sample 313-145, discussed below, Table 3.6; Fig. 3.10). Given the onset crystallization age of the P porphyry is 16.065 ± 0.024 Ma, the aplite is at least 0.061 ± 0.081 myr older, and by inference, we consider the aplite predates the P porphyry. Further, based on the minimum age of the aplite, the aplite could be up to ~1 myr younger than the Rongmucuola pluton.

Existing Re-Os dates have appreciable uncertainties of 1.3 - 12.1 %, which is predominately due to the analytical challenges during the early stages of Re-Os studies, e.g., imprecise determinations of the stoichiometry of Os salts use for calibration of spikes (Yin et al., 2001), and ICP-MS analysis (Stein, 2014). Nevertheless, the nominal Re-Os dates from the previous studies suggest that the timing of mineralization occurred between 16.85 ± 0.20 and 15.36 ± 0.22 Ma, proposing a 1.49 ± 0.29 myr duration for mineralization.

The Re-Os dates of this study coincide with the majority of the dates from previous studies. However, the Re-Os dates of this study are considerably more precise (~0.1 %) (Fig. 3.10) and suggest that the bulk of the mineralization occurred between 16.126 ± 0.008 and 15.860 ± 0.010 Ma. Our new Re-Os dates propose that the main phase of mineralization had a duration of 266 ± 13 kyr. Although the sample set used here, to our best knowledge, is representative of the mineralization of the Qulong system (e.g., vein types and alteration) (Li et al., 2016), there is no absolute geological evidence to exclude the presence of mineralization beyond this interval. In addition, the youngest Re-Os age of this study agrees with the biotite and sericite Ar-Ar plateau ages of 15.7 ± 0.2 Ma (Zhao et al., 2016), and indicates that if mineralization postdates this time it is minor or that the temperature of the

hydrothermal fluid was below that of the Ar-Ar closure temperature (~300 ^{o}C) (Chiaradia et al., 2014). To summarize, we suggest the main mineralization at Qulong was formed within 266 ± 13 kyr between 16.126 ± 0.008 and 15.860 ± 0.010 Ma.

3.5.2 Integrating magmatic and hydrothermal timescales

Previous genetic models at Qulong assume all the mineralization at Qulong were precipitated following the emplacement of the P porphyry (Yang et al., 2009; Hu et al., 2015; Li et al., 2016; Zhao et al., 2016) based on the field observations, e.g., the close spatial association between P porphyry and high grade ore (Zheng et al., 2004; Yang et al., 2009), and chronology evidence, e.g., the ages of the P porphyry and mineralization overlaps within uncertainties (Fig. 3.2B).

With all uncertainties propagated, 3 of the 16 published Re-Os dates are older than the emplacement age of P porphyry, but all are younger than the emplacement age of the Rongmucuola pluton (Table 3.2). These data agree with the field observations that all mineralization at Qulong postdate the Rongmucuola pluton and predate the quartz diorite. Outside any analytical issues, the three Re-Os dates predate P porphyry further imply a phase of mineralization before the emplacement of P porphyry, which is likely associated with either the Rongmucuola pluton, the aplite or unexposed intrusions.

The genetic model of porphyry deposits suggests the metals from the magma chamber are transported through porphyry stocks (Sillitoe, 2010; Richards, 2011; Kouzmanov and Pokrovski, 2012; Cooke et al., 2014). At Qulong, the P porphyry is the only observed porphyry stock that can be regarded as a conduit for hydrothermal fluids released from a magma chamber. This implies all the

mineralization should be younger than the emplacement age of P porphyry, if we assume all metals are transported through the P porphyry. Comparison of the high precision molybdenite Re-Os with the zircon U-Pb dates of the P porphyry shows that only molybdenite from sample 313-145 (hosted by aplite) is older than the P porphyry (Fig. 3.10). Seven other molybdenite samples possess dates that are nominally older, but overlap within uncertainties of the P porphyry U-Pb zircon systematics (Fig. 3.10). The remaining molybdenite samples (n = 5) all yield Re-Os dates that are younger than the P porphyry (Fig. 3.10). Interestingly, all Re-Os dates overlap or are slightly younger than the U-Pb systematics for zircon from the P porphyry that are considered to record the onset of crystallization (Fig. 3.10). This implies, if we assume all metals are transported through the P porphyry, either the metals are transported while P porphyry is still not fully crystalized, or there is a small discrepancy between the U-Pb and Re-Os dates.

The spatial association between the mineralization and the N-S trending fault and the P porphyry at Qulong suggests that the fault may have also acted as a conduit for hydrothermal fluids during and before the emplacement of the P porphyry. The agreement of the U-Pb zircon and Re-Os molybdenite dates shown by a recent study of the ~7 Ma Bajo de la Alumbrera deposit support the field relationships, whereby molybdenite mineralization is younger (nominally ~13 kyrs) than the host rock, and thus supports the lack of systematic discrepancy between U-Pb and Re-Os systematics (Buret et al., 2016). As discussed above, both Re-Os and U-Pb dates in this study are reproducible and suggest consistency of the isotope systematics, but a minor systematic bias between the Re-Os and U-Pb systematics may also account for the discrepancy. If we assume sample 313-145 (aplite hosted) is contemporaneous with the emplacement of the P porphyry, this would imply a

0.73 % bias between the Re-Os molybdenite and U-Pb zircon chronometers. However, using this bias value makes the molybdenite Re-Os ages of the Bajo de la Alumbrera deposit to 7.0373 Ma, which is ~59 kyrs younger than the LP3 porphyry that postdates the mineralization. As such we consider a bias between the chronometers of 0.73% unlikely. Additionally, the seven other molybdenite samples at Qulong that possess dates that are nominally older, but overlap within uncertainties of the P porphyry U-Pb zircon systematics (Fig. 3.10), may suggest a bias of 0.61 to 0.01 % between the Re-Os and U-Pb chronometers. The Re-Os and U-Pb study of the Bajo de la Alumbrera deposit suggests that the maximum permitted bias between the chronometers is $\leq 0.066 \pm 0.391$ %, which is at the same level with the uncertainty of decay uncertainty (Smoliar et al., 1996; Selby et al., 2007). We therefore consider the Re-Os dates of this and previous studies to indicate that a portion of the mineralization at Qulong occurred soon after the emplacement of the Rongmucuola pluton and aplite, with further mineralization occurring both broadly coincident and coeval with the emplacement of the P porphyry (Fig. 3.12).

3.5.3 Cyclical mineralization pulses

The alteration assemblages and vein types in porphyry copper deposits are classified as potassic, propylitic and phyllic, and A, B and D, respectively (Fig. 3.3), which record a progressive change in the fluid nature, e.g., temperature, pH and/or oxygen fugacity and are widely used to trace fluid evolution processes (Gustafson and Hunt, 1975; Sillitoe, 2010; Bodnar et al., 2014). However, in most cases the relative chronology of alteration assemblages and vein types cannot be confidently correlated at the deposit-scale due to a lack of deposit-wide crosscutting

relationships. In addition, field observations and high precision dating demonstrate the presence of repetitive A-B-D veins (Sillitoe, 2010; Stein, 2014; Spencer et al., 2015), and multiple overprinting hydrothermal events that occur at timescales significantly longer than can be sustainable by a single magmatic episode (Mercer et al., 2015). These observations require the need to understand ore-forming process based on absolute chronology.

With the confidence of high precision Re-Os molybdenite dating (Stein, 2014; Zimmerman et al., 2014; Spencer et al., 2015; Buret et al., 2016) and the discussion above, here we establish an absolute timeframe for the molybdenite bearing quartz veins. Based on our sample set, assessing the chronology of Qulong in absolute time indicates that mineralization process was not consistent during the 266 ± 13 kyr interval (Fig. 3.10), and demonstrates that the vein types were cyclical (Fig. 3.11A) with the presence of at least two A-B-D cycles and one incomplete (B-D) cycle. It is likely that more cycles are present. The two short-lived A-B-D cycles last for 38 ± 11 and 59 ± 10 kyr with gap of 48 ± 10 kyr. The timescales of mineralization cycles constrained here (tens of kyr) are comparable with those recently proposed through high-precision dating (Buret et al., 2016; Tapster et al., 2016b), titanium diffusion in quartz (Mercer et al., 2015) and numerical modeling (Weis et al., 2012).

3.5.4 Rapid cooling during mineralization

The cooling process of a hydrothermal system is balanced between heat gain (e.g., magmatism and volatiles fluxing) and heat loss (e.g., conduction and meteoric fluid circulation) (Cathles et al., 1997; Weis et al., 2012). Correlating the Re-Os dates in this study and fluid inclusion data (Li et al., 2016) suggests that the entire

hydrothermal system cooled from 425 to 280 ºC within 266 ± 13 kyrs (R^2 = 0.797, Fig. 3.11B). This suggests that the Qulong porphyry system as a whole cooled over the period of ore formation with a cooling rate of 0.55 ± 0.11 ºC/kyr. The cooling rate estimated from the fluid inclusion and Re-Os geochronology data propose a much faster rate than established from thermochronology (0.2 ºC/kyr maximum) (Zhao et al., 2016).

In addition to the long-term cooling trend, the cooling rates of the two A-B-D cycles are 1.19 ± 0.82 and 1.27 ± 0.53 ºC/kyr, respectively (Fig. 3.11B). These cooling trends overlap with the long-term cooling rate within uncertainties, but are much faster that the long term cooling of the overall Qulong porphyry system.

The rapid and episodic cooling process discussed above predicts resetting of thermal chronometers, as supported by the identical Ar-Ar ages of potassic stage biotite and phyllic stage sericite, and age differences given by zircon U-Th-He systematics that are beyond analytical uncertainties from the same intrusions (Zhao et al., 2016).

At Qulong, the main known thermal contributors are the Rongmucuola pluton, P porphyry, X porphyry, quartz diorite and exsolved volatiles, with heat loss controlled by cooling via conduction and meteoric water circulation. The Rongmucuola pluton, which hosts the majority of the ore at Qulong, is ~1 myr older than the P porphyry (Fig. 3.9). Heat loss modelling predicts that a 40 km wide, 2 km thick sill intruded between 16-18 km depth can only sustain a maximum hydrothermal discharge >200 ºC for 0.8 myr, and this duration decreases to 1000 years for systems at shallower depth (Cathles et al., 1997). Given the much smaller size and shallower emplacement depth of the Rongmucuola pluton, we conclude the pluton was cooled to <200 ºC before the emplacement of the P porphyry. As the

volume of the X porphyry and aplite is small, they would have had limited thermal contribution during ore formation as indicated by their short thermal history timescale (<a few kyr) constrained by quartz titanium diffusion and heat loss models (Cathles et al., 1997; Mercer et al., 2015). Here, we suggest that the main thermal contributors are the P porphyry and exsolved volatiles, but do not exclude further contribution from unexposed intrusions. The crystallization process of the P porphyry occurred likely over 55 ± 23 kyr, with the assumption that mineralization occurred broadly contemporaneously with the emplacement of the P porphyry. This implies that the hydrothermal system, and by inference a thermal anomaly, contined for a further 211 ± 26 kyr following the P porphyry emplacement. This duration is much longer than the timescale (a few kyr) that can be sustained by small porphyry intrusions (Cathles et al., 1997; Mercer et al., 2015), and can only be considered reasonable when significant additional thermal contribution associated with multiple exsolution of volatiles and/or unexposed intrusions are present.

The thermal anomalies and faster cooling process discussed above need a mechanism to explain the rapid heat removal, while a increase of heat loss through conduction is not expected. The most likely scenario is rapid thermal removing via the meteoric water circulation model (Weis et al., 2012; Fekete et al., 2016). The discrepancy of cooling speed between this study and thermochronology potentially illustrates the problem of the simplified cooling model used in thermochronology, which does not account for the thermal input associated with fluid fluxing (Weis et al., 2012).

3.6 Implications

Multiple short-lived mineralization cycles have been proposed for deposits with prolonged durations. For example, at Los Pelambres, traditional alteration assemblage defined 'later-stage' D vein is indeed 1 myr older than 'earlier-stage' B vein (Stein, 2014), which implies multiple A-B-D cycles are operated for deposits with long durations, as supported by study at El Teniente (Spencer et al., 2015). However, it is not clear whether multiple mineralization cycles are also present for deposits with short durations. The Re-Os dates in this study suggest that the multiple cycles observed by Stein (2014) and Spencer et al. (2015) operates for deposits with shorts durations, e.g. tens to hundreds of kyr. Very similar processes are recorded in plagioclase, quartz and zircon zoning/resorption textures (Mercer et al., 2015; Tapster et al., 2016b; Williamson et al., 2016). Here we suggest that periodic re-fertilization of magmatism/ mineralization (Fig. 3.12) linked with magma chamber evolution is critical to form giant deposits, and is the key to differentiate economic and sub-economic deposits. This periodic process potentially is controlled by the periodic re-charging of the magma chamber, or pressure release due to the progressive crystallization of magma. In addition, the similar periodic pattern observed in Miocene ice-sheet expansion has been attributed to Earth's orbital configuration (Holbourn et al., 2005), whether there is a link between the orbital configuration of Earth and porphyry ore formation is unclear, e.g., by influencing the meteoric water fluxing, but definitely worthy investigation. The data presented here further refine the duration of mineralization cycles down to tens of thousands years, and directly supports the lifetime of hydrothermal systems proposed by thermal and diffusion simulation (Weis et al., 2012; Mercer et al., 2015) and U-Pb geochronology (Von Quadt et al., 2011; Chelle-Michou et al., 2015; Buret et al., 2016; Tapster et al., 2016b).

Correlating fluid inclusion and Re-Os dates at Qulong indicates a much faster cooling rate of the hydrothermal system than those estimated by thermochronology at Qulong (Zhao et al., 2016) and thermal modelling of porphyry deposits in general (McInnes et al., 2005). We attribute this rapid cooling to thermal contribution associated with volatiles fluxing, which are balanced by meteoric water circulation. In addition, the periodic nature of mineralization and fluid fluxing will reset chronometers with low closure temperatures, e.g., Ar-Ar and U-Th-He, and add uncertainties to thermal chronology studies. This requires the examination of the one-stage cooling model used in thermal chronology studies.

The porphyry system genetic model suggests mineralization follows the emplacement of porphyry stocks (Sillitoe, 2010), and stand as the basis to bracket mineralization duration by dating porphyries (Von Quadt et al., 2011; Buret et al., 2016; Tapster et al., 2016b). This scenario can be tested via high precision dating of mineralization and magmatism. The approaches of Buret et al. (2016) and this study seems support this hypothesis. However, it is hard to argue, that for the studied porphyry systems that the earliest mineralization phases have been sampled and that unexposed porphyry stocks could exist. If this is the case, then uncertainties in our genetic understanding of porphyry systems remain. In addition, when U-Pb and Re-Os dates are compared, including the spike calibration and decay constants uncertainties, which are several times larger than the analytical uncertainties, limits the temporal resolution to understand the mineralization process in further detail. Some of these uncertainties can be removed through cross-calibration between Re-Os and U-Pb as proposed by Chiaradia et al. (2013).

3.7 References

Bodnar, R.J., Lecumberri-Sanchez, P., Moncada, D., Steele-MacInnis, M., 2014. 13.5 - Fluid Inclusions in Hydrothermal Ore Deposits, in: Turekian, H.D.H.K. (Ed.), Treatise on Geochemistry (Second Edition). Elsevier, Oxford, pp. 119-142.

Bowring, J., McLean, N.M., Bowring, S., 2011. Engineering cyber infrastructure for U‐Pb geochronology: Tripoli and U‐Pb_Redux. Geochemistry, Geophysics, Geosystems 12.

Buret, Y., von Quadt, A., Heinrich, C., Selby, D., Wälle, M., Peytcheva, I., 2016. From a long-lived upper-crustal magma chamber to rapid porphyry copper emplacement: Reading the geochemistry of zircon crystals at Bajo de la Alumbrera (NW Argentina). Earth and Planetary Science Letters 450, 120-131.

Burnham, A.D., Berry, A.J., 2012. An experimental study of trace element partitioning between zircon and melt as a function of oxygen fugacity. Geochimica et Cosmochimica Acta 95, 196-212.

Cathles, L.M., Erendi, A.H.J., Barrie, T., 1997. How long can a hydrothermal system be sustained by a single intrusive event? Economic Geology 92, 766-771.

Chelle-Michou, C., Chiaradia, M., Selby, D., Ovtcharova, M., Spikings, R.A., 2015. High-Resolution Geochronology of the Coroccohuayco Porphyry-Skarn Deposit, Peru: A Rapid Product of the Incaic Orogeny. Economic Geology 110, 423-443.

Cheng, H., Edwards, R., Hoff, J., Gallup, C., Richards, D., Asmerom, Y., 2000. The half-lives of uranium-234 and thorium-230. Chemical Geology 169, 17-33.

Chiaradia, M., Schaltegger, U., Spikings, R., 2014. Time Scales of Mineral Systems-Advances in Understanding Over the Past Decade. Soc Econ Geol Spec P, 37-58.

Chiaradia, M., Schaltegger, U., Spikings, R., Wotzlaw, J.-F., Ovtcharova, M., 2013. How Accurately Can We Date the Duration of Magmatic-Hydrothermal Events in Porphyry Systems?—An Invited Paper. Economic Geology 108, 565-584.

Condon, D.J., Schoene, B., McLean, N.M., Bowring, S.A., Parrish, R.R., 2015. Metrology and traceability of U-Pb isotope dilution geochronology (EARTHTIME Tracer Calibration Part I). Geochimica Et Cosmochimica Acta 164, 464-480.

Cooke, D.R., Hollings, P., Wilkinson, J.J., Tosdal, R.M., 2014. 13.14 - Geochemistry of Porphyry Deposits, in: Turekian, H.D.H.K. (Ed.), Treatise on Geochemistry (Second Edition). Elsevier, Oxford, pp. 357-381.

Creaser, R.A., Papanastassiou, D.A., Wasserburg, G.J., 1991. Negative Thermal Ion Mass-Spectrometry of Osmium, Rhenium, and Iridium. Geochimica Et Cosmochimica Acta 55, 397-401.

Deckart, K., Clark, A.H., Cuadra, P., Fanning, M., 2012. Refinement of the time-space evolution of the giant Mio-Pliocene Río Blanco-Los Bronces porphyry Cu–

Mo cluster, Central Chile: new U–Pb (SHRIMP II) and Re–Os geochronology and 40Ar/39Ar thermochronology data. Mineralium Deposita 48, 57-79.

Fekete, S., Weis, P., Driesner, T., Bouvier, A.-S., Baumgartner, L., Heinrich, C.A., 2016. Contrasting hydrological processes of meteoric water incursion during magmatic–hydrothermal ore deposition: An oxygen isotope study by ion microprobe. Earth and Planetary Science Letters 451, 263-271.

Gerstenberger, H., Haase, G., 1997. A highly effective emitter substance for mass spectrometric Pb isotope ratio determinations. Chemical geology 136, 309-312.

Gustafson, L.B., Hunt, J.P., 1975. The porphyry copper deposit at El Salvador, Chile. Economic Geology 70, 857-912.

Hiess, J., Condon, D.J., McLean, N., Noble, S.R., 2012. 238U/235U Systematics in terrestrial uranium-bearing minerals. Science 335, 1610-1614.

Holbourn, A., Kuhnt, W., Schulz, M., Erlenkeuser, H., 2005. Impacts of orbital forcing and atmospheric carbon dioxide on Miocene ice-sheet expansion. Nature 438, 483-487.

Hou, Z.Q., Gao, Y.F., Qu, X.M., Rui, Z.Y., Mo, X.X., 2004. Origin of adakitic intrusives generated during mid-Miocene east-west extension in southern Tibet. Earth and Planetary Science Letters 220, 139-155.

Hou, Z.Q., Yang, Z.M., Qu, X.M., Meng, X.J., Li, Z.Q., Beaudoin, G., Rui, Z.Y., Gao, Y.F., Zaw, K., 2009. The Miocene Gangdese porphyry copper belt generated during post-collisional extension in the Tibetan Orogen. Ore Geology Reviews 36, 25-51.

Hu, Y.B., Liu, J.Q., Ling, M.X., Ding, W., Liu, Y., Zartman, R.E., Ma, X.F., Liu, D.Y., Zhang, C.C., Sun, S.J., Zhang, L.P., Wu, K., Sun, W.D., 2015. The formation of Qulong adakites and their relationship with porphyry copper deposit: Geochemical constraints. Lithos 220, 60-80.

Jaffey, A.H., Flynn, K.F., Glendenin, L.E., Bentley, W.C., Essling, A.M., 1971. Precision Measurement of Half-Lives and Specific Activities of ^{235}U and ^{238}U. Physical Review C 4, 1889-1906.

Kouzmanov, K., Pokrovski, G.S., 2012. Hydrothermal controls on metal distribution in porphyry Cu (-Mo-Au) systems. Special Publication of the Society of Economic Geologists 16, 573–618.

Krogh, T., 1973. A low-contamination method for hydrothermal decomposition of zircon and extraction of U and Pb for isotopic age determinations. Geochimica et cosmochimica acta 37, 485-494.

Lawley, C.J.M., Selby, D., 2012. Re-Os GEOCHRONOLOGY OF QUARTZ-ENCLOSED ULTRAFINE MOLYBDENITE: IMPLICATIONS FOR ORE GEOCHRONOLOGY. Economic Geology 107, 1499-1505.

Li, G.-M., Liu, B., Qu, W.-J., Lin, F.-C., Yu, H.-Q., Feng, C.-Y., 2005. The porphyry- skarn ore- forming system in Gangdese Metallogenic Belt, southern Xizang: Evidence from molybdenite Re-Os age of porphyry- type copper deposits and skarn- type copper polymetallic deposits. Geotectonica et Metallogenia 29, 482-490.

Li, Y., Selby, D., Feely, M., Costanzo, A., Li, X.-H., 2016. Fluid inclusion characteristics and molybdenite Re-Os geochronology of the Qulong porphyry copper-molybdenum deposit, Tibet. Mineralium Deposita.

Ludwig, K.R., 2003. User's manual for Isoplot 3.00: a geochronological toolkit for Microsoft Excel. Kenneth R. Ludwig.

Luo, Y., Ayers, J.C., 2009. Experimental measurements of zircon/melt trace-element partition coefficients. Geochimica et Cosmochimica Acta 73, 3656-3679.

Markey, R., Stein, H.J., Hannah, J.L., Zimmerman, A., Selby, D., Creaser, R.A., 2007. Standardizing re-os geochronology: A new molybdenite reference material (Henderson, USA) and the stoichiometry of Os salts. Chemical Geology 244, 74-87.

Mattinson, J.M., 2005. Zircon U-Pb chemical abrasion ("CA-TIMS") method: Combined annealing and multi-step partial dissolution analysis for improved precision and accuracy of zircon ages. Chemical Geology 220, 47-66.

McInnes, B.I., Evans, N.J., Fu, F., Garwin, S., Belousova, E., Griffin, W., Bertens, A., Sukarna, D., Permanadewi, S., Andrew, R., 2005. Thermal history analysis of selected Chilean, Indonesian, and Iranian porphyry Cu-Mo-Au deposits. Super Porphyry Copper and Gold Deposits: A Global Perspective (Porter, TM; editor). Porter Geoconsultancy Publishing, de Adelaide, Australia, 27-42.

McLean, N.M., Bowring, J.F., Bowring, S.A., 2011. An algorithm for U-Pb isotope dilution data reduction and uncertainty propagation. Geochemistry, Geophysics, Geosystems 12, n/a-n/a.

McLean, N.M., Condon, D.J., Schoene, B., Bowring, S.A., 2015. Evaluating uncertainties in the calibration of isotopic reference materials and multi-element isotopic tracers (EARTHTIME Tracer Calibration Part II). Geochimica Et Cosmochimica Acta 164, 481-501.

Meng, X.-J., Hou, Z.-Q., Gao, Y.-F., Huang, W., Qu, X.-M., Qu, W.-J., 2003. Re-Os dating for molybdenite from Qulong porphyry copper deposit in Gangdese metallogenic Belt, Xizangand its metallogenic significance. Geological Review 49, 660-666.

Mercer, C.N., Reed, M.H., Mercer, C.M., 2015. Time Scales of Porphyry Cu Deposit Formation: Insights from Titanium Diffusion in Quartz. Economic Geology 110, 587-602.

Richards, J.P., 2011. Magmatic to hydrothermal metal fluxes in convergent and collided margins. Ore Geology Reviews 40, 1-26.

Richards, J.P., 2015. Tectonic, magmatic, and metallogenic evolution of the Tethyan orogen: From subduction to collision. Ore Geology Reviews 70, 323-345.

Rubatto, D., Hermann, J., 2007. Experimental zircon/melt and zircon/garnet trace element partitioning and implications for the geochronology of crustal rocks. Chemical Geology 241, 38-61.

Schaltegger, U., Schmitt, A.K., Horstwood, M.S.A., 2015. U-Th-Pb zircon geochronology by ID-TIMS, SIMS, and laser ablation ICP-MS: Recipes, interpretations, and opportunities. Chemical Geology 402, 89-110.

Schärer, U., 1984. The effect of initial230Th disequilibrium on young UPb ages: the Makalu case, Himalaya. Earth and Planetary Science Letters 67, 191-204.

Selby, D., Creaser, R.A., 2001. Re-Os geochronology and systematics in molybdenite from the Endako porphyry molybdenum deposit, British Columbia, Canada. Economic Geology and the Bulletin of the Society of Economic Geologists 96, 197-204.

Selby, D., Creaser, R.A., Stein, H.J., Markey, R.J., Hannah, J.L., 2007. Assessment of the Re-187 decay constant by cross calibration of Re-Os molybdenite and U-Pb zircon chronometers in magmatic ore systems. Geochimica Et Cosmochimica Acta 71, 1999-2013.

Sillitoe, R.H., 2010. Porphyry Copper Systems. Economic Geology 105, 3-41.

Sillitoe, R.H., Mortensen, J.K., 2010. Longevity of Porphyry Copper Formation at Quellaveco, Peru. Economic Geology 105, 1157-1162.

Smoliar, M.I., Walker, R.J., Morgan, J.W., 1996. Re-Os ages of group IIA, IIIA, IVA, and IVB iron meteorites. Science 271, 1099-1102.

Spencer, E.T., Wilkinson, J.J., Creaser, R.A., Seguel, J., 2015. The Distribution and Timing of Molybdenite Mineralization at the El Teniente Cu-Mo Porphyry Deposit, Chile. Economic Geology 110, 387-421.

Stein, H.J., 2014. 13.4 - Dating and Tracing the History of Ore Formation, in: Turekian, H.D.H.K. (Ed.), Treatise on Geochemistry (Second Edition). Elsevier, Oxford, pp. 87-118.

Stein, H.J., Markey, R.J., Morgan, J.W., Hannah, J.L., Schersten, A., 2001. The remarkable Re-Os chronometer in molybdenite: how and why it works. Terra Nova 13, 479-486.

Tapster, S., Condon, D.J., Naden, J., Noble, S.R., Petterson, M.G., Roberts, N.M.W., Saunders, A.D., Smith, D.J., 2016a. Rapid thermal rejuvenation of high-crystallinity magma linked to porphyry copper deposit formation; evidence from the Koloula Porphyry Prospect, Solomon Islands. Earth and Planetary Science Letters.

Tapster, S., Condon, D.J., Naden, J., Noble, S.R., Petterson, M.G., Roberts, N.M.W., Saunders, A.D., Smith, D.J., 2016b. Rapid thermal rejuvenation of high-

crystallinity magma linked to porphyry copper deposit formation; evidence from the Koloula Porphyry Prospect, Solomon Islands. Earth and Planetary Science Letters 442, 206-217.

Von Quadt, A., Erni, M., Martinek, K., Moll, M., Peytcheva, I., Heinrich, C.A., 2011. Zircon crystallization and the lifetimes of ore-forming magmatic-hydrothermal systems. Geology 39, 731-734.

Wang, L.-L., Mo, X.-X., B, L., G-C, D., Zhao, Z.-D., 2006. Geochronology and geochemistry of the ore-bearing porphyry in Qulong Cu (Mo) deposit, Tibet. Acta Petrologica Sinica 22, 1001-1008.

Wang, R., Richards, J.P., Hou, Z.Q., Yang, Z.M., 2014. Extent of underthrusting of the Indian plate beneath Tibet controlled the distribution of Miocene porphyry Cu-Mo +/- Au deposits. Mineralium Deposita 49, 165-173.

Wang, R., Richards, J.P., Zhou, L.M., Hou, Z.Q., Stern, R.A., Creaser, R.A., Zhu, J.J., 2015. The role of Indian and Tibetan lithosphere in spatial distribution of Cenozoic magmatism and porphyry Cu-Mo deposits in the Gangdese belt, southern Tibet. Earth-Science Reviews 150, 68-94.

Weis, P., Driesner, T., Heinrich, C.A., 2012. Porphyry-copper ore shells form at stable pressure-temperature fronts within dynamic fluid plumes. Science 338, 1613-1616.

Wendt, I., Carl, C., 1991. The Statistical Distribution of the Mean Squared Weighted Deviation. Chemical Geology 86, 275-285.

Williamson, B.J., Herrington, R.J., Morris, A., 2016. Porphyry copper enrichment linked to excess aluminium in plagioclase. Nature Geoscience 9, 237-U169.

Yang, Z.M., Hou, Z.Q., White, N.C., Chang, Z.S., Li, Z.Q., Song, Y.C., 2009. Geology of the post-collisional porphyry copper-molybdenum deposit at Qulong, Tibet. Ore Geology Reviews 36, 133-159.

Yang, Z.M., Lu, Y.J., Hou, Z.Q., Chang, Z.S., 2015. High-Mg Diorite from Qulong in Southern Tibet: Implications for the Genesis of Adakite-like Intrusions and Associated Porphyry Cu Deposits in Collisional Orogens. Journal of Petrology 56, 227-253.

Yin, Q.Z., Jacobsen, S.B., Lee, C.T., McDonough, W.F., Rudnick, R.L., Horn, I., 2001. A gravimetric K2OsCl6 standard: Application to precise and accurate Os spike calibration. Geochimica Et Cosmochimica Acta 65, 2113-2127.

Zhao, J., Qin, K., Xiao, B., McInnes, B., Li, G., Evans, N., Cao, M., Li, J., 2016. Thermal history of the giant Qulong Cu–Mo deposit, Gangdese metallogenic belt, Tibet: Constraints on magmatic–hydrothermal evolution and exhumation. Gondwana Research 36, 390-409.

Zheng, Y.Y., Sun, X., Gao, S.B., Wu, S., Xu, J., Jiang, J.S., Chen, X., Zhao, Z.Y., Liu, Y., 2015. Metallogenesis and the minerogenetic series in the Gangdese polymetallic copper belt. Journal of Asian Earth Sciences 103, 23-39.

Zheng, Y.Y., Xue, Y.X., Cheng, L.J., Fan, Z.H., Gao, S.B., 2004. Finding,Characteristics and Significances of Qulong Superlarge Porphyry Copper (Molybdenum) Deposit, Tibet. Earth Sciences 29, 103-108 (In Chinese with English Abstract).

Zhu, D.C., Wang, Q., Zhao, Z.D., Chung, S.L., Cawood, P.A., Niu, Y., Liu, S.A., Wu, F.Y., Mo, X.X., 2015. Magmatic record of India-Asia collision. Sci Rep 5, 14289.

Zimmerman, A., Stein, H.J., Morgan, J.W., Markey, R.J., Watanabe, Y., 2014. Re–Os geochronology of the El Salvador porphyry Cu–Mo deposit, Chile: Tracking analytical improvements in accuracy and precision over the past decade. Geochimica et Cosmochimica Acta 131, 13-32.

3.8 List of figures

Fig. 3.7 Molybdenite Re-Os dates of Henderson molybdenite standard analysed during this study.

Fig. 3.8 CL images of analysed zircon grains of the Rongmucuola pluton, the P porphyry and post-ore quartz diorite.

Fig. 3.9 CA-ID-TIMS zircon $^{206}Pb/^{238}U$ ages of the Rongmucuola pluton, the P porphyry and post-ore quartz diorite.

Fig. 3.10 ID-NTIMS molybdenite Re-Os geochronology data of molybdenite veins at Qulong, with probability density plot showing at the left.

Fig. 3.11 A) Probability density plots of Re-Os dates of A, B and D veins dated in this study; B) Cooling history of Qulong hydrothermal system, with vein-formation ages and temperatures constrained by molybdenite Re-Os dating in this study and fluid inclusion data of Li et al. (2016).

Fig. 3.12 Cartoon showing the periodically re-fertilization of magmatism and mineralization process at Qulong controlled by the magma chamber evolution.

3.9 List of tables

Figure 3.1

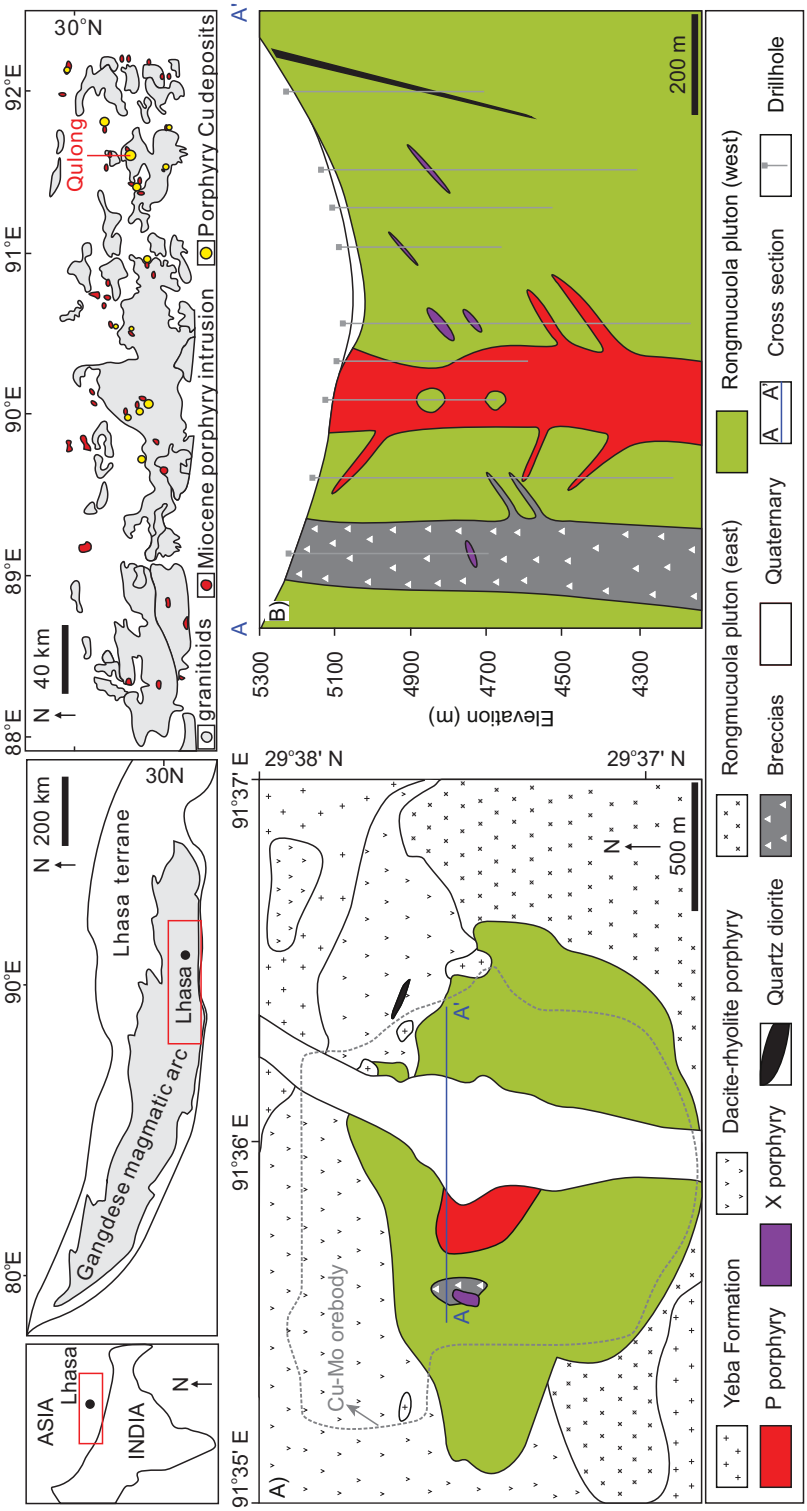
ASIA
Lhasa
INDIA
N
80°E
90°E
N 200 km
30N
Lhasa terrane
Gangdese magmatic arc
Lhasa
88°E
89°E
90°E
91°E
92°E
30°N
N 40 km
Qulong
granitoids
Miocene porphyry intrusion
Porphyry Cu deposits
A)
91°35' E
91°36' E
91°37' E
29°38' N
29°37' N
Cu-Mo orebody
A
A'
N
500 m
B)
A
A'
5300
5100
4900
4700
4500
4300
Elevation (m)
200 m
Yeba Formation
P porphyry
Dacite-rhyolite porphyry
X porphyry
Quartz diorite
Rongmucuola pluton (east)
Breccias
Quaternary
Rongmucuola pluton (west)
Cross section
Drillhole

Figure 3.2

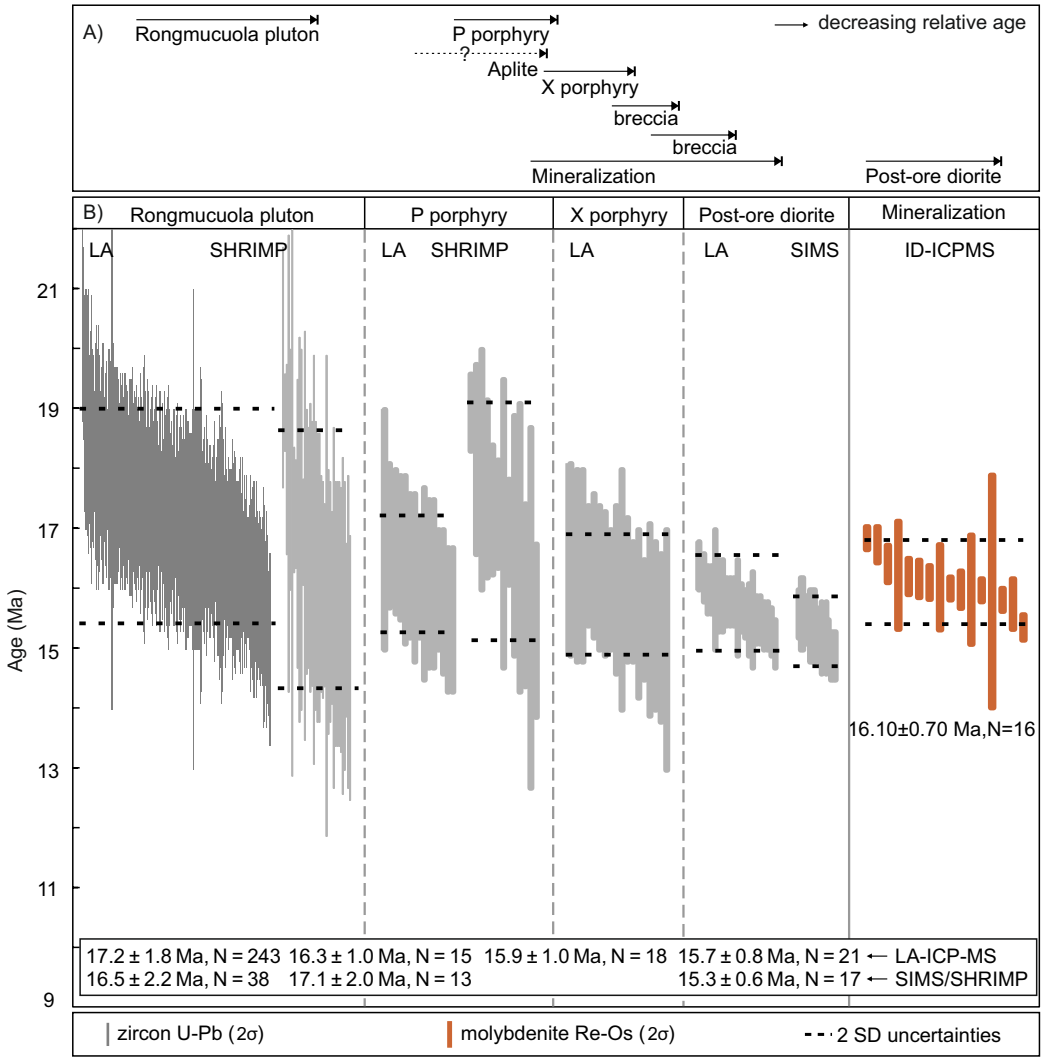
A)
Rongmucuola pluton
P porphyry
?
Aplite
X porphyry
breccia
breccia
Mineralization
Post-ore diorite
decreasing relative age
B)
Rongmucuola pluton
P porphyry
X porphyry
Post-ore diorite
Mineralization
LA
SHRIMP
LA
SHRIMP
LA
LA
SIMS
ID-ICPMS
Age (Ma)
21
19
17
15
13
11
9
16.10±0.70 Ma,N=16
17.2 ± 1.8 Ma, N = 243
16.5 ± 2.2 Ma, N = 38
16.3 ± 1.0 Ma, N = 15
17.1 ± 2.0 Ma, N = 13
15.9 ± 1.0 Ma, N = 18
15.7 ± 0.8 Ma, N = 21 ← LA-ICP-MS
15.3 ± 0.6 Ma, N = 17 ← SIMS/SHRIMP
zircon U-Pb (2σ)
molybdenite Re-Os (2σ)
2 SD uncertainties

Figure 3.3

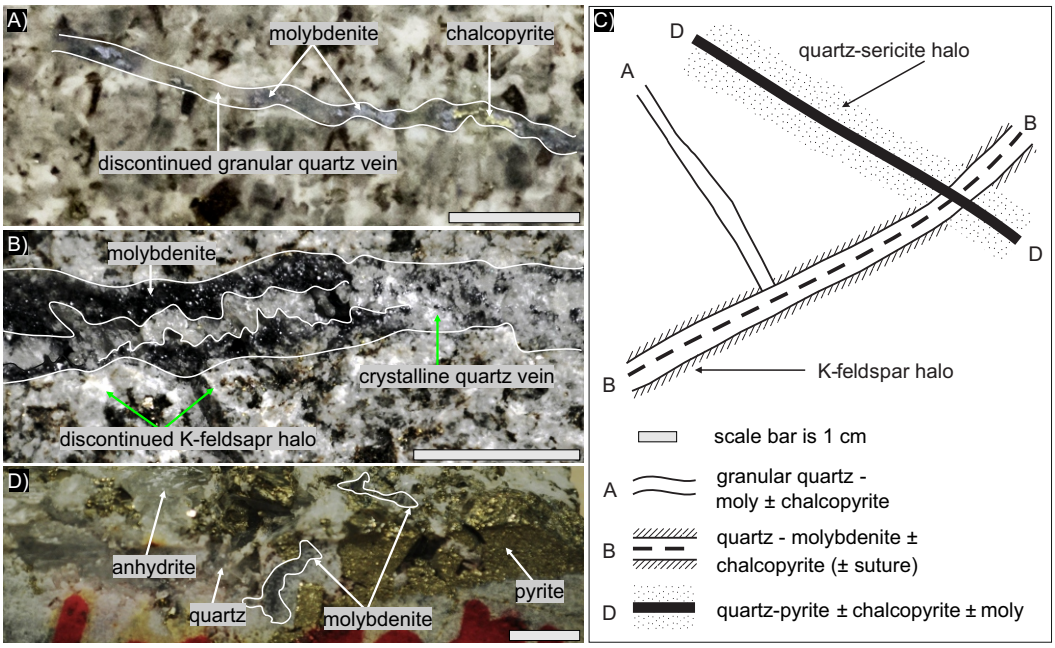
A)
molybdenite
chalcopyrite
discontinued granular quartz vein
B)
molybdenite
crystalline quartz vein
discontinued K-feldsapr halo
D)
anhydrite
quartz
molybdenite
pyrite
C)
D
quartz-sericite halo
A
B
D
B
K-feldspar halo
scale bar is 1 cm
A
granular quartz -
moly ± chalcopyrite
B
quartz - molybdenite ±
chalcopyrite (± suture)
D
quartz-pyrite ± chalcopyrite ± moly

Figure 3.4

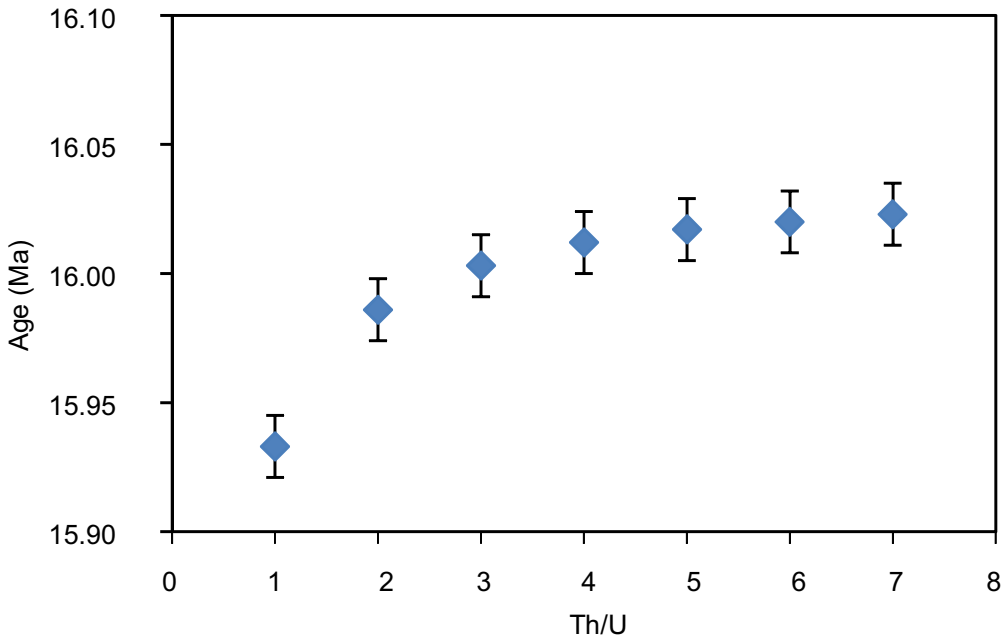

Figure 3.5

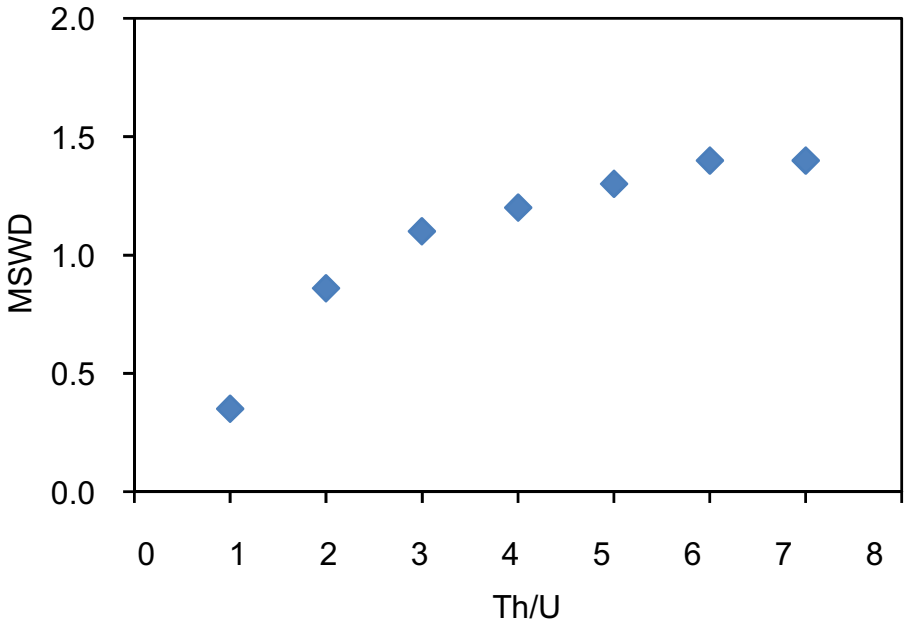

Figure 3.6

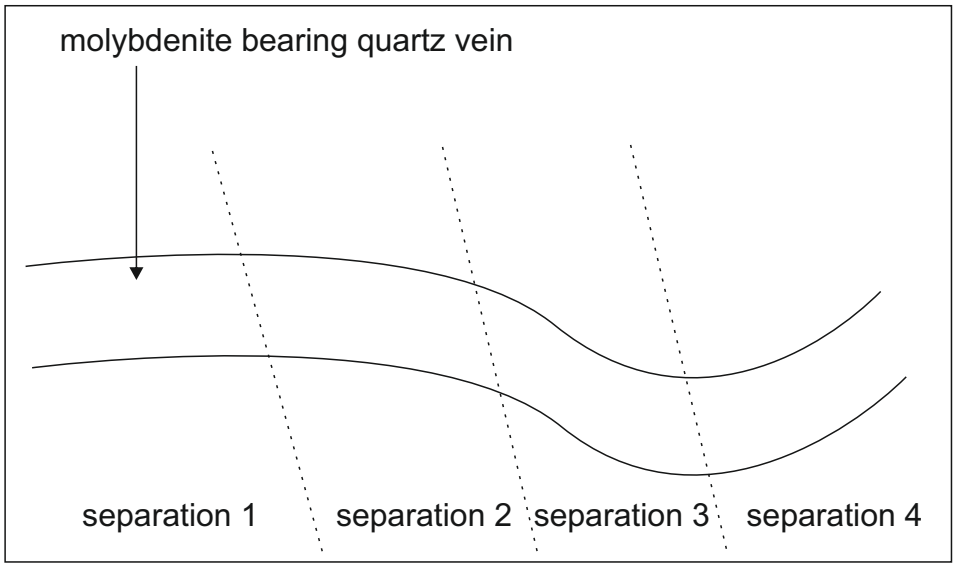
molybdenite bearing quartz vein
separation 1
separation 2
separation 3
separation 4

Figure 3.7

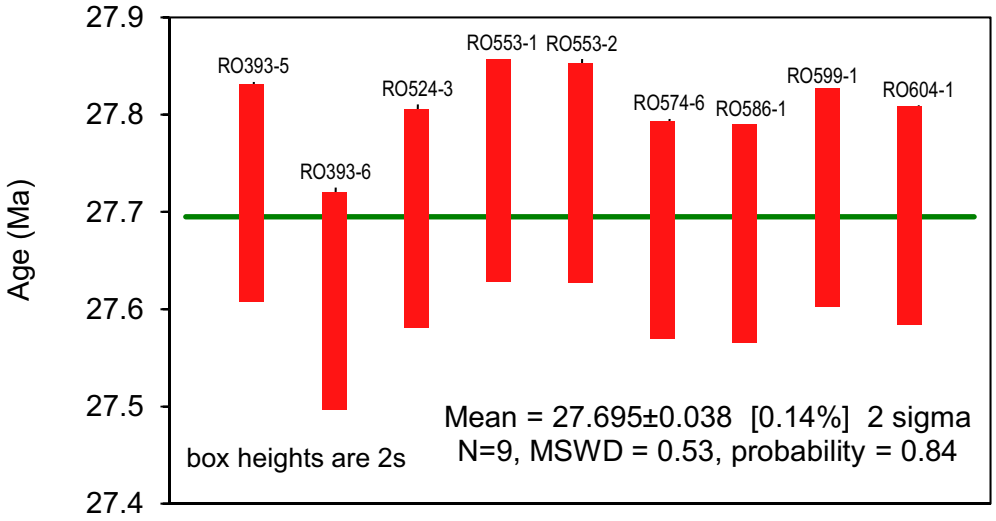
27.9
27.8
27.7
27.6
27.5
27.4
Age (Ma)
RO393-5
RO393-6
RO524-3
RO553-1
RO553-2
RO574-6
RO586-1
RO599-1
RO604-1
box heights are 2s
Mean = 27.695±0.038 [0.14%] 2 sigma
N=9, MSWD = 0.53, probability = 0.84

Figure 3.8

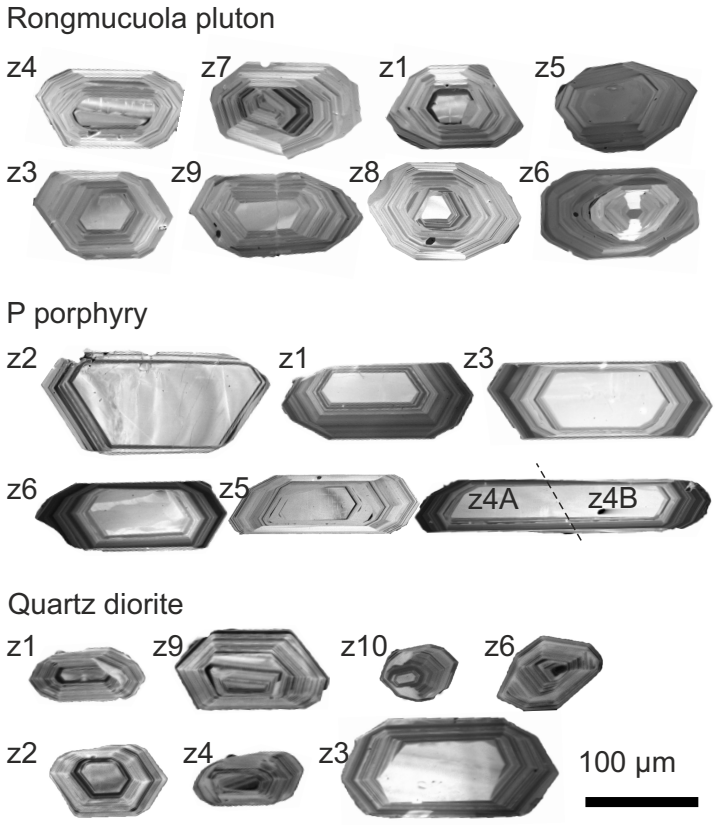
Rongmucuola pluton
z4
z7
z1
z5
z3
z9
z8
z6
P porphyry
z2
z1
z3
z6
z5
z4A
z4B
Quartz diorite
z1
z9
z10
z6
z2
z4
z3
100 μm

Figure 3.9

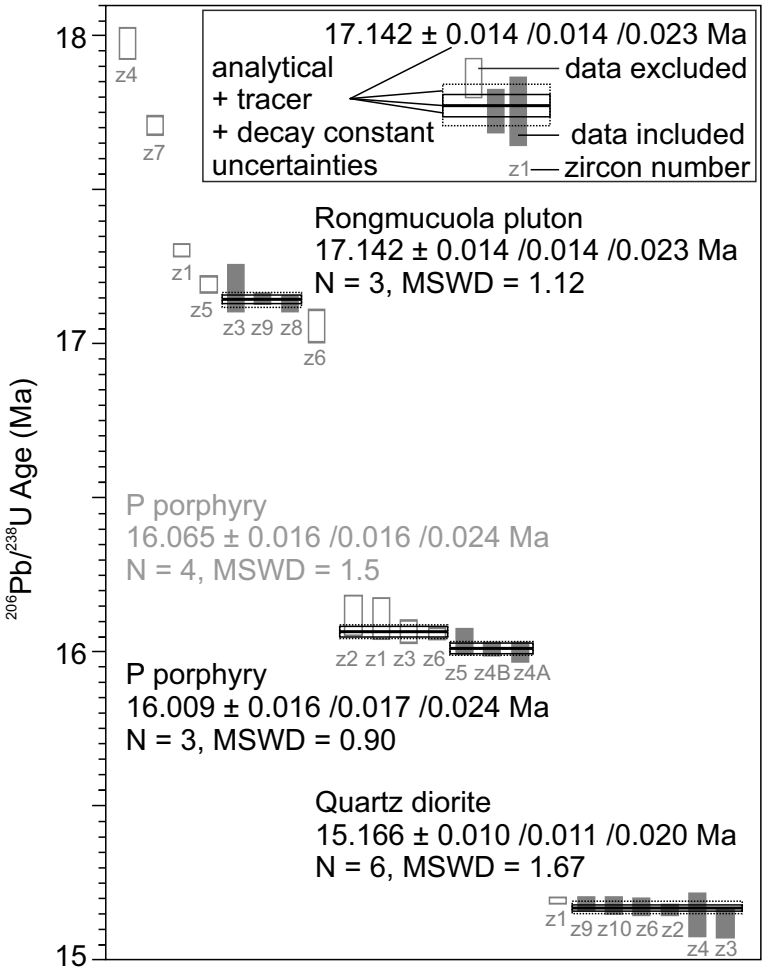
18
17
16
15
$^{206}Pb/^{238}U$ Age (Ma)
17.142 ± 0.014 /0.014 /0.023 Ma
analytical
+ tracer
+ decay constant
uncertainties
data excluded
data included
z1— zircon number
z4
z7
Rongmucuola pluton
17.142 ± 0.014 /0.014 /0.023 Ma
N = 3, MSWD = 1.12
z1
z5
z3 z9 z8
z6
P porphyry
16.065 ± 0.016 /0.016 /0.024 Ma
N = 4, MSWD = 1.5
z2 z1 z3 z6
z5 z4B z4A
P porphyry
16.009 ± 0.016 /0.017 /0.024 Ma
N = 3, MSWD = 0.90
Quartz diorite
15.166 ± 0.010 /0.011 /0.020 Ma
N = 6, MSWD = 1.67
z1
z9 z10 z6 z2
z4 z3

Figure 3.10

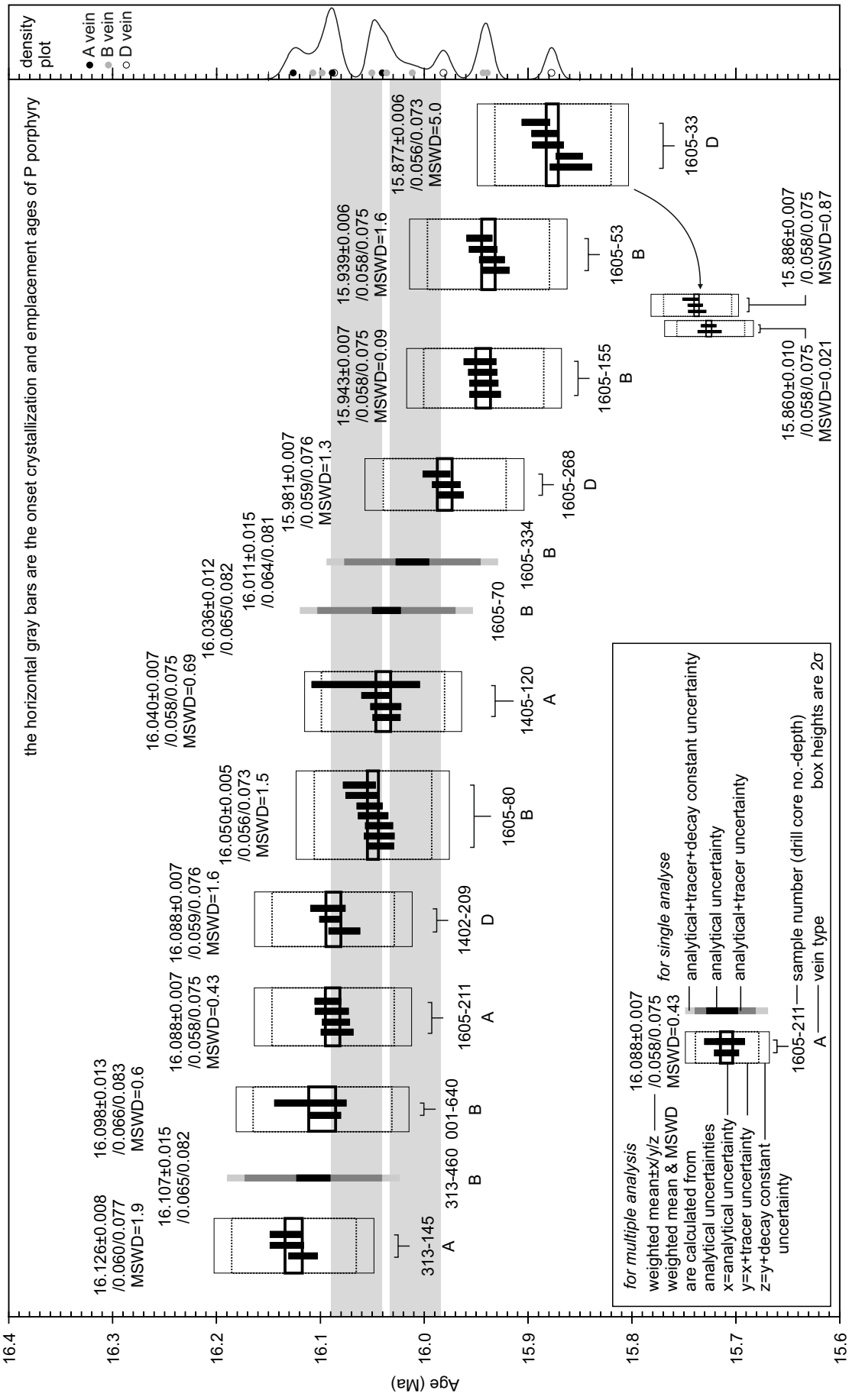
density plot
A vein
B vein
D vein
the horizontal gray bars are the onset crystallization and emplacement ages of P porphyry
16.126±0.008 /0.060/0.077 MSWD=1.9
16.098±0.013 /0.066/0.083 MSWD=0.6
16.107±0.015 /0.065/0.082
16.088±0.007 /0.058/0.075 MSWD=0.43
16.088±0.007 /0.059/0.076 MSWD=1.6
16.050±0.005 /0.056/0.073 MSWD=1.5
16.040±0.007 /0.058/0.075 MSWD=0.69
16.036±0.012 /0.065/0.082
16.011±0.015 /0.064/0.081
15.981±0.007 /0.059/0.076 MSWD=1.3
15.943±0.007 /0.058/0.075 MSWD=0.09
15.939±0.006 /0.058/0.075 MSWD=1.6
15.877±0.006 /0.056/0.073 MSWD=5.0
15.860±0.010 /0.058/0.075 MSWD=0.021
15.886±0.007 /0.058/0.075 MSWD=0.87
313-145 A
313-460 001-640 B B
1605-211 A
1402-209 D
1605-80 B
1405-120 A
1605-70 B
1605-334 B
1605-268 D
1605-155 B
1605-53 B
1605-33 D
for multiple analysis
weighted mean±x/y/z
weighted mean & MSWD are calculated from analytical uncertainties
x=analytical uncertainty
y=x+tracer uncertainty
z=y+decay constant uncertainty
16.088±0.007 /0.058/0.075 MSWD=0.43
for single analyse
analytical+tracer+decay constant uncertainty
analytical uncertainty
analytical+tracer uncertainty
1605-211— sample number (drill core no.-depth)
A —— vein type
box heights are 2σ
Age (Ma)
16.4
16.3
16.2
16.1
16.0
15.9
15.8
15.7
15.6

Figure 3.11

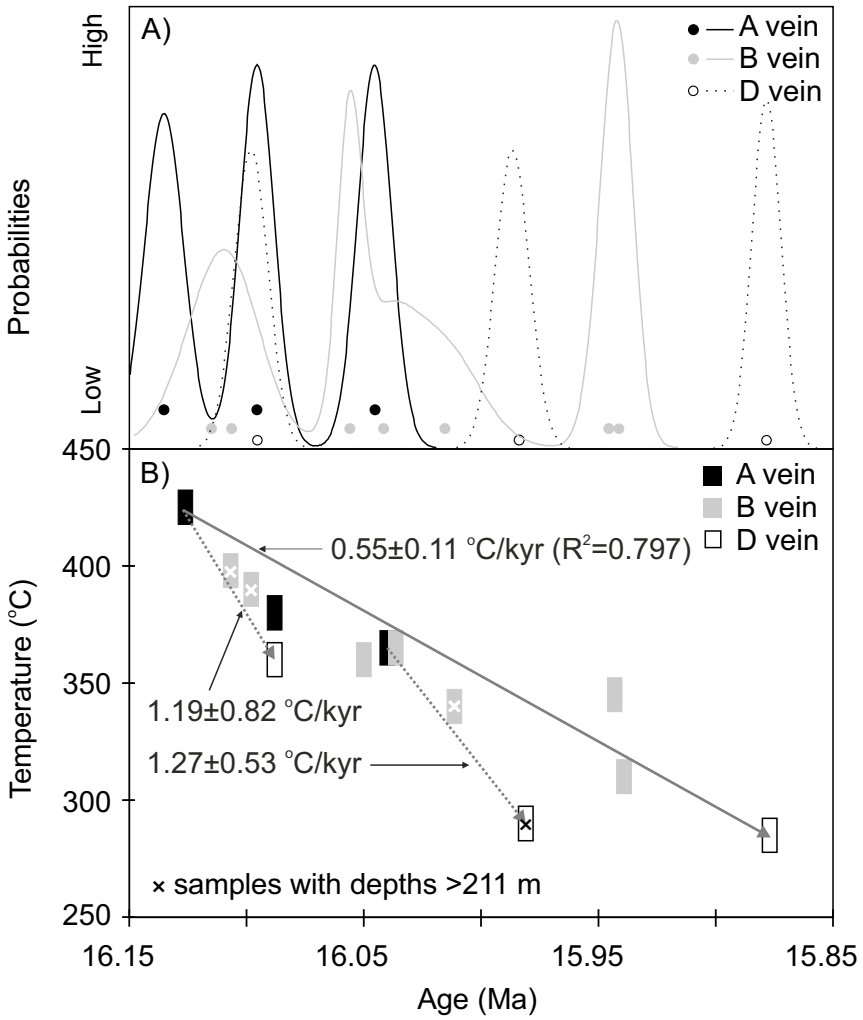
A)
High
Low
Probabilities
A vein
B vein
D vein
B)
A vein
B vein
D vein
0.55±0.11 °C/kyr (R²=0.797)
1.19±0.82 °C/kyr
1.27±0.53 °C/kyr
× samples with depths >211 m
Temperature (°C)
450
400
350
300
250
16.15
16.05
15.95
15.85
Age (Ma)

Figure 3.12

A) ~17 Ma, Magma chamber starts to crystalize and release small amount of hydrothermal fluid. The hydrothermal fluid rise up with the pluton and aplite cause minor alteration and mineralization. This is represented by the emplacement of the Rongmucuola pluton into the Jurassic countryrock, and followed by the formation of the aplite. The fault is a potential conduit for magmatism and hydrothermal fluid.

B) ~16 Ma, Continuing crystallization of the magma chamber release further fluid. The fluid periodically rise up and cause intensive alteration and mineralization. The P porphyry emplaced at this time, and followed by the formation of the X porphyry. P porphyry and the fault are the main conduits. The alteration and mineralization can be earlier than the final crystallization age of the P porphyry.

C) ~15.9 Ma, Further crystallization of the magma chamber released fluid build the pressure up and finally cause eruptive fluids release and breccia formation. Hydrothermal fluids cause further alteration and mineralization.

D) ~15.2 Ma, The magma chamber completely crystalized with minor release of hydrothermal fluid. This is represented by the emplacement of quartz diorite. The minor fluid caused low temperature alteration to the quartz diorite without further mineralization.

Table 3.1 Published zircon U-Pb geochronology dates at Qulong

$^{206}Pb/^{238}U$ age	2 sigma	methods	references
Rongmucuola			
16.3	1.4	LA-ICPMS	Hu YB 2015
17.1	1.4	LA-ICPMS	Hu YB 2015
18.0	1.2	LA-ICPMS	Hu YB 2015
17.4	1.6	LA-ICPMS	Hu YB 2015
17.5	2.2	LA-ICPMS	Hu YB 2015
16.4	1.0	LA-ICPMS	Hu YB 2015
16.8	1.6	LA-ICPMS	Hu YB 2015
16.3	1.0	LA-ICPMS	Hu YB 2015
17.0	2.0	LA-ICPMS	Hu YB 2015
17.1	1.8	LA-ICPMS	Hu YB 2015
17.0	2.0	LA-ICPMS	Hu YB 2015
16.7	1.8	LA-ICPMS	Hu YB 2015
16.9	2.0	LA-ICPMS	Hu YB 2015
16.6	1.4	LA-ICPMS	Hu YB 2015
17.3	2.0	LA-ICPMS	Hu YB 2015
16.2	1.0	LA-ICPMS	Hu YB 2015
16.7	1.8	LA-ICPMS	Hu YB 2015
15.7	2.0	LA-ICPMS	Hu YB 2015
15.9	1.2	LA-ICPMS	Hu YB 2015
16.8	1.6	LA-ICPMS	Hu YB 2015
16.7	1.6	LA-ICPMS	Hu YB 2015
18.5	1.4	LA-ICPMS	Hu YB 2015
17.3	2.0	LA-ICPMS	Hu YB 2015
16.4	1.8	LA-ICPMS	Hu YB 2015
17.1	2.0	LA-ICPMS	Hu YB 2015
17.3	1.0	LA-ICPMS	Hu YB 2015
16.6	1.2	LA-ICPMS	Hu YB 2015
18.5	1.8	LA-ICPMS	Hu YB 2015
16.7	2.2	LA-ICPMS	Hu YB 2015
16.7	2.0	LA-ICPMS	Hu YB 2015
17.4	1.8	LA-ICPMS	Hu YB 2015
16.4	1.4	LA-ICPMS	Hu YB 2015
17.2	1.8	LA-ICPMS	Hu YB 2015
16.8	1.0	LA-ICPMS	Hu YB 2015
18.5	2.4	LA-ICPMS	Hu YB 2015
16.9	2.8	LA-ICPMS	Hu YB 2015
15.6	1.8	LA-ICPMS	Hu YB 2015
16.0	1.2	LA-ICPMS	Hu YB 2015
16.0	1.8	LA-ICPMS	Hu YB 2015
17.9	1.8	LA-ICPMS	Hu YB 2015
15.4	1.0	LA-ICPMS	Hu YB 2015
17.9	2.2	LA-ICPMS	Hu YB 2015
17.6	1.6	LA-ICPMS	Hu YB 2015
17.3	1.4	LA-ICPMS	Hu YB 2015
16.9	2.6	LA-ICPMS	Hu YB 2015
18.0	1.6	LA-ICPMS	Hu YB 2015
16.2	1.0	LA-ICPMS	Hu YB 2015
16.4	1.4	LA-ICPMS	Hu YB 2015
16.7	1.2	LA-ICPMS	Hu YB 2015

18.4	1.4	LA-ICPMS	Hu YB 2015
17.8	1.8	LA-ICPMS	Hu YB 2015
18.0	1.4	LA-ICPMS	Hu YB 2015
17.9	1.8	LA-ICPMS	Hu YB 2015
15.0	1.6	LA-ICPMS	Hu YB 2015
18.2	2.2	LA-ICPMS	Hu YB 2015
16.7	2.6	LA-ICPMS	Hu YB 2015
15.5	1.8	LA-ICPMS	Hu YB 2015
15.9	1.4	LA-ICPMS	Hu YB 2015
17.5	2.4	LA-ICPMS	Hu YB 2015
17.0	1.6	LA-ICPMS	Hu YB 2015
19.0	1.8	LA-ICPMS	Hu YB 2015
16.8	1.2	LA-ICPMS	Hu YB 2015
16.1	1.8	LA-ICPMS	Hu YB 2015
16.7	2.4	LA-ICPMS	Hu YB 2015
16.5	2.0	LA-ICPMS	Hu YB 2015
16.3	1.6	LA-ICPMS	Hu YB 2015
17.5	1.2	LA-ICPMS	Hu YB 2015
15.8	1.4	LA-ICPMS	Hu YB 2015
17.7	1.6	LA-ICPMS	Hu YB 2015
17.2	2.0	LA-ICPMS	Hu YB 2015
20.4	1.6	LA-ICPMS	Hu YB 2015
14.8	1.4	LA-ICPMS	Hu YB 2015
17.7	1.2	LA-ICPMS	Hu YB 2015
16.2	1.2	LA-ICPMS	Hu YB 2015
16.3	1.2	LA-ICPMS	Hu YB 2015
17.8	1.6	LA-ICPMS	Hu YB 2015
16.6	0.8	LA-ICPMS	Hu YB 2015
16.9	1.4	LA-ICPMS	Hu YB 2015
17.5	1.8	LA-ICPMS	Hu YB 2015
17.9	1.8	LA-ICPMS	Hu YB 2015
18.3	1.6	LA-ICPMS	Hu YB 2015
16.4	1.4	LA-ICPMS	Hu YB 2015
17.2	2.2	LA-ICPMS	Hu YB 2015
17.8	1.8	LA-ICPMS	Hu YB 2015
18.1	1.8	LA-ICPMS	Hu YB 2015
17.3	1.8	LA-ICPMS	Hu YB 2015
16.9	1.6	LA-ICPMS	Hu YB 2015
18.1	1.2	LA-ICPMS	Hu YB 2015
17.1	1.2	LA-ICPMS	Hu YB 2015
18.2	1.0	LA-ICPMS	Hu YB 2015
17.8	1.4	LA-ICPMS	Hu YB 2015
17.7	1.2	LA-ICPMS	Hu YB 2015
16.1	1.4	LA-ICPMS	Hu YB 2015
17.2	1.0	LA-ICPMS	Hu YB 2015
17.7	1.8	LA-ICPMS	Hu YB 2015
17.5	1.2	LA-ICPMS	Hu YB 2015
17.6	1.8	LA-ICPMS	Hu YB 2015
16.0	1.8	LA-ICPMS	Hu YB 2015
18.1	1.6	LA-ICPMS	Hu YB 2015
16.9	1.8	LA-ICPMS	Hu YB 2015
17.9	1.8	LA-ICPMS	Hu YB 2015

17.3	1.2	LA-ICPMS	Hu YB 2015
17.4	2.0	LA-ICPMS	Hu YB 2015
20.1	1.6	LA-ICPMS	Hu YB 2015
18.1	2.0	LA-ICPMS	Hu YB 2015
17.8	1.8	LA-ICPMS	Hu YB 2015
16.1	1.6	LA-ICPMS	Hu YB 2015
15.7	1.4	LA-ICPMS	Hu YB 2015
16.7	1.8	LA-ICPMS	Hu YB 2015
18.2	1.8	LA-ICPMS	Hu YB 2015
16.8	1.4	LA-ICPMS	Hu YB 2015
17.7	1.8	LA-ICPMS	Hu YB 2015
18.3	1.0	LA-ICPMS	Hu YB 2015
16.2	1.2	LA-ICPMS	Hu YB 2015
19.1	1.8	LA-ICPMS	Hu YB 2015
18.4	1.6	LA-ICPMS	Hu YB 2015
16.9	1.4	LA-ICPMS	Hu YB 2015
16.6	1.6	LA-ICPMS	Hu YB 2015
17.2	1.8	LA-ICPMS	Hu YB 2015
17.9	1.8	LA-ICPMS	Hu YB 2015
17.6	1.4	LA-ICPMS	Hu YB 2015
17.7	1.2	LA-ICPMS	Hu YB 2015
18.3	1.8	LA-ICPMS	Hu YB 2015
17.3	2.0	LA-ICPMS	Hu YB 2015
17.0	1.8	LA-ICPMS	Hu YB 2015
17.6	1.6	LA-ICPMS	Hu YB 2015
17.0	1.8	LA-ICPMS	Hu YB 2015
17.8	1.6	LA-ICPMS	Hu YB 2015
18.8	2.2	LA-ICPMS	Hu YB 2015
16.0	1.2	LA-ICPMS	Hu YB 2015
18.0	1.8	LA-ICPMS	Hu YB 2015
15.1	1.2	LA-ICPMS	Hu YB 2015
16.9	1.2	LA-ICPMS	Hu YB 2015
16.9	2.0	LA-ICPMS	Hu YB 2015
17.7	1.8	LA-ICPMS	Hu YB 2015
17.5	2.0	LA-ICPMS	Hu YB 2015
15.8	1.4	LA-ICPMS	Hu YB 2015
15.9	1.2	LA-ICPMS	Hu YB 2015
16.4	1.6	LA-ICPMS	Hu YB 2015
18.1	2.0	LA-ICPMS	Hu YB 2015
17.4	1.2	LA-ICPMS	Hu YB 2015
16.5	1.6	LA-ICPMS	Hu YB 2015
16.7	1.2	LA-ICPMS	Hu YB 2015
18.2	2.2	LA-ICPMS	Hu YB 2015
16.6	1.4	LA-ICPMS	Hu YB 2015
17.1	1.4	LA-ICPMS	Hu YB 2015
17.6	1.2	LA-ICPMS	Hu YB 2015
18.2	1.6	LA-ICPMS	Hu YB 2015
15.6	1.2	LA-ICPMS	Hu YB 2015
17.0	1.6	LA-ICPMS	Hu YB 2015
17.2	1.4	LA-ICPMS	Hu YB 2015
16.0	1.8	LA-ICPMS	Hu YB 2015
17.1	1.6	LA-ICPMS	Hu YB 2015

17.7	2.0	LA-ICPMS	Hu YB 2015
15.5	1.4	LA-ICPMS	Hu YB 2015
15.8	1.2	LA-ICPMS	Hu YB 2015
17.0	1.6	LA-ICPMS	Hu YB 2015
17.2	1.6	LA-ICPMS	Hu YB 2015
17.6	1.2	LA-ICPMS	Hu YB 2015
15.0	1.6	LA-ICPMS	Hu YB 2015
17.1	1.8	LA-ICPMS	Hu YB 2015
16.4	1.2	LA-ICPMS	Hu YB 2015
16.8	1.6	LA-ICPMS	Hu YB 2015
16.5	1.8	LA-ICPMS	Hu YB 2015
17.1	1.6	LA-ICPMS	Hu YB 2015
16.6	1.4	LA-ICPMS	Hu YB 2015
17.5	1.8	LA-ICPMS	Hu YB 2015
16.8	2.0	LA-ICPMS	Hu YB 2015
17.3	1.6	LA-ICPMS	Hu YB 2015
17.6	2.0	LA-ICPMS	Hu YB 2015
16.9	1.4	LA-ICPMS	Hu YB 2015
16.6	1.4	LA-ICPMS	Hu YB 2015
17.4	1.4	LA-ICPMS	Hu YB 2015
17.0	1.4	LA-ICPMS	Hu YB 2015
16.8	1.0	LA-ICPMS	Hu YB 2015
16.6	1.4	LA-ICPMS	Hu YB 2015
16.4	1.8	LA-ICPMS	Hu YB 2015
17.6	1.6	LA-ICPMS	Hu YB 2015
17.0	1.6	LA-ICPMS	Hu YB 2015
15.8	1.4	LA-ICPMS	Hu YB 2015
17.1	1.4	LA-ICPMS	Hu YB 2015
15.7	1.6	SHRIMP	Wang LL 2006
16.8	2.2	SHRIMP	Wang LL 2006
16.1	1.8	SHRIMP	Wang LL 2006
15.4	2.8	SHRIMP	Wang LL 2006
18.1	3.8	SHRIMP	Wang LL 2006
15.5	2.2	SHRIMP	Wang LL 2006
16.6	2.2	SHRIMP	Wang LL 2006
16.2	2.4	SHRIMP	Wang LL 2006
15.6	2.2	SHRIMP	Wang LL 2006
19.7	2.0	SHRIMP	Wang LL 2006
17.0	3.2	SHRIMP	Wang LL 2006
16.4	2.4	SHRIMP	Wang LL 2006
16.0	1.8	SHRIMP	Wang LL 2006
15.8	2.2	SHRIMP	Wang LL 2006
15.3	2.6	SHRIMP	Wang LL 2006
16.2	2.4	SHRIMP	Wang LL 2006
16.5	3.4	SHRIMP	Wang LL 2006
17.0	3.0	SHRIMP	Wang LL 2006
15.6	2.2	SHRIMP	Wang LL 2006
14.7	2.2	SHRIMP	Wang LL 2006
15.6	2.2	SHRIMP	Wang LL 2006
16.7	2.0	SHRIMP	Wang LL 2006
15.9	4.0	SHRIMP	Wang LL 2006
15.4	2.4	SHRIMP	Wang LL 2006

15.8	2.0	SHRIMP	Wang LL 2006
17.7	4.8	SHRIMP	Wang LL 2006
19.0	0.6	SHRIMP	Li GM 2004
~~11.7~~	~~7.4~~	SHRIMP	Li GM 2004
16.7	2.4	SHRIMP	Li GM 2004
15.3	1.4	SHRIMP	Li GM 2004
18.2	1.6	SHRIMP	Li GM 2004
17.3	0.9	SHRIMP	Li GM 2004
17.0	0.9	SHRIMP	Li GM 2004
15.7	3.0	SHRIMP	Li GM 2004
15.9	1.5	SHRIMP	Li GM 2004
17.1	2.4	SHRIMP	Li GM 2004
16.9	3.4	SHRIMP	Li GM 2004
18.0	2.0	SHRIMP	Li GM 2004
17.3	1.0	SHRIMP	Li GM 2004
17.9	1.4	LA-ICPMS	Zhao JX 2015
18.1	1.2	LA-ICPMS	Zhao JX 2015
17.2	1.2	LA-ICPMS	Zhao JX 2015
17.6	1.2	LA-ICPMS	Zhao JX 2015
17.7	1.4	LA-ICPMS	Zhao JX 2015
17.7	1.0	LA-ICPMS	Zhao JX 2015
16.8	1.0	LA-ICPMS	Zhao JX 2015
17.9	1.6	LA-ICPMS	Zhao JX 2015
17.6	1.4	LA-ICPMS	Zhao JX 2015
17.4	1.6	LA-ICPMS	Zhao JX 2015
15.9	1.4	LA-ICPMS	Zhao JX 2015
18.7	1.2	LA-ICPMS	Zhao JX 2015
17.0	2.0	LA-ICPMS	Zhao JX 2015
16.8	1.4	LA-ICPMS	Zhao JX 2015
18.9	2.0	LA-ICPMS	Zhao JX 2015
18.0	1.0	LA-ICPMS	Zhao JX 2015
17.4	1.4	LA-ICPMS	Zhao JX 2015
17.8	1.8	LA-ICPMS	Zhao JX 2015
17.2	1.8	LA-ICPMS	Zhao JX 2015
18.0	2.0	LA-ICPMS	Zhao JX 2015
17.0	4.0	LA-ICPMS	Zhao JX 2015
17.0	2.0	LA-ICPMS	Zhao JX 2015
17.0	2.0	LA-ICPMS	Zhao JX 2015
18.0	2.0	LA-ICPMS	Zhao JX 2015
17.2	1.8	LA-ICPMS	Zhao JX 2015
17.4	1.8	LA-ICPMS	Zhao JX 2015
17.0	2.0	LA-ICPMS	Zhao JX 2015
17.0	2.0	LA-ICPMS	Zhao JX 2015
17.4	2.0	LA-ICPMS	Zhao JX 2015
17.1	1.8	LA-ICPMS	Zhao JX 2015
17.5	1.6	LA-ICPMS	Zhao JX 2015
17.1	1.4	LA-ICPMS	Zhao JX 2015
16.4	1.2	LA-ICPMS	Zhao JX 2015
17.3	1.2	LA-ICPMS	Zhao JX 2015
17.1	1.4	LA-ICPMS	Zhao JX 2015
17.4	1.4	LA-ICPMS	Zhao JX 2015
17.0	1.2	LA-ICPMS	Zhao JX 2015

18.0	1.4	LA-ICPMS	Zhao JX 2015
17.8	1.6	LA-ICPMS	Zhao JX 2015
17.0	2.0	LA-ICPMS	Zhao JX 2015
17.9	1.2	LA-ICPMS	Zhao JX 2015
16.7	2.0	LA-ICPMS	Zhao JX 2015
17.0	2.0	LA-ICPMS	Zhao JX 2015
17.4	1.0	LA-ICPMS	Zhao JX 2015
16.3	1.4	LA-ICPMS	Zhao JX 2015
16.9	1.6	LA-ICPMS	Zhao JX 2015
17.2	1.8	LA-ICPMS	Zhao JX 2015
17.5	1.2	LA-ICPMS	Zhao JX 2015
18.0	1.8	LA-ICPMS	Zhao JX 2015
19.0	2.0	LA-ICPMS	Zhao JX 2015
17.4	1.2	LA-ICPMS	Zhao JX 2015
19.0	2.0	LA-ICPMS	Zhao JX 2015
18.0	4.0	LA-ICPMS	Zhao JX 2015
16.7	1.8	LA-ICPMS	Zhao JX 2015
17.9	1.2	LA-ICPMS	Zhao JX 2015
16.3	1.6	LA-ICPMS	Zhao JX 2015
18.0	4.0	LA-ICPMS	Zhao JX 2015
17.7	1.6	LA-ICPMS	Zhao JX 2015
17.2	1.0	LA-ICPMS	Zhao JX 2015
16.4	1.8	LA-ICPMS	Zhao JX 2015
16.9	1.2	LA-ICPMS	Zhao JX 2015
17.0	2.0	LA-ICPMS	Zhao JX 2015

P porphyry

age	2sigma	methods	references
16.2	1.4	LA-ICPMS	Zhao JX 2015
16.1	1.6	LA-ICPMS	Zhao JX 2015
16.1	1.4	LA-ICPMS	Zhao JX 2015
16.5	1.4	LA-ICPMS	Zhao JX 2015
15.8	1.2	LA-ICPMS	Zhao JX 2015
15.5	1.2	LA-ICPMS	Zhao JX 2015
17.0	2.0	LA-ICPMS	Zhao JX 2015
16.8	1.2	LA-ICPMS	Zhao JX 2015
16.9	1.2	LA-ICPMS	Zhao JX 2015
16.2	1.0	LA-ICPMS	Zhao JX 2015
16.4	1.2	LA-ICPMS	Zhao JX 2015
16.1	1.4	LA-ICPMS	Zhao JX 2015
16.0	1.0	LA-ICPMS	Zhao JX 2015
15.5	1.2	LA-ICPMS	Zhao JX 2015
16.7	1.2	LA-ICPMS	Zhao JX 2015
19.0	0.6	SHRIMP	Hou ZQ 2004
16.7	2.4	SHRIMP	Hou ZQ 2004
15.3	1.4	SHRIMP	Hou ZQ 2004
18.2	1.6	SHRIMP	Hou ZQ 2004
17.3	0.9	SHRIMP	Hou ZQ 2004
17.0	0.9	SHRIMP	Hou ZQ 2004
15.7	3.0	SHRIMP	Hou ZQ 2004
15.9	1.5	SHRIMP	Hou ZQ 2004
17.1	2.4	SHRIMP	Hou ZQ 2004

16.9	2.0	SHRIMP	Hou ZQ 2004
18.0	2.0	SHRIMP	Hou ZQ 2004
17.3	1.1	SHRIMP	Hou ZQ 2004
17.7	1.5	SHRIMP	Hou ZQ 2004

X porphyry

age	2sigma	methods	references
15.2	1.4	LA-ICPMS	Zhao JX 2015
16.4	1.6	LA-ICPMS	Zhao JX 2015
15.5	1.0	LA-ICPMS	Zhao JX 2015
15.4	1.4	LA-ICPMS	Zhao JX 2015
15.6	1.4	LA-ICPMS	Zhao JX 2015
16.0	1.0	LA-ICPMS	Zhao JX 2015
16.0	1.4	LA-ICPMS	Zhao JX 2015
16.4	1.6	LA-ICPMS	Zhao JX 2015
16.1	1.2	LA-ICPMS	Zhao JX 2015
15.0	2.0	LA-ICPMS	Zhao JX 2015
16.4	1.0	LA-ICPMS	Zhao JX 2015
16.4	1.2	LA-ICPMS	Zhao JX 2015
16.0	2.0	LA-ICPMS	Zhao JX 2015
16.0	1.2	LA-ICPMS	Zhao JX 2015
16.2	1.2	LA-ICPMS	Zhao JX 2015
16.5	1.6	LA-ICPMS	Zhao JX 2015
15.5	1.6	LA-ICPMS	Zhao JX 2015
15.8	1.0	LA-ICPMS	Zhao JX 2015

Post-ore quartz diorite

age	2sigma	methods	references
15.4	0.4	LA-ICPMS	Yang ZM 2015
16.0	0.4	LA-ICPMS	Yang ZM 2015
16.4	0.4	LA-ICPMS	Yang ZM 2015
15.8	0.4	LA-ICPMS	Yang ZM 2015
15.7	0.8	LA-ICPMS	Yang ZM 2015
15.5	0.6	LA-ICPMS	Yang ZM 2015
15.9	0.6	LA-ICPMS	Yang ZM 2015
15.8	0.4	LA-ICPMS	Yang ZM 2015
15.1	0.4	LA-ICPMS	Yang ZM 2015
15.9	0.6	LA-ICPMS	Yang ZM 2015
16.0	0.4	LA-ICPMS	Yang ZM 2015
16.2	0.4	LA-ICPMS	Yang ZM 2015
15.5	0.8	LA-ICPMS	Yang ZM 2015
15.5	0.4	LA-ICPMS	Yang ZM 2015
15.4	0.4	LA-ICPMS	Yang ZM 2015
15.5	0.4	LA-ICPMS	Yang ZM 2015
15.6	0.4	LA-ICPMS	Yang ZM 2015
15.3	0.4	LA-ICPMS	Yang ZM 2015
15.8	0.4	LA-ICPMS	Yang ZM 2015
16.0	1.0	LA-ICPMS	Yang ZM 2015
15.7	0.4	LA-ICPMS	Yang ZM 2015
15.4	0.6	SIMS	Zhao JX 2015
15.2	0.4	SIMS	Zhao JX 2015
15.5	0.4	SIMS	Zhao JX 2015

14.9	0.4	SIMS	Zhao JX 2015
15.5	0.4	SIMS	Zhao JX 2015
15.2	0.6	SIMS	Zhao JX 2015
15.4	0.6	SIMS	Zhao JX 2015
15.6	0.4	SIMS	Zhao JX 2015
15.2	0.4	SIMS	Zhao JX 2015
15.3	0.4	SIMS	Zhao JX 2015
15.6	0.6	SIMS	Zhao JX 2015
14.9	0.4	SIMS	Zhao JX 2015
15.4	0.6	SIMS	Zhao JX 2015
15.1	0.4	SIMS	Zhao JX 2015
14.9	0.4	SIMS	Zhao JX 2015
15.6	0.6	SIMS	Zhao JX 2015
15.2	0.6	SIMS	Zhao JX 2015

Table 3.2 Published molybdenite Re-Os geochronology dates at Qulong

Mineralization age	2 sigma	with additional decay uncertainties	methods	references
16.85	0.19	0.20	ICPMS Molybdenite	Wang LL 2006
16.74	0.30	0.31	ICPMS Molybdenite	Meng Xiang-Jin 2003
16.42	0.31	0.32	ICPMS Molybdenite	Meng Xiang-Jin 2003
16.23	0.90	0.90	ICPMS Molybdenite	Li Guangming 2005
16.21	0.30	0.31	ICPMS Molybdenite	Meng Xiang-Jin 2003
16.17	0.31	0.32	ICPMS Molybdenite	Meng Xiang-Jin 2003
16.11	0.28	0.29	ICPMS Molybdenite	Meng Xiang-Jin 2003
16.03	0.71	0.71	ICPMS Molybdenite	Li Guangming 2005
16.01	0.19	0.20	ICPMS Molybdenite	Wang LL 2006
15.99	0.31	0.32	ICPMS Molybdenite	Meng Xiang-Jin 2003
15.99	0.91	0.91	ICPMS Molybdenite	Zheng YY 2004
15.98	0.19	0.20	ICPMS Molybdenite	Wang LL 2006
15.96	1.94	1.94	ICPMS Molybdenite	Li Guangming 2005
15.82	0.19	0.20	ICPMS Molybdenite	Wang LL 2006
15.75	0.42	0.42	ICPMS Molybdenite	Li Guangming 2005
15.36	0.21	0.22	ICPMS Molybdenite	Zheng YY 2004

Table 3.3 Th/U sensitivity test for the ~16 Ma P porphyry

Th/U of magma	Weighted mean dates from statistically acceptable population	2 sigma abs	MSWD	N
1	15.933	0.012	0.35	3
2	15.986	0.012	0.86	3
3	16.003	0.012	1.10	3
4	16.012	0.012	1.20	3
5	16.017	0.012	1.30	3
6	16.020	0.012	1.40	3
7	16.023	0.012	1.40	3

Table 3.4 Re-Os ddata of the Henderson molybdenite standard

Batch	Sample	wt g	Re ppm	2 sigma abs	^{187}Re ppm	2 sigma abs	^{187}Os ppb	2 sigma abs	Age Ma	2 sigma abs/without decay
RO393-5	RO393-5 H2A	0.102	11.032	0.035	6.934	0.022	3.203	0.008	27.72	0.11
RO393-6	RO393-6 H2A	0.104	11.160	0.036	7.014	0.023	3.227	0.008	27.61	0.11
RO524-3	RO524-3_H2A	0.100	11.055	0.036	6.948	0.022	3.206	0.008	27.69	0.11
RO553-1	RO553-1_H2A	0.100	11.066	0.036	6.955	0.022	3.215	0.009	27.74	0.11
RO553-2	RO553-2_H2A	0.100	10.977	0.035	6.899	0.022	3.189	0.008	27.74	0.11
RO574-6	RO574-6_H2A	0.116	11.207	0.036	7.044	0.023	3.249	0.008	27.68	0.11
RO586-1	RO586-1_H2A	0.100	11.087	0.036	6.969	0.022	3.214	0.008	27.68	0.11
RO599-1	RO599-1_H2A	0.105	11.348	0.037	7.133	0.023	3.294	0.008	27.71	0.11
RO604-1	RO604-1_H2A	0.100	11.086	0.036	6.968	0.022	3.216	0.008	27.69	0.11
recommended		27.65	0.07		Markey et al 2007					

Table 3.5 CA-ID-TIMS U-Pb data of Miocene intrusive rocks at Qulong

		Composition						Isotopic Ratios										Dates (Ma)							
sample	Fraction	Th/ U d	Pb* (pg) e	Pbc (pg) f	Pb*/ Pbc g	Th/U[magma]	±2σ abs	^{206}Pb/ ^{204}Pb h	^{207}Pb/ ^{235}U i	±2σ %	^{206}Pb/ ^{238}U i	±2σ %	^{207}Pb/ ^{206}Pb i	±2σ %	^{206}Pb/ ^{238}U a	±2σ abs	^{206}Pb/ ^{238}U b	±2σ abs	^{207}Pb/ ^{235}U b	±2σ abs	^{207}Pb/ ^{206}Pb b	±2σ abs	discordance %	Corr. coef.
1605-296	z4	0.59	1.95	0.56	3.47	4.00	2.00	222	0.01866	3.0	0.002778	0.28	0.04873	2.9	17.975	0.050	17.882	0.049	18.77	0.55	134	69	87	0.122
	z7	0.55	3.38	0.27	12.63	4.00	2.00	769	0.01724	1.7	0.002736	0.17	0.04573	1.7	17.708	0.031	17.614	0.030	17.36	0.29	-18	41	-	0.065
	z1	0.57	4.82	0.50	9.66	4.00	2.00	590	0.01727	1.1	0.002673	0.11	0.04687	1.1	17.302	0.020	17.208	0.019	17.38	0.19	41	26	58	0.195
	z5	0.52	2.71	0.31	8.88	4.00	2.00	552	0.01693	1.5	0.002656	0.15	0.04626	1.5	17.193	0.027	17.098	0.026	17.05	0.26	10	36	-67	0.391
	z3	0.47	0.59	0.26	2.26	4.00	2.00	156	0.01715	4.8	0.002654	0.43	0.04688	4.7	17.180	0.074	17.084	0.074	17.26	0.81	42	111	59	0.284
	z9	0.52	9.02	0.35	25.94	4.00	2.00	1573	0.01726	0.5	0.002648	0.09	0.04728	0.4	17.145	0.016	17.051	0.015	17.37	0.08	62	11	72	0.168
	z8	0.51	9.31	0.62	15.02	4.00	2.00	921	0.01706	0.8	0.002646	0.15	0.04679	0.8	17.129	0.026	17.034	0.025	17.18	0.14	37	19	54	0.245
	z6	0.59	1.59	0.36	4.40	4.00	2.00	277	0.01688	3.6	0.002635	0.31	0.04649	3.4	17.057	0.053	16.964	0.052	17.00	0.60	22	82	23	0.458
001-550	z2	1.11	4.58	1.42	3.22	3.60	2.00	185	0.01613	4.0	0.002491	0.39	0.04697	3.9	16.115	0.065	16.040	0.062	16.25	0.64	47	92	66	0.335
	z1	1.05	2.41	0.81	2.99	3.60	2.00	175	0.01627	4.9	0.002490	0.40	0.04742	4.8	16.107	0.067	16.030	0.064	16.39	0.80	69	113	77	0.342
	z3	0.84	5.10	0.72	7.12	3.60	2.00	411	0.01618	2.2	0.002482	0.21	0.04730	2.1	16.063	0.036	15.979	0.033	16.30	0.36	63	51	75	0.306
	z6	0.55	25.24	1.48	17.10	3.60	2.00	1036	0.01587	0.6	0.002480	0.11	0.04643	0.6	16.057	0.019	15.965	0.017	15.98	0.10	19	15	14	0.204
	z5	1.11	4.78	0.92	5.19	3.60	2.00	287	0.01605	2.3	0.002478	0.22	0.04698	2.3	16.031	0.039	15.956	0.035	16.16	0.37	47	54	66	0.208
	z4B	0.94	6.07	0.30	20.33	3.60	2.00	1113	0.01603	0.8	0.002474	0.09	0.04703	0.8	16.008	0.021	15.928	0.014	16.15	0.13	50	18	68	0.294
	z4A	0.92	3.40	0.33	10.20	3.60	2.00	571	0.01589	1.5	0.002472	0.17	0.04664	1.4	15.998	0.031	15.917	0.027	16.01	0.23	30	33	46	0.494
1605-81	~~z8~~	~~1.13~~	~~1.25~~	~~1.03~~	~~1.21~~	~~4.97~~	~~2.00~~	~~80~~	~~0.03674~~	~~18.0~~	~~0.005629~~	~~1.46~~	~~0.04737~~	~~17.0~~	~~36.267~~	~~0.528~~	~~36.183~~	~~0.528~~	~~36.64~~	~~6.47~~	~~67~~	~~406~~	46	~~0.668~~
	z1	0.50	7.23	0.30	23.78	4.97	2.00	1452	0.01513	0.4	0.002344	0.06	0.04683	0.4	15.189	0.009	15.091	0.009	15.24	0.07	39	10	61	0.222
	z9	1.14	2.97	0.26	11.38	4.97	2.00	604	0.01494	1.2	0.002344	0.13	0.04625	1.2	15.179	0.019	15.095	0.019	15.06	0.18	10	28	-59	0.226
	z10	0.60	3.35	0.28	11.82	4.97	2.00	713	0.01503	1.1	0.002342	0.16	0.04657	1.0	15.173	0.025	15.077	0.025	15.15	0.17	26	25	42	0.717
	z6	0.48	3.95	0.73	5.42	4.97	2.00	347	0.01520	1.8	0.002341	0.17	0.04712	1.8	15.171	0.026	15.073	0.026	15.32	0.28	54	43	72	0.138
	z2	0.72	8.33	0.83	9.99	4.97	2.00	587	0.01510	1.1	0.002340	0.11	0.04682	1.1	15.158	0.016	15.065	0.016	15.22	0.16	39	26	61	0.166
	z4	0.57	2.39	1.03	2.33	4.97	2.00	156	0.01542	4.8	0.002337	0.44	0.04789	4.8	15.143	0.067	15.047	0.067	15.54	0.75	93	113	84	0.253
	z3	0.81	4.47	1.27	3.52	4.97	2.00	214	0.01498	3.1	0.002333	0.29	0.04660	3.0	15.116	0.044	15.025	0.044	15.10	0.46	27	73	45	0.185

a Corrected for initial Th/U disequilibrium using radiogenic ^{208}Pb and Th/U[magma]

b Isotopic dates calculated using the decay constants λ238 = 1.55125E-10 and λ235 = 9.8485E-10 (Jaffey et al. 1971).

c % discordance = 100 - (100 * (^{206}Pb/^{238}U date) / (^{207}Pb/^{206}Pb date))

d Th contents calculated from radiogenic ^{208}Pb and the ^{230}Th-corrected ^{206}Pb/^{238}U date of the sample, assuming concordance between the U-Pb and Th-Pb systems

e Total mass of radiogenic Pb.

f Total mass of common Pb.

g Ratio of radiogenic Pb (including 208Pb) to common Pb.

h Measured ratio corrected for fractionation and spike contribution only.

i Measured ratios corrected for fractionation, tracer and blank.

Table 3.6 Re-Os data of molybdenite samples from Qulong

Sample	wt	Re(ppm)	2 sigma	^{187}Re(ppm)	2 sigma	^{187}Os(ppb)	2 sigma	Age	2 sigma	average	sigma abs uncertainti			vein type	depth	Temperature
	g	ppm	abs	ppm	abs	ppb	abs	Ma	abs	Ma	X a	Y b	Z c		meter	^{o}C d
313-145-3-3*	0.029	64.35	0.24	40.45	0.15	10.86	0.03	16.117	0.006							
313-145 2/3	0.011	59.55	0.29	37.43	0.18	10.06	0.04	16.132	0.008	16.126	0.008	0.060	0.077	A	145	425
313-145-1-3	0.042	65.97	0.22	41.46	0.14	11.14	0.03	16.133	0.007							
313-460*	0.014	143.32	0.61	90.08	0.39	24.17	0.09	16.107	0.008	16.107	0.015	0.065	0.082	B	460	398
001-640	0.010	104.16	0.53	65.47	0.33	17.56	0.08	16.096	0.007	16.098	0.013	0.066	0.083	B	640	390
001-640-4-4	0.021	99.73	0.38	62.68	0.24	16.83	0.05	16.110	0.017							
1605-211-3-5	0.042	210.21	0.69	132.12	0.44	35.41	0.09	16.084	0.007							
1605-211-1-5	0.032	226.85	0.77	142.58	0.48	38.21	0.11	16.085	0.006	16.088	0.007	0.058	0.075	A	211	360
1605-211 2/3	0.030	239.26	0.82	150.38	0.52	40.31	0.11	16.089	0.008							
1605-211-4-5	0.040	247.89	0.82	155.81	0.52	41.78	0.11	16.093	0.006							
1402-209-1-3	0.022	274.49	1.00	172.52	0.63	46.22	0.14	16.077	0.007							
1402-209-3-3	0.020	454.32	1.69	285.55	1.06	76.56	0.24	16.091	0.005	16.088	0.007	0.059	0.076	D	209	380
1402-209-2-3	0.044	257.37	0.84	161.76	0.53	43.38	0.12	16.093	0.008							
1605-80 1/7rpt	0.038	421.27	1.40	264.77	0.88	70.77	0.19	16.042	0.006							
1605-80-3-7	0.051	434.01	1.41	272.78	0.89	72.92	0.19	16.043	0.007							
1605-80-2-7	0.053	437.17	1.42	274.77	0.89	73.45	0.19	16.043	0.006							
1605-80-5-7	0.048	435.00	1.42	273.41	0.89	73.11	0.19	16.049	0.007	16.050	0.005	0.056	0.073	B	80	360
1605-80-4-7	0.071	466.37	1.49	293.12	0.94	78.40	0.20	16.053	0.006							
1605-80-7-7	0.050	435.30	1.42	273.59	0.89	73.21	0.19	16.060	0.007							
1605-80-6-7	0.050	411.14	1.34	258.41	0.84	69.16	0.18	16.062	0.007							
1405-120-2	0.020	250.55	0.93	157.48	0.59	42.08	0.13	16.036	0.006							
1405-120rpt	0.013	259.74	1.15	163.25	0.72	43.62	0.17	16.037	0.007	16.040	0.007	0.058	0.075	A	120	365
1405-120-1	0.021	250.25	0.92	157.29	0.58	42.05	0.13	16.047	0.006							
1405-120	0.012	261.78	1.27	164.53	0.80	44.02	0.18	16.056	0.025							
1605-70	0.013	125.25	0.55	78.72	0.35	21.03	0.08	16.036	0.006	16.036	0.012	0.065	0.082	B	70	365
1605-334*	0.039	224.51	0.75	141.11	0.47	37.64	0.10	16.011	0.007	16.011	0.015	0.064	0.081	B	334	340

1605-268-2	0.013	492.72	2.20	309.68	1.38	82.43	0.33	15.975	0.006							
1605-268_3_3	0.022	503.97	1.84	316.76	1.16	84.33	0.26	15.979	0.006	15.981	0.007	0.059	0.076	D	268	290
1605-268_1_3	0.024	503.96	1.80	316.75	1.13	84.38	0.25	15.988	0.006							
1605-155_3_4	0.023	171.95	0.62	108.07	0.39	28.71	0.09	15.941	0.007							
1605-155-2-4	0.031	137.18	0.47	86.22	0.29	22.90	0.06	15.943	0.006	15.943	0.007	0.058	0.075	B	155	345
1605-155_1/4*	0.020	232.94	0.87	146.41	0.54	38.89	0.12	15.944	0.006							
1605-155_4_4	0.019	210.91	0.79	132.56	0.50	35.22	0.11	15.946	0.007							
1605-53-4-4	0.011	372.86	1.80	234.35	1.13	62.21	0.27	15.931	0.006							
1605-53_1-2	0.030	401.51	1.37	252.36	0.86	67.00	0.19	15.935	0.005	15.939	0.006	0.058	0.075	B	53	310
1605-53-2	0.017	348.01	1.37	218.73	0.86	58.11	0.20	15.943	0.006							
1605-53-3-4	0.012	395.30	1.82	248.45	1.14	66.02	0.28	15.947	0.006							
1605-33	0.013	310.74	1.37	195.31	0.86	51.61	0.21	15.859	0.010							
1605-33-1-5	0.045	311.94	1.02	196.06	0.64	51.81	0.14	15.860	0.006							
~~1605-33*~~	~~0.012~~	~~323.60~~	~~1.47~~	~~203.39~~	~~0.92~~	~~53.82~~	~~0.22~~	~~15.881~~	~~0.007~~	15.860	0.010	0.058	0.075	D	33	285
~~1605-33-2-5~~	~~0.024~~	~~298.67~~	~~1.07~~	~~187.72~~	~~0.67~~	~~49.68~~	~~0.15~~	~~15.884~~	~~0.006~~							
~~1605-33~~	~~0.020~~	~~284.14~~	~~1.06~~	~~178.59~~	~~0.67~~	~~47.29~~	~~0.15~~	~~15.892~~	~~0.006~~							

a, analytical uncertainty
b, analytical and tracer uncertainty
c, analytical, tracer and decay constant uncertainty of Smoliar et al., 1996
d, vein formation temperatures constrained by fluid inclusion study from Li etal., 2016
*, data reprocessed from Li et al 2016, Mineralium Deposita

Chapter 4

SIMS quartz oxygen isotopic composition of the Qulong porphyry Cu-Mo deposit, Tibet, China: Implications for metal deposition triggered by fluid mixing*

*A version of this chapter will be submitted to Geochimica et Cosmochimica Acta, co-authored with Xian-Hua Li and David Selby.

4.1 Introduction

Porphyry Cu deposits are the world's primary source of Cu, Mo and Re, and additionally contribute to the source of Au (Sillitoe, 2010). As such understanding the process of metal enrichment is particularly important. The current consensus is that metals are transported by magmatic fluids derived from a magma chamber, that are ultimately precipitated in a restricted zone as sulfides with associated alteration assemblages within and surrounding porphyry stocks/country rocks overlying the progenitor magma chamber (Sillitoe, 2010; Richards, 2011; Cooke et al., 2014). Although porphyry Cu deposits have been intensively studied, mechanisms of precipitation of ore sulfides remain debated (Kouzmanov and Pokrovski, 2012; Cooke et al., 2014). Depressurization, fluid mixing and unmixing, cooling, magnetite crystallization and water-rock interaction have been proposed as triggers for metal deposition (Kouzmanov and Pokrovski, 2012; Sun et al., 2013; Cooke et al., 2014). All these processes are conceptually feasible, and indicate either the primary trigger mechanism varies from deposit to deposit or at least some of these precipitation controls only operate at smaller scales. Recently, high-resolution oxygen isotope analysis of vein quartz from two porphyry Cu deposits demonstrated that the expulsion of magmatic fluids coupled with meteoric water is necessary to maintain the thermal anomaly of a porphyry/magmatic system, with meteoric water involvement during the time of ore mineral precipitation (Fekete et al., 2016).

There is growing evidence to suggest that at least some porphyry Cu deposits are formed through multi-pulsed magmatic-hydrothermal episodes (Chapter3; Sillitoe, 2010; Stein, 2014; Mercer et al., 2015; Spencer et al., 2015; Williamson et al., 2016). For such porphyry systems the hypothesis of Fekete et al. (2016) predicts increased meteoric involvement into the magmatic-hydrothermal system due to a loss

of the shielding force from the magmatic fluids from the progenitor intrusion during the intermittent period of ore formation, which is then shut down by the replenishment of magmatic fluids. This model can be evaluated by tracing the fluid evolution of a porphyry system under an absolute timescale.

Tracing the evolution paths of ore-forming fluids traditionally relies largely on H-O isotope and fluid inclusion data of gangue minerals, e.g., quartz (Cooke et al., 2014). A temporal relationship between ore sulfides and gangue minerals is used for fluid inclusion and isotope geochemistry studies must be unequivocally established to provide an absolute constrains on the evolution of ore-forming fluids (Redmond et al., 2004; Wilkinson et al., 2009). However, the presence of complicated textures or zoning in quartz representing the dynamics of fluid evolution adds uncertainties to data collected by bulk analysis (Allan and Yardley, 2007; Tanner et al., 2013; Vasyukova et al., 2013; Fekete et al., 2016). Further, a porphyry system formed by multiple episodes of magmatism and hydrothermal activity additionally challenges establishing a clear chronology of both vein and alteration assemblages, and consequently the fluid evolution of the ore system. More importantly, reconstructing the fluid oxygen isotopic composition from quartz veins is not straightforward (Allan and Yardley, 2007; Tanner et al., 2013; Vasyukova et al., 2013). For example, oxygen isotope volume diffusion, quartz overgrowth, dissolution and recrystallization, out of oxygen isotope exchange equilibrium between quartz and water, and boiling associated isotope fractionation, all of which are potential mechanisms that can bias the calculated fluid oxygen isotopic composition (Tanner et al., 2013).

The inability to account for the uncertainties mentioned above hinders distinguishing among possible depositional mechanisms related to ore formation, as

demonstrated by the controversial role of meteoric water. Stable isotopes, fluid inclusions and numerical simulation have suggested progressive involvement of meteoric water during ore-forming process, but such an external component was considered negligible in the early stages of mineralization and have limited/no contribution to ore formation (Stein and Hannah, 1985; Cooke and McPhail, 2001; Watanabe and Hedenquist, 2001; Ulrich et al., 2002). In contrast, other studies argue that meteoric water is an essential component during the entire ore-forming process (Friedman et al., 1974; Sun and Eadington, 1987; Hedenquist and Aoki, 1991; Sheets et al., 1996; Selby et al., 2001; D'Errico et al., 2012).

To further understand the controls of ore formation and test the model proposed by Fekete et al. (2016) and the role of meteoric water in porphyry ore formation, we report a detailed Secondary Ion Mass Spectrometry (SIMS) quartz oxygen isotope study of quartz veins from the giant Qulong porphyry Cu-Mo deposit. The paleo-elevation of the terrain in the vicinity of the Qulong porphyry system at its time (Miocene) of emplacement was >4595 m (Currie et al., 2005). The paleo meteoric water possessed a depleted oxygen isotopic composition of -15.6 ± 3.6 ‰ (Currie et al., 2005). The stark contrast between the paleo meteoric water $\delta^{18}O$ composition to that of magmatic water ($\delta^{18}O$ = ~7.6 ‰) makes the Qulong porphyry system an ideal candidate to investigate the potential mixing of meteoric water with magmatic. The absolute timeframe and formation temperatures for the quartz veins studied for quartz oxygen isotopic compositions are obtained from high precision quartz-hosted-molybdenite Re-Os dating (Chapter3) and fluid inclusion study (Li et al., 2016), respectively. We demonstrate that the vein quartz records the primary oxygen isotope signature and reached oxygen isotope fractionation equilibrium with ore-forming fluids. We use the quartz oxygen isotope data to infer that meteoric

water involvement induced cooling, and that this process is a key factor for the formation/metal deposition of the giant Qulong porphyry Cu-Mo deposit, and may have implications for metal enrichment processes of porphyry systems elsewhere.

4.2 Geological framework of Qulong

Qulong is China's largest porphyry Cu-Mo deposit, containing 11 Mt of Cu and 0.6 Mt of Mo (Li et al., 2016). The deposit geology has been intensively studied (Chapter3; Yang and Hou, 2009a; Yang et al., 2009; Xiao et al., 2012; Qin et al., 2014; Hu et al., 2015; Yang et al., 2015; Li et al., 2016; Zhao et al., 2016) and is summarized here. The Qulong system occurs in the Lhasa terrane, with the deposit geology comprising Jurassic volcanic and intrusive rocks, plus Miocene porphyries (Yang et al., 2009; Hu et al., 2015; Li et al., 2016; Zhao et al., 2016) (Fig. 4.1). The emplacement sequence of the Miocene porphyries at Qulong is; (1) the pre-ore Rongmucuola monzogranite pluton, (2) the syn-ore monzogranite P porphyry and aplite, (3) the syn-ore monzogranite X porphyry, and (4) the post-ore quartz diorite. In addition, two stages of hydrothermal breccia developed following the emplacement of the X porphyry. The Cu-Mo mineralization at Qulong is predominately hosted by the west portion of the Rongmucuola pluton while the east portion is barren, and is spatially associated with potassic and to a lesser extent, with propylitic and phyllic alteration assemblages (Yang et al., 2009). The spatial association of the P porphyry with the most intensive alteration and highest-grade ore, together with the much smaller size of X porphyry and aplite, may suggest that mineralization at Qulong is, in part, genetically linked with the emplacement of the P porphyry, with less contribution from the X porphyry and the aplite (Chapter3; Yang et al., 2009; Hu et al., 2015; Li et al., 2016; Zhao et al., 2016). After the

crystallization of post-ore quartz diorite, no further magmatism and metamorphism is documented at Qulong (Yang et al., 2015; Zhao et al., 2016).

Previous high precision zircon U-Pb dating suggest the Rongmucuola pluton, P porphyry, and the quartz-diorite emplaced at 17.142 ± 0.023 Ma (including ^{238}U decay constant uncertainty), 16.009 ± 0.024 Ma, 15.166 ± 0.020 Ma, respectively (Chapter 3). The Re-Os geochronology (n = 13 veins) constrains the mineralization at Qulong from 16.126 ± 0.077 Ma to 15.860 ± 0.075 Ma, proposing a mineralization duration of 266 ± 13 kyr (Chapter3).

4.3 Samples and analytical methods

4.3.1 Samples

In addition to the uncertainties arising from analysing multi-stage quartz grains by bulk analysis, the multiple ore-forming events at Qulong makes it very challanging to evaluate fluid evolution using a relative chronology defined by traditional alteration assemblages. To overcome these complexities, in-situ quartz oxygen isotope analysis guided by CL imaging was conducted, with quartz formation temperatures and ages constrained by a fluid inclusion study (Li et al., 2016) and high precision Re-Os molybdenite dating (Chapter3), respectively. To the best of our knowledge, this is the first approach evaluating ore-forming fluid evolution path constrained by an absolute timeframe.

Zircon and groundmass quartz grains were separated from two fresh Rongmucuola monzogranite samples. One sample was collected from the western Rongmucuola monzogranite (QL14_23W) and a second from the east portion of the intrusion (QL14_52E) (Fig. 4.1). These samples were collected to provide the best estimates the oxygen isotopic composition of the magmatic fluid and to evaluate the

potential variations of the magmatic water oxygen isotope values across the Rongmucuola pluton. The P porphyry is not used for this purpose because it has experienced intensive hydrothermal alteration.

A single sinusoidal quartz vein hosted by an aplite dyke (Fig. 4.3A) is analysed to evaluate the fluid nature during the formation of the aplite. The aplite was hosted by the Rongmucuola pluton and is considered to have formed earlier than the P porphyry (Chapter3; Li et al., 2016). Thirteen molybdenite bearing quartz veins constrained by Re-Os molybdenite dates (Chapter3) were analysed by CL and SIMS to image successive generations of quartz and oxygen isotopic compositions, respectively. For the same veins a fluid inclusion study has been completed to constrain the P-T-X conditions of vein formation (Li et al., 2016). Quartz grains were isolated from same quartz veins selected for Re-Os molybdenite dating. Only quartz grains with a spatial association with molybdenite, e.g., enclosing fine-grained molybdenite, are used. An additional 7 molybdenite-free, but chalcopyrite-bearing veins are analysed to account for any potential bias caused by predominantly investigating quartz veins that are molybdenite bearing. A feldspar-molybdenite vein, overprinted by an anhydrite-pyrite assemblage (Fig. 4.3G), was only selected to test the resolvability of multi-stage quartz growth history by SIMS oxygen isotope analysis.

4.3.2 SIMS quartz oxygen isotope analytical method

CL imaging was conducted with a Hitachi SU-70 SEM at Durham University (Li et al., 2016; Li et al., 2017). Examination was carried out at a 15 kv accelerating voltage with a beam current of 100 nA at a 20 mm working distance under a high

vacuum mode. Secondary electron images were taken using the same accelerating voltage and working distance, but at a lower beam current (1 nA).

Guided by CL images, quartz SIMS oxygen isotope analysis was carried out at the Institute of Geology and Geophysics, Chinese Academy of Sciences with a CAMECA IMS-1280 SIMS (Li et al., 2010). Quartz bearing assemblages were mounted with the NBS-28 and Qinghu quartz standards, polished and then coated with gold. The Cs^+ primary ion beam was accelerated at 10 kV, with an intensity of ca. 2 nA and rastered over a 10 μm area. The spot size as an ellipse was ~10 × 20 μm in diameter. Oxygen isotopes were measured using multi-collection mode on two off-axis Faraday cups. The intensity of ^{16}O was typically 10^9 cps during this study. The instrumental mass fractionation factor (IMF) was corrected using NBS-28 with a $\delta^{18}O$ value of 9.5 ‰ (VSMOW) (Matsuhisa, 1974). Measured $^{18}O/^{16}O$ ratios were normalized by using VSMOW compositions ($^{18}O/^{16}O$ = 0.0020052), and then corrected for the IMF, uncertainties on individual analysis were usually better than 0.3 ‰ (2 SE). All measurements were bracketed or interspersed with spot analyses of Qinghu quartz that served as an internal standard. This study was conducted at the same period with that of Li et al. (2017). During this study the $\delta^{18}O$ value of the Qinghu quartz ranged between 8.34 ± 0.23 and 8.92 ± 0.37 ‰, and yields a weighted mean of 8.66 ± 0.05 ‰. These results are within uncertainty of the preferred $\delta^{18}O$ value for the Qinghu quartz of 8.6 ± 0.2 ‰ (2 SD) (Li et al., 2017).

For each analysed quartz vein, CL images and the distribution of $\delta^{18}O$ values are used to evaluate the potential presence of recognizable multiple growth history. When single quartz growth history was demonstrated, we interpret the weighted mean as the best estimate of the $\delta^{18}O$ value of that vein (Rollinson, 1993).

4.3.3 Fluid oxygen isotopic composition and source constrains

Experimentally determined quartz-water oxygen isotope fractionation equation (Matsuhisa et al., 1979) was used to calculate the $\delta^{18}O$ values of ore-forming fluid ($\delta^{18}O_f$) with quartz formation temperatures constrained by a previous fluid inclusion study (Li et al., 2016).

To evaluate the percentage contribution of meteoric water to the magmatic-hydrothermal system we apply a binary mixing model using the end members of meteoric water and magmatic water. The equation used in the binary model is as below where X is the percentage of meteoric water contribution.

$$\delta^{18}O_{bulk\ fluid} = X * \delta^{18}O_{magmatic\ fluid} + (1 - X) * \delta^{18}O_{meteoric\ water}$$

4.4 Results

4.4.1 Oxygen isotope of quartz and zircon from Rongmucuola pluton

Groundmass quartz and zircon from the two less altered Rongmucuola pluton possess homogenous oxygen isotopic compositions, with a $\delta^{18}O_{quartz}$ of 8.70 ± 0.06 ‰ (n = 26) and a $\delta^{18}O_{zircon}$ of 6.14 ± 0.05 (n = 23, Table 4.1, Fig. 4.2). The $\delta^{18}O$ quartz and zircon values yield a $\Delta^{18}O_{quartz\text{-}zircon}$ of 2.56 ± 0.08 ‰. This value corresponds to an equilibrium temperature of oxygen isotope fractionation between zircon and quartz of 680 ± 52 °C (Trail et al., 2009).

4.4.2 Quartz of the sinusoidal vein

The sinusoidal quartz vein hosted by an aplite dyke (Fig. 4.3A), which formed before the emplacement of the P porphyry, represents a vein formed prior the bulk mineralization at Qulong (Chapter3; Li et al., 2016). This vein comprises fine-

grained (0.2 - 0.5 mm) euhedral quartz grains, with CL petrography revealing core resorption-dissolution and rim overgrowth textures (Fig. 4.3B). Three core to rim transects in two quartz crystals show similar $\delta^{18}O$ values increasing from 5.40 ± 0.27 (core) to 7.89 ± 0.31 (rim) ‰ (Fig. 4.3C; Table 4.2).

4.4.3 Textures and oxygen isotope of quartz grains associated with mineralization

In general, studied quartz grains from mineralized veins exhibit no evidence of any hydrothermal overprint. The CL images of the quartz grains (0.4 - 1 mm; Fig. 4.3D) exhibit clear euhedral oscillating growth banded zones or dark luminescence. The grains are occasionally crosscut by 5-30 µm wide discontinuous fractures (Fig. 4.3E). SIMS analysis reveals homogeneous $\delta^{18}O$ values for the same vein regardless of the presence/absence of fractures and zonation (Fig. 4.3F, Table 4.2), with weighted means varying between 8.30 ± 0.15 and 11.90 ± 0.10 ‰ (Fig. 4.4, Table 4.3). The $\delta^{18}O$ values of quartz veins of the early mineralization stage show the largest variability. For example, in chronological order constrained by Re-Os molybdenite dates, the $\delta^{18}O$ values rise from 8.39 ± 0.09 to 9.16 ± 0.08 ‰ and then to 11.90 ± 0.10 ‰, which then decrease to 9.75 ± 0.08, 8.78 ± 0.07 and 8.30 ± 0.15 ‰ (Fig. 4.4). Overall, the $\delta^{18}O$ values between 16.040 and 15.860 Ma are consistent between 8.74 ± 0.09 and 9.38 ± 0.09 ‰. Each of the additional 7 molybdenite-free, chalcopyrite-bearing veins possess a homogeneous oxygen isotopic composition and yield $\delta^{18}O$ values between 8.86 ± 0.06 and 9.98 ± 0.08 ‰ (Table 4.2). Given the similar results between the molybdenite-bearing samples and molybdenite-free samples, we consider using molybdenite-bearing samples for fluid evolution study is representative.

Quartz grain from a molybdenite-bearing vein overprinted by a pyrite-anhydrite assemblage exhibit both diagnostic dark- and bright-luminescence (Fig.

4.3H). Quartz with a dark-luminescence (Q1) shows no variation in luminescence intensity. In contrast, quartz exhibiting a bright-luminescence (Q2) are characterized by banded zones with various intensities of luminescence. Both Q1 and Q2 have homogenous oxygen isotopic compositions, but yield contrasting $\delta^{18}O$ values of 8.45 ± 0.21 (Q1, n = 9) and 0.12 ± 0.31 ‰ (Q2, n = 8), respectively (Fig. 4.3I).

Collectively, 87 % of the 308 analyses (n = 268) from the 22 samples possess $\delta^{18}O$ values between 8 and 10 ‰, and yield a mean of 9.05 ± 1.01 (2SD) (Fig. 4.5).

4.5 Discussion

4.5.1 Primary oxygen isotope signature of vein quartz

Oxygen isotope exchange through volume diffusion is an important mechanism that modifies the primary isotopic composition of zircon and quartz (Valley and Graham, 1996). Other mechanisms that can also modify the primary oxygen isotopic composition of quartz include recrystallization, overgrowths and precipitation of new materials along microfractures (Farver and Yund, 1991; Valley and Graham, 1996).

Magmatic zircon and quartz grains from the Rongmucuola pluton both yield homogenous oxygen isotopic compositions, and a $\Delta_{quartz\text{-}zircon}$ value (2.58 ± 0.08 ‰) that suggests oxygen isotope equilibrium at 680 ± 52 °C (Fig. 4.4) (Valley et al., 1994; Trail et al., 2009). The refractory and resistant nature of zircon, together with the limited evidence of hydrothermal overprint and homogeneous zircon-quartz $\delta^{18}O$ values across the Rongmucuola pluton, coupled with the agreement of temperatures between zircon-quartz equilibrium estimation and the temperature constraints of the granite solidus (Johannes, 1984), all suggest that the zircon and quartz recorded the primary magmatic oxygen isotopic composition of the Rongmucuola pluton.

For mineralized hydrothermal quartz grains, despite the frequent presence of micro-fractures (Fig. 4.3), no dependence between $\delta^{18}O$ values and presence of fractures is observed, which argues against modification of the oxygen isotopes through diffusion along fractures (Valley and Graham, 1996). Oxygen isotope exchange through volume diffusion occurs inwards from grain boundaries, therefore partial ^{18}O exchange in a mineral will produce isotopically zoned grains (Valley and Graham, 1996; Monani and Valley, 2001). With the exception of the quartz vein hosted by the aplite dyke, all quartz grains yield homogeneous oxygen isotopic compositions. These observations suggest that the hydrothermal quartz grains are either free from post-crystallization oxygen isotope diffusion or experienced complete oxygen isotope exchange. The time needed for complete oxygen diffusion exchange in quartz grains at a given temperature can be estimated by the equation $t=X^2/D$, where X is diffusion distance, D is diffusion coefficient (Farver and Yund, 1991; Valley and Graham, 1996). For a 400 μm quartz grain, which is the average quartz grain size in this study (Fig. 4.3B), complete oxygen exchange over a distance of 200 μm requires ~1.3 myr at 500 ^{o}C. This time will dramatically increase to >10 myr at 400 ^{o}C. High precision dating and fluid inclusion studies indicate that the studied quartz veins were formed between 425 and 280 ^{o}C within 266 ±13 kyrs, and post-mineralization magmatism is limited (Chapter3; Yang et al., 2009; Li et al., 2016; Zhao et al., 2016). Therefore the time and temperature necessary for quartz reaching complete oxygen isotope exchange at Qulong is unlikely.

Quartz grains from the K-feldspar-molybdenite vein overprinted by an anhydrite-pyrite assemblage have characteristic features in CL images that are indicative of two-stage quartz growth. The SIMS analysis easily resolved this two-stage quartz growth history (Fig. 4.4H) and demonstrated that the approach used in

this study has the ability to distinguish multiple generations of quartz growth when present.

4.5.2 Equilibrium oxygen fractionation between quartz and water

Based on the temperature (680 ± 52 ^{o}C) constrained by zircon-quartz oxygen isotope equilibrium, magmatic water associated with Rongmucuola pluton had a $\delta^{18}O$ value of 7.56 ± 0.26 ‰. This $\delta^{18}O$ fluid ($\delta^{18}O_f$) value is almost identical to that (~7.7 ‰) estimated by Yang and Hou (2009a), and agrees with the reported range of magmatic water $\delta^{18}O_f$ values (Cooke et al., 2014). Given no appreciable variations of quartz and zircon $\delta^{18}O$ values were observed across the pluton, and that the Rongmucuola pluton, and P and X porphyries have very similar Sr-Nd-Pb isotopic compositions (Qin et al., 2014), no significant variations in the magmatic water $\delta^{18}O$ value between the Rongmucuola pluton and the P and X porphyries is expected (Monani and Valley, 2001; Jones et al., 2015). As such, we suggest that the best estimate for the $\delta^{18}O_f$ value for magma water responsible for mineralization is 7.56 ± 0.26 ‰.

For hydrothermal quartz, calculating the fluid oxygen isotopic composition is only possible when equilibrium oxygen isotope fractionation between quartz and water is reached (Allan and Yardley, 2007; Tanner et al., 2013). The equilibrium conditions can be evaluated through comparing oxygen isotope exchange rates in quartz-water system and quartz growth speed. Equilibrium is expected when quartz growth speed is slower than the isotope exchange rate. There is a lack of direct experimental study to quantify the oxygen isotope exchange rate between quartz and water. However, using the experimental study of a granite-fluid system (water/mineral ratio of 5, salinity of 5.8 wt. % NaCl equiv.) as an alternative, with

quartz of an average grain size of 0.2 cm, oxygen isotope equilibrium is reached within 100 years at 300 ^{o}C (Yang and Hou, 2009b). The experimental study further predicted a reduction in the equilibrium time with increased temperature, fluid salinity and water/mineral ratio.

Previous fluid inclusion study (Li et al., 2016) suggests the hydrothermal fluids at Qulong have temperatures of 425 – 280 ^{o}C (average = 340 ^{o}C) with salinities of >5 wt. % NaCl equiv. (Table 4.4). Considering the maximum Cu concentration in porphyry ore-forming fluids as ~1 % (Landtwing et al., 2005; Kouzmanov and Pokrovski, 2012), the volume of hydrothermal fluids at Qulong is >1.1 × 10^{9} m^{3} if 100 % metal deposition efficiency is assumed. Vein density in porphyry deposits is typically < 25 % and in most cases varies between 5 and 10 % in the ore shells (Weis et al., 2012). At Qulong the volume of ore is 2200 million tonnes (Li et al., 2016), with the quartz volume at Qulong being estimated to be 4.3 - 8.5 × 10^{7} m^{3}. The fluid and quartz volumes suggest a minimum water/mineral ratio of 13-26. The hydrothermal quartz grains at Qulong possess a maximum grain radius of <0.2 cm (Fig. 4.3), suggesting a precipitation time of ~1.38*10^{5} and 1.09*10^{3} years at 300 and 400 ^{o}C, respectively (Pollington et al., 2016). This growth time for 0.2 cm quartz is orders of magnitude longer than the time needed to reach oxygen isotope equilibrium, and suggests that oxygen isotope equilibrium was established between quartz and water. In addition, the actual equilibrium time will be further reduced since it decreases with increased fluid salinity and water/mineral ratio. In summary, we suggest that the hydrothermal quartz at Qulong, for the most part, reached oxygen isotope exchange equilibrium at the time of formation.

For fluids with a salinity <20 wt % NaCl equiv., oxygen isotope fractionation between aqueous and vapor phases through boiling is < 0.5 ‰ at 350- 450 ^{o}C

(Shmulovich et al., 1999). The levels of fractionation is the same order, within uncertainty, when considering the uncertainty derived from quartz-fluid oxygen isotope fractionation equation, together with limited evidence of boiling at Qulong (Yang et al., 2009; Xiao et al., 2012; Li et al., 2016), we suggest the effect of oxygen isotope fractionation associated with fluid boiling is most likely negligible.

4.5.3 Oxygen isotope of ore-forming fluid and meteoric water contribution

The sinusoidal quartz vein hosted by formed at 425 ºC (Li et al., 2016). The quartz grains of the sinusoidal vein show a bright CL rim in comparison to the core. The resorption surface between core and rim, plus the discordant rim overgrowth are suggestive of dissolution and resorption of the core occurred during the overgrowths of the rim (Fig. 4.3B). The $\delta^{18}O$ values progressively increase from core to rim (Fig. 4.3C). These features argue against volume diffusion and are interpreted as secondary features with the core experiencing the least overprint/alteration. Although the core does show some heterogeneity in its $\delta^{18}O$ values (Fig. 4.3B), the inner core records the most primary $\delta^{18}O$ value (5.4 ± 0.27 ‰) and is the best representation of the fluid during its formation, corresponding to a $\delta^{18}O_f$ of 1.84 ± 0.48 ‰ at 425 ºC. The heavier $\delta^{18}O$ values of the rim (7.1-7.9 ‰) suggest that resorption and overgrowth is the result of a later ^{18}O-rich fluid.

For the remaining mineralized quartz samples, the $\delta^{18}O_f$ evolution for Qulong is presented against an absolute timeframe based on the Re-Os molybdenite geochronology (Fig. 4.4). The $\delta^{18}O_f$ recorded by quartz veins show significant variations up to 5.76 ‰, and are characterized by both abrupt and gradual shifts (Fig. 4.4, Table 4.4). Based on the Re-Os molybdenite chronology, the earliest veins at 16.126 and 16.107 Ma possess $\delta^{18}O_f$ values of 4.83 ± 0.41 ‰ and 5.04 ± 0.45 ‰. At

16.008 Ma a vein has a $\delta^{18}O_f$ value of 7.59 ± 0.47 ‰. Three younger veins from 16.088 to 16.050 Ma show a decrease in $\delta^{18}O_f$ values with age from 5.21 ± 0.49 to 3.25 ± 0.55 ‰. Samples at 16.040 and 16.030 Ma have $\delta^{18}O_f$ of 3.82 ± 0.53 and 4.18 ± 0.52 ‰, with the younger vein showing lower $\delta^{18}O_f$ values (3.26 ± 0.59 ‰) to a nadir of 1.83 ± 0.76 ‰ at 15.981 Ma. There is a slight increase in the $\delta^{18}O_f$ values (3.55 ± 0.58 ‰) at 15.943 Ma and then a decrease from 2.34 ± 0.69 ‰ at 15.939 Ma to 1.93 ± 0.78 ‰ at 15.877 Ma.

With the exception of sample 001-640 at 16.098 Ma, which possesses a $\delta^{18}O_f$ value of 7.59 ± 0.47 ‰, all $\delta^{18}O_f$ values are significantly lower (1.83 ± 0.76 to 5.21 ± 0.49 ‰; Fig. 4.4) than that of magmatic water (7.56 ± 0.26 ‰), and require the involvement of a fluid with lower $\delta^{18}O$ values. The most likely source of water enriched with a light oxygen isotopic composition is meteoric water (Hedenquist and Aoki, 1991; Sheets et al., 1996). Using the best estimated values for magmatic water (7.56 ± 0.26 ‰; this study) and meteoric water (-15.6 ± 3.6 ‰, Currie et al., 2005), a 25.33 ± 4.87 % meteoric water contribution is estimated by the sinusoidal vein before the main stage of porphyry mineralization, with 11-12 % meteoric water involvement during the early mineralization stage (16.126-16.107 Ma).

The similarity of the $\delta^{18}O_f$ values for sample 001-640 with magmatic water suggests the predominance of magmatic water in the ore fluids at 16.098 Ma. We attribute the origin of this magmatic fluid to be associated with the emplacement of X porphyry. The remaining $\delta^{18}O_f$ values (16.088-15.877 Ma) overall suggest a progressive increased involvement of meteoric water with the hydrothermal fluids (10.40 ± 3.00 % at 16.088 Ma to 24.93 ± 5.55 % at 15.877 Ma). Moreover, the repetitive decrease-increase trends are indicative of interaction between magmatic fluid and meteoric water periodically. As shown in Figure 4.4, during each of the

mineralization pulses, the meteoric water contribution is higher at the beginning, and then decrease in the middle, and then rebound again at the end. This observation is expected as the system is dominated by magmatic fluid during ore formation, while in the intermittent period, the reduction in the force of the over pressured magmatic fluid will permit meteoric water mixing (Fekete et al., 2016). The sinusoidal vein records a highly depleted $\delta^{18}O_f$ signature and indicates a high meteoric water component in the ore system before the emplacement of the P porphyry. This is expected as without the shielding of magmatic fluids, meteoric water will dominate the fluid budget of the system (Fekete et al., 2016). The subsequent emplacement of the P porphyry and exsolution of magmatic fluids resulted in an increase in the $\delta^{18}O_f$ values.

Due to a lack of formation temperatures and chronologic constrains for the molybdenite-free samples, we do not use them to evaluate the fluid evolution process, but as discussed earlier, the molybdenite-bearing samples are representative of the entire duration of the Qulong porphyry system. Of the entire quartz $\delta^{18}O$ data, 87 % of the analyses have a $\delta^{18}O$ value of 8-10 ‰ (Fig. 4.5), which corresponds to a fluid with $\delta^{18}O_f$ of 3.59 ± 1.77 ‰, when considering an average mineralization temperature of 350 ± 50 ºC. The $\delta^{18}O_f$ values imply an average meteoric water contribution of 17.58 ± 8.55 %.

Considering that meteoric water would evolve to isotopically heavier $\delta^{18}O$ values through interaction with the Jurassic-Miocene magmatic rocks, the estimated meteoric water contributions are a minimum. Similar $\delta^{18}O_f$ evolution trends (Fig. 4.4) are observed with temperatures of 420, 350 and 300 ºC, which are the upper limit, average and lower limit of the mineralization temperatures both at Qulong (Li et al., 2016) and in typical porphyry deposits (Rusk and Reed, 2002; Redmond et al., 2004;

Kouzmanov and Pokrovski, 2012; Cooke et al., 2014). The agreement of meteoric water contributions trends between different temperatures shown in Figure 4.4 excludes the possibility of meteoric water contribution caused by incorrect temperatures calibrations. In addition, this study demonstrates that bulk isotope analysis utilised in porphyry deposit studies are only informative when the sample set does not record any post formation overprint.

4.6 Fluid mixing induced cooling as a trigger for ore formation

The final step of fluid evolution in porphyry Cu system is the efficient deposition of metals as sulphides. The main processes proposed as triggers of metal deposition are: decompression, boiling, cooling, fluid-rock interaction, magnetite crystallization and mixing with external fluid (Kouzmanov and Pokrovski, 2012; Cooke et al., 2014). These processes are discussed in detail below.

4.6.1 Significance of decompression, boiling, magnetite crystallization and water-rock interaction

Pressure fluctuations between lithostatic and hydrostatic conditions were suggested as triggers for metals deposition in porphyry deposits, as supported by the sharp decrease of quartz solubility with decreasing pressure at ~450 ^{o}C (Fig. 4.6A) (Rusk and Reed, 2002). However, thermodynamic data indicates solubilities of Cu and Mo show minor dependence on pressure and argue against this scenario (Kouzmanov and Pokrovski, 2012). Since the most direct effect of decompression is boiling, an alternative approach to evaluate the effect of pressure is evaluating boiling. Boiling, especially continuous boiling initiated by cycles of fluid release and

accumulation caused by carapace failure, has been regarded as one of the fundamental mechanisms to generate the classic mineralized stockworks observed in porphyry deposits (Cooke et al., 2014). The evidence for fluid inclusion assemblages (FIA) representing boiling at Qulong is limited (Yang and Hou, 2009a; Xiao et al., 2012; Li et al., 2016). This observation would imply that boiling is not the main trigger mechanism for metal deposition at Qulong.

Copper is transported in comparable proportions by vapor and brine after fluid boiling, with Cu deposition occurring well above the region of phase separation after fluid cooling and expansion (Kouzmanov and Pokrovski, 2012). This suggests cooling and phase expansion instead of boiling controls metal deposition, as supported by the strong dependence of Cu concentrations with temperatures in fluid inclusions (Fig. 4.6B) (Kouzmanov and Pokrovski, 2012). Molybdenite is believed to crystalize from a vapor phase when oxygen fugacity falls below the SO_2-H_2S buffer with declining temperature (Hannah et al., 2007). Thermodynamic data indicates that the solubilities of chalcopyrite and molybdenite, the major ore minerals at Qulong, have minor dependence on pressure in the liquid-phase and dense supercritical-fluid domain. And when compared to pH, salinity and S content, both Cu and Mo solubilities are predominantly controlled by temperature (Kouzmanov and Pokrovski, 2012), with the net effect of boiling being most favourable for ore formation at lower temperatures (Drummond and Ohmoto, 1985).

Other mechanisms of ore deposition include magnetite crystallization and fluid rock interaction (Kouzmanov and Pokrovski, 2012; Sun et al., 2013; Cooke et al., 2014). However, despite the presence of magnetite in alteration assemblages at Qulong, its presence is only minor (Yang et al., 2009; Li et al., 2016). Therefore, magnetite may have only locally promoted metal deposition (Sun et al., 2013), and if

not considered as a major contributing mechanism. Furthermore, the efficiency of fluid and rock interaction is implicitly involved for deposits where replacement-style sulfide mineralization predominate (Cooke et al., 2014). Such processes are not favourable for porphyry ore systems.

To summarize, we consider cooling to be the fundamental control for metal deposition at Qulong.

4.6.2 Metals deposition triggered by fluid mixing

As discussed above and shown in Fig. 4.6B, extreme temperature gradients are required to accounts for the efficient and rapid metal deposition at Qulong. However, the inefficiency of both conductive and rapid cooling and ore-formation (Chapter3) is a paradox, which has been explained by enhanced heat removal through circulation of meteoric water (Weis et al., 2012).

A simple calculation suggests that if a 500 ^{o}C supercritical fluid is mixed with a 100 ^{o}C meteoric water with a volume ratio of 9:1 (10% meteoric water involvement), the temperature of the mixed fluid is ~406 ^{o}C. This mixed fluid temperature will decrease to ~310 ^{o}C with a volume ratio of 8:2 (20% meteoric water involvement). These results are in excellent agreement with the observed mineralization temperature at Qulong between 425 - 285 ^{o}C (Li et al., 2016), as well as the temperature window at which Cu shows strong dependence on temperature (Fig. 4.6B). In this case, we propose fluid mixing between cold meteoric water and hot magmatic water is the key to generate the extreme temperature gradient needed for efficient metal deposition at Qulong (Chapter 3), and as proposed for other porphyry system by Fekete et al. (2016).

Similarly, significant meteoric water involvement in porphyry deposits has been documented by a number of previous studies (Sun and Eadington, 1987; Hedenquist and Aoki, 1991; Sheets et al., 1996; Selby et al., 2001), and have been further highlighted by a recent SIMS oxygen isotopic study (Fekete et al., 2016), which demonstrate that meteoric water is an essential component in the mineralization process of porphyry systems. Our results support the conclusion of these studies and further demonstrate that meteoric water involvement occurs throughout the magmatic-hydrothermal evolution process, and further emphasises the critical role of meteoric water in metal deposition via cooling magmatic fluids.

Fluid mixing between magmatic fluid and meteoric water also causes a decrease in pH, which will result in an increase in the acidity of alteration assemblages (Cooke and McPhail, 2001). This predicted phenomenon has been observed at Qulong, as well as porphyry deposits elsewhere, which show the progressive evolution of alteration assemblages to more acidic compositions (e.g., from potassic to propylitic to phyllic to advanced argillic alteration assemblages) (Yang et al., 2009; Sillitoe, 2010; Li et al., 2016).

Given the fact that meteoric water mixing is a common phenomenon in porphyry deposits worldwide and it can generate the critical temperature gradient for metal depositions, and can explain the widely documented increase in acidity of alteration assemblages through time, we conclude that the fluid mixing mechanism proposed here is also valid for metals enrichment process in other porphyry deposits.

4.7 Conclusion

Zircon and groundmass quartz from the Rongmucuola pluton have $\delta^{18}O$ values of 6.14 ± 0.05 and 8.70 ± 0.06 ‰ and suggest oxygen fractionation

equilibrium occurred at 680 ± 52 ºC. The best estimate for the $\delta^{18}O$ value for the magmatic fluids associated with the formation of the Qulong porphyry system is 7.56 ± 0.26 ‰.

The absence of any relationship between fractures and SIMS $\delta^{18}O$ values of vein quartz, plus the lack of time and temperature necessary for quartz to reach complete oxygen isotope exchange, and the duration of quartz growth compared with time needed to reach oxygen isotope equilibrium, suggest that the studied samples reached oxygen isotope equilibrium with the fluids and record primary formation oxygen isotopic compositions.

In contrast to the magmatic water value of 7.56 ± 0.26 ‰, for the duration on dated molybdenite mineralization (16.126 – 15.860 Ma) vein quartz yields $\delta^{18}O_f$ values (calculated based on fluid inclusion data at 420 – 280 ºC, Li et al., 2016) between 1.83 ± 0.76 - 7.59 ± 0.47 ‰. The vein quartz $\delta^{18}O_f$ values indicate the involvement of meteoric water during the ore formation process at Qulong. The percentage of meteoric water contribution is ~10 % at 16.126 Ma and progressively increases to ~25 % at 15.860 Ma. With an average mineralization temperature of 350 ± 50 ºC the meteoric water contribution to the porphyry magmatic-hydrothermal system is estimated as 17.58 ± 8.55 %. In addition to the overall increase of meteoric water contribution to the magmatic-hydrothermal system over the duration of porphyry formation, the $\delta^{18}O_f$ data also potentially demonstrates intermittent pulses of magmatic fluid activity during ore formation.

The strong dependence of the solubility of Cu and Mo with temperature, and the lack of evidence to support a mechanism of metal deposition by decompression, boiling, magnetite crystallization and water-rock interaction at Qulong, suggests that cooling via the involvement of meteoric water is a fundamental control of metal

precipitation at Qulong and likely other porphyry systems worldwide (Fekete et al., 2016).

4.8 References

Allan, M.M., Yardley, B.W.D., 2007. Tracking meteoric infiltration into a magmatic-hydrothermal system: A cathodoluminescence, oxygen isotope and trace element study of quartz from Mt. Leyshon, Australia. Chemical Geology 240, 343-360.

Chapter3, Understanding magmatic-hydrothermal evolution of the world class Qulong porphyry Cu-Mo system through high precision U-Pb and Re-Os dating.

Cooke, D.R., Hollings, P., Wilkinson, J.J., Tosdal, R.M., 2014. 13.14 - Geochemistry of Porphyry Deposits, in: Turekian, H.D.H.K. (Ed.), Treatise on Geochemistry (Second Edition). Elsevier, Oxford, pp. 357-381.

Cooke, D.R., McPhail, D.C., 2001. Epithermal Au-Ag-Te mineralization, Acupan, Baguio district, Philippines: Numerical simulations of mineral deposition. Economic Geology and the Bulletin of the Society of Economic Geologists 96, 109-131.

Currie, B.S., Rowley, D.B., Tabor, N.J., 2005. Middle Miocene paleoaltimetry of southern Tibet: Implications for the role of mantle thickening and delamination in the Himalayan orogen. Geology 33, 181-184.

D'Errico, M.E., Lackey, J.S., Surpless, B.E., Loewy, S.L., Wooden, J.L., Barnes, J.D., Strickland, A., Valley, J.W., 2012. A detailed record of shallow hydrothermal fluid flow in the Sierra Nevada magmatic arc from low- 18O skarn garnets. Geology 40, 763-766.

Drummond, S.E., Ohmoto, H., 1985. Chemical Evolution and Mineral Deposition in Boiling Hydrothermal Systems. Economic Geology 80, 126-147.

Farver, J.R., Yund, R.A., 1991. Oxygen Diffusion in Quartz - Dependence on Temperature and Water Fugacity. Chemical Geology 90, 55-70.

Fekete, S., Weis, P., Driesner, T., Bouvier, A.-S., Baumgartner, L., Heinrich, C.A., 2016. Contrasting hydrological processes of meteoric water incursion during magmatic–hydrothermal ore deposition: An oxygen isotope study by ion microprobe. Earth and Planetary Science Letters 451, 263-271.

Friedman, I., Lipman, P.W., Obradovich, J.D., Gleason, J.D., Christiansen, R.L., 1974. Meteoric water in magmas. Science 184, 1069-1072.

Hannah, J.L., Stein, H.J., Wieser, M.E., de Laeter, J.R., Varner, M.D., 2007. Molybdenum isotope variations in molybdenite: Vapor transport and Rayleigh fractionation of Mo. Geology 35, 703-706.

Hedenquist, J.W., Aoki, M., 1991. Meteoric Interaction with Magmatic Discharges in Japan and the Significance for Mineralization. Geology 19, 1041-1044.

Hu, Y.B., Liu, J.Q., Ling, M.X., Ding, W., Liu, Y., Zartman, R.E., Ma, X.F., Liu, D.Y., Zhang, C.C., Sun, S.J., Zhang, L.P., Wu, K., Sun, W.D., 2015. The formation of Qulong adakites and their relationship with porphyry copper deposit: Geochemical constraints. Lithos 220, 60-80.

Johannes, W., 1984. Beginning of melting in the granite system Qz-Or-Ab-An-H_2O. Contributions to Mineralogy and Petrology 86, 264-273.

Jones, R.E., Kirstein, L.A., Kasemann, S.A., Dhuime, B., Elliott, T., Litvak, V.D., Alonso, R., Hinton, R., Facility, E.I.M., 2015. Geodynamic controls on the contamination of Cenozoic arc magmas in the southern Central Andes: Insights from the O and Hf isotopic composition of zircon. Geochimica Et Cosmochimica Acta 164, 386-402.

Kouzmanov, K., Pokrovski, G.S., 2012. Hydrothermal controls on metal distribution in porphyry Cu (-Mo-Au) systems. Special Publication of the Society of Economic Geologists 16, 573–618.

Landtwing, M.R., Pettke, T., Halter, W.E., Heinrich, C.A., Redmond, P.B., Einaudi, M.T., Kunze, K., 2005. Copper deposition during quartz dissolution by cooling magmatic-hydrothermal fluids: The Bingham porphyry. Earth and Planetary Science Letters 235, 229-243.

Li, X.H., Li, W.X., Li, Q.L., Wang, X.C., Liu, Y., Yang, Y.H., 2010. Petrogenesis and tectonic significance of the similar to 850 Ma Gangbian alkaline complex in South China: Evidence from in situ zircon U-Pb dating, Hf-O isotopes and whole-rock geochemistry. Lithos 114, 1-15.

Li, Y., Li, J.-W., Li, X.-H., Selby, D., Huang, G.-H., Chen, L.-J., Zheng, K., 2017. An Early Cretaceous carbonate replacement origin for the Xinqiao stratabound massive sulfide deposit, Middle-Lower Yangtze Metallogenic Belt, China. Ore Geology Reviews 80, 985-1003.

Li, Y., Selby, D., Feely, M., Costanzo, A., Li, X.-H., 2016. Fluid inclusion characteristics and molybdenite Re-Os geochronology of the Qulong porphyry copper-molybdenum deposit, Tibet. Mineralium Deposita.

Matsuhisa, Y., 1974. $^{18}O/^{16}O$ ratios for NBS-28 and some silicate reference samples. Geochem. J 8, 103-107.

Matsuhisa, Y., Goldsmith, J.R., Clayton, R.N., 1979. Oxygen Isotopic Fractionation in the System Quartz-Albite-Anorthite-Water. Geochimica Et Cosmochimica Acta 43, 1131-1140.

Mercer, C.N., Reed, M.H., Mercer, C.M., 2015. Time Scales of Porphyry Cu Deposit Formation: Insights from Titanium Diffusion in Quartz. Economic Geology 110, 587-602.

Monani, S., Valley, J.W., 2001. Oxygen isotope ratios of zircon: magma genesis of low δ18O granites from the British Tertiary Igneous Province, western Scotland. Earth and Planetary Science Letters 184, 377-392.

Pollington, A.D., Kozdon, R., Anovitz, L.M., Georg, R.B., Spicuzza, M.J., Valley, J.W., 2016. Experimental calibration of silicon and oxygen isotope fractionations between quartz and water at 250°C by in situ microanalysis of experimental products and application to zoned low δ30Si quartz overgrowths. Chemical Geology 421, 127-142.

Qin, K.-Z., Xia, D.-X., Li, G.-M., Xiao, B., Duo, J., Jiang, G.-W., Zhao, J.-X., 2014. Qulong Porphyry-Skarn Cu-Mo Deposit, Tibet. Science Press, Beijing.

Redmond, P.B., Einaudi, M.T., Inan, E.E., Landtwing, M.R., Heinrich, C.A., 2004. Copper deposition by fluid cooling in intrusion-centered systems: New insights from the Bingham porphyry ore deposit, Utah. Geology 32, 217-220.

Richards, J.P., 2011. Magmatic to hydrothermal metal fluxes in convergent and collided margins. Ore Geology Reviews 40, 1-26.

Rollinson, H.R., 1993. Using geochemical data: evaluation, presentation, interpretation. Routledge.

Rusk, B., Reed, M., 2002. Scanning electron microscope-cathodoluminescence analysis of quartz reveals complex growth histories in veins from the Butte porphyry copper deposit, Montana. Geology 30, 727-730.

Selby, D., Nesbitt, B.E., Creaser, R.A., Reynolds, P.H., Muehlenbachs, K., 2001. Evidence for a nonmagmatic component in potassic hydrothermal fluids of porphyry Cu-Au-Mo systems, Yukon, Canada. Geochimica Et Cosmochimica Acta 65, 571-587.

Sheets, R.W., Nesbitt, B.E., Muehlenbachs, K., 1996. Meteoric water component in magmatic fluids from porphyry copper mineralization, Babine Lake area, British Columbia. Geology 24, 1091-1094.

Shmulovich, K.I., Landwehr, D., Simon, K., Heinrich, W., 1999. Stable isotope fractionation between liquid and vapour in water-salt systems up to 600 degrees C. Chemical Geology 157, 343-354.

Sillitoe, R.H., 2010. Porphyry Copper Systems. Economic Geology 105, 3-41.

Spencer, E.T., Wilkinson, J.J., Creaser, R.A., Seguel, J., 2015. The Distribution and Timing of Molybdenite Mineralization at the El Teniente Cu-Mo Porphyry Deposit, Chile. Economic Geology 110, 387-421.

Stein, H.J., 2014. 13.4 - Dating and Tracing the History of Ore Formation, in: Turekian, H.D.H.K. (Ed.), Treatise on Geochemistry (Second Edition). Elsevier, Oxford, pp. 87-118.

Stein, H.J., Hannah, J.L., 1985. Movement and Origin of Ore Fluids in Climax-Type Systems. Geology 13, 469-474.

Sun, S.S., Eadington, P.J., 1987. Oxygen Isotope Evidence for the Mixing of Magmatic and Meteoric Waters during Tin Mineralization in the Mole Granite, New-South-Wales, Australia. Economic Geology 82, 43-52.

Sun, W.D., Liang, H.Y., Ling, M.X., Zhan, M.Z., Ding, X., Zhang, H., Yang, X.Y., Li, Y.L., Ireland, T.R., Wei, Q.R., Fan, W.M., 2013. The link between reduced porphyry copper deposits and oxidized magmas. Geochimica Et Cosmochimica Acta 103, 263-275.

Tanner, D., Henley, R.W., Mavrogenes, J.A., Holden, P., 2013. Combining in situ isotopic, trace element and textural analyses of quartz from four magmatic-hydrothermal ore deposits. Contributions to Mineralogy and Petrology 166, 1119-1142.

Trail, D., Bindeman, I.N., Watson, E.B., Schmitt, A.K., 2009. Experimental calibration of oxygen isotope fractionation between quartz and zircon. Geochimica Et Cosmochimica Acta 73, 7110-7126.

Ulrich, T., Günther, D., Heinrich, C.A., 2002. The Evolution of a Porphyry Cu-Au Deposit, Based on LA-ICP-MS Analysis of Fluid Inclusions: Bajo de la Alumbrera, Argentina. Economic Geology 97, 1889-1920.

Valley, J.W., Chiarenzelli, J.R., Mclelland, J.M., 1994. Oxygen-Isotope Geochemistry of Zircon. Earth and Planetary Science Letters 126, 187-206.

Valley, J.W., Graham, C.M., 1996. Ion microprobe analysis of oxygen isotope ratios in quartz from Skye granite: Healed micro-cracks, fluid flow, and hydrothermal exchange. Contributions to Mineralogy and Petrology 124, 225-234.

Vasyukova, O.V., Kamenetsky, V.S., Goemann, K., Davidson, P., 2013. Diversity of primary CL textures in quartz from porphyry environments: implication for origin of quartz eyes. Contributions to Mineralogy and Petrology 166, 1253-1268.

Watanabe, Y., Hedenquist, J., 2001. Mineralogic and stable isotope zonation at the surface over the El Salvador porphyry copper deposit, Chile. Economic Geology and the Bulletin of the Society of Economic Geologists 96, 1775-1797.

Weis, P., Driesner, T., Heinrich, C.A., 2012. Porphyry-copper ore shells form at stable pressure-temperature fronts within dynamic fluid plumes. Science 338, 1613-1616.

Wilkinson, J.J., Stoffell, B., Wilkinson, C.C., Jeffries, T.E., Appold, M.S., 2009. Anomalously metal-rich fluids form hydrothermal ore deposits. Science 323, 764-767.

Williamson, B.J., Herrington, R.J., Morris, A., 2016. Porphyry copper enrichment linked to excess aluminium in plagioclase. Nature Geoscience 9, 237-U169.

Xiao, B., Qin, K.Z., Li, G.M., Li, J.X., Xia, D.X., Chen, L., Zhao, J.X., 2012. Highly Oxidized Magma and Fluid Evolution of Miocene Qulong Giant Porphyry Cu-Mo Deposit, Southern Tibet, China. Resource Geology 62, 4-18.

Yang, Z.-M., Hou, Z.-Q., 2009a. Genesis of Giant Porphyry Cu Deposit at Qulong, Tibet: Constrains from Fluid Inclusions and H-O Isotopes. Acta Geologica Sinica 83, 1838-1859.

Yang, Z.M., Hou, Z.M., 2009b. Genesis of Giant Porphyry Cu Deposit at Qulong, Tibet: Constrains from Fluid Inclusions and H-O Isotopes. Acta Geologica Sinica 83, 1838-1859 (In Chinese with English Abstract).

Yang, Z.M., Hou, Z.Q., White, N.C., Chang, Z.S., Li, Z.Q., Song, Y.C., 2009. Geology of the post-collisional porphyry copper-molybdenum deposit at Qulong, Tibet. Ore Geology Reviews 36, 133-159.

Yang, Z.M., Lu, Y.J., Hou, Z.Q., Chang, Z.S., 2015. High-Mg Diorite from Qulong in Southern Tibet: Implications for the Genesis of Adakite-like Intrusions and Associated Porphyry Cu Deposits in Collisional Orogens. Journal of Petrology 56, 227-253.

Zhao, J., Qin, K., Xiao, B., McInnes, B., Li, G., Evans, N., Cao, M., Li, J., 2016. Thermal history of the giant Qulong Cu–Mo deposit, Gangdese metallogenic belt, Tibet: Constraints on magmatic–hydrothermal evolution and exhumation. Gondwana Research 36, 390-409.

4.9 List of figures

Fig. 4.4. $\delta^{18}O$ plot shows the dynamic interaction between magmatic fluid and meteoric water during ore-forming process at Qulong. The absolute timeframe is determined by Re-Os dates from molybdenite bearing quartz veins. Calculated fluid $\delta^{18}O$ values and meteoric water percentage contribution are given at 420, 350 300 ^{o}C and fluid inclusion estimated formation temperature. The data shows a progressively meteoric water involvement trend with temporal magmatic fluid flooding. See text for discussions.

Fig. 4.5 All analysed quartz $\delta^{18}O$ values in this study infer the contribution of meteoric water during ore-formation. The calculated fluid $\delta^{18}O$ values are based on the average mineralization temperature (350 ^{o}C) at Qulong and porphyry Cu deposits in general. The data suggests the minimum meteoric water contribution in mineralization processes is 13-22 %.

Fig. 4.6. Quartz solubility (silicon concentration) in pure water as a function of temperature at different pressures (A). Concentrations of Cu measured in fluid inclusions as a function of homogenization temperature in Bingham and Morococha porphyry Cu deposits (B). Both figures are modified from Kuzmanovic et al. (2012).

4.10 List of tables

Figure 4.1

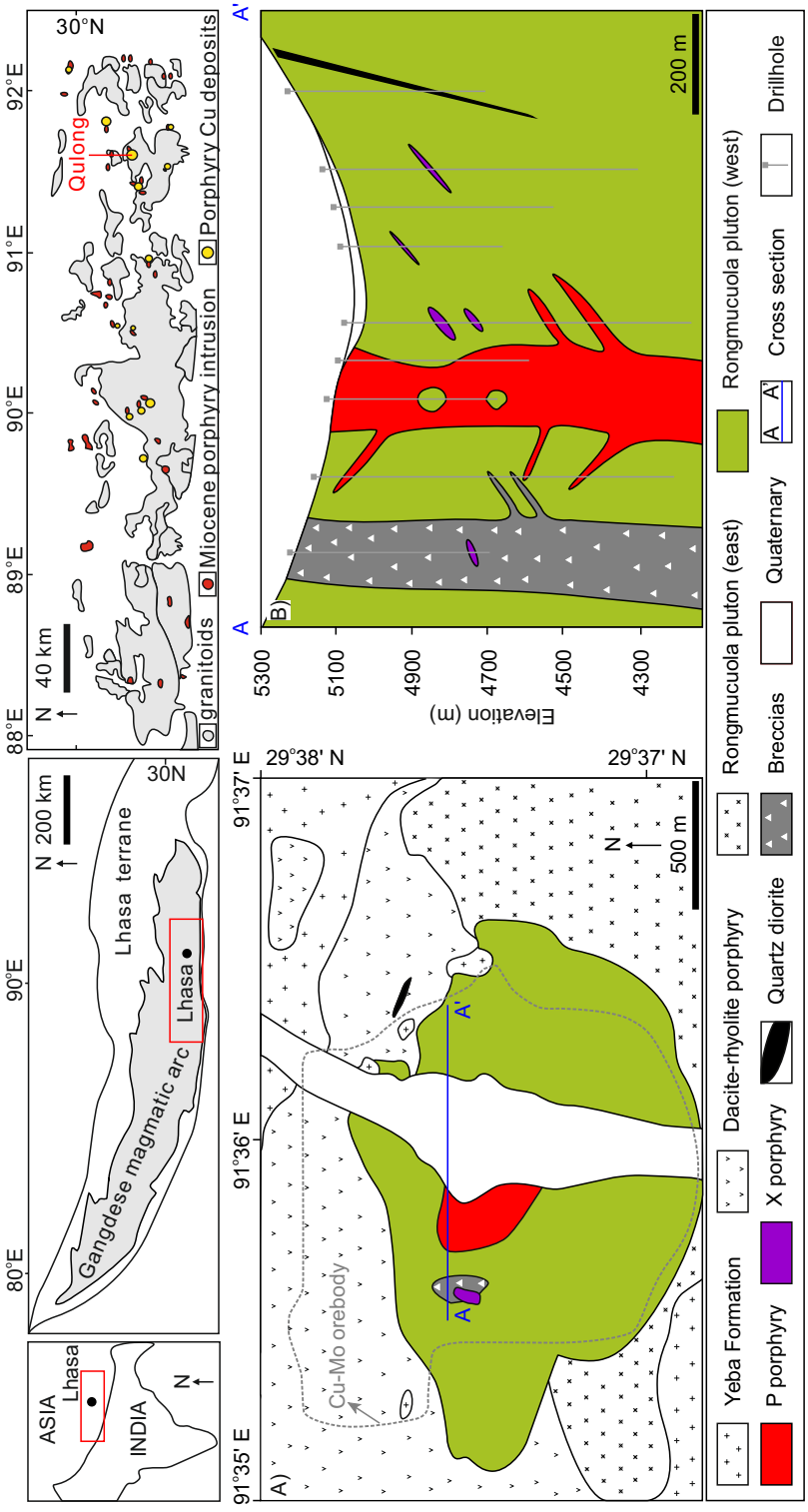
ASIA
Lhasa
INDIA
N
80°E
90°E
N 200 km
30N
Lhasa terrane
Gangdese magmatic arc
Lhasa
88°E
89°E
90°E
91°E
92°E
30°N
N 40 km
Qulong
granitoids
Miocene porphyry intrusion
Porphyry Cu deposits
A)
91°35' E
91°36' E
91°37' E
29°38' N
29°37' N
Cu-Mo orebody
A
A'
N
500 m
B)
A
A'
Elevation (m)
5300
5100
4900
4700
4500
4300
200 m
Yeba Formation
P porphyry
Dacite-rhyolite porphyry
X porphyry
Quartz diorite
Rongmucuola pluton (east)
Breccias
Quaternary
Rongmucuola pluton (west)
Cross section
Drillhole

Figure 4.2

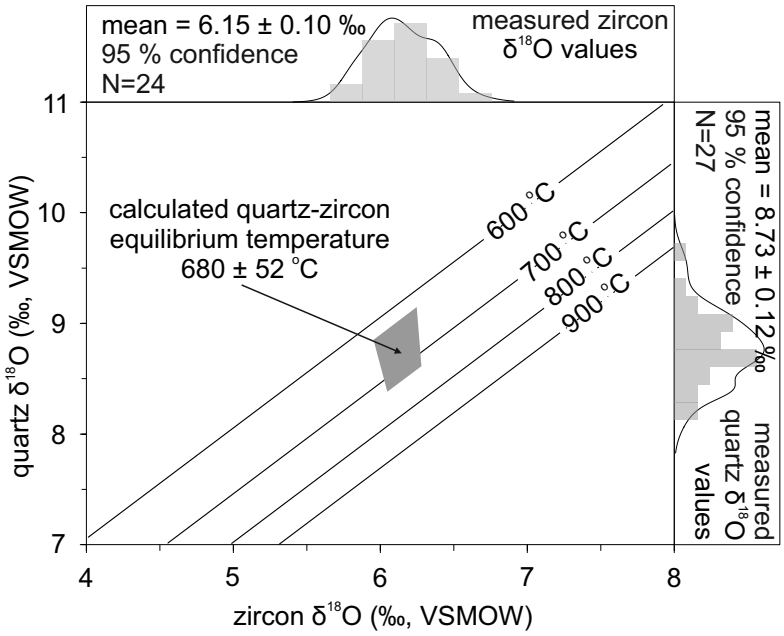
mean = 6.15 ± 0.10 ‰
95 % confidence
N=24
measured zircon
δ18O values
mean = 8.73 ± 0.12 ‰
95 % confidence
N=27
measured
quartz δ18O
values
calculated quartz-zircon
equilibrium temperature
680 ± 52 °C
600 °C
700 °C
800 °C
900 °C
quartz δ18O (‰, VSMOW)
zircon δ18O (‰, VSMOW)
11
10
9
8
7
4
5
6
7
8

Figure 4.3

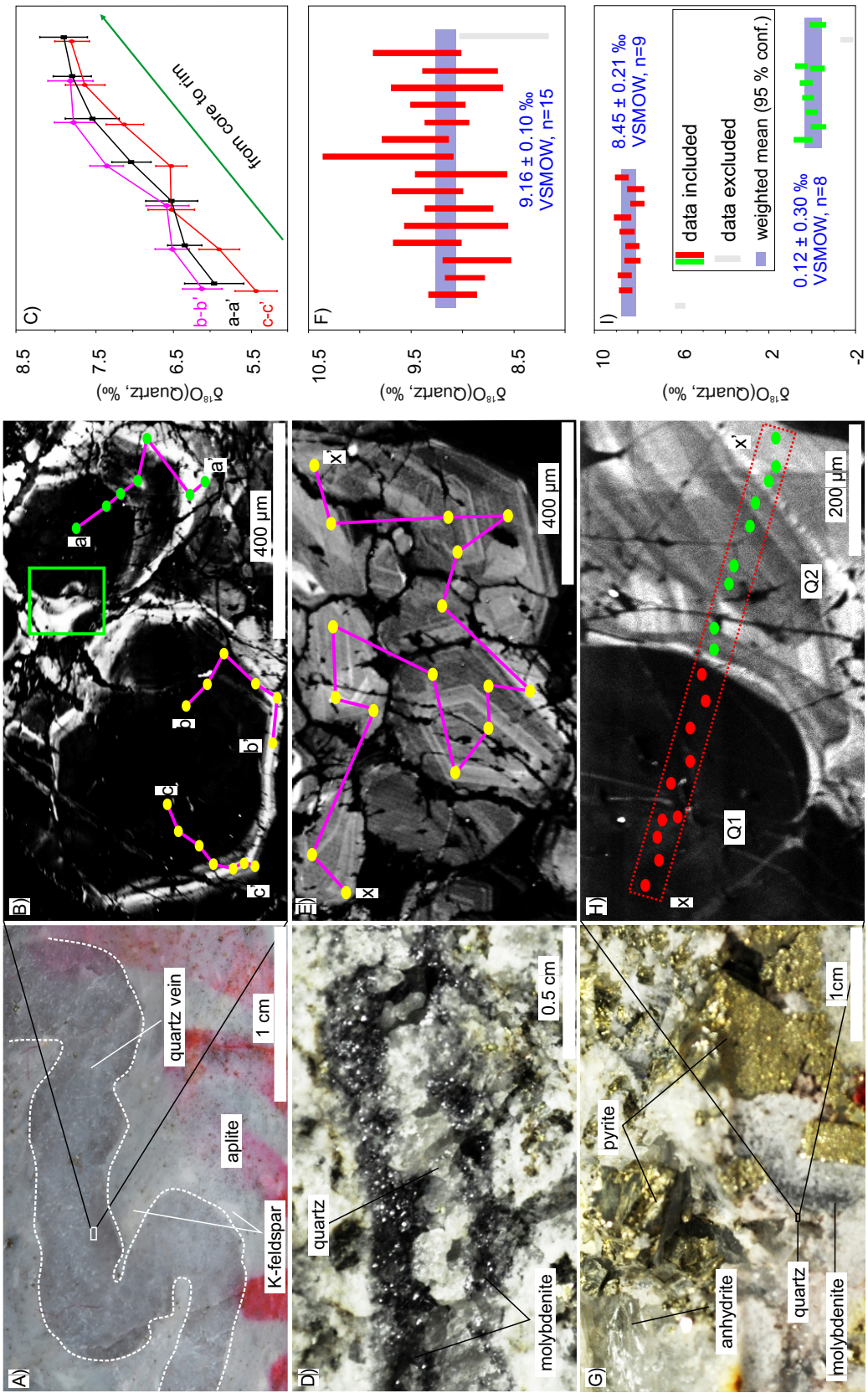
A)
quartz vein
1 cm
aplite
K-feldspar
B)
400 µm
C)
δ18O(Quartz, ‰)
8.5
7.5
6.5
5.5
from core to rim
a-a'
b-b'
c-c'
D)
0.5 cm
quartz
molybdenite
E)
400 µm
F)
δ18O(Quartz, ‰)
10.5
9.5
8.5
9.16 ± 0.10 ‰
VSMOW, n=15
G)
1cm
pyrite
anhydrite
quartz
molybdenite
H)
200 µm
Q1
Q2
I)
δ18O(Quartz, ‰)
10
6
2
-2
8.45 ± 0.21 ‰
VSMOW, n=9
data included
data excluded
weighted mean (95 % conf.)
0.12 ± 0.30 ‰
VSMOW, n=8

Figure 4.4

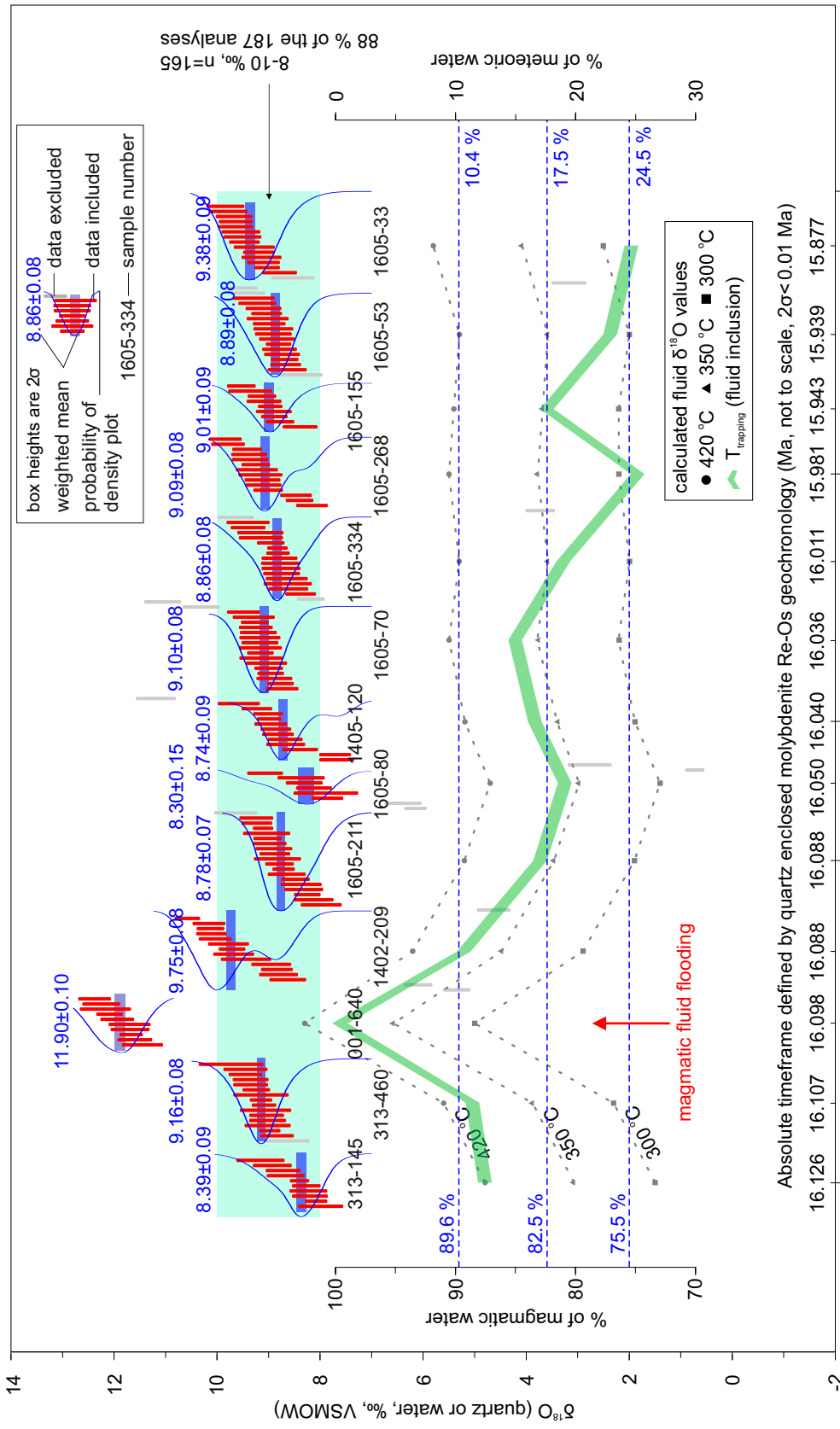

Note, to maximize the visualization of the oxygen isotope data, the horizontal axis is not to scale.

Figure 4.5

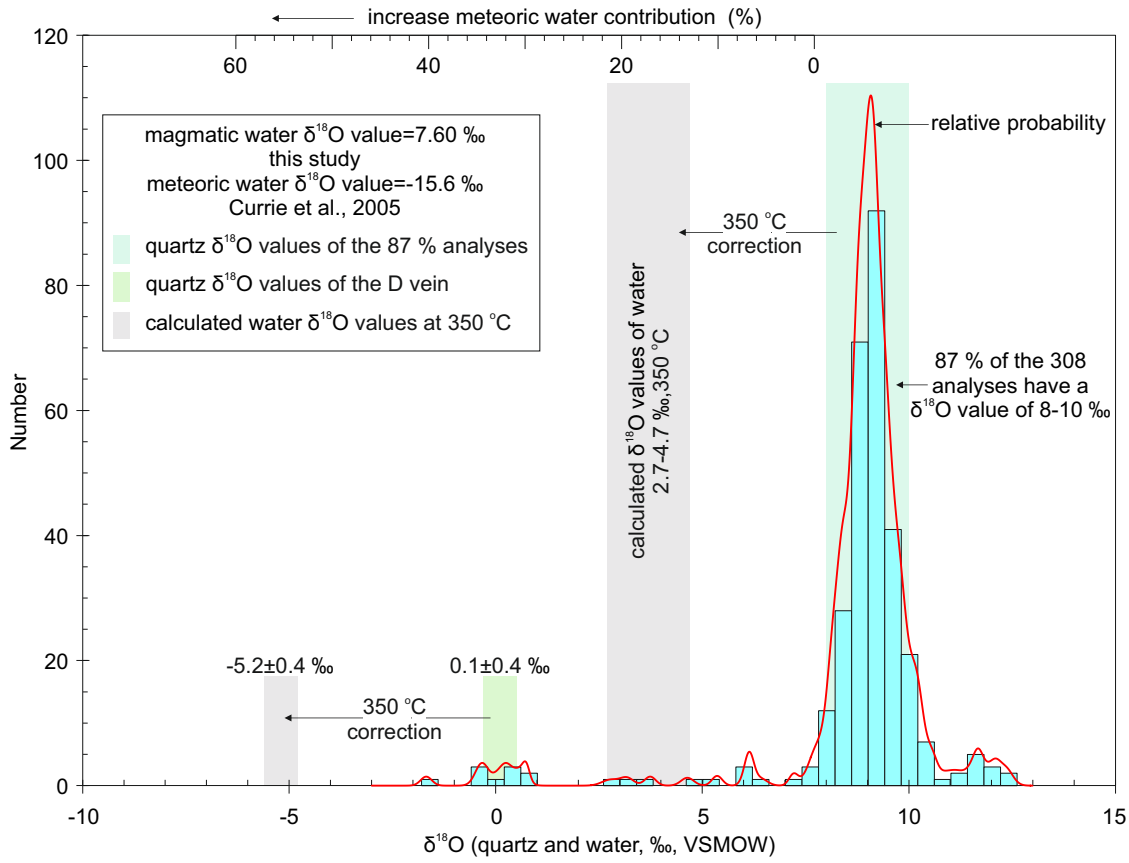
increase meteoric water contribution (%)
60
40
20
0
magmatic water δ18O value=7.60 ‰
this study
meteoric water δ18O value=-15.6 ‰
Currie et al., 2005
quartz δ18O values of the 87 % analyses
quartz δ18O values of the D vein
calculated water δ18O values at 350 °C
relative probability
350 °C
correction
calculated δ18O values of water
2.7-4.7 ‰,350 °C
87 % of the 308
analyses have a
δ18O value of 8-10 ‰
-5.2±0.4 ‰
0.1±0.4 ‰
350 °C
correction
Number
120
100
80
60
40
20
0
-10
-5
0
5
10
15
δ18O (quartz and water, ‰, VSMOW)

Figure 4.6

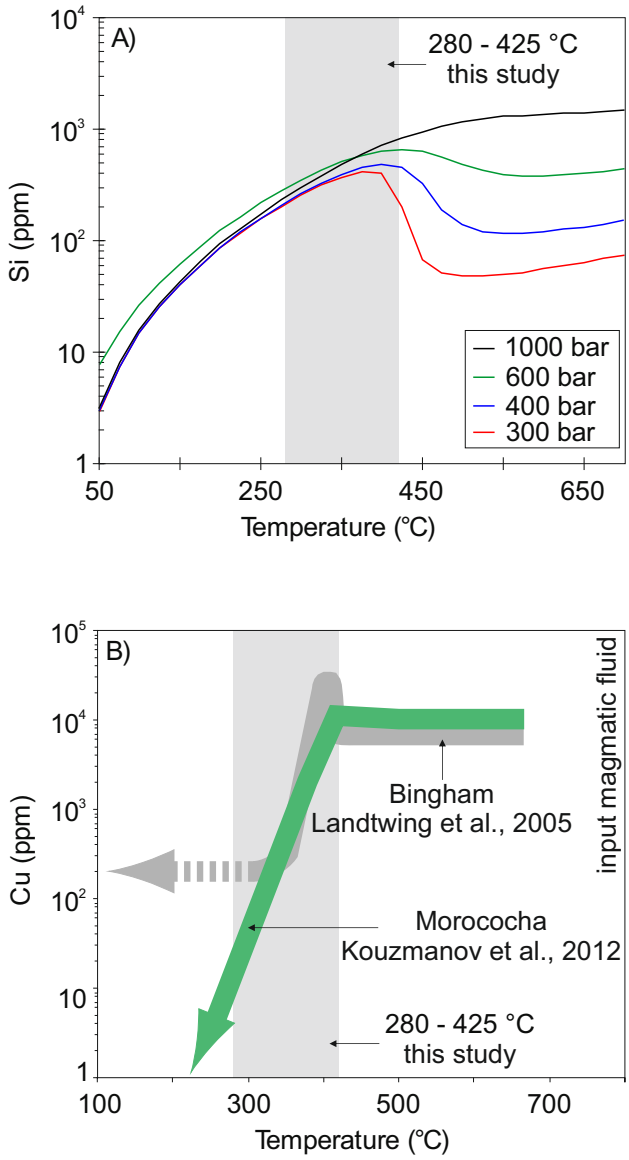
A)
280 - 425 °C
this study
Si (ppm)
1000 bar
600 bar
400 bar
300 bar
Temperature (°C)
B)
input magmatic fluid
Bingham
Landtwing et al., 2005
Morococha
Kouzmanov et al., 2012
280 - 425 °C
this study
Cu (ppm)
Temperature (°C)

Table 4.1 SIMS δ18O values of zircon and groundmass quartz of the Rongmucuola pluton

Sample NO.	$\delta^{18}O$	2σ	Weighte mean (2 sigma)	
Zircon sample				
QL14_23W@1	6.43	0.19		
QL14_23W@2	6.00	0.18		
QL14_23W@3	5.82	0.16		
QL14_23W@5	5.92	0.28	QL14_23W	
QL14_23W@6	6.44	0.21	Mean = 6.15±0.07 2σ.	
QL14_23W@7	6.37	0.17	Wtd by data-pt errs only, 0 of 11 rej.	
QL14_23W@8	5.80	0.26	MSWD = 5.4, probability = 0.000	
QL14_23W@9	6.10	0.26		
QL14_23W@10	6.28	0.25		
QL14_23W@11	6.16	0.32		
QL14_23W@12	6.19	0.29		QL14_23W + QL14_52E
QL14_52E@1	6.17	0.26		
QL14_52E@2	5.99	0.21		Mean = 6.14±0.05 2σ.
QL14_52E@3	6.12	0.22		Wtd by data-pt errs only, 1 of 24 rej.
QL14_52E@4	6.01	0.32		MSWD = 3.3, probability = 0.000
QL14_52E@5	5.99	0.27		
QL14_52E@6	~~6.55~~	~~0.29~~	QL14_52E	
QL14_52E@7	6.01	0.29	Mean = 6.13±0.08 2σ.	
QL14_52E@10	6.18	0.25	Wtd by data-pt errs only, 1 of 13 rej.	
QL14_52E@11	6.21	0.32	MSWD = 1.8, probability = 0.048	
QL14_52E@12	5.94	0.42		
QL14_52E@13	6.50	0.45		
QL14_52E@14	6.13	0.23		
QL14_52E@15	6.38	0.22		
quartz sample				
QL14_23W@1	8.49	0.36		

QL14_23W@3	9.12	0.22
QL14_23W@4	8.95	0.29
QL14_23W@5	8.45	0.29
QL14_23W@8	9.05	0.33
~~QL14_23W@9~~	~~9.99~~	~~0.22~~
QL14_23W@10	8.74	0.25
QL14_23W@11	8.87	0.3
QL14_23W@12	9.38	0.46
QL14_23W@13	8.79	0.3
QL14_23W@14	9.56	0.31
QL14_23W@15	8.4	0.16
QL14_23W@16	8.16	0.36
QL14_52E@2	8.69	0.21
QL14_52E@3	8.6	0.35
QL14_52E@4	8.96	0.31
QL14_52E@5	8.97	0.35
~~QL14_52E@7~~	~~7.03~~	~~0.27~~
QL14_52E@10	8.91	0.32
QL14_52E@11	8.59	0.35
QL14_52E@12	8.7	0.5
QL14_52E@13	9.21	0.39
~~QL14_52E@15~~	~~9.68~~	~~0.22~~
QL14_52E@16	8.93	0.28
QL14_52E@17	8.71	0.32
QL14_52E@18	8.6	0.29
QL14_52E@19	8.73	0.29
QL14_52E@20	8.38	0.22
QL14_52E@21	8.26	0.31
QL14_52E@22	8.81	0.35

QL14_23W
Mean = 8.76±0.08 2σ.
Wtd by data-pt errs only, 1 of 13 rej.
MSWD = 8.0, probability = 0.000

QL14_52E
Mean = 8.70±0.08 2σ.
Wtd by data-pt errs only, 2 of 17 rej.
MSWD = 2.5, probability = 0.002

QL14_23W + QL14_52E

Mean = 8.70±0.06 2σ.
Wtd by data-pt errs only, 4 of 30 rej.
MSWD = 4.8, probability = 0.000

QL14_23W and QL14_52E are fresh samples from the west and east of the Rongmucuola pluton, respectively.

Table 4.2 SIMS $\delta^{18}O$ values of hydrothermal quartz from Qulong

Sample No.	$\delta^{18}O$	2σ
Sinusoidal like quartz vein		
Section A		
817-290@A1	6.11	0.26
817-290@A2	6.49	0.22
817-290@A3	6.55	0.28
817-290@A4	7.33	0.22
817-290@A5	7.75	0.27
817-290@A6	7.80	0.29
Section B		
817-290@B1	5.95	0.38
817-290@B2	6.33	0.22
817-290@B3	6.50	0.33
817-290@B4	7.01	0.25
817-290@B5	7.52	0.35
817-290@B6	7.78	0.24
817-290@B7	7.89	0.31
Section C		
817-290@C1	5.40	0.27
817-290@C2	5.88	0.26
817-290@C3	6.49	0.30
817-290@C4	6.50	0.20
817-290@C5	7.10	0.24
817-290@C6	7.61	0.26
817-290@C7	7.78	0.22
Sample No.	$\delta^{18}O$	2σ
313-145@1	8.09	0.20
313-145@2	8.41	0.17
313-145@3	8.73	0.32
313-145@4	8.00	0.42
313-145@5	8.28	0.26
313-145@6	8.21	0.33
313-145@7	8.94	0.36
313-145@8	9.17	0.45
313-145@9	8.24	0.35
313-145@10	8.68	0.35
313-460@1	9.10	0.22
313-460@2	8.99	0.19
313-460@3	8.85	0.31
313-460@4	9.36	0.32
313-460@5	9.07	0.48
313-460@6	9.05	0.32
313-460@7	9.36	0.33
313-460@8	9.03	0.43
313-460@9	9.74	0.61

313-460@10	9.46	0.31
313-460@11	9.16	0.20
313-460@12	9.25	0.25
313-460@13	9.16	0.52
313-460@14	9.03	0.34
313-460@15	9.46	0.41
~~313-460@16~~	~~8.64~~	~~0.41~~
001-640@1	12.10	0.24
001-640@2	12.26	0.35
001-640@3	11.46	0.38
001-640@4	11.68	0.21
001-640@5	11.71	0.39
001-640@6	12.39	0.30
001-640@7	12.18	0.48
001-640@8	11.61	0.32
001-640@9	11.95	0.31
001-640@10	11.70	0.36
1402-209@1	10.17	0.30
1402-209@2	10.59	0.23
1402-209@3	9.79	0.38
1402-209@4	9.69	0.38
1402-209@5	9.72	0.24
~~1402-209@6~~	~~5.36~~	~~0.25~~
~~1402-209@7~~	~~6.11~~	~~0.26~~
1402-209@8	10.14	0.25
1402-209@9	10.12	0.28
1402-209@10	9.45	0.47
1402-209@11	10.05	0.30
1402-209@12	8.82	0.36
1402-209@13	8.64	0.34
1402-209@14	8.96	0.37
1402-209@15	8.85	0.29
~~1605-211@1~~	~~4.64~~	~~0.31~~
1605-211@2	8.26	0.24
1605-211@20	9.05	0.44
1605-211@3	8.33	0.36
1605-211@4	8.99	0.31
1605-211@5	8.84	0.44
1605-211@6	9.12	0.18
1605-211@7	9.24	0.28
1605-211@8	9.03	0.26
1605-211@9	9.25	0.31
1605-211@10	8.72	0.20
1605-211@11	8.49	0.26
1605-211@12	8.89	0.28
1605-211@13	7.99	0.38
~~1605-211@14~~	~~9.65~~	~~0.40~~

1605-211@15	8.91	0.34
1605-211@16	8.80	0.26
1605-211@17	8.14	0.37
1605-211@18	8.66	0.35
1605-211@19	8.38	0.38
1605-80@1	9.08	0.33
1605-80@2	7.87	0.29
1605-80@3	8.32	0.34
~~1605-80@4~~	~~6.16~~	~~0.20~~
1605-80@5	7.90	0.61
1605-80@6	8.13	0.33
~~1605-80@7~~	~~6.40~~	~~0.34~~
1605-80@8	8.38	0.44
1405-120@1	8.69	0.32
1405-120@2	8.40	0.33
1405-120@3	8.97	0.30
1405-120@4	8.87	0.28
1405-120@5	9.02	0.27
1405-120@6	8.68	0.36
1405-120@7	8.83	0.29
1405-120@8	9.00	0.22
1405-120@9	9.59	0.39
~~1405-120@10~~	~~0.74~~	~~0.17~~
~~1405-120@11~~	~~2.78~~	~~0.41~~
~~1405-120@12~~	~~11.20~~	~~0.37~~
1405-120@13	7.69	0.32
1405-120@14	7.72	0.29
1405-120@15	9.24	0.28
1605-70@1	9.26	0.31
1605-70@2	9.28	0.25
1605-70@3	8.97	0.24
1605-70@4	9.50	0.30
1605-70@5	9.01	0.26
1605-70@6	8.75	0.30
1605-70@7	8.90	0.33
1605-70@8	9.21	0.34
1605-70@9	9.16	0.40
1605-70@10	9.05	0.38
1605-70@11	9.18	0.34
1605-70@12	9.18	0.38
1605-70@13	9.17	0.24
~~1605-70@14~~	~~10.32~~	~~0.34~~
~~1605-70@15~~	~~11.07~~	~~0.34~~
1605-70@16	8.78	0.24
1605-70@17	9.17	0.40
1605-70@18	9.30	0.39
1605-334@1	8.76	0.34

1605-334@2	9.17	0.43
1605-334@3	8.84	0.18
1605-334@4	8.64	0.45
1605-334@5	9.41	0.32
1605-334@6	9.16	0.41
1605-334@7	8.63	0.37
1605-334@8	9.41	0.40
~~1605-334@9~~	~~9.65~~	~~0.34~~
~~1605-334@10~~	~~8.19~~	~~0.25~~
1605-334@11	8.66	0.39
1605-334@12	8.97	0.25
1605-334@13	8.78	0.36
1605-334@14	8.39	0.28
1605-334@15	8.80	0.33
1605-334@16	8.77	0.36
1605-334@17	8.83	0.21
~~1605-268@1~~	~~3.74~~	~~0.27~~
1605-268@2	9.26	0.26
1605-268@3	9.17	0.41
1605-268@4	9.13	0.33
1605-268@5	9.80	0.31
1605-268@6	8.48	0.29
1605-268@7	9.37	0.34
1605-268@8	9.43	0.27
1605-268@9	9.39	0.33
1605-268@10	9.11	0.33
1605-268@11	9.02	0.27
1605-268@12	9.85	0.30
1605-268@13	9.24	0.39
1605-268@14	8.17	0.29
1605-268@15	8.41	0.25
1605-155@1	9.37	0.41
1605-155@2	8.91	0.33
1605-155@3	8.98	0.22
1605-155@4	9.14	0.26
1605-155@5	9.54	0.26
1605-155@6	9.10	0.32
1605-155@7	8.79	0.26
1605-155@8	8.40	0.32
1605-155@9	8.90	0.24
~~1605-53@1~~	~~9.41~~	~~0.31~~
~~1605-53@2~~	~~8.39~~	~~0.41~~
1605-53@3	8.68	0.28
1605-53@4	8.92	0.34
1605-53@5	8.82	0.23
1605-53@6	8.92	0.37
1605-53@7	9.23	0.35

1605-53@8	9.05	0.28
1605-53@9	9.30	0.39
1605-53@10	8.70	0.25
1605-53@12	9.11	0.33
1605-53@13	9.03	0.39
1605-53@14	8.80	0.32
1605-53@15	8.75	0.33
1605-53@16	8.65	0.36
1605-53@17	8.85	0.33
~~1605-53@18~~	~~9.51~~	~~0.27~~
1605-53@19	9.00	0.30
1605-33@1	9.15	0.37
1605-33@2	9.20	0.29
1605-33@3	9.29	0.38
1605-33@4	9.52	0.35
1605-33@5	9.11	0.30
~~1605-33@6~~	~~3.18~~	~~0.32~~
1605-33@7	9.79	0.35
1605-33@8	9.68	0.34
~~1605-33@9~~	~~8.54~~	~~0.40~~
1605-33@10	9.55	0.36
1605-33@11	9.04	0.23
1605-33@12	9.65	0.32
1605-33@13	9.85	0.35
1605-33@14	9.48	0.28
1605-33@15	8.80	0.32
1605-33@16	9.65	0.31
313-72@1	9.84	0.40
313-72@2	9.88	0.31
313-72@3	9.56	0.32
313-72@4	9.81	0.24
313-72@5	9.98	0.37
313-72@6	9.70	0.33
313-72@7	9.53	0.34
313-72@8	10.28	0.20
313-72@9	10.17	0.29
313-72@10	10.12	0.30
313-72@11	10.32	0.26
313-72@12	10.06	0.39
313-72@13	9.92	0.25
313-496@1	10.17	0.33
313-496@2	9.67	0.36
313-496@3	9.20	0.46
313-496@4	9.19	0.27
313-496@5	9.73	0.27
313-496@6	9.00	0.26
313-496@7	9.12	0.33

313-496@8	9.11	0.36
313-496@9	9.21	0.24
313-496@10	8.88	0.35
313-496@11	9.78	0.28
313-496@12	9.51	0.32
313-496@13	9.98	0.35
313-496@14	10.17	0.21
313-465@1	8.32	0.30
313-465@2	8.64	0.30
313-465@3	8.31	0.35
313-465@4	8.71	0.22
313-465@5	8.79	0.36
313-465@6	9.20	0.22
313-465@7	9.84	0.42
313-465@8	9.19	0.28
~~313-465@9~~	~~10.48~~	~~0.29~~
313-465@10	9.30	0.26
313-465@11	9.10	0.21
313-465@12	9.31	0.38
313-465@13	8.51	0.25
313-465@14	9.51	0.25
~~313-465@15~~	~~10.52~~	~~0.37~~
~~313-465@16~~	~~10.84~~	~~0.30~~
1605-194@1	9.09	0.38
~~1605-194@2~~	~~7.21~~	~~0.22~~
~~1605-194@3~~	~~7.60~~	~~0.39~~
1605-194@8	9.20	0.50
1605-194@9	8.38	0.38
1605-194@10	8.06	0.46
1605-194@12	9.38	0.34
1605-194@13	8.83	0.32
1405-1-120@1	9.37	0.23
1405-1-120@2	9.22	0.25
1405-1-120@3	9.38	0.35
1405-1-120@4	9.26	0.36
1405-1-120@5	9.31	0.44
1405-1-120@6	9.54	0.26
1405-1-120@7	9.48	0.21
1405-1-120@8	9.64	0.33
~~1405-1-120@9~~	~~10.44~~	~~0.32~~
1405-1-120@10	9.63	0.35
1405-1-120@11	9.75	0.49
1405-1-120@12	9.51	0.30
1405-1-120@13	8.90	0.21
1405-1-120@15	9.07	0.48
1605-209@1	8.71	0.25
1605-209@2	8.41	0.26

1605-209@21	8.66	0.28
1605-209@3	8.65	0.37
1605-209@4	8.29	0.34
1605-209@5	8.37	0.31
1605-209@6	8.40	0.24
1605-209@7	9.14	0.27
1605-209@8	9.09	0.28
1605-209@9	8.78	0.29
1605-209@10	9.11	0.25
1605-209@11	8.80	0.29
1605-209@12	9.42	0.16
1605-209@13	9.09	0.26
1605-209@14	9.27	0.53
1605-209@15	9.05	0.25
1605-209@16	8.96	0.35
1605-209@17	9.06	0.29
1605-209@18	9.24	0.46
1605-209@19	8.67	0.27
1605-209@20	8.75	0.27
1605-480@1	9.98	0.29
1605-480@2	9.69	0.41
1605-480@3	9.04	0.27
1605-480@4	9.23	0.34
1605-480@5	9.12	0.32
1605-480@6	9.28	0.29
1605-480@7	8.70	0.44
1605-480@8	9.34	0.28
1605-480@9	8.82	0.25
1605-480@10	9.81	0.26
1605-480@11	9.60	0.45
1605-480@12	9.33	0.30
1605-480@13	9.13	0.27
1605-480@14	9.04	0.36
1605-480@15	8.69	0.27
1605-480@16	9.04	0.21
1602-81@1	8.61	0.27
1602-81@2	8.63	0.29
1602-81@3	8.27	0.32
1602-81@4	8.28	0.28
1602-81@5	8.52	0.31
~~1602-81@6~~	~~6.11~~	~~0.22~~
1602-81@7	8.76	0.36
1602-81@8	8.05	0.28
1602-81@9	8.12	0.36
1602-81@10	8.79	0.29
1602-81@11	0.54	0.40
1602-81@12	-0.32	0.32

1602-81@13	0.05	0.26
1602-81@14	0.22	0.24
1602-81@15	0.33	0.27
1602-81@16	-0.34	0.30
1602-81@17	0.60	0.27
~~1602-81@18~~	~~-1.68~~	~~0.27~~
1602-81@19	-0.32	0.35

Table 4.3 Weighted mean of SIMS quartz $\delta^{18}O$ values of mineralized quartz at Qulong

Sample	Age	2σ	$\delta^{18}O$	2σ	Temperature
Thirteen mineralizaed quartz veins with Re-Os ages					
313-145	16.126	0.008	8.39	0.09	425˚C
313-460	16.107	0.015	9.16	0.08	398 ˚C
001-640	16.098	0.013	11.90	0.10	390 ˚C
1402-209	16.088	0.007	9.75	0.08	380 ˚C
1605-211	16.088	0.007	8.78	0.07	360 ˚C
1605-80	16.050	0.005	8.30	0.15	360 ˚C
1405-120	16.040	0.007	8.74	0.09	365 ˚C
1605-70	16.036	0.012	9.10	0.08	365 ˚C
1605-334	16.011	0.015	8.86	0.08	340 ˚C
1605-268	15.981	0.007	9.09	0.08	290 ˚C
1605-155	15.943	0.007	9.01	0.09	345 ˚C
1605-53	15.939	0.006	8.90	0.08	310 ˚C
1605-33	15.860	0.010	9.38	0.09	285 ˚C

Additional 7 mineralized quartz veins without Re-Os ages

Sample	$\delta^{18}O$	2σ
313-72	9.98	0.08
313-496	9.52	0.08
1405-1-120	9.43	0.09
1605-480	9.17	0.08
313-465	8.98	0.08
1605-209	8.89	0.06
1605-194	8.86	0.06
1602-81	8.45	0.10
1602-81	0.12	0.10

Table 4.4 Calculated fluid $\delta^{18}O$ and meteoric water contribution

ample numb	$\delta^{18}O$quartz		Formation T		fluid $\delta^{18}O$ with formation T		meteoric %		fluid $\delta^{18}O$ and meteoric % with estimated T					
	value	2σ	value	2σ	value	2σ	value	2σ	420°C		350°C		300°C	
313-145	8.39	0.09	425	20	4.83	0.41	12.08	2.93	4.7	12.1%	3.1	19.3%	1.5	26.0%
313-460	9.16	0.08	398	20	5.04	0.45	11.15	2.95	5.5	8.8%	3.9	15.9%	2.3	22.7%
001-640	11.90	0.10	390	20	7.59	0.47	-0.15	2.42	8.3	-3.0%	6.6	4.1%	5.0	10.9%
1402-290	9.75	0.08	380	20	5.21	0.49	10.40	3.00	6.1	6.3%	4.5	13.4%	2.9	20.2%
1605-211	8.78	0.07	360	20	3.73	0.54	16.96	3.88	5.1	10.5%	3.5	17.6%	1.9	24.3%
1605-80	8.30	0.15	360	20	3.25	0.55	19.09	4.17	4.7	12.5%	3.0	19.7%	1.4	26.4%
1405-120	8.74	0.09	365	20	3.82	0.53	16.56	3.80	5.1	10.6%	3.4	17.8%	1.9	24.5%
1605-70	9.10	0.08	365	20	4.18	0.52	14.96	3.58	5.5	9.1%	3.8	16.2%	2.2	23.0%
1605-334	8.86	0.08	340	20	3.26	0.59	19.04	4.28	5.2	10.1%	3.6	17.2%	2.0	24.0%
1605-268	9.09	0.08	290	20	1.83	0.76	25.38	5.55	5.4	9.1%	3.8	16.2%	2.2	23.0%
1605-155	9.01	0.09	345	20	3.55	0.58	17.76	4.09	5.4	9.5%	3.7	16.6%	2.2	23.3%
1605-53	8.89	0.08	310	20	2.34	0.69	23.12	5.07	5.2	10.0%	3.6	17.1%	2.0	23.9%
1605-33	9.38	0.09	280	20	1.93	0.78	24.93	5.55	5.7	7.9%	4.1	15.0%	2.5	21.7%

Chapter 5

Conclusions and outlook

Chapter 5 Conclusions and outlook

This PhD thesis addresses the magmatic and mineralization history of the Qulong porphyry Cu-Mo system by applying state-of-the-art high precision geochronology (molybdenite Re-Os and zircon U-Pb) and high spatial resolution SIMS quartz oxygen isotope geology, based on detailed petrographic study and fluid inclusion microthermetry. As this thesis was written as a series of papers each chapter has its own specific conclusion section. This concluding chapter briefly draws together the key aspects of each chapter and then suggests possible directions for future research.

5.1 Nature of ore-forming fluid of the Qulong Cu-Mo deposit

Chapter 2 discusses fluid inclusion and U-Pb zircon geochronology of the aplite phase of the Qulong porphyry. The U-Pb study showed that the aplite contained purely Jurassic aged zircons. These zircon possess a low oxygen isotopic composition (4.85 ± 0.23 ‰), and sieve textures and mineral inclusions (quartz, feldspar and fluorapatite), which are interpreted to indicate that the aplite potentially represents a remelt of the Jurassic rocks with involvement of meteoric water.

A fluid inclusion study indicates that the ore-forming fluid contains Na, K, Ca, Fe, Cu and Mo, along with Cl and S. Fluorine is also an essential component as demonstrated by the presence of fluorapatite in zircon grains, as well as the dissolution textures of K-feldspar from the potassic stage and quartz phenocrysts in the P porphyry. Fluid inclusion study confirms the magmatic-hydrothermal transition occurred at ~425 ^{o}C under lithostatic pressure, while potassic, propylitic and phyllic alteration occurred at hydrostatic pressure with temperature progressively decreasing from 425 to 280 ^{o}C. The fluid inclusion data presented here suggest the Qulong porphyry system was formed at a paleo depth of ~2.7 km. This implies that ~2.3 km of erosion has occurred

at Qulong after its formation, which may be related with regional uplift of the Lhasa terrane.

5.2 Timescale and cooling history of Qulong porphyry system

Chapter 3 discusses the timescale and cooling history of Qulong porphyry system. The emplacement ages of the Rongmucuola pluton, the P porphyry and the quartz diorite at Qulong have been refined to 17.142 ± 0.014/0.014/0.023, 16.009 ± 0.016/0.017/0.024 and 15.166 ± 0.016/0.017/0.024 Ma. The mineralization lifetime, defined by Re-Os molybdenite geochronology, of the Qulong porphyry Cu-Mo deposit is 266 ±13 kyrs. The Re-Os dates indicate multiple short-lived mineralization cycles which have a duration of tens of kyrs, which are comparable with those recently proposed through high-precision dating (Buret et al., 2016; Tapster et al., 2016), titanium diffusion in quartz (Mercer et al., 2015) and numerical modeling (Weis et al., 2012).

Existing Re-Os dates have appreciable uncertainties of 1.3 - 12.1 %, which is predominately due to the analytical challenges during the early stages of Re-Os studies, e.g., imprecise determinations of the stoichiometry of Os salts used for calibration of spikes (Yin et al., 2001), and ICP-MS analysis (Stein, 2014). The uncertainties (3.8-13.8 %) for the *in-situ* zircon dates come from analytical issues, e.g., U and Pb fractionation, matrix effects, common lead, standard heterogeneity, data reduction and sample problems, e.g., lead loss, inheritance. As a result this study supports the issues of over interpreting low precision data as previous discussed (Von Quadt et al. (2011); Schaltegger et al. (2015). This study reiterates that high precision geochronology is necessary for resolving the magmatic timescale of young porphyry deposits, such as Qulong.

Correlating the Re-Os dates and fluid inclusion data (Li et al., 2016) suggests that the entire hydrothermal system cooled from 425 to 280 °C with a cooling rate of 0.55 ± 0.11 °C/kyr and much faster cooling rates (~1.2 °C/kyr) for the individual pulses. These cooling rates are much faster than that established from thermochronology (0.2 °C/kyr maximum) (Zhao et al., 2016), and potentially illustrates the problem of the simplified cooling model used in thermochronology, which does not account for the thermal input associated with fluid fluxing (Weis et al., 2012).

Integrating U-Pb and Re-Os data need to consider the systematic uncertainties from spike calibration and decay constants which are a magnitude larger than the analytical uncertainties (Chiaradia et al., 2013; Schoene et al., 2013; Schoene, 2014) and as a result lose the necessary resolution to further understand the detailed magmatic-hydrothermal processes associated with porphyry systems.

5.3 Meteoric water involvement triggered metal deposition at Qulong

Chapter 4 discusses the evidence of meteoric water involvement and role in triggering metal deposition at Qulong. Zircon and groundmass quartz oxygen isotope analysis of the Rongmucuola pluton suggests oxygen isotope equilibrium occurred at 680 ± 52 °C. The groundmass quartz provides the best estimate for the $\delta^{18}O$ value for the magmatic fluids associated with the formation of the Qulong porphyry system as 7.56 ± 0.26 ‰.

The absence of any relationship between fractures and SIMS $\delta^{18}O$ values of vein quartz, plus the lack of time and temperature necessary for quartz to reach complete oxygen isotope exchange, and the duration of quartz growth compared with the time needed to reach oxygen isotope equilibrium, suggest that the studied samples

reached oxygen isotope equilibrium with the fluids and record primary formation oxygen isotopic compositions.

In contrast to the magmatic water value of 7.56 ± 0.26 ‰, for the duration of dated molybdenite mineralization (16.126 – 15.860 Ma), vein quartz yields $\delta^{18}O_f$ values (calculated based on fluid inclusion data at 420 – 280 °C) between 1.83 ± 0.76 - 7.59 ± 0.47 ‰. The vein quartz $\delta^{18}O_f$ values indicate the involvement of meteoric water during the ore formation process at Qulong. The percentage of meteoric water contribution is ~10 % at 16.126 Ma and progressively increases to ~25 % at 15.860 Ma. With an average mineralization temperature of 350 ± 50 °C the meteoric water contribution to the porphyry magmatic-hydrothermal system is estimated as 17.58 ± 8.55 %. In addition to the overall increase of meteoric water contribution to the magmatic-hydrothermal system over the duration of porphyry formation, the $\delta^{18}O_f$ data also potentially demonstrates intermittent pulses of magmatic fluid activity during ore formation (Fekete et al., 2016).

The strong dependence of the solubility of Cu and Mo with temperature (Kouzmanov and Pokrovski, 2012), and the lack of evidence to support a mechanism of metal deposition by decompression, boiling, magnetite crystallization and water-rock interaction at Qulong, suggests that cooling via the involvement of meteoric water is a fundamental control of metal precipitation at Qulong and likely other porphyry systems worldwide (Selby et al., 2001; Fekete et al., 2016).

5.4 Outlook

The fluid inclusion study constrains the paleo-depth of Qulong as ~2.7 km and indicates a ~2.3 km erosion after the formation of Qulong (Li et al., 2016). This erosion has been supported by the absence of volcanic rocks at the top of Qulong porphyry

system, which is typical for porphyry systems formed in extensional settings (Sillitoe, 2010). Interestingly, it is generally accepted that the Lhasa terrane experienced no or limited uplift and erosion since the Miocene (Currie et al., 2005; Rowley and Currie, 2006). The exact reason for this discrepancy is unknown and needs further study. Given the importance to understand the uplifting history of Lhasa terrane, e.g., Tibet uplift and its climate impact (Raymo and Ruddiman, 1992; Zhisheng et al., 2001), exposure and preservation of porphyry Cu systems (Richards, 2015), more detailed and robust control for the uplift and erosion history of the Lhasa terrane should be conducted. In addition, this study highlights the involvement of fluorine in ore-forming fluid, and potentially is very important for the alteration and mineralization processes (McPhie et al., 2011), but this remains poorly constrained and is worth pursuing.

This study demonstrates the mineralization at Qulong is comprised of multiple short-lived pulses (tens of kyrs) based on direct dating of the ore mineral molybdenite, but at what level this multi-pulsed mineralization process controls the formation of giant deposits needs to be further explored. Further, this pulsed magmatic-hydrothermal process is directly linked with the evolution of the magma chamber at depth (Buret et al., 2016; Tapster et al., 2016), which is currently poorly understood. An interesting finding is that both the Miocene ice-sheet expansion and the metals enrichment process at Qulong share similar periodic pattern, whether there is a link between the orbital configuration of Earth and porphyry ore formation is unclear but definitely worthy investigation.

In addition, the Re-Os and U-Pb geochronology, and fluid inclusion data are interpreted to propose that the thermal cooling of the Qulong hydrothermal history was 2.5 times quicker than previous estimates based on thermochronology. As a result this study suggests the need to refine the model used in thermochronology studies, and

future thermal history studies should take the thermal contribution associated with magmatic fluids into account.

Although the involvement of meteoric water has been documented in many porphyry deposits worldwide (Friedman et al., 1974; Sun and Eadington, 1987; Hedenquist and Aoki, 1991; Sheets et al., 1996; Selby et al., 2001; D'Errico et al., 2012), it is generally accepted that its role in the deposition of ore minerals is negligible. Correlating high precision geochronology and high spatial resolution geochemical data has demonstrated to be a promising tool to evaluate the fluid evolution process of hydrothermal deposits. The involvement of meteoric water at Qulong has been suggested in this study as the trigger of sulfide mineral precipitation. This interpretation is in accord with recent studies using either geochemical or modelling methodologies emphasize the critical role of meteoric water in the formation of several deposit types (Lackey et al., 2011; D'Errico et al., 2012; Weis et al., 2012; Beaudoin and Chiaradia, 2016; Fekete et al., 2016). Further research will permit the development of genetic models of hydrothermal deposits that initially alluded to nearly 40 years ago, but were variably discredited.

The rapid metals deposition process proposed in this study should be further tested in other class deposits, e.g., the giant ones in Andes. Although Qulong is the biggest porphyry copper deposit in China, but it is still much smaller than these documented in subduction settings, does the short duration actually due to its smaller size or tectonic setting is still unknown, and should be tested in deposits of different sizes and tectonic settings in further research.

The role of meteoric water proposed in this study is supported by other studies, however, it should be noted that there are also many porphyry copper deposits that does not involve detectable involvement of meteoric water. The reasons for the lack

of meteoric water in some deposits can be the similarity of oxygen isotopes in magmatic water and meteoric water makes it difficult to trace involvement of meteoric water in small amount, e.g., < 20 %. If this is the case, hydrogen isotopes should be more sensitive and should be conducted in future studies.

This study is focused on the metals enrichment process, the outcome also has broad implications for the exploration industry. For example, the thickness of erosion can be used to guide exploration strategy, where limited erosion indicates good preservation while intensive erosion potentially means the orebody is lost. In general, with the mineralization age tightly constrained, the mineralization potential of a given intrusion can be evaluated with higher confidence, e.g., if the age of a given intrusion is identical with the known mineralization in the same area, mineralization accompanying that intrusion is expected. As meteoric water potentially controls the efficiency of metals deposition, when limited meteoric water is involved during the emplacement of an intrusion, less mineralization is expected in general.

Lastly, the uncertainties of spike calibration and decay constants currently are the major limiting factor of the resolution when comparing Re-Os and U-Pb dates. As such an urgent goal for the Re-Os community is to develop a shared spike across laboratories similar to that carried out for the U-Pb community (Bowring et al., 2011; McLean et al., 2011; Condon et al., 2015; McLean et al., 2015) to permit an improved cross-calibration between the Re-Os and U-Pb radiometric clocks to reduce these uncertainties (Chiaradia et al., 2013).

5.5 References

Beaudoin, G., Chiaradia, M., 2016. Fluid mixing in orogenic gold deposits: Evidence from the H-O-Sr isotope composition of the Val-d'Or vein field (Abitibi, Canada). Chemical Geology 437, 7-18.

Bowring, J., McLean, N.M., Bowring, S., 2011. Engineering cyber infrastructure for U-Pb geochronology: Tripoli and U-Pb_Redux. Geochemistry, Geophysics, Geosystems 12.

Buret, Y., von Quadt, A., Heinrich, C., Selby, D., Wälle, M., Peytcheva, I., 2016. From a long-lived upper-crustal magma chamber to rapid porphyry copper emplacement: Reading the geochemistry of zircon crystals at Bajo de la Alumbrera (NW Argentina). Earth and Planetary Science Letters 450, 120-131.

Chiaradia, M., Schaltegger, U., Spikings, R., Wotzlaw, J.-F., Ovtcharova, M., 2013. How Accurately Can We Date the Duration of Magmatic-Hydrothermal Events in Porphyry Systems?—An Invited Paper. Economic Geology 108, 565-584.

Condon, D.J., Schoene, B., McLean, N.M., Bowring, S.A., Parrish, R.R., 2015. Metrology and traceability of U-Pb isotope dilution geochronology (EARTHTIME Tracer Calibration Part I). Geochimica Et Cosmochimica Acta 164, 464-480.

Currie, B.S., Rowley, D.B., Tabor, N.J., 2005. Middle Miocene paleoaltimetry of southern Tibet: Implications for the role of mantle thickening and delamination in the Himalayan orogen. Geology 33, 181-184.

D'Errico, M.E., Lackey, J.S., Surpless, B.E., Loewy, S.L., Wooden, J.L., Barnes, J.D., Strickland, A., Valley, J.W., 2012. A detailed record of shallow hydrothermal fluid flow in the Sierra Nevada magmatic arc from low- 18O skarn garnets. Geology 40, 763-766.

Fekete, S., Weis, P., Driesner, T., Bouvier, A.-S., Baumgartner, L., Heinrich, C.A., 2016. Contrasting hydrological processes of meteoric water incursion during magmatic–hydrothermal ore deposition: An oxygen isotope study by ion microprobe. Earth and Planetary Science Letters 451, 263-271.

Friedman, I., Lipman, P.W., Obradovich, J.D., Gleason, J.D., Christiansen, R.L., 1974. Meteoric water in magmas. Science 184, 1069-1072.

Hedenquist, J.W., Aoki, M., 1991. Meteoric Interaction with Magmatic Discharges in Japan and the Significance for Mineralization. Geology 19, 1041-1044.

Kouzmanov, K., Pokrovski, G.S., 2012. Hydrothermal controls on metal distribution in porphyry Cu (-Mo-Au) systems. Special Publication of the Society of Economic Geologists 16, 573–618.

Lackey, J.S., Romero, G.A., Bouvier, A.S., Valley, J.W., 2011. Dynamic growth of garnet in granitic magmas. Geology 40, 171-174.

Li, Y., Selby, D., Feely, M., Costanzo, A., Li, X.-H., 2016. Fluid inclusion characteristics and molybdenite Re-Os geochronology of the Qulong porphyry copper-molybdenum deposit, Tibet. Mineralium Deposita.

McLean, N.M., Bowring, J.F., Bowring, S.A., 2011. An algorithm for U-Pb isotope dilution data reduction and uncertainty propagation. Geochemistry, Geophysics, Geosystems 12, n/a-n/a.

McLean, N.M., Condon, D.J., Schoene, B., Bowring, S.A., 2015. Evaluating uncertainties in the calibration of isotopic reference materials and multi-element isotopic tracers (EARTHTIME Tracer Calibration Part II). Geochimica Et Cosmochimica Acta 164, 481-501.

McPhie, J., Kamenetsky, V., Allen, S., Ehrig, K., Agangi, A., Bath, A., 2011. The fluorine link between a supergiant ore deposit and a silicic large igneous province. Geology 39, 1003-1006.

Mercer, C.N., Reed, M.H., Mercer, C.M., 2015. Time Scales of Porphyry Cu Deposit Formation: Insights from Titanium Diffusion in Quartz. Economic Geology 110, 587-602.

Raymo, M., Ruddiman, W.F., 1992. Tectonic forcing of late Cenozoic climate. Nature 359, 117-122.

Richards, J.P., 2015. Tectonic, magmatic, and metallogenic evolution of the Tethyan orogen: From subduction to collision. Ore Geology Reviews 70, 323-345.

Rowley, D.B., Currie, B.S., 2006. Palaeo-altimetry of the late Eocene to Miocene Lunpola basin, central Tibet. Nature 439, 677-681.

Schaltegger, U., Schmitt, A.K., Horstwood, M.S.A., 2015. U-Th-Pb zircon geochronology by ID-TIMS, SIMS, and laser ablation ICP-MS: Recipes, interpretations, and opportunities. Chemical Geology 402, 89-110.

Schoene, B., 2014. 4.10 - U–Th–Pb Geochronology, in: Turekian, H.D.H.K. (Ed.), Treatise on Geochemistry (Second Edition). Elsevier, Oxford, pp. 341-378.

Schoene, B., Condon, D.J., Morgan, L., McLean, N., 2013. Precision and Accuracy in Geochronology. Elements 9, 19-24.

Selby, D., Nesbitt, B.E., Creaser, R.A., Reynolds, P.H., Muehlenbachs, K., 2001. Evidence for a nonmagmatic component in potassic hydrothermal fluids of porphyry Cu-Au-Mo systems, Yukon, Canada. Geochimica Et Cosmochimica Acta 65, 571-587.

Sheets, R.W., Nesbitt, B.E., Muehlenbachs, K., 1996. Meteoric water component in magmatic fluids from porphyry copper mineralization, Babine Lake area, British Columbia. Geology 24, 1091-1094.

Sillitoe, R.H., 2010. Porphyry Copper Systems. Economic Geology 105, 3-41.

Stein, H.J., 2014. 13.4 - Dating and Tracing the History of Ore Formation, in: Turekian, H.D.H.K. (Ed.), Treatise on Geochemistry (Second Edition). Elsevier, Oxford, pp. 87-118.

Sun, S.S., Eadington, P.J., 1987. Oxygen Isotope Evidence for the Mixing of Magmatic and Meteoric Waters during Tin Mineralization in the Mole Granite, New-South-Wales, Australia. Economic Geology 82, 43-52.

Tapster, S., Condon, D.J., Naden, J., Noble, S.R., Petterson, M.G., Roberts, N.M.W., Saunders, A.D., Smith, D.J., 2016. Rapid thermal rejuvenation of high-crystallinity

magma linked to porphyry copper deposit formation; evidence from the Koloula Porphyry Prospect, Solomon Islands. Earth and Planetary Science Letters 442, 206-217.

Von Quadt, A., Erni, M., Martinek, K., Moll, M., Peytcheva, I., Heinrich, C.A., 2011. Zircon crystallization and the lifetimes of ore-forming magmatic-hydrothermal systems. Geology 39, 731-734.

Weis, P., Driesner, T., Heinrich, C.A., 2012. Porphyry-copper ore shells form at stable pressure-temperature fronts within dynamic fluid plumes. Science 338, 1613-1616.

Yin, Q.Z., Jacobsen, S.B., Lee, C.T., McDonough, W.F., Rudnick, R.L., Horn, I., 2001. A gravimetric K2OsCl6 standard: Application to precise and accurate Os spike calibration. Geochimica Et Cosmochimica Acta 65, 2113-2127.

Zhao, J., Qin, K., Xiao, B., McInnes, B., Li, G., Evans, N., Cao, M., Li, J., 2016. Thermal history of the giant Qulong Cu–Mo deposit, Gangdese metallogenic belt, Tibet: Constraints on magmatic–hydrothermal evolution and exhumation. Gondwana Research 36, 390-409.

Zhisheng, A., Kutzbach, J.E., Prell, W.L., Porter, S.C., 2001. Evolution of Asian monsoons and phased uplift of the Himalaya–Tibetan plateau since Late Miocene times. nature 411, 62-66.